

CONJUGATED POLYMERS AND ORGANIC CATIONS FOR
OPTOELECTRONIC APPLICATIONS

A THESIS SUBMITTED TO
THE GRADUATE SCHOOL OF NATURAL AND APPLIED SCIENCES
OF
MIDDLE EAST TECHNICAL UNIVERSITY

BY

MUSTAFA YAŞA

IN PARTIAL FULFILLMENT OF THE REQUIREMENTS
FOR
THE DEGREE OF DOCTOR OF PHILOSOPHY
IN
POLYMER SCIENCE AND TECHNOLOGY

JANUARY 2022

Approval of the thesis:

**CONJUGATED POLYMERS AND ORGANIC CATIONS FOR
OPTOELECTRONIC APPLICATIONS**

submitted by **MUSTAFA YAŞA** in partial fulfillment of the requirements for the degree of **Doctor of Philosophy in Polymer Science and Technology, Middle East Technical University** by,

Prof. Dr. Halil Kalıpçılar
Dean, Graduate School of **Natural and Applied Sciences**

Prof. Dr. Necati Özkan
Head of the Department, **Polymer Science and Technology**

Prof. Dr. Levent Toppare
Supervisor, **Polymer Science and Technology, METU**

Prof. Dr. Yasemin Arslan Udum
Co-Supervisor, Technical Sciences Vocational School, **Gazi University**

Examining Committee Members:

Prof. Dr. Ali Çırpan
Chemistry, METU

Prof. Dr. Levent Toppare
Polymer Science and Technology, METU

Prof. Dr. Ertuğrul Şahmetlioğlu
Faculty of Engineering Architecture and Design, Engineering
Basic Sciences, Kayseri University

Prof. Dr. Metin Ak
Chemistry, Pamukkale University

Prof. Dr. İrem Erel Göktepe
Chemistry, METU

Date: 27.01.2022

I hereby declare that all information in this document has been obtained and presented in accordance with academic rules and ethical conduct. I also declare that, as required by these rules and conduct, I have fully cited and referenced all material and results that are not original to this work.

Name Last name : Mustafa Yaşa

Signature :

ABSTRACT

CONJUGATED POLYMERS AND ORGANIC CATIONS FOR OPTOELECTRONIC APPLICATIONS

Yaşa, Mustafa

Doctor of Philosophy, Polymer Science and Technology

Supervisor: Prof. Dr. Levent Toppare

Co-Supervisor: Prof. Dr. Yasemin Arslan Udum

January 2022, 238 pages

There are several studies on organic solar cells based on conjugated polymers in literature, and various new materials are being designed. The Donor-Acceptor approach has been the most common approach for designing and synthesizing conjugated polymers. In this study, thienopyrroledione bearing conjugated polymers were synthesized via Stille and Suzuki polycondensation reactions. In the first part of this thesis, the polymers obtained via Stille polycondensation were employed to fabricate organic solar cells (OSCs). Both non-fullerene and fullerene-based devices were fabricated. The best non-fullerene-based device performed a power conversion efficiency of 7.94%, whereas the best fullerene-based device performed 7.62%. In the second part, one of the polymers obtained via Stille polycondensation was used to fabricate biosensors for catechol detection. The biosensor exhibited linearity between 1.25 and 175 μM catechol, with a LOD of 1.23 μM and sensitivity of 737.4 $\mu\text{A}.\text{mM}^{-1}.\text{cm}^{-2}$. In the third part, the polymers obtained via Suzuki polycondensation were examined to see the effect of a second acceptor unit through random polymerization, and the study revealed that the introduction of a selenophene moiety decreased the optical band gaps of the polymers whereas the introduction of a second

acceptor moiety increased the optical band gaps. As another emerging technology for energy conversion, Perovskite solar cells have been the point of attraction. Therefore, the last part covers syntheses of a series of chalcogenophene containing molecules to be employed as organic cations for surface treatment of 3D perovskite films in the fabrication of Perovskite solar cells. The best perovskite solar cell device constructed with the utilization of one of the molecules exhibited a power conversion efficiency of 22.43%.

Keywords: Conjugated Polymers, Thienopyrroledione, Organic Solar Cells, Biosensors, Perovskite Solar Cells

ÖZ

OPTOELEKTRONİK UYGULAMALAR İÇİN KONJÜGE POLİMERLER VE ORGANİK KATYONLAR

Yaşa, Mustafa

Doktora, Polimer Bilim ve Teknolojisi

Tez Yöneticisi: Prof. Dr. Levent Toppare

Ortak Tez Yöneticisi: Prof. Dr. Yasemin Arslan Udum

Ocak 2022, 238 sayfa

Literatürde, konjüge polimer tabanlı organik güneş hücreleri ilgili bir çok çalışma mevcuttur ve bu alanda yeni malzemeler geliştirilmeye devam etmektedir. Konjüge polimerlerin tasarımı için Donör-Akseptör yaklaşımı en çok başvurulan yöntem olmuştur. Bu çalışmada, tiyeniropirolidion içeren konjüge polimerler Stille ve Suzuki polikondenzasyon reaksiyonları ile sentezlenmiştir. Bu tezin ilk kısmında, Stille polikondenzasyon yöntemi ile elde edilen polimerler organik güneş hücrelerinin yapımında kullanılmıştır. Fulleren içeren ve fulleren içermeyen organik güneş hücreleri tasarlanmıştır. Fulleren içermeyen hücrelerden elde edilen en iyi güç dönüşüm verimi %7,94'dir. Bunun yanında, fulleren içeren hücrelerden elde edilen en iyi güç dönüşüm verimi de %7,62 olarak kaydedilmiştir. İkinci kısımda ise Stille polikondenzasyon yöntemi ile elde edilen polimerlerden bir tanesi katekol analizi için tasarlanan biyosensör yapımında kullanılmıştır. Elde edilen biyosensör 1,23 μM tayin limiti ve 737,4 $\mu\text{A.mM}^{-1}.\text{cm}^{-2}$ hassasiyet ile birlikte 1,25 ve 175 μM katekol aralığında lineerlik göstermiştir. Üçüncü kısımda ise ikinci bir akseptör ünitesinin Suzuki polikondenzasyon yöntemi ile elde edilen rastgele polimerlerin iskeletine eklenmesinin etkileri incelenmiştir. Gelişmekte olan bir yeni güneş enerjisi

teknolojisi de Perovskit güneş hücreleri olup dikkatleri çekmeyi başarmıştır. Bu nedenle, bu tezin son kısmı 3B perovskit filminin iyileştirilmesinde kullanılabilmesi için kalkojen içeren organik katyonların sentezine ayrılmıştır. Tasarlanan perovskit hücrelerinden elde edilem en iyi güç dönüşüm verimi %22,43 olarak kaydedilmiştir.

Anahtar Kelimeler: Konjüge polimerler, Organik Güneş Hücreleri, Biyosensörler, Perovskit Güneş Hücreleri

To my parents

ACKNOWLEDGMENTS

I am incredibly grateful to my supervisor Prof. Dr. Levent Toppare. He has been both an advisor and a family member to me. I have been fortunate to be a student of such a supervisor who cared for me so much and always valued my work.

I would like to pay special thanks to my co-supervisor, Prof. Dr. Yasemin Arslan Udum, for her guidance, advice, criticism, encouragement, and insight throughout the research.

I would like to extend my special thanks to Assoc. Prof. Dr. Görkem Günbaş for his suggestions, comments, encouragement, and guidance throughout the research.

I would like to thank Prof. Dr. Ali Çırpan, Assoc. Prof. Dr. Özgül Persil Çetinkol, and Assist. Prof. Dr. Erol Yıldırım for their collaboration.

Assoc. Prof. Dr. Şerife Özdemir Hacıoğlu is gratefully acknowledged for her assistance in electrochemical studies.

Gizem Atakan Alkan, Aliekber Karabağ, Figen Varlıoğlu Yaylalı, and Osman Karaman, I know you are always there for me. What I know for sure is that I am so lucky to have you guys. And Dilan Ece Dikbiyık, Cevahir Ceren Akgül, Çağlayan Kızıleniş, Sena Tarım, I very much appreciate your consideration on providing a perfect environment during writing this thesis.

Eda Alemdar Yılmaz, Mert Can Erer, and Dr. Gönül Hızalan Özsoy, I am grateful for your efforts in the fabrication of organic solar cells. Without you and your insight, it would be challenging to go further.

Ecem Aydan Alkan, Lab D156 would not have such an enjoyable environment without you.

Dear Kia, your encouragement and advice opened a new path in my life. I owe you a lot, my friend.

All Toppare, Günbaşı (Flair Lab), and Çırpan Research Group members are gratefully acknowledged.

This work is partially funded by the Scientific and Technological Research Council of Turkey under grant number TÜBİTAK 118M061.

TABLE OF COTENTS

ABSTRACT	v
ÖZ.....	vii
ACKNOWLEDGMENTS	x
TABLE OF COTENTS	xii
LIST OF TABLES	xvi
LIST OF FIGURES.....	xviii
LIST OF ABBREVIATIONS	xxii
LIST OF SYMBOLS.....	xxv
CHAPTERS	
1 CONJUGATED POLYMERS FOR ORGANIC ELECTRONICS	1
1.1 Conjugated Polymers: Way to synthetic metals.....	1
1.1.1 Preparation of CPs	2
1.2 Applications of CPs.....	7
1.2.1 Organic Solar Cells.....	7
1.2.2 Biosensors.....	11
1.2.3 Electrochromism.....	17
1.3 Aim of the thesis.....	18
2 NON-FULLERENE OSCs BASED ON TPD COMPRISING POLYMERS	21
2.1 Literature Review	21
2.1.1 Preparation TPD and TPD-based conjugated polymers	23
2.1.2 TPD-based conjugated polymers used as Donors.....	25
2.1.3 TPD-based conjugated polymers used as Acceptors	40

2.2	Aim of the study.....	43
2.3	Non-fullerene organic solar cells based on thienopyrroledione and chalcogenophene comprising random copolymers	44
2.3.1	Introduction	45
2.3.2	Experimental	47
2.3.3	Results	55
2.3.4	Conclusions	70
2.4	Effect of introduction of a second TPD unit with different donor moieties on photovoltaic performance	71
2.4.1	Syntheses of the polymers (ME5 and ME6)	72
2.4.2	Results	73
2.4.3	Electrochemical and spectroelectrochemical investigations	73
2.4.4	OSC studies	76
2.5	Thienothiophene and benzochalcodiazoles containing conjugated polymers.....	77
2.5.1	Experimental	78
2.5.2	Syntheses of the monomers and the polymers	78
2.5.3	Results	82
3	CONSTRUCTION OF AMPEROMETRIC BIOSENSOR MODIFIED WITH CONDUCTING POLYMER/CARBON DOTS FOR THE ANALYSIS OF CATECHOL	87
3.1	Introduction.....	88
3.2	Experimental.....	90
3.2.1	Syntheses of CDs and PFTBDT	91
3.2.2	Preparation of modified electrode for biosensor application	93

3.2.3	Amperometric measurements for detection of catechol	94
3.2.4	Computational Studies	95
3.3	Results	95
3.3.1	Electrochemical and optical properties of the polymer	95
3.3.2	Electrochemical and surface characterization of electrodes and carbon dot nanoparticles	98
3.3.3	Optimization of the modified biosensor	100
3.3.4	Analytical merits of the catechol biosensor	102
3.3.5	Real sample analysis	105
3.3.6	Computational results	106
3.4	Conclusions	109
4	EFFECT OF RANDOM COPOLYMERIZATION ON THE OPTICAL PROPERTIES OF SELENOPHENE AND TPD CONJUGATED POLYMERS	111
4.1	Introduction	111
4.2	Methods, Instrumentation, and Experimental	113
4.2.1	Synthesis of polymers	114
4.3	Results and Discussion	117
4.4	Conclusions	123
5	ORGANIC CATIONS FOR TREATMENT OF 3D PEROVSKITE FILMS	125
5.1	Brief History	126
5.2	Structure of Perovskite Materials	126
5.3	Aim of the study	127
5.4	Phenylmethanamine-based organic cations	128
5.4.1	Syntheses of phenylmethanamine-based organic cations	129

5.4.2	Experimental and results	134
5.5	Syntheses of aniline-based organic halide cations	136
5.5.1	Synthesis.....	137
5.6	Synthesis of pyridine-based organic halide cation.....	139
5.6.1	Synthesis.....	139
6	OUTLOOK	141
	REFERENCES	143
	APPENDICES	
A.	NMR Spectra	181
	CURRICULUM VITAE	235

LIST OF TABLES

TABLES

Table 2.1 Photovoltaic properties of TPD-based conjugated polymers incorporated with thiophene	27
Table 2.2 Photovoltaic properties of TPD-based conjugated polymers incorporated with thieno [3,2-b]thiophene	32
Table 2.3 Photovoltaic properties of biTPD-based conjugated polymers	35
Table 2.4 Photovoltaic properties of TPD-based random conjugated polymers	39
Table 2.5 Photovoltaic properties of TPD-based acceptor conjugated polymers ...	42
Table 2.6 Molecular weights and PDI values of ME1, ME2, ME3, and ME4	54
Table 2.7 Electrochemical properties of ME1-ME4	57
Table 2.8 Optical properties of ME1-ME4	59
Table 2.9 Colors of (a) ME1, (b) ME2, (c) ME3, and (d) ME4 films at neutral and oxidized/reduced states with intermediate colors	59
Table 2.10 Kinetic properties of ME1-ME4	62
Table 2.11 Photovoltaic parameters of ME1-ME4:ITIC devices	64
Table 2.12 Photovoltaic parameters of ME1-ME4:PC ₇₁ BM devices	64
Table 2.13 Electrochemical properties of ME6	74
Table 2.14 Optical properties of ME6	75
Table 2.15 Colors of ME6 film at neutral and reduced states	76
Table 2.16 Kinetic properties of ME6	76
Table 2.17 Photovoltaic parameters of ME6:ITIC/PC ₇₁ BM devices	77
Table 2.18 Electrochemical properties of ME7 and ME8	83
Table 2.19 Colors of ME7 and ME8 film at neutral and oxidized/reduced states ..	84
Table 2.20 Kinetic properties of ME7 and ME8	85
Table 3.1 Analytical merits comparison of the proposed biosensor and the previously reported laccase-based biosensors for electrochemical detection/sensing of catechol	103
Table 3.2 Determination of catechol in tap water	105

Table 4.1 Molecular weights and PDI values of PS1, and PS2, RPS1, and RPS2	116
Table 4.2 Electrochemical parameters for the polymers.....	118
Table 4.3 Color changes and L, a, and b values of PS1, PS2, RPS1, and RPS2 ..	118
Table 4.4 Optical properties of PS1, PS2, RPS1, and RPS2	122
Table 4.5 Kinetic properties of PS1, PS2, RPS1, and RPS2	123
Table 5.1 Photovoltaic parameters of compound 21 containing devices with different concentrations.....	135

LIST OF FIGURES

FIGURES

Figure 1.1. Chemical structures of common conjugated polymers	2
Figure 1.2. Typical mechanism of Stille Coupling.....	4
Figure 1.3. The typical mechanism of Suzuki Coupling	5
Figure 1.4. General mechanism of DHAP through CMD ²⁴	6
Figure 1.5. Structure of a) bilayer and b) BHJ OSCs	8
Figure 1.6. J-V curve of an operating OSC	11
Figure 1.7. Typical representation of a biosensor	12
Figure 1.8. Enzyme immobilization methods.....	15
Figure 2.1. Two synthetic routes for TPD	24
Figure 2.2. Syntheses of TPD-based conjugated polymers via DHAP and Stille/Suzuki Polycondensation	25
Figure 2.3. Structures of TPD-based conjugated polymers bearing thiophene moiety	26
Figure 2.4. Structures of TPD-based conjugated polymers bearing thieno [3,2- b]thiophene moiety	30
Figure 2.5. Structures of biTPD-based conjugated polymers.....	36
Figure 2.6. Structures of TPD-based random conjugated polymers	37
Figure 2.7. Structures of TPD-based acceptor conjugated polymers	41
Figure 2.8. Synthetic route for M1 and M2	48
Figure 2.9. Synthetic routes for ME1-ME4	53
Figure 2.10. Single scan cyclic voltammograms of (a) ME1, (b) ME2, (c) ME3, and (d) ME4 on ITO electrode in 0.1 M TBAPF ₆ /ACN electrolyte/solvent couple at a scan rate of 100 mV/s.	56
Figure 2.11. Electronic absorption spectra of ME1-ME4 in 0.1 M TBAPF ₆ /ACN solution between 0.0 V and 1.4 V for ME1 (a), 0.0 V and 1.4 V for ME2 (b), 0.0 V and 1.5 V for ME3 (c), and (d) 0.0 V and 1.6 V for ME4.....	58

Figure 2.12. Percent transmittance changes for (a) ME1, (b), ME2, (c) ME3, and (d) ME4 in 0.1 M TBAPF ₆ /ACN solution.	61
Figure 2.13. Current-voltage characteristics of (a) ME1/ME2:ITIC and (b) ME3/ME4:PC ₇₁ BM devices under AM 1.5 G solar simulator.	65
Figure 2.14. 2D AFM images of (a) ME1:ITIC, (b) ME2:ITIC, (c) ME1:ITIC w/ 1% CN, d) ME1:PC ₇₁ BM, e) ME2:PC ₇₁ BM	66
Figure 2.15. 3D AFM images of (a) ME1:ITIC, (b) ME2:ITIC, (c) ME1:ITIC w/ 1% CN, (d) ME1:PC ₇₁ BM, (e) ME2:PC ₇₁ BM.....	66
Figure 2.16. TEM images of (a) ME1:ITIC, (b) ME2:ITIC, (c) ME1:ITIC w/1% CN (d) ME1:PC ₇₁ BM, (e) ME2:PC ₇₁ BM	67
Figure 2.17. 2D AFM images of (a) ME3:PC ₇₁ BM, (b) ME3:PC ₇₁ BM w/6% DPE, (c) ME4:PC ₇₁ BM, (d) ME4:PC ₇₁ BM w/6% DPE.....	67
Figure 2.18. 3D AFM images of (a) ME3:PC ₇₁ BM, (b) ME3:PC ₇₁ BM w/ 6%DPE, (c) ME4:PC ₇₁ BM, (d) ME4:PC ₇₁ BM w/6%DPE.....	68
Figure 2.19. TEM images of a) ME3:PC ₇₁ BM, b) ME3:PC ₇₁ BM w/6% DPE, c) ME4:PC ₇₁ BM, d) ME4:PC ₇₁ BM w/6% DPE.....	69
Figure 2.20. EQE curves of a) ME1: ITIC and ME2: ITIC, and b) ME1-ME4:PC ₇₁ BM devices.....	70
Figure 2.21. Synthetic routes for ME5 and ME6	72
Figure 2.22. Cyclic voltammograms of ME6 on ITO electrode in 0.1 M TBAPF ₆ /ACN electrolyte/solvent couple at a scan rate of 100 mV/s	74
Figure 2.23. (a) Electronic absorption spectra of ME6 solution between 0.0 V and 1.4 V, (b) Percent transmittance changes for ME6 in 0.1 M TBAPF ₆ /ACN solution.	75
Figure 2.24. Current-voltage characteristics of (a) the best devices based on ME6:ITIC/PC ₇₁ BM and (b) ME6:PC ₇₁ BM under AM 1.5 G solar simulator.	77
Figure 2.25. Synthetic route for the monomer M3	78
Figure 2.26. Synthetic routes for ME7 and ME8	81
Figure 2.27. Cyclic voltammograms of ME7 and ME8 on ITO electrode in 0.1 M TBAPF ₆ /ACN electrolyte/solvent couple at a scan rate of 100 mV/s	83

Figure 2.28. Electronic absorption spectra in 0.1 M TBAPF ₆ /ACN solution between (a), 0.0 V and 1.4 V for ME7 (b), 0.0 V and 1.25 V for ME8	84
Figure 2.29. Percent transmittance changes for (a) ME7 and (b) ME8 in 0.1 M TBAPF ₆ /ACN solution.....	85
Figure 3.1. Synthetic route for PFTBDT.....	93
Figure 3.2. Design of the biosensor constructed for this study	94
Figure 3.3. (a) Cyclic voltammogram of PFTBDT in 0.1 M TBAPF ₆ /ACN solution and (b) electrochemical parameters of PFTBDT.....	96
Figure 3.4. (a) Electronic absorption spectra and (b) Colorimetric measurements of PFTBDT thin film in 0.1 M TBAPF ₆ /ACN solution	97
Figure 3.5. (a) Percent transmittance change at 515 and 755 nm with respect to time and (b) kinetic parameters obtained for PFTBDT thin film in 0.1 M TBAPF ₆ /ACN solution at 515 nm and 755 nm.....	98
Figure 3.6. Cyclic voltammograms of GE, modified GE/CDs/PFTBDT and GE/CDs/PFTBDT/Lac electrodes	99
Figure 3.7. SEM images of modified surfaces (a) GE/CDs/PFTBDT (b) GE/CDs/PFTBDT /Lac	100
Figure 3.8. The effect of (a) CD amount, (b) polymer amount, (c) laccase amount and (d) pH on laccase biosensor response	101
Figure 3.9. (a) Calibration curve of the modified electrode for catechol (in 50 mM acetate buffer, pH 5.5, 25 °C, -0.3 V) (b) Amperometric responses of the modified electrode in the presence of different concentrations of catechol	103
Figure 3.10. The response of the modified biosensor toward (a) different substrates including catechol (b) phenol derivatives including 125 µM catechol in 50 mM acetate buffer (pH 5.5) at - 0.3 V.....	105
Figure 3.11. (a) Star shape conformation of PFTBDT (conf1), (b) planar conformation of PFTBDT (conf2), (c) Electrostatic potential surface (ESP) of conf1, (d) ESP of conf2, (e) Contour plots of the HOMO for conf1, (f) HOMO for conf2, (g) LUMO for conf1, (h) LUMO for conf2, (i) LUMO for conf1 and catechol complex, (j) LUMO for conf2 and catechol complex, (k) interaction and	

ESP of conf1 and catechol complex, (l) ESP of conf2 and catechol complex, (m) interaction and ESP of conf2 and catechol complex.....	107
Figure 4.1. Synthetic routes for the polymers	116
Figure 4.2. Single scan cyclic voltammograms of a) PS1, b) PS2, c) RPS1 d) RPS2 on ITO in 0.1 M TBAPF ₆ /ACN electrolyte/solvent couple at the scan rate of 100 mV·s ⁻¹	120
Figure 4.3. Changes in electronic absorption spectra of a) PS1, (b) PS2, c) RPS1 d) RPS2 upon stepwise oxidative doing in a 0.1 M solution of TBAPF ₆ /CAN.....	121
Figure 4.4. Percent transmittance and electrochromic switching changes of (a) PS1, (b) PS2, (c) RPS1, (d) RPS2	123
Figure 5.1. The general structure of a 3D perovskite material	127
Figure 5.2. Synthetic route for the syntheses of phenylmethanamine-based organic cations	129
Figure 5.3. Structure of the devices fabricated in this study.....	134
Figure 5.4. Methodology of device fabrication.....	134
Figure 5.5. Photovoltaic parameters of compound 21 containing devices with different concentrations (a) J-V, (b) EQE.....	136
Figure 5.6. Synthetic routes for the compounds 28 and 29.....	137
Figure 5.7. Synthetic route for the compound 31	139

LIST OF ABBREVIATIONS

ABBREVIATIONS

OSC/OPV	Organic Solar Cell/Organic Photovoltaic
OLED	Organic Light-Emitting Diode
OFET	Organic Field-Effect Transistor
CP	Conjugated/Conducting Polymer
PPV	Poly(p-phenylene vinylene)
PANI	Poly(aniline)
PT	Poly(thiophene)
PPP	Poly(p-phenylene)
PEDOT	Poly(3,4-ethylenedioxythiophene)
PF	Poly(fluorene)
DHA	Direct Heteroarylation
DHAP	Direct Heteroarylation Polymerization
CMD	Concerted Metalation-Deprotonation
PCE	Power Conversion Efficiency
BHJ	Bulk Heterojunction
D:A	Donor:Acceptor
PC ₆₁ BM	Phenyl-C61-butyric acid methyl ester
P3HT	poly(3-hexylthiophene)
HOMO	Highest Occupied Molecular Orbital

LUMO	Lowest Unoccupied Molecular Orbital
ITO	Indium Tin Oxide
FF	Fill Factor
PEDOT:PSS	Polyethylenedioxythiophene:Polystyrenesulfonate
ECD	Electrochromic Device
CV	Cyclic Voltammetry
NFA	Non-fullerene Acceptor
TPD	Thienopyrroledione
PSC	Polymer Solar Cell
FA	Fullerene Acceptor
BT	Benzothiadiazole
BTA	Benzotriazole
ICT	Intramolecular Charge Transfer
BDT	Benzodithiophene
BiTPD	Bithienopyrroledione
ATRFTIR	Attenuated Total Reflectance Fourier Transform Infrared
SEC	Size Exclusion Chromatography
LiF	Lithium Fluoride
AFM	Atomic Force Microscopy
TEM	Transmission Electron Microscopy
NMR	Nuclear Magnetic Resonance
Et ₂ O	Diethyl ether

DMF	Dimethylformamide
DCM	Dichloromethane
TFA	Trifluoroacetic acid
THF	Tetrahydrofuran
PDI	Polydispersity Index
EQE	External Quantum Efficiency
TBAPF ₆	Tetrabutylammonium hexafluorophosphate
ACN	Acetonitrile
UV-Vis	Ultraviolet-Visible
CB	Chlorobenzene
ODCB	1,2-Dichlorobenzene or <i>o</i> -dichlorobenzene
DIO	Diiodooctane
EtOH	Ethyl alcohol
CD	Carbon Dot
LDR	Linear Dynamic Range
LOD	Limit of Detection
XRD	X-ray Diffraction
DFT	Density Functional Theory
CIE	Commission Internationale de l'Eclairage
GE	Graphite Electrode
DMSO	Dimethyl Sulfoxide

LIST OF SYMBOLS

SYMBOLS

V_{oc}	Open-circuit Voltage
J_{sc}	Short-circuit Current Density
E_g	Band gap
M_n	Number-average molecular weight
M_w	Weight-average molecular weight
kDa	Kilodalton
Cz	Carbazole
Fl	Fluorene
L	Luminescence
a	Hue
b	Saturation

CHAPTER 1

CONJUGATED POLYMERS FOR ORGANIC ELECTRONICS

Solid and rapidly growing apprehensions for global warming and a limited reserve of fossil fuels drive humanity to seek cost-effective, green, and renewable energy resources. Therefore, the quest for more efficient technologies has increased. As a result, intensive research and industrialization play a pivotal role in developing and utilizing these sources. Since the sun is the most significant energy source, generating energy from sunlight is the cleanest and most sustainable technology ¹. Photovoltaic technology is a pivotal way to convert sunlight to energy. Upon solar irradiation, photovoltaics (Organic Solar Cells, OSCs) convert light into electrical power. Here, solution-processed OSCs come into play. For OSCs, conjugated polymers have been the most utilized materials for the past decades. In addition to solar devices, conjugated polymers were used for many other applications like electrochromism, biosensors, organic light-emitting diodes (OLEDs), organic field-effect transistors (OFETs), etc. Conjugated polymers designed and synthesized for this thesis study were implemented in the application of electrochromism, biosensors, and OSCs.

1.1 Conjugated Polymers: Way to synthetic metals

Since the discovery that conjugated polymers (CPs) can conduct electricity, they have been the main components in the design and fabrication of organic electronics. It all started with doping polyacetylene with halogen in 1977 ². Heeger and co-workers obtained conducting polyacetylene upon oxidation with iodine and, this achievement brought the Nobel Prize in Chemistry in 2000. Burroughs and co-workers discovered electroluminescence in poly(p-phenylene vinylene) (PPV), and this discovery ushered in a new era of light-emitting diodes ³. Following these

discoveries, numerous conjugated polymers were synthesized, and limited accessibility of doped CPs paved the way for new alternatives for the preparation of new polymeric materials. Low cost, being environmentally friendly, ease of accessibility, applications in large surfaces, ease of modification of the optical and electronic properties have made CPs the most desirable candidate materials for organic electronics^{4,5}. The main polymeric materials for organic electronics included PPV, poly(aniline) (PANI), poly(thiophene) (PT), poly(p-phenylene) (PPP), poly(3,4-ethylenedioxythiophene) (PEDOT), and poly(fluorene) (PF) (Figure 1.1).

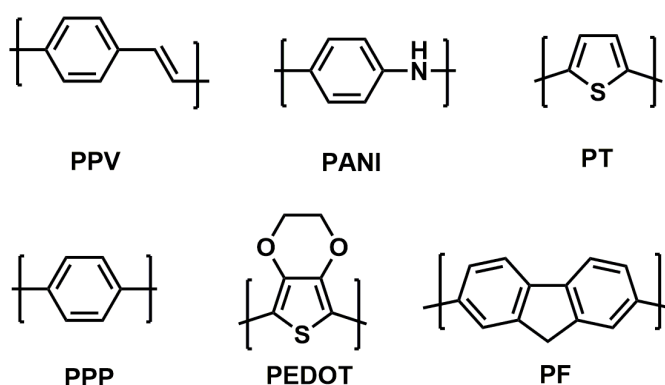


Figure 1.1. Chemical structures of common conjugated polymers

The neat CPs almost show no conductivity. However, conductivity can be enhanced upon reduction and oxidation (redox) processes. The polaron length, chain length of the polymer, and conjugation length are crucial factors affecting the conductivity of the polymer⁶.

1.1.1 Preparation of CPs

CPs are primarily synthesized by chemical and electrochemical polymerization methods. Large applications areas of conjugated polymers led to new approaches for the synthetic methods to prepare desired CPs for specific targets. Since the doping process of PA, synthetic methods for CPs have explosively developed, and numerous polymers were reported for organic electronic applications. Tuning optoelectronic properties of CPs is highly dependent on the backbone design. For example, while

the introduction of chalcogenophenes to polymer backbones alters the absorption properties of the polymers, the introduction of fused structures tunes the polymers' geometry. Both are essential parameters for the performance of the conjugated polymers in OSCs applications ⁷⁻¹¹. To eliminate concerns faced in the preparation of conjugated polymers due to transition metals, halides, and toxic solvents, green approaches are also available for the syntheses of CPs. Polycondensation reactions like Stille, Suzuki, Sonogashira, and Heck coupling are prevalent for the syntheses of CPs as well as green approaches like Direct Heteroarylation Polymerization (DHAP). In this section, Stille/Suzuki Polycondensation and DHAP are explained briefly.

1.1.1.1 Stille Polycondensation

Stille polycondensation reaction has been one of the most useful polymerization methods for the preparation of conjugated polymers for organic electronics applications and the development of next-generation organic semiconducting materials ¹²⁻¹⁴. Stille coupling provides new C-C bond formation between stannane derivatives and aryl halides ^{15,16}. Having advantages like consisting of two or more monomers, mild reaction conditions, Stille coupling has been widely used for synthesizing CPs. Stille coupling facilitates the preparation of high molecular weight conjugated polymers with various functional groups mild reaction conditions, and it provides stereospecificity and regioselectivity. The compounds that go under Stille coupling do not require protecting groups in the monomers; hence organo-stannane compounds and halide compounds can easily be prepared. Stille coupling is a palladium-catalyzed cross-coupling reaction. Stille et al. reported the preparation of ketones from acyl chlorides and organo-stannanes ¹⁶. The general reaction mechanism is illustrated in Figure 1.2.

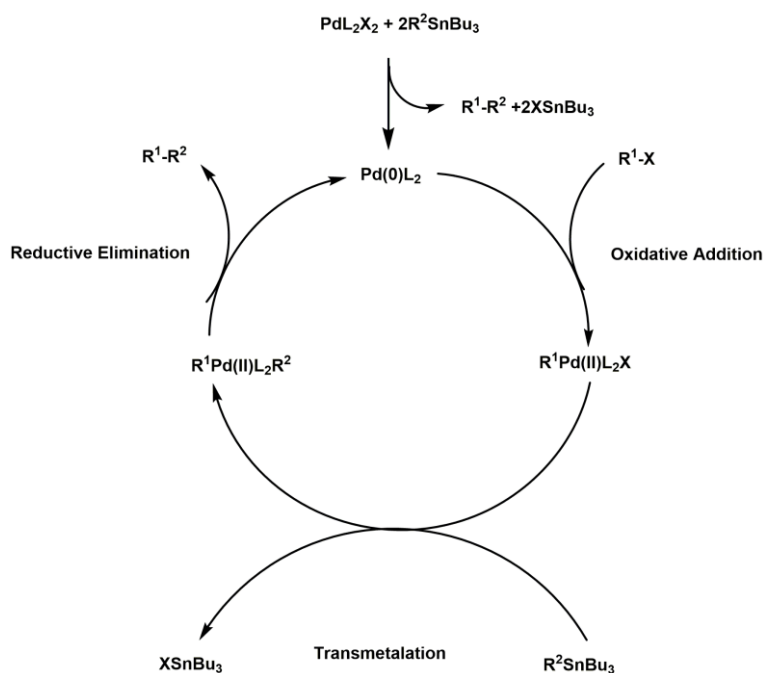


Figure 1.2. Typical mechanism of Stille Coupling

The reaction follows three steps; oxidative addition, transmetalation, and reductive elimination. In the first step, an organohalide compound is oxidatively added and forms a Pd(II) intermediate. The second step is the rate-determining step, where transmetalation takes place. In this step, Sn-C bond cleavage by Pd(II) complex takes place¹⁷. For organic electronics applications, Stille coupling has proved to be one of the most efficient synthetic procedures along with its advantages.

1.1.1.2 Suzuki Polycondensation

Suzuki polycondensation is one of the most versatile methods for preparing conjugated polymers. Also known as Suzuki-Miyaura, Suzuki coupling is a metal-mediated cross-coupling reaction where a new C-C bond is formed between an aryl/vinyl boronic acid/ester and aryl/vinyl halide¹⁸. This method brought the Nobel Prize in Chemistry in 2010. Suzuki coupling creates a new C-C bond, stereoselectivity, and regioselectivity. Suzuki cross-coupling is highly preferred due to its mild reaction conditions, non-toxic side products, and readily available

reactants. Mechanistically, Suzuki coupling follows a similar path with Stille coupling (Figure 1.3).

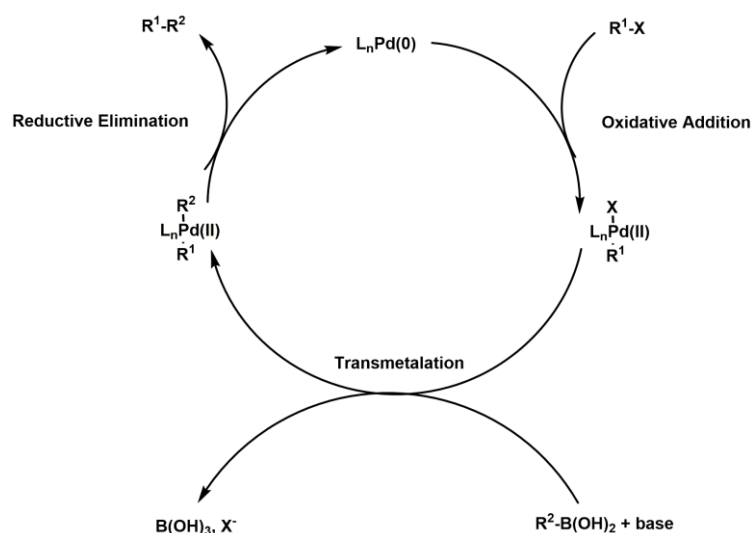


Figure 1.3. The typical mechanism of Suzuki Coupling

The first step is the oxidative addition of an organic halide to the palladium complex, which results in an intermediate like in Stille coupling. The second step is a transmetalation reaction between the intermediate and boron compound. This step is followed by reductive elimination of the product and regeneration of the catalyst ¹⁹.

1.1.1.3 Direct Heteroarylation Polymerization

DHAP is the most recent method for the preparation of conjugated polymers. Pd-mediated method presents a cross-coupling reaction between heteroaromatic C-H and C-X bonds (X: halogen). Compared to Stille polycondensation, DHAP does not end up with toxic side products ²⁰. Utilization of DHAP simplify and shortens the synthetic route for the syntheses of a large number of building blocks and monomers; hence, removal of the byproducts is minimized, which makes the method time saver. These features present an efficient synthetic method for the large-scale production of numerous compounds for organic electronics ^{21–23}. Mechanistically, C-H

activation follows three possible pathways; aromatic substitution, Heck-type coupling, and concerted metalation-deprotonation (CMD). Studies reported earlier suggested Heck-type or electrophilic aromatic substitution processes. However, these mechanistic approaches were thought of as incomplete or inconclusive. Generally, the direct heteroarylation (DHA) mechanism includes oxidative addition of an aryl halide substrate on Pd catalyst, followed by C-H bond cleavage of another aromatic substrate. Subsequently, the formation of a new C-C is succeeded through reductive elimination. The majority of heterocycles go under the base-assisted CMD route in DHAP. CMD explains the reactivity and selectivity of carbonate and carboxylate-assisted direct Heteroarylation (DHA) reactions. In this process, the oxidative addition of the C-X bond is the first step, followed by the formation of the Pd complex. The Pd complex deprotonates the first aromatic substrate (C-H containing) by the carboxylate ligand along with the formation of a metal-carbon bond followed by the formation of a transition state. Subsequently, a new C-C bond is generated via reductive elimination by forming an aryl coupled product (Figure 1.4.).

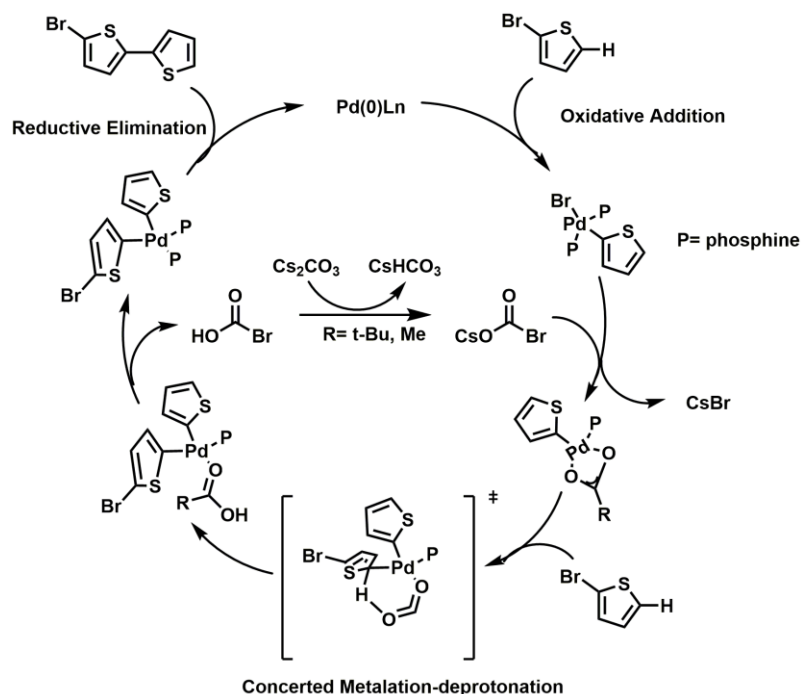


Figure 1.4. General mechanism of DHAP through CMD ²⁴

DHAP provides accessibility to the polymers which were inaccessible and difficult to synthesize via conventional polymerization methods. The method presents an environmentally friendly, economical, and shortened alternative to conventional cross-coupling reactions.

1.2 Applications of CPs

Application of conjugated polymers covers various field like OSCs, OLEDs, OFETs, biosensors, and electrochromism. Herein, OSCs, biosensors, and electrochromism are explained in brief.

1.2.1 Organic Solar Cells

Potential advantages of OSCs over inorganic-based solar cells drew scientists' attention to intensive research. Especially advantages like low cost, light weight, and ease of production make OSCs a potential candidate for energy harvesting soon. OSCs typically contain p-type and n-type semiconductors as donor and acceptor units, respectively. The first OSC had a bilayer structure and exhibited a power conversion efficiency of 1%²⁵. A new approach, bulk heterojunction (BHJ) has come into play, and PCEs increased from 1% to 18%²⁶. After the first report on BHJ²⁷, research on it has explosively risen, and numerous OSCs were reported with increasing efficiencies along with new methodologies. In comparison to the bilayer structure, BHJ provides minimized traveling distance for electron-hole pairs (excitons) to donor:acceptor (D:A) interface and maximized D:A interfacial area, hence triggering excitons dissociation for the generation of free charge carriers. Rather than bilayer architecture, BHJ provides the self-assembly of nanoscale heterojunctions through phase separation of donor and acceptor. Subsequently, charge separation heterojunctions are generated along with the active layer. For a long time, P3HT:PC₆₁BM (poly(3-hexylthiophene):1-(3-methoxycarbonyl)propyl-1-phenyl[6,6]C₆₁) based OSCs were ruling the research field^{28–35}. However, with

the new approaches for the preparation of new materials started an impact. Currently, numerous conjugated polymers are commercially available, providing high PCEs, and intensive research on the developing new promising materials is ongoing.

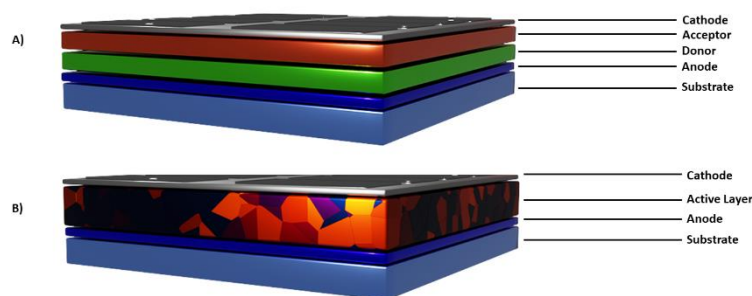


Figure 1.5. Structure of a) bilayer and b) BHJ OSCs

1.2.1.1 How does an organic solar cell function?

The conversion of the incident light into electricity in OSCs requires four steps; absorption of the incident light, diffusion of the excitons followed by charge separation, charge transport, and charge collection at the opposite electrodes. In OSCs, the absorption spectrum of the organic layer is the key to the light collection. The better it matches the solar emission spectrum; the better light will be harvested. The thickness of the active layer is pivotal in this case, and it should be optimized to absorb the incident light. Increasing the thickness is advantageous for absorption; however, it can disturb the charge transport in the active interface layer if it is too thick. Upon absorption of the incident light by one of the materials (donor or acceptor), an electron is transferred from the Highest Occupied Molecular Orbital (HOMO) to the Lowest Unoccupied Molecular Orbital (LUMO). The absorbed incident light generates excitons that require higher energy than the optical band gap of the organic material. When an electron is transferred from HOMO to LUMO, it leaves a positively-charged hole at the HOMO level. However, due to the low dielectric constants of the organic materials, this electron and the hole remain bounded as excitons. Following the formation of excitons, they diffuse to a region

where the donor and acceptor materials are blended to dissociate through promoting an electron from the HOMO of the donor material to the LUMO of the acceptor material, which is energetically more favorable for jumping of charges. At this process lifetime of the excitons is pivotal for effective dissociation and collection of the generated charges. In order to prevent radiative/non-radiative decay of the generated excitons, the diffusion length should be similar to the donor:acceptor phase separation length in magnitude ^{36–38}.

For charge collection at the opposite electrodes, charges must transport within their lifetimes. The driving force for the charges to reach the electrodes is the electric field created in the solar cell device by the varying work functions of the electrodes. This electric field is generated in donor:acceptor junction, determining the maximum open-circuit voltage (V_{OC}). Subsequently, the electrode with a lower work function collects electrons, and the electrode with a higher work function collects holes.

1.2.1.2 Fabrication and characterization of OSCs

For OSCs, several approaches are available for fabrication, like solution-processed and evaporation of small molecules. Polymer-based BHJ OSCs are fabricated via the solution-processed method. For solution-processed OSCs, p-type and n-type materials are dissolved in suitable solvents and cast on a transparent substrate with a high work function. The transparent substrate can be both rigid and flexible. In BHJ OSCs, indium tin oxide (ITO), a high work function electrode, has been used widely ^{39–41}. Onto the transparent electrode, a hole conducting layer is coated. For BHJ OSCs PEDOT:PSS is used widely. PEDOT:PSS is a water dispersed blend of two polymers ^{42–45}. It facilitates hole collection and reduces the roughness of the anode. Following the coating of the hole conducting layer, the active layer (BHJ layer: the donor and the acceptor) is spin-casted. The active layer can be deposited via spray or blade coating, as well ^{46–50}. Above the layers, a metallic cathode is thermally deposited, which can be aluminum, silver, etc. ^{51–53}.

Power conversion efficiency (PCE) of an OSC is the maximum output power obtained as the ratio of power output to power input. PCE is determined by the critical parameters of an operation OSC; the open-circuit voltage (V_{OC}), the short-circuit current density (J_{SC}), and the fill factor (FF). Being related to the energy difference between the HOMO of the donor and the LUMO of the acceptor, V_{OC} is the maximum potential that can be obtained while the applied current is zero. V_{OC} is highly dependent on the energy levels of organic semiconductors and the chemical structures of the polymers. Theoretically, conjugated polymers exhibiting deep HOMO levels provide higher V_{OC} , but this is not always the case. HOMO levels of polymers can be deepened to a certain point where a minimum energy difference (0.3 eV) between LUMO levels of the donor and the acceptor is needed to ease excitons dissociation⁵⁴⁻⁵⁶. V_{OC} is calculated from the following formula;

$$V_{OC} = (1/e)(|E_{Donor}^{HOMO}| - |E_{Acceptor}^{LUMO}|) - 0.3 V$$

where e is the elementary charge.

Short-circuit current density (J_{SC}) is directly related to the absorption capacity of the active layer, excitons diffusion, dissociation, charge transport. Strong absorption by the active layer provides higher J_{SC} hence the absorption of the active layer should match the solar spectrum to enhance excitons generation^{56,57}. The fill factor of an OSC can be described as the ratio of the maximum power generated by the solar device to the external short-circuit current density and open-circuit voltage. Even the perfect FF is 100% (representing a perfect square in the current density-voltage (J-V) curve), it never reaches that value, not even inorganic solar cells, which show way higher PCEs than organic solar cells. In fact, FF tells us how the J-V curve will look like⁵⁸. FF and PCE are determined by the following formulae;

$$FF = \frac{P_m}{J_{SC}V_{OC}} = \frac{J_m V_m}{J_{SC}V_{OC}}$$

$$PCE = \frac{P_m}{P_{in}} = \frac{FFV_{OC}J_m}{P_{in}}$$

The current density-voltage (J-V) curve is obtained from the solar cell under illumination. The following figure is a typical J-V curve where J_{SC} and V_{OC} are labeled.

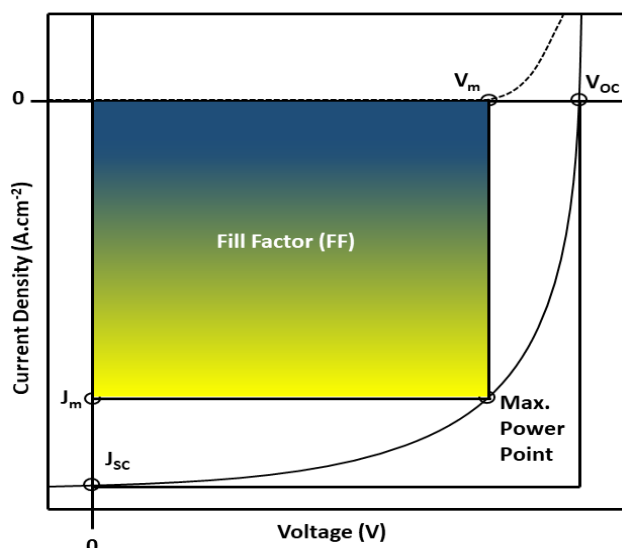


Figure 1.6. J-V curve of an operating OSC

1.2.2 Biosensors

Portability, cost-effectiveness, and rapid detection have made biosensor boost in analytical chemistry. Since the last decades, biosensors have caught great attention. Numerous biosensors have been designed for the simultaneous detection of various analytes in daily life. Application areas of biosensors cover the food industry, medicine, environment, research monitoring, etc.^{59–61} In comparison to conventional sensors; biosensors are cheaper and time saver. Biosensors are analytical devices comprising a biological sensing element and a transducer that converts the biological signal into data. Various biomolecules have been utilized as biological sensing elements; antibodies, receptors, microorganisms, and enzymes^{62–64}. In a general perspective, signals are generated by the interaction of the analyte with the biological element. Biological elements can be classified as catalytic and non-catalytic. Catalytic elements cover tissues, enzymes, microorganisms, and enzymes, whereas

non-catalytic elements can be classified as anti-bodies, receptors, and nucleic acids. Biosensor studies were first started in 1956 by Clark et al.⁶⁵ Biosensors are categorized based on the transducers classified as electrochemical, optical, colorimetric, and acoustic⁶⁶. Herein, electrochemical biosensors are explained briefly.

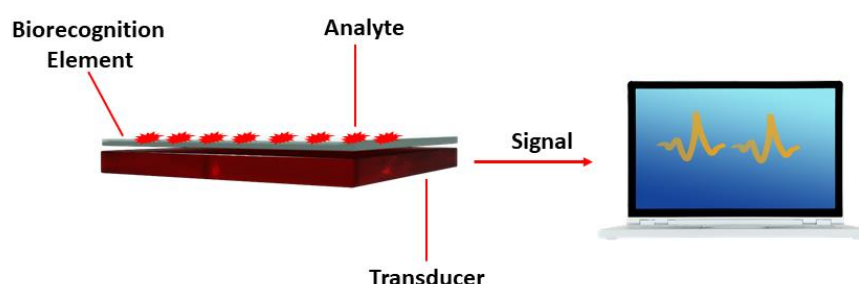


Figure 1.7. Typical representation of a biosensor

1.2.2.1 Electrochemical Biosensors

Electrochemical biosensors have proven efficient for the detection of biologically important components. Advantageous, like being cheap, fast response, portability, and high selectivity, have made electrochemical biosensors the point of interest in analytical chemistry. Electrochemical biosensors are chemically altered electrodes onto which semiconducting materials are coated⁶⁷. In an operating electrochemical biosensor, the key point is the correlation between the electrons produced or consumed during the biochemical reaction and concentration of the target analyte. Electrochemical biosensors are categorized as amperometric, potentiometric, and conductometric biosensors. Amperometric biosensors have proven the most successful since they have been utilized commercially.

1.2.2.1.1 Amperometric Biosensors

Amperometric biosensors operate based on measuring the current obtained from redox reactions of the biological element. Output is specific quantitative analytical data. In amperometric biosensors, the oxidation state of the analyte or the biomolecule changes at the incorporated electrode. Upon this change, the signal from electron transfer is measured, which is proportional to the amount of the redox-active samples at the electrode. Changes in the current which is generated by the electrochemical redox process are determined with time during a constant potential applied to the working electrode in connection with the reference electrode. The measurements are conducted via changing the potential to the desired value and measuring the current. The output current is proportional to the concentration of the species ^{59,68–70}.

1.2.2.1.2 Potentiometric Biosensors

As an efficient analytical method, potentiometry is highly used to detect various analytes. Potentiometric biosensors are a class of electrochemical biosensors, and the main principle is that the device operates with respect to an electrochemical transducer. A biochemical reaction takes place resulting in a simpler chemical moiety and subsequently electrochemical detection. A potentiometric biosensor provides an electrical potential as the analytical signal. In a potentiometric biosensor, the potential difference between an indicator electrode and the reference electrode is determined. While a constant potential is supplied with the reference electrode, the indicator electrode provides a varying potential dependent on the ions presented in the analyte ⁷¹.

1.2.2.1.3 Conductometric Biosensors

In principle, conductometry is the measure of the ability of ions in an analyte to transfer the current between corresponding electrodes. Conductometric biosensors operate on measuring the analytes' capacity to conduct current between the electrodes upon application of an alternating potential. Conductometric biosensors are limited for applications due to the variety of ionic compounds in the analytes and the measurement of small conductivity changes in the samples with high ionic strength. Enzymatic reactions change the ionic conductivity and strength of a medium between two electrodes. Therefore, in many cases, conductometric biosensors have been utilized in enzyme-based biosensors, and they can be used to investigate enzymatic reactions altering the concentration of ionic species in a medium⁷²⁻⁷⁴.

1.2.2.2 Enzyme-based biosensors

Enzymatic biosensors have been widely used in biomedical research and analytical chemistry. The incorporation of enzymes with substrates has made enzymatic biosensors great devices for detecting biological molecules like glucose, creatinine, and urea via their corresponding enzymes⁷⁵. Qualitative and quantitative analyses of various compounds in the diagnosis of diseases, in biochemistry research, environment, and food safety can be conducted by enzymatic biosensors⁷⁶. Being the pivotal component, the enzyme provides selectivity; hence the enzyme electrodes bridge the high specificity of the enzyme and the advantages of electrochemical detection, including high sensitivity, cost-effectiveness, and ease of instrumentation.

For the design of enzymatic biosensors, enzyme immobilization is the key feature to construct efficient devices along with the optimized performance of stability, sensitivity, response time, etc. Standard immobilization techniques (Figure 1.8) can be classified as adsorption, covalent bonding, entrapment, cross-linking, and electropolymerization^{77,78}.

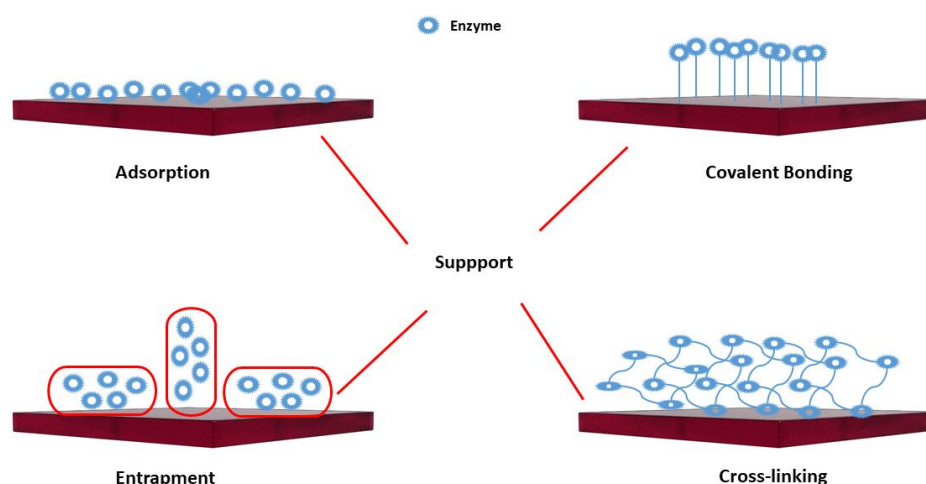


Figure 1.8. Enzyme immobilization methods

1.2.2.2.1 Adsorption

Adsorption of an enzyme onto the substrate is the easiest method for immobilization. The desired enzyme is dissolved in an appropriate solvent, and the solution is contacted with the substrate. After a period of time, the excess enzyme solution which is not adsorbed by the substrate is removed by washing the substrate with buffer solution. The adsorption of the enzyme follows Van der Waal's forces and electrostatic/hydrophobic interactions. The method is non-destructive for the enzyme; a little enzyme inactivation might be observed. Although it is the easiest method for enzyme immobilization, there are some drawbacks. Enzymes might form weak interactions with the substrate, and the enzyme's desorption might be observed due to the changes in ambient temperature, pH, and ionic strength. Hence, enzymatic biosensors based on the adsorption of enzymes have the potential to operate poorly^{79,80}. In summary, this method is not preferred mostly, and in order to overcome the abovementioned drawbacks, numerous enzymes have been immobilized with other immobilization methods.

1.2.2.2.2 Immobilization through covalent bonding

Another method for enzyme immobilization is covalent bonding. The method represents immobilization of enzymes via the probe immobilization by the generation of covalent bonds between functional sites of the enzymes and the electrode. Considering enzymes, the covalent bond is generally formed between -NH₂ site of specific enzymes and functional groups of the moiety located on the electrode. The process is usually started by activating the surface with multifunctional reagents like glutaraldehyde and carbodiimide. The activation is followed by enzyme coupling to the activated support. Finally, the excess amount of the enzyme is removed. The activated support can be either organic or inorganic material. Covalent bonding provides permanent/stable attachment of enzymes to the activated support, although some enzyme molecules might be deactivated during the coupling reaction ^{76,80}.

1.2.2.2.3 Entrapment

Entrapment of enzymes in matrices is as simple as adsorption. The idea is that the biological component is blended till a homogeneous state with the support material followed by applying onto the electrode as an additional layer. With this method, enzyme stability can be enhanced. The main advantage of this method is that it is compatible with the mass fabrication of biosensors. Also, enhanced enzyme loading, reduced enzyme leakage, protected bioactivity, and protection from the external environment are other advantages of the entrapment method. One of the popular methods for entrapment is sol-gel. Following the gelation of the sol-gel, the enzyme is entrapped within a porous or inorganic glass matrix. This way, the enzymes allow the diffusion of solution and analyte molecules through the porous or inorganic glass matrix to the immobilized enzyme molecules. Although sol-gel is a suitable method for entrapment, high alcohol concentration, elevated temperatures, and pH damage enzymes ^{76–78}.

1.2.2.2.4 Cross-linking

For the fabrication of enzymatic biosensors, cross-linking with glutaraldehyde or other bifunctional reagents is another method for enzyme immobilization. In this method, the enzyme molecules are cross-linked in the presence of a cross-linking agent to form a 3D structure. The reagents act as cross-linkers to connect enzyme molecules into 3D cross-linked aggregates. This large network does not require supporting material. Cross-linking is an attractive method due to its simplicity and robust chemical binding formed between biomolecules. Hence, enzyme leakage is minimized. The main drawback is the loss of enzyme activity which is caused by severe modifications in enzyme molecules and changes in conformation⁸¹⁻⁸³.

1.2.3 Electrochromism

Reversible optical change induced by an external electrical potential in a material (inorganic or organic materials) is known as electrochromism. Many organic and inorganic materials have the affinity to show electrochromism throughout the electromagnetic spectrum. Electrochromism was first realized in 1961 by Platt, and the first examples of electrochromic materials were revealed by Deb^{84,85}. Deb reported an electrochromic device (ECD) based on tungsten trioxide film (WO_3) color of which was observed to change reversibly. Inorganic materials have been studied for a considerable period of time, especially transition-metal oxides⁸⁶⁻⁹⁰. Intensive synthetic efforts have been shown to prepare a diverse array of new electrochromic materials covering visible spectrum⁹¹. Chemical compounds present more than one reduction and oxidation state along with their electronic absorption spectra. This is resulted from either an electronic excitation or an intervalence optical charge transfer⁹². Organic small molecules are the second class of electrochromic materials, such as viologens, a class of small molecules that are transparent in the stable dicationic state⁹³⁻⁹⁷. When an electron is reduced, highly colored and stable radical cations are generated. Polyviologens and *N*-substituted viologens exhibit

thin-film electrochromism. The applications areas of electrochromic materials span smart windows, displays, mirrors, sunglasses, etc.^{98–100}

As a third class of electrochromic materials, CPs come into play. When electrochemically reduced and oxidized, fused and neat aromatic molecules like pyrrole, aniline, thiophene, furan, carbazole, azulene, indole, and thienothiophene can produce electrically active conjugated polymers^{101–104}. These materials exhibited color changes and are electrochromic as thin films. CPs in oxidized states possess positive charge carriers, and are charge-balanced with counter anions, and possess delocalized π -electron-band structures. These positive charges can migrate to neighbor polymer chains responsible for conductivity¹⁰⁵. Electrochemical and spectroelectrochemical characterizations have been developed to understand the electrochromic processes in CPs. Redox changes of CPs can be monitored with cyclic voltammetry (CV), and in this way, HOMO and LUMO energy levels of the polymers can be determined as well as electronic band gap (E_g). Electronic absorption changes are monitored via UV-Vis spectrophotometry and optical band gap (E_{op}) can be determined with respect to onset absorption values.

1.3 Aim of the thesis

The aim of the thesis is to present new random conjugated polymers and organic cations for optoelectronic applications. For this thesis study, TPD containing conjugated polymers and organic cations were synthesized and employed in optoelectronic applications. In the first chapter, the readers will find a brief history of CPs followed by popular preparation techniques. In the first chapter, applications of CPs covering OSCs, biosensors, and electrochromism were briefly reviewed, as well. In the second chapter, a literature review emphasizing the recent studies of NFA-based OSCs based fabricated from TPD containing conjugated polymers is presented. Following the literature review, a series of random conjugated polymers containing selenophene as π -spacer were employed as donor materials for the fabrication of NFA OSCs, and the effect of alkyl chains were investigated on the

photovoltaic performance. In the same chapter, two random conjugated polymers containing two different donor moieties (BDT and DTP) as well as TPD and selenophene were employed as donor materials for the fabrication of NFA OSCs. Preliminary results for these two polymers are discussed. In the last part of the second chapter, two random conjugated polymers were used as donor materials. The polymers contain thienothiophene as π -spacer and benzochalcodiazoles as second acceptor moieties in the polymer backbones. The idea is to investigate the effect of the introduction of thienothiophene and benzochalcodiazoles on photovoltaic performance. For these polymers, preliminary results are discussed. Although the second chapter focuses on the fabrication of NFA-based OSCs, for comparison, the polymers were blended with PC₇₁BM as well. The third chapter includes a study on constructing a catechol electrochemical biosensor by laccase immobilization onto the modified working electrode via the physical adsorption technique. In the study, a random conjugated polymer containing TPD moiety and furan as π -spacer was employed. The fourth chapter focuses on the effect of selenophene on the electronic properties of random conjugated polymers. The chapter discusses the changes in absorption, band gaps, and other electronic properties. In the fifth chapter, a series of organic cations employed to treat 3D perovskite films were reported. The study reveals that with the use of organic cations, the performance of Perovskite solar cells can be enhanced via the treatment of 3D perovskite films. Overall, this thesis represents a comprehensive study on OSCs, biosensors, electrochromism, and Perovskite solar cells.

CHAPTER 2

NON-FULLERENE OSCs BASED ON TPD COMPRISING POLYMERS

Donor-acceptor (D-A) CPs have gotten significant attention in the past decades. Wide application area, ease of production, and cost-effectiveness have made the D-A conjugated polymers a pivotal class of organic electronics. Organic solar cells (OSCs) became one of the most critical application areas of conjugated polymers among many. Intensive research has been conducted on fullerene-based OSCs up to the last decade. Drawbacks of fullerene derivatives like high cost, production obstacles, and difficulties in modifying molecular structure made the academia seek new alternatives. Emerging non-fullerene acceptors (NFAs) drew a new path for academia to tune OSCs' power conversion efficiency (PCE). With the ease of synthesis and purification, modification of molecular structure via various functional groups, NFAs started outperforming fullerene-based acceptors. Thieno[3,4-c]pyrrole-4,6-dione (TPD) is widely used in D-A conjugated polymers for high-performance OSCs. As a robust electron-withdrawing group, TPD provides deepened lowest unoccupied molecular orbital (LUMO) energy level and wide band gaps when introduced into polymer backbones, enhancing optoelectronic properties photovoltaic performance. Herein, we provide an overview of the applications of TPD-based donor and acceptor type conjugated polymers for non-fullerene and all-polymer solar cells (PSCs) in the last five years.

2.1 Literature Review

Having advantages like low cost, flexibility, ease of construction, and environmentally friendly, organic solar cells have taken great attention. Tang constructed the first organic solar cell in 1986 with a power conversion efficiency (PCE) of 1%. Since then, intensive research has led to power conversion efficiency

extending from 1% to 18% during the past three decades ^{25,106}. Various applications (energy storage devices, organic field-effect transistors (OFETs), organic light-emitting diodes (OLEDs), electrochromic devices (ECDs), biosensors, capacitors, etc.) of conjugated polymers made them pivotal materials as organic semiconductors ^{107–112}. In typical bulk heterojunction (BHJ) OSCs, the active layer is a blend of an electron-donor material and a fullerene-based electron-acceptor material. Fullerene acceptors (FAs) have proven significant at charge transport features, creating phase separation in nanoscales ^{113–115}. Hassles in tuning optoelectronic properties, air sensitivity, limitation in light absorption, and high purification cost of fullerene-based acceptors have made material scientists search for alternatives ^{116–118}. Ready preparation and purification of NFAs made them a significant class of acceptor materials. Introduction of various functional and pendant groups tunes properties of NFAs. Such modifications subsequently enhanced light absorption ability, electronic and optoelectronic properties, morphology obtained via blending donor and acceptor units. In recent literature, NFA-based OSCs have exhibited improved PCEs ^{106,119,120}.

An essential class of donor materials for OSCs is conjugated D-A copolymers. Due to its promising structural properties, thieno[3,4-c]pyrrole-4,6-dione (TPD) moiety has been broadly used as a great acceptor in D-A copolymers ^{121,122,131,123–130}. TPD unit exhibits better quinoidal nature compared to benzene-bearing electron-deficient units like benzothiadiazole (BT), benzotriazole (BTA), thienopyrazine, and quinoxaline (Qx) ^{132–137}. Intramolecular interactions of sulfur and oxygen or hydrogen and oxygen atoms on TPD subsequently improve the molecular geometry (planarity) and enhance intramolecular charge transfer (ICT) ¹³⁸. Due to diimide characteristics, TPD is a robust electron-withdrawing moiety. This property results in stabilized lowest unoccupied molecular orbital (LUMO) energy level and low band gap conjugated polymers; subsequently, higher open-circuit voltage (V_{oc}) ^{139,140}. Modifying fundamental moieties in D-A polymers' backbone is crucial for solubility and optoelectronic performance. In this respect, TPD is a great candidate. Various pendant groups can be introduced to TPD moiety (pyrrole connection) to enhance both optoelectronic properties and solubility of resultant polymers.

Incorporation of TPD with different electron-donating moieties resulted in p-type copolymers exhibiting PCE values ranging from 7% to 16% ^{141–145}.

This part of the thesis presents an outline of the synthesis of TPD-based conjugated polymers and their applications both as donor and acceptor materials in non-fullerene OSCs, reported in the past five years.

2.1.1 Preparation TPD and TPD-based conjugated polymers

First TPD-based conjugated polymers were first synthesized by Tour, who also proposed a synthetic route for TPD preparation (Figure 2.1.a). Following the bromination of thiophene, 3,4-dibromo thiophene was coupled with CuCN to prepare 3,4-dicyano-thiophene. Following preparation of 2,5-dibromothiophene-3,4-dicarboxylic acid, with the addition of oxalyl chloride 2,5-dibromothiophene-3,4-dicarbonyl dichloride was obtained. Subsequently, by an imidization reaction TPD unit was synthesized ¹⁴⁶. Another approach for TPD synthesis was proposed by Leclerc et al. ¹⁴⁷; via Gewald reaction, an amino thiophene derivative was prepared first. Sandmeyer's transformation resulted in mono-halo- compounds, condensation with an alkyl amine gave the target product (Figure 2.1.b).

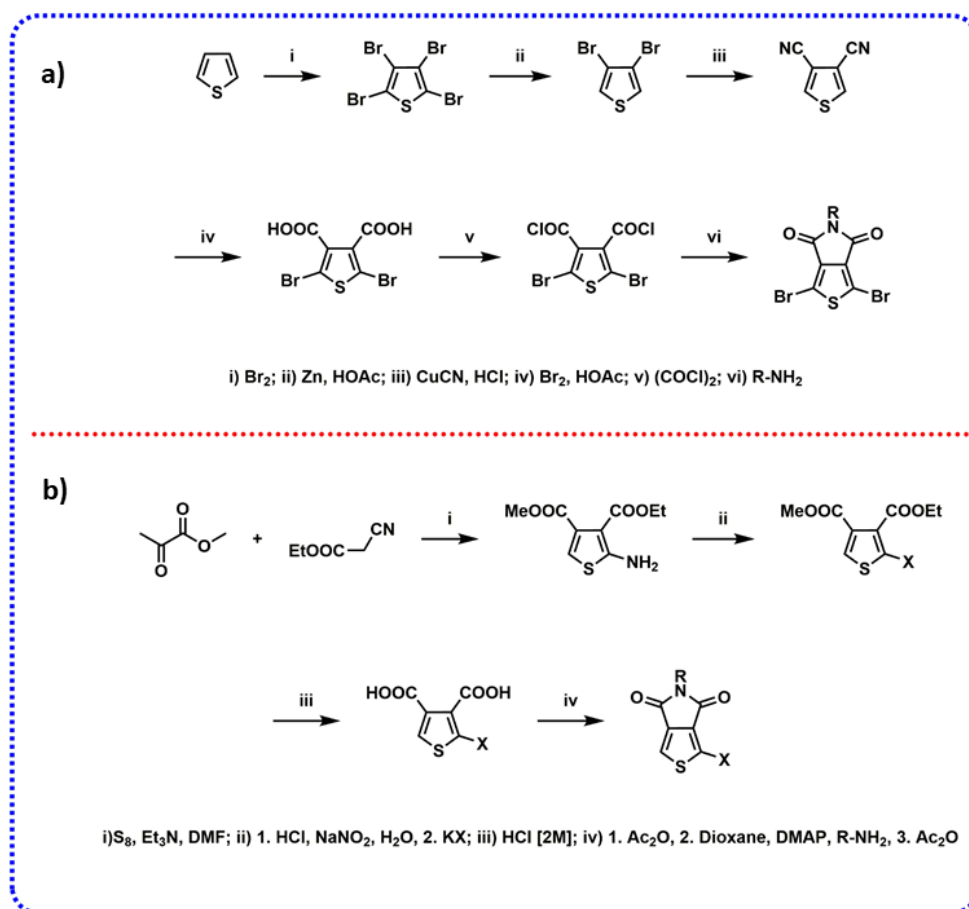


Figure 2.1. Two synthetic routes for TPD

Most TPD-based conjugated polymers were synthesized via Stille Polycondensation in literature^{148–151}. TPD is also an excellent unit for polymers synthesized via Suzuki Polycondensation^{125,152}. Stille and Suzuki Polycondensation reactions are commonly applied for TPD-based conjugated polymer syntheses. Although the resulting polymers have excellent yields, high molecular weights, and low polydispersity indices, organic tin and boron compounds are concerning¹⁵³. For green syntheses of TPD-based conjugated polymers, Leclerc's group was the first one to synthesize TPD-based conjugated polymers via Direct Heteroarylation Polymerization (DHAP)¹⁵⁴.

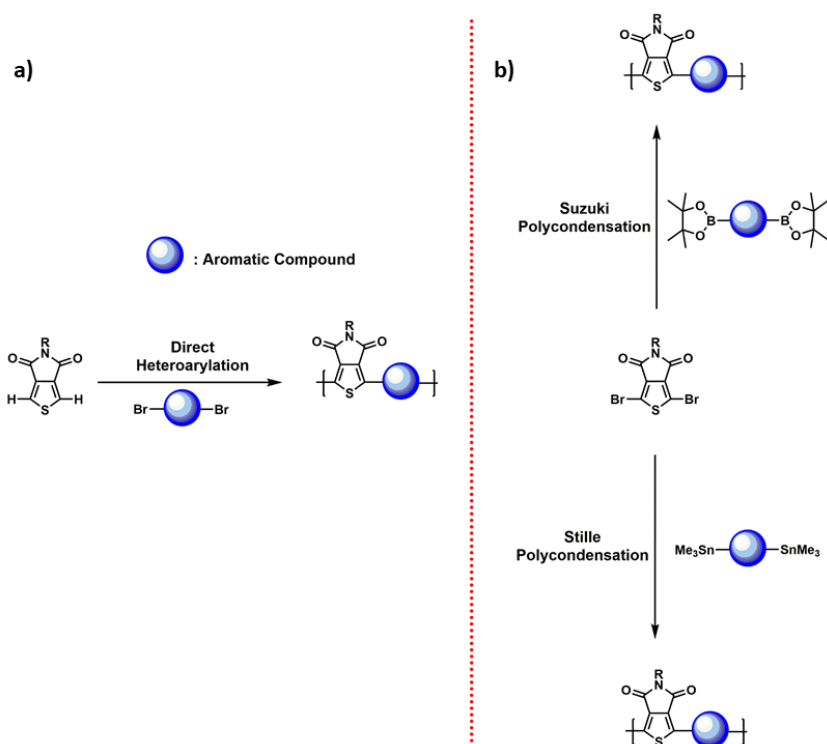


Figure 2.2. Syntheses of TPD-based conjugated polymers via DHAP and Stille/Suzuki Polycondensation

TPD-polymers have been used widely in the active layer to prepare OSCs. This review provides recently reported NFA OSCs where TPD-polymers were used as both donor and acceptor in the active layers of the devices.

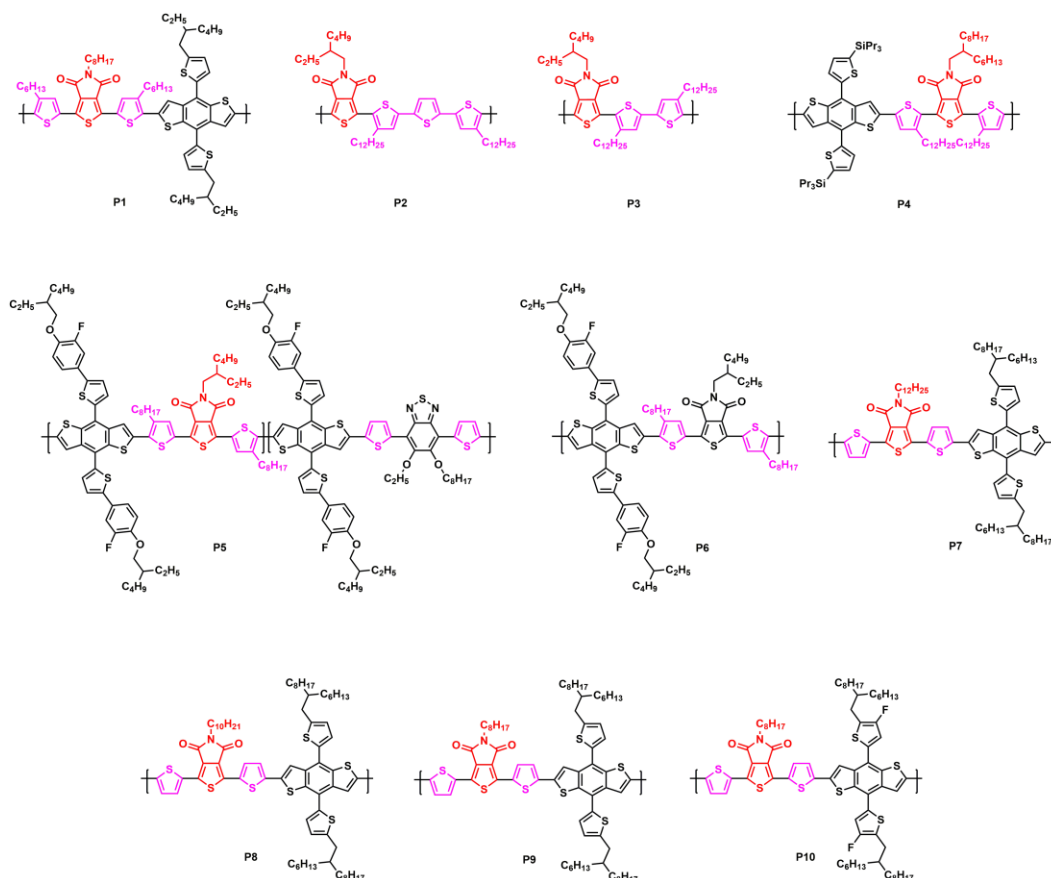
2.1.2 TPD-based conjugated polymers used as Donors

This section provides various moieties incorporated with TPD to obtain donor polymers utilized to prepare non-fullerene organic solar cells.

2.1.2.1 Incorporated with thiophene

Thiophene is one of the most critical units in preparing conjugated polymers designed for organic electronics. Insertion of thiophene provides an extensive

absorption range, tuning frontier energy levels (HOMO and LUMO) and film morphology, subsequently photovoltaic performances. Besides, modification of thiophene with alkyl chains will improve the solubility of polymers¹⁵⁵. The chemical structures of TPD-based conjugated polymers containing thiophene are illustrated in Figure 2.3 and the photovoltaic properties are summarized in Table 2.1.



non-fullerene small molecule was used as the acceptor in the active layer. The best device performed a power conversion efficiency of 10.2%, with a V_{OC} of 0.97, a J_{SC} of 15.40 mA.cm^{-2} , and a FF of 0.68. The active layer exhibited controlled morphology that provided excessive segregation of ITIC, which was attributed to the miscibility with P1.

Table 2.1 Photovoltaic properties of TPD-based conjugated polymers incorporated with thiophene

Donor:Acceptor	V_{OC} (V)	J_{SC} (mA.cm^{-2})	FF	PCE (%)
P1:ITIC	0.97	15.40	0.68	10.20
P2:ITIC	0.91	13.50	0.68	8.40
P3:ITIC	0.96	12.30	0.60	7.00
P4:m-ITIC	1.03	11.10	0.56	7.00
P4:IDIC	0.95	12.00	0.54	6.18
P4:AIDIC	0.96	5.90	0.40	2.06
P5:ITIC:Th	0.83	15.75	0.63	8.22
P6:ITIC:Th	0.80	15.35	0.60	7.37
P7:IT-4F	0.81	19.40	0.75	11.70
P8:IT-4F	0.81	19.16	0.74	11.80
P9:IT-4F	0.80	20.10	0.75	12.10
P10:IT-4F	0.93	21.10	0.72	14.40

Li et al. designed and synthesized donor wide-band gap TPD-copolymers (P2 and P3) incorporated with terthiophene and bithiophene¹⁵⁷. The polymers were used in the active layer with ITIC as the acceptor. The best device based on P2 performed a PCE of 8.4% with an open-circuit voltage of 0.91 V. The device based on P3 exhibited a PCE of 7.0% with a V_{OC} of 0.96 V. This drastic difference between the two devices is attributed to the decrease in J_{SC} . For comparison, they synthesized a polymer-based on TPD and BDT only, as well. The device based on this polymer exhibited the best V_{OC} (1.05 V), although the PCE (5.4%) was relatively lower than thiophene-based polymer donors. The study showed that a significant V_{OC} could be obtained via tuning the chemical structures.

Yang et al. synthesized a copolymer (P4), based on TPD and alkylated thiophene units, used as donor in an active layer blend where three different non-fullerene acceptors were used¹⁵⁸. The best device in which m-ITIC was used as an acceptor in the active blend performed a PCE of 6.41%. Comparatively, P4:IDIC and P4:AIDIC blends exhibited 6.18% and 2.06% PCE, respectively. Various V_{OC} values of the devices were attributed to the different HOMO energy levels of P4, whereas obtained J_{SC} and FF were thought to be dependent on the crystallinity of the components and morphology of the blend films in which an improved small molecule acceptor order along with the formation of the 3D structure was observed.

Jin et al. investigated the effect of irregularity ascribed to random π -conjugated random copolymers on the photovoltaic performance of NFA OSCs¹⁵⁹. The group synthesized an asymmetric random copolymer, asy-PBDTPBT (herein P5), and used PBDTP (herein P6) as the control polymer to prepare NFA OSCs. The best PCE value was obtained from the device based on P5:ITIC:Th active layer. With a PCE value of 8.22%, V_{OC} , J_{SC} , and FF were determined as 0.83 V, 15.75 mA.cm⁻², and 0.63, respectively. The higher PCE value exhibited by P5 is ascribed to the tendency of irregularity of the polymer. The irregularity of the polymer resulted in a crucial morphology; the blend of donor:acceptor exhibited lower surface roughness due to the lower crystallinity preventing recombination of charges. With the higher degree of irregularity of the asymmetric polymer (P5), the control polymer (P6) showed a higher crystallinity.

Facchetti et al. reported a series of TPD-based polymers (P7, P8, P9, and P10) blended with IT-4F¹⁶⁰. Obtained polymers were soluble in halogen-free solvents, and the performance of the devices ranged between 12% and 14%. The devices were fabricated under N₂ or ambient and with two film deposition techniques; spin coating and blade. The devices fabricated via the two techniques yet exhibit comparable results. P7, P8, P9, and P10 showed PCE values between 11.7% and 12.1%. The polymers have different alkyl chains starting -C₈H₁₇ (P7), -C₁₀H₂₁ (P8), and -C₁₂H₂₅ (P9) on the core unit, TPD. The best device showed a PCE of 14.4% with a V_{OC} of 0.93 V, a J_{SC} of 21.1 mA.cm⁻², and a FF of 0.72. The blend of this device (P10:IT-

4F) was processed with a halogen-free solvent (xylene), and a module of this device with a 20.4 cm² area performed a PCE of 10.13%, a V_{OC} of 4.52 V, an I_{SC} of 71.4 mA, and a FF of 0.64, and was certified at 10.08%.

2.1.2.2 Incorporated with Thieno [3,2-b]thiophene

Being a minimal and rigid unit, thienothiophene is a fused structure with two annulated thiophene units. Having four isomers, thieno[3,2-b]thiophene, thieno [3,4-b]thiophene, thieno [2,3-b]thiophene, and thieno[3,4-c]thiophene, thienothiophenes are known as electron-rich moieties and widely used in conjugated polymers' backbones. Thienothiophene was reported in the formation of porous structures. Thieno[3,2-b]thiophene can form high π -stacking interactions. This part reviews the photovoltaic performance of TPD-based conjugated polymers bearing thieno [3,2-b]thiophene. Thienothiophene was reported in the formation of porous structures^{161–164}. The chemical structures of TPD-based conjugated polymers containing thieno[3,2-b]thiophene are illustrated in Figure 2.4 and the photovoltaic properties are summarized Table 2.2.

Liang et al. reported two TPD, thienothiophene and benzodithiophene bearing conjugated polymers which were used in active blends¹⁶⁵. The group studied two polymers PMOT16 and PBDTT-6ttTPD, herein P11 and P12, respectively. Thieno[3,2-b]thiophene was introduced to enhance the absorption coefficients of the donor- π -acceptor polymers. In P11, 4-methoxythiophene enhanced intermolecular interactions between polymer chains and deepened the HOMO energy level. The polymers were blended with both ITIC and IDIC, as well PCBM. The study revealed that active blends with NFAs exhibited better photovoltaic performance compared to PCBM blends. The performance of the devices prepared from fullerene-based blends showed PCE values from 6.59% (P11) to 7.74% (P11), whereas devices prepared from NFA blends performed PCE values from 7.63% (P11) to 10.04% (P12). Although P11 mixed with IDIC exhibited the best efficiency and J_{SC}, the best

V_{OC} was performed via blending with ITIC. Replacing ITIC with IDIC enhanced the efficiency for P11, but for P12, the same trend was not observed.

Cao et al. prepared a set of OSCs based on a wide-band gap ($E_g=1.89$ eV) TPD/benzodithiophene conjugated polymer (PMOT40, herein P13) and IDIC, and i-IEICO-4F¹⁶⁶. BDT contains two thiophene moieties, and one of them has a 3-methoxyl group. It is ascribed that this 3-methoxylthiophene (MOT) pendant can lower the HOMO energy level of the donor polymer and improve hole mobility. Besides, the asymmetrical design of the polymer drives a better matching energy level with IDIC compared to symmetrical thiophene or 3-methoxylthiophene counterparts. The PCE values obtained from P13:IDIC based devices range between 10.5 and 12.2%, where P13: i-IEICO-4F based devices exhibited PCEs ranging from 11.7% to 13%. The best device from P13:IDIC performed a PCE of 12.2% with a FF of 0.73, a J_{SC} of 17.4 mA.cm⁻², and a V_{OC} of 0.97 V. The best result was obtained from P13: i-IEICO-4F is 13%. The device exhibited a V_{OC} of 0.97 V, a J_{SC} of 20.6 mA.cm⁻², and a FF of 0.65.

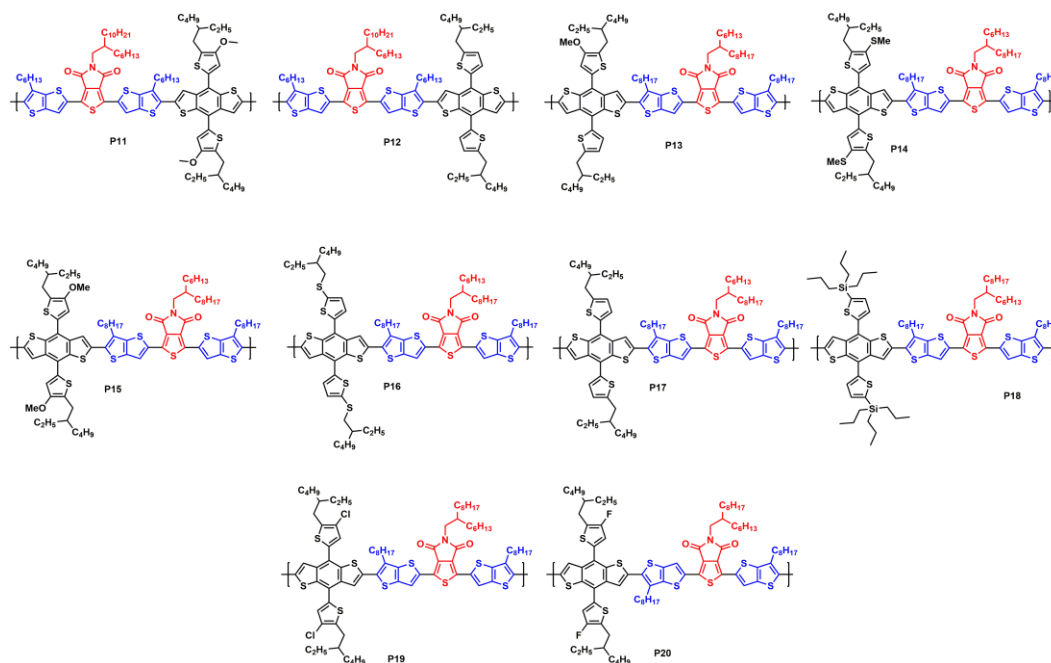


Figure 2.4. Structures of TPD-based conjugated polymers bearing thieno [3,2-b]thiophene moiety

In 2019, Liang et al. reported three conjugated polymers mixed with IT-2F to prepare non-fullerene OSCs ¹⁶⁷. In the study, 5-alkyl-4-(methylthio)thiophene, 5-alkyl-4-methoxythiophene, and 5-(alkylthio)thiophene were utilized as conjugated side chains of the polymers, herein PMTT56 (P14), PMOT39 (P15), and PEHTT (P16), respectively. The polymer P14, containing 5-alkyl-4-(methylthio)thiophene exhibited lower energy levels than its counterparts. OSCs were processed from toluene. P14 with 5-alkyl-4-(methylthio)thiophene exhibited better solubility, and the devices based on P14 performed better than the other two polymers when blended with IT:2F. P14 provided enhanced J_{SC} , V_{OC} , and FF, and it has the advantage over P16 with better solubility in toluene substantially better morphology of the active film. The best efficiency provided by P14 was 12.6% with a J_{SC} of 18.67 mA.cm^{-2} , a V_{OC} of 0.94 V, and a FF of 0.71. To further investigate the photovoltaic performance of P14, the group introduced PC₇₁BM as the second acceptor in the devices. This further enhanced the device's performance up to 13.2%, with a higher J_{SC} = 19.75 mA.cm^{-2} .

Table 2.2 Photovoltaic properties of TPD-based conjugated polymers incorporated with thieno [3,2-b]thiophene

Donor:Acceptor	V _{oc} (V)	J _{sc} (mA.cm ⁻²)	FF	PCE (%)
P11: ITIC	1.00	13.00	0.59	7.63
P12: ITIC	0.94	15.63	0.68	9.98
P11: IDIC	0.92	16.13	0.67	10.04
P12: IDIC	0.82	15.93	0.65	8.58
P13: IDIC	0.97	17.40	0.73	12.20
P13: <i>i</i>-IEICO-4F	0.97	20.60	0.65	13.00
P14:IT-2F	0.94	18.67	0.71	12.60
P15:IT-2F	0.90	17.84	0.66	10.50
P16:IT-2F	0.89	18.90	0.64	10.80
P17-L:ITIC	0.92	11.47	0.55	5.76
P17-M:ITIC	0.93	14.79	0.60	8.27
P17-H:ITIC	0.93	17.52	0.68	11.05
P17: P(NDI2OD-T2)	0.94	12.37	0.64	7.47
P17:Y6	0.73	22.89	0.53	8.85
P16: P(NDI2OD-T2)	0.98	9.07	0.55	4.90
P16:Y6	0.78	21.93	0.49	8.38
P18: P(NDI2OD-T2)	1.00	5.84	0.45	3.14
P18:Y6	0.86	21.40	0.65	12.02
P17:Y6	0.74	24.91	0.63	11.84
P19:Y6	0.85	25.69	0.71	15.63
P20:Y6	0.83	25.36	0.68	14.86

Hwang et al. synthesized three batches of a polymer donor with three different molecular weights containing alkylated thienothiophene as π -bridge and TPD with BDT¹⁶⁸. The study revealed the correlation between molecular weight and photovoltaic performance. As the molecular weight increased, absorption coefficient, morphology, carrier mobility, and π - π stacking of the films improved, hence the efficiency of the devices. The obtained polymer exhibited a strong absorption at around 700 nm. Polymers with different molecular weights were assigned as PBDTT-8tTPD-L (lowest molecular weight), here P17-L, PBDTT-

8ttTPD-M (medium molecular weight), here P17-M, and PBDTT-8ttTPD-H (highest molecular weight), here P17-H. The efficiency of the devices was enhanced via the utilization of polymers starting from P17-L to P17-H. The best result was obtained P17-H based device with a PCE value of 11.05%, a V_{OC} of 0.93 V, a J_{SC} of 17.52 mA.cm^{-2} , and a FF of 0.68.

In 2020, Kim et al. reported a set of polymers implemented to fabricate all-polymer and NFA-Polymer solar cells ¹⁶⁹. The study focuses on the effects of polymer aggregation on the blend morphology and solar cell performance for both all-polymer and NFA-polymer solar cells. For this purpose, three polymers with different side chains were synthesized, P-EH, P-SEH, and P-Si (herein P17, P16, P18, respectively). P-Si, herein P18, showed the most robust aggregation behavior and caused greater phase separation in the active layer comprising the polymer and the acceptor. Hence, the device based on this polymer exhibited the lowest efficiency of the all-polymer solar cell, 3.14%. On the other hand, when P18 was implemented in NFA-polymer solar cells, the efficiency boosted up to 12.02%. This was attributed to the different molecular sizes of the polymer acceptor and NFA, a small-molecule acceptor. The performance of all polymers was enhanced when blended with a small-molecule acceptor instead of a polymer acceptor. The best result was obtained with P18/NFA active layer with a V_{OC} of 0.86 V, a J_{SC} of 21.40 mA.cm^{-2} , and a FF of 0.65.

A set of three polymer donors comprising thienothiophene, TPD, and BDT were reported by Kim et al. ¹⁴⁴. Two polymers have halogenated side chains that improve the device's charge transport and recombination properties. Authors ascribe this to crystallinity and hole mobility of donor polymers. OSCs were prepared via blending the polymer donors with Y6small molecules. Considering crystallinity, all three polymers P17, 19, and 20, exhibited delicate intermolecular structures in their films. This trend was observed in the blends with Y6 as well. P19:Y6 blends showed better crystallinity and domain purity among all other blends, consequently better charge transport and limited charge recombination. The devices based on P19:Y6 blends performed up to 15.63% of PCE. Compared to P17:Y6 based device, P20 performed

better as well. The study is an excellent example of demonstrating the effect of halogenation on photovoltaic properties of polymer-based OSCs.

2.1.2.3 BiTPD containing conjugated polymers

Having a planar structure and showing great electron-withdrawing ability, 1,1'-bithienopyrrolodione (biTPD) competes with its derivative thieno [3,4-c]pyrrole-4,6-dione, which makes it a good candidate as an acceptor for donor-acceptor polymers. BiTPD has an anticoplanar structure leading to noncovalent interaction between sulfur and oxygen atoms, providing better intermolecular interactions. Besides, electron-deficient units in biTPD provide lower LUMO energy levels and provide better solubility due to the presence of side chains that are vacant to alkyl chains^{147,149,170}. The chemical structures of biTPD-based conjugated polymers are illustrated in Figure 2.5 and the photovoltaic properties are summarized in Table 2.3.

Cai et al. reported three biTPD-based donor polymers implemented in the preparation of BHJ OSCs¹⁷¹. The polymers were modified with different alkyl chain positioning. Polymers, as noted, are 2HD/C8, C8/2BO/C6, and 2BO/C6/C6, herein P21, 22, and P23. The study reveals the effect of alkyl-chain positioning on the optoelectronic and morphological properties of the polymers, hence the photovoltaic performance of NFA-OSCs. Based on UV-vis absorption investigations, the introduction of -C₈H₁₇ and -C₆H₁₃ to the thiophene moieties in the polymer backbone widens the optical band gap of the polymers P21 and P22. NFA-OSCs were prepared with the blend of polymers and Y6 as active layers. The best device was constructed from P21. P22 exhibited way lower efficiency than P21 and P23, demonstrating moderate efficiency. The results showed that the introduction of alkyl chains to the spacer thiophene and thiophenyl ring on the BDT, rather than N-site of TPD, resulted in lower power conversion efficiency. P21 exhibited a PCE value of 14.14%, with a V_{OC} of 0.827 V, a J_{SC} of 25.51 mA.cm⁻², and a FF of 0.668.

Table 2.3 Photovoltaic properties of biTPD-based conjugated polymers

Donor:Acceptor	V _{oc} (V)	J _{sc} (mA.cm ⁻²)	FF	PCE (%)
P21:Y6	0.83	25.51	0.67	14.14
P22:Y6	0.79	9.57	0.31	2.35
P23:Y6	0.86	21.09	0.48	8.67
P24:Y6	0.82	25.90	0.67	14.10
P25:Y6	0.81	23.70	0.58	11.10
P26:Y6	0.80	20.90	0.47	7.80

Another study investigating the effect of alkyl chains on optical and photovoltaic properties was reported by Huang et al. in 2021¹⁷². Three biTPD-based conjugated polymers were synthesized with varying alkyl chains. The optical properties of the different polymers were investigated to see the effect of side-chain engineering. All of the polymers PBDTbiTPD(C48), PBDT-BiTPD(C52), and PBDT-BiTPD(C56), here P24, 25, and P26 exhibited similar absorption spectra in the range of 400-700 nm. Similarly, the energy levels of the polymers were found similar as well. Hence, the effect of alkyl side chains was counted as negligible. This was ascribed to the same backbone structure of the polymers. However, the side chains affected the aggregation in solution and self-assembly in thin films. When the length of the alkyl chain decreased from C56 to C48, it was observed that face-on orientation increased and molecular order enhanced in donor: acceptor blends. NFA devices were fabricated with polymer:Y6 blends. The polymer P24 with the shortest alkyl chain exhibited the best performance, a PCE of 14.1%. The efficiency of the devices decreases as the chain length increase. P25 and P26 showed an efficiency of 11.1% and 7.8%, respectively.

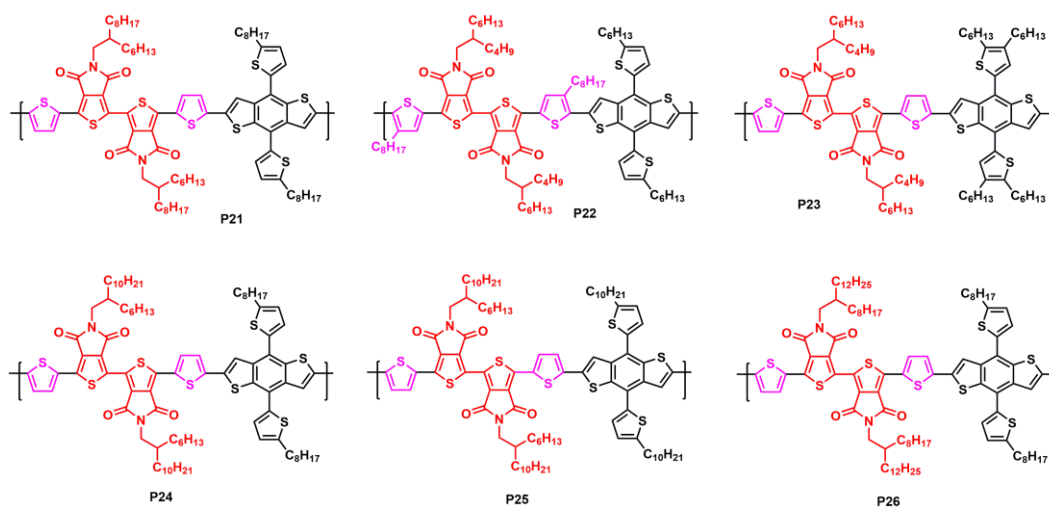


Figure 2.5. Structures of biTPD-based conjugated polymers

2.1.2.4 TPD-based random conjugated polymers

Numerous conjugated polymers bearing electron-rich and electron-deficient moieties have been utilized as donor materials in NFA-OSCs fabrication. Structural design and synthetic procedures are critical concerns for the enhancement of OSC performance. In this sense, random copolymers have been one of the new approaches for polymer synthesis. The introduction of multiple moieties into polymer backbones via random polymerization can expand the absorption and alter optoelectronic and physical properties of the polymers, enhancing photovoltaic performance. Being a facile method of tuning optoelectronic properties, random polymerization has emerged as an important approach for synthesizing new polymeric materials as donors and acceptor materials in the application of OSCs^{173–176}. The chemical structures of TPD-based random conjugated polymers are illustrated in Figure 2.6 and the photovoltaic properties are summarized in Table 2.4.

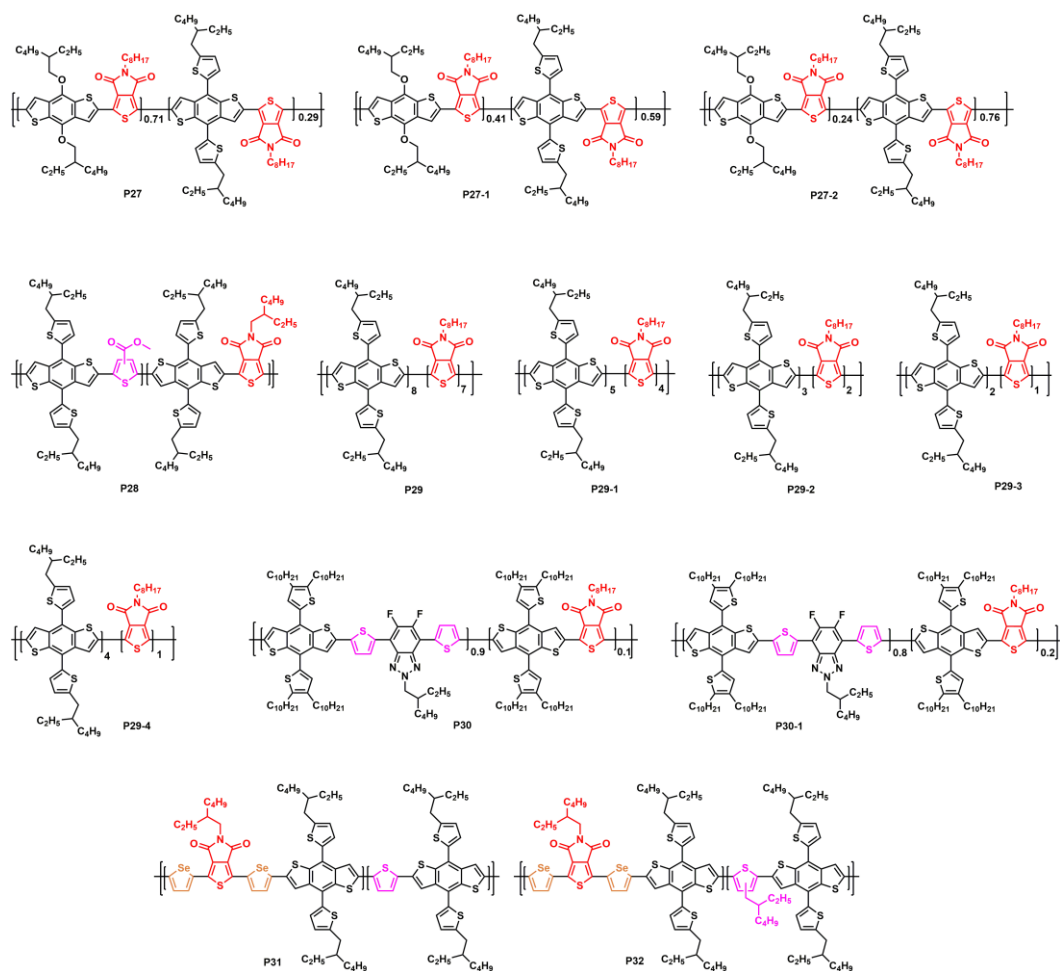


Figure 2.6. Structures of TPD-based random conjugated polymers

Kim et al. synthesized a set of random polymers with different feed ratios¹⁷⁷. The study focused on the investigation of the importance of 2D conjugated side chains of BDT. The polymers were compared with two copolymers consisting of TPD and BDT only. The results showed that the introduction of conjugated side chains into the BDT unit enhances the photovoltaic performance of the polymers. In the study, this modification is performed on the random polymers' backbones. As noted in the study, the random polymers are PBDTT_{0.29}-TPD (P27), PBDTT_{0.59}-TPD (P27-1), and PBDTT_{0.76}-TPD (P27-2). The polymers were implemented with P(NDI2HD-T) (NFA acceptor) to prepare the active layers for the solar devices. As the feed ratio of the monomers decreased, the efficiency of the devices increased. Enhancement of the solar devices is attributed to 2D conjugated sides that provided molecular

orientation and order and enhanced domain purity. The best device was fabricated from P30-2, providing an efficiency of 5.32%, with a V_{OC} of 0.96 V, a J_{SC} of 10.43 $\text{mA}\cdot\text{cm}^{-2}$, and a FF of 0.51. The study is a delicate example of investigating the effects of conjugated side chains on the photovoltaic performance of all-polymer solar cells.

In 2018, Choi et al. reported a random terpolymer based on TPD, BDT, and methyl thiophene-3-carboxylate (3MT) moieties¹⁷⁸. As noted in the article, the terpolymer Ter-3MTTPD (P28) was implemented with a selenophene and NDI containing polymer acceptor. With the addition of DPE, P28 based device showed an efficiency of 7.66%. Shelf-life investigation for this polymer: acceptor blend was also performed. And it showed a shelf-life up to 1000 hours under ambient conditions. After 100 hours under ambient conditions, the morphology was examined again, and it was observed that the film maintained a similar morphology. Other photovoltaic parameters for P28:NDI-Se based device were as the followings; V_{OC} is 1.01 V, J_{SC} is 11.47 $\text{mA}\cdot\text{cm}^{-2}$, and FF is 0.66.

Ling et al. synthesized a group of random conjugated polymers with varying feed ratios consisting of TPD and BDT. The polymers were blended with P(NDI2HD-T) to prepare all-polymer solar cells¹⁷⁹. The authors investigated the synergistic effects of processing solvent and composition of donor-acceptor type polymers in all-polymer solar cells. The obtained random polymers had higher molecular weights than alternating polymer P(TPD-BDT). This was attributed to that random polymerization increases the molecular weight of the polymers. The polymers were processed with a green solvent known as 2-MeTHF (2-methyltetrahydrofuran), and the polymers showed good solubility in halogenated solvents, as well. The best photovoltaic performance was obtained with P29-1 with an efficiency of 8.20%, which outperformed the reference device of P(TPD-BDT) polymer (6.41%). The other photovoltaic parameters of the polymer P29-1 are; V_{OC} is 1.02 V, J_{SC} is 14.42 $\text{mA}\cdot\text{cm}^{-2}$, and FF is 0.557. The study is an excellent example of how random polymerization affects all-PSCs' photovoltaic performance.

Table 2.4 Photovoltaic properties of TPD-based random conjugated polymers

Donor:Acceptor	V _{oc} (V)	J _{sc} (mA.cm ⁻²)	FF	PCE (%)
P27: P(NDI2HD-T)	0.96	7.65	0.43	3.16
P27-1: P(NDI2HD-T)	0.99	8.73	0.51	4.41
P27-2: P(NDI2HD-T)	1.00	10.43	0.51	5.32
P28:NDI-Se	1.01	11.47	0.66	7.66
P29: P(NDI2HD-T)	1.03	11.97	0.48	5.95
P29-1: P(NDI2HD-T)	1.02	14.42	0.56	8.20
P29-2: P(NDI2HD-T)	1.00	11.49	0.56	6.43
P29-3: P(NDI2HD-T)	0.96	9.85	0.44	4.17
P29-4: P(NDI2HD-T)	0.91	6.87	0.37	2.29
P30: PNDI-T00	0.88	11.10	0.67	6.50
P30: PNDI-T10	0.87	9.90	0.65	5.50
P30: PNDI-T20	0.88	8.90	0.60	4.70
P30-1: PNDI-T00	0.89	9.90	0.66	5.80
P30-1: PNDI-T10	0.89	9.50	0.63	5.30
P30-1: PNDI-T20	0.90	8.60	0.61	4.70
P31:ITIC	0.83	6.31	0.377	1.96
P32:ITIC	0.86	18.45	0.501	7.94

Janssen et al. synthesized a group of donor and acceptor polymers to fabricate all-PSCs. The study focuses on how the control of crystallinity of donor and acceptor polymers affects photovoltaic performance¹⁸⁰. The donor polymers comprise BDT as the donor, TPD, and fluorinated BTz as acceptors, whereas the acceptor polymers comprise NDI, thiophene, and bithiophene moieties. Two random donor and acceptor polymers (P30, P30-1, and PNDI-T10, PNDI-T20) with the same structures were synthesized utilizing different feed ratios and alternative donor and acceptor copolymers (P30 and PNDI-T00). Random donor polymers yielded higher number-average molecular weights than the alternative copolymer, whereas random acceptor polymers yielded lower number-average molecular weights than the alternative acceptor copolymer. The polymer crystallinity decreased when the feed ratio of BDTPD (in donor polymers) and NDITh (in acceptor polymers) fragments increased. Energy levels and optical absorption properties did not change upon

increasing the abovementioned feed ratio. However, investigations of the photovoltaic performance showed that reduction in the polymer crystallinity results in a decrease in J_{SC} , FF, and efficiency. Both P30 and P30-1 were blended with PNDI-T00, PNDI-T10, and PNDI-T20. The best solar cell was obtained via combining P30 with PNDI-T00 yielding an efficiency of 6.5% with a V_{OC} of 0.88 V, J_{SC} of 11.1 mA.cm⁻², and a FF of 0.67.

In 2020, Toppare et al. reported two random donor polymers (P31 and P32) blended with ITIC to fabricate NFA OSCs. The polymers comprise BDT, thiophene, and TPD moieties¹⁸¹. Selenophene was introduced to the polymers' backbone as a π -bridge. The study focuses on the effect of alkyl chains on photovoltaic performance. The number-average molecular weight of P32 is higher than that of P31, and this was attributed to the alkyl chain located on thiophene. P31 exhibited lower power conversion efficiency (1.96%) compared to P32 (7.94%). It is ascribed that the lower molecular weight of the polymer P31 distorts the homogeneity in the morphology of the donor: acceptor blend and morphological investigations supported this. It was also observed that the solubility of the lower molecular weight polymer is poor due to the lack of alkyl chains. The photovoltaic parameters obtained from P32 are as the followings; V_{OC} is 0.86 V, J_{SC} is 18.45 mA.cm⁻², and FF is 0.501. The study provides a synthetic approach to demonstrate the effect of alkyl chains on photovoltaic parameters.

2.1.3 TPD-based conjugated polymers used as Acceptors

As small or fullerene-based molecules, conjugated polymers can also play a role as acceptors for the fabrication of OSCs since they provide deepened LUMO energy levels, matching absorbance, narrow band gaps, and fine crystallinity. Herein, recent TPD-based conjugated polymers utilized as acceptors are reviewed. The chemical structures of TPD-based conjugated polymers used as acceptor materials are illustrated in Figure 2.7 and the photovoltaic parameters are summarized in Table 2.5.

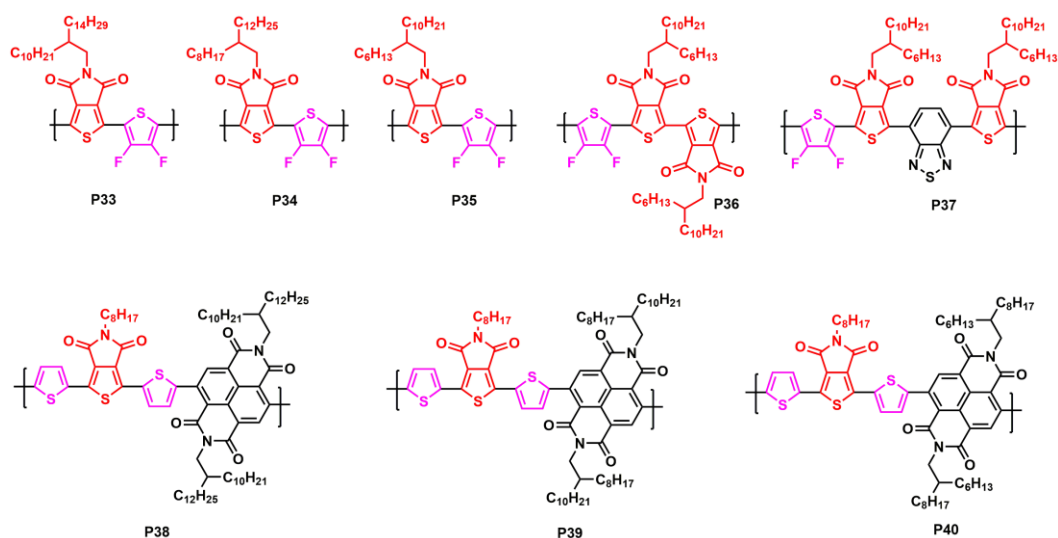


Figure 2.7. Structures of TPD-based acceptor conjugated polymers

Beaujuge et al. reported a set of polymers comprising TPD and fluorinated thiophene moieties¹⁸². The study shines a light on the alternative acceptors to fullerene-based acceptors. Being derivatives of PTPD[2F]T, the polymers (P33, P34, and P35) have varying branched alkyl chains in the polymer backbone. Solar devices were prepared for each polymer, and the efficiency of the devices tends to increase upon shortening the branched alkyl chains. The same trend was observed in the J_{SC} and FF values as well. While P33 showed a J_{SC} of 2.1 mA.cm^{-2} , P34 and P35 showed J_{SC} values of 6.5 and 8.4 mA.cm^{-2} , respectively. The best results were obtained with P35, exhibiting an efficiency of 4.4%, with a V_{OC} of 1.1 V, a J_{SC} of 8.4 mA.cm^{-2} , and a FF of 0.44. It is concluded that the side chain engineering affected the morphology of the active layers and charge transport patterns. The polymer with the shorter alkyl chain demonstrated the most balanced carrier mobility. The study shows that TPD and fluorinated thiophene-based conjugated polymers are potential candidates for polymer acceptors, and side-chain engineering is a crucial method to alter the photovoltaic performance of the polymers.

Table 2.5 Photovoltaic properties of TPD-based acceptor conjugated polymers

Donor:Acceptor	V _{oc} (V)	J _{sc} (mA.cm ⁻²)	FF	PCE (%)
PCE10:P33	0.8	2.10	0.30	0.70
PCE10:P34	1.0	6.50	0.37	2.90
PCE10:P35	1.1	8.40	0.44	4.40
PBDT-TS1:P36	1.1	6.00	0.41	2.60
PBDT-TS1:P37	1.0	11.00	0.44	4.80
PBDTTTPD:P38	1.01	7.67	0.59	4.55
PBDTTTPD:P39	1.00	10.19	0.57	5.78
PBDTTTPD:P40	1.00	12.07	0.55	6.62

In 2017, Beaujuge et al. reported another study on the TPD-based polymer acceptors. The polymers are analogous to the previously reported PTPD[2F]T¹⁸³. In this study, a biTPD and 2,1,3-benzothiadiazole (BT) were introduced to the polymer backbones, and the effect of a second electron-deficient moiety (BT) on optical and electronic properties was investigated. The introduction of BT resulted in a narrower optical band gap and extended optical absorption of the polymer to longer wavelengths. The active layers were prepared with P36/P37 and PBDT-TS1, which was used as the donor polymer. The study shows that introducing a second electron deficient group increases the power conversion efficiency up to 4.8% from 2.2% and proves that the applicability of P37 as a polymer acceptor in BHJ OSCs is higher than its analogue due to its narrow band gap. The best result was obtained from the P37: PBDT-TS1 blend with an efficiency of 4.8%, a V_{oc} of 1 V, a J_{sc} of 11.0 mA.cm⁻², and a FF of 0.44.

Michinobu et al. reported a series of polymers based on NDI (acceptor moiety), TPD (acceptor moiety), and thiophene (donor moiety)¹⁸⁴. As noted in the study, the polymer PNT-R was functionalized with different alkyl chains introduced to the imide site of NDI to obtain P38,39 and P40 with varying alkyl chains. The polymers were utilized for the fabrication of both field-effect transistors and all-PSCs. The active layers were prepared from PNT-R derivatives and PBDTTTPD. Shortening the length of the alkyl chain, the absorption ranges of the polymers expanded, hence

a deep LUMO energy level was obtained. Moreover, the molecular packing properties and crystallinity in the solid-state were enhanced, supported by spectroscopic analyses. Accordingly, the photovoltaic performance of the devices raised from 4.55% to 6.62%. The best performance was obtained from the active layer P40: PBDTTTPD. The device demonstrated an efficiency of 6.62% with a V_{OC} of 1.00 V, a J_{SC} of 12.07 mA.cm⁻², and a FF of 0.550.

This summary of recent studies suggests more attention on TPD-based conjugated polymers. Robust electron deficiency, structure modification, and ease of synthesis make TPD a great candidate moiety to obtain wide band gap and absorption range, enhanced optoelectronic properties, and excellent performing D-A type conjugated polymers for NFA OSCs. The ease of introduction of π -bridging units like thiophene, thienothiophene, and selenophene helps TPD-based polymers show better absorption and electron transfer through polymer backbones. BiTPD needs more research and attention, as well, since it has similar properties and potential application era. To sum up, ease of preparation, deepened frontier energy levels, robust crystallinity, and improving efficiency up to almost 16% prove TPD-based polymers will perform better in the near future by new design approaches.

This summary of these recent studies is reproduced from Macromol. Chem. Phys. 2022, 2100421 with the permission of John Wiley & Sons.

2.2 Aim of the study

In this study, a series of new random conjugated polymers based on TPD and selenophene were designed and synthesized. The polymers were used as donor materials in the fabrication of NFA OSCs via mixing with ITIC to obtain active layer. As well as NFA, PCBM based devices were also fabricated for comparison.

A part of this study was published in *Renewable Energy*.

2.3 Non-fullerene organic solar cells based on thienopyrroledione and chalcogenophene comprising random copolymers

Four new random D-A copolymers, signed as ME1, ME2, ME3, and ME4, were designed and synthesized. Electrochemical and spectroelectrochemical measurements were performed to investigate the absorption, energy levels, electronic and optical band gaps for comparison. The polymers were used as donor polymers in the active layer to fabricate non-fullerene, bulk heterojunction (BHJ) organic photovoltaics (OPVs). Investigations were carried out through the conventional BHJ structure; ITO/PEDOT:PSS/ Active Layer/LiF/Al, where active layer consists of 3,9-bis(2-methylene-(3-(1,1-dicyanomethylene)- indanone))-5,5,11,11 tetrakis(4-hexylphenyl)-dithieno[2,3-d:20,30-d']-s-indaceno[1,2-b:5,6-b']dithiophene (ITIC) as the acceptor and thienopyrroledione containing donors. The device based on ME1:ITIC(1:1) blend with a thickness of 161 nm gave the best performance with a power conversion efficiency (PCE) of 7.94%, an open-circuit voltage (V_{OC}) of 0.86 V, a short-current density (J_{SC}) of 18.45 mA cm⁻² and an FF of 50.12%. The highest PCE obtained from ME2 based organic solar cell is 1.96%. ME2 exhibited low solubility attributed to the lack of alkyl groups enhancing polymer solubility, electronic properties, and photovoltaic performances. For ME3, the best result was found 1.4% from ME3:ITIC (1:1) blend and ME4:ITIC (1:1) gave an efficiency of 1.32%. When ME1 was blended with PC₇₁BM, the device was not efficient as the one prepared from ME1:ITIC; it resulted an efficiency of 7.62%. In contrast to ME1, ME2 blended with PC₇₁BM performed an efficiency of 6.30%, which is superior to the ME2:ITIC blend. Similar to the ME2:PC₇₁BM blend, the devices based on ME3/ME4:PC₇₁BM blends resulted better performance compared to ME3/ME4:ITIC, giving efficiencies of 2.27 and 2.45%, respectively.

2.3.1 Introduction

Conventional organic photovoltaics (OPVs) generally include a bulk heterojunction (BHJ) architecture, a blend of a donor, and an acceptor moiety. Absorption of light by this blend generates excitons splitting into free chargers^{38,185,186}. Although OPVs bear various components, acceptor materials significantly define the solar cell device's power conversion efficiency (PCE)¹⁸⁷. Fullerene derivatives with unsurpassed charge transport features and the superior ability to create phase separation in nanoscale in the blend led them to be utilized in the BHJ solar cells as promising acceptor moieties^{113–115,188}. Although fullerene-based acceptors have these superior properties, there are various drawbacks, including the cost of purification and production, vulnerability to air, limited light absorption, and difficulties in adjusting optoelectronic properties. These aspects brought a challenge in increasing the PCE of OPVs^{116,118,189,190}. Non-fullerene acceptors (NFAs) have caught great attention. NFA molecules can be synthesized and purified easily via various functional groups that can adjust optoelectronic properties compared to fullerene derivatives. In addition to the synthesis facilities, enhanced light absorption, morphology, and electronic properties eliminate fullerene derivatives acceptors^{191,192}. Considering features mentioned earlier (superior electronic and optical properties, ease of production, enhanced absorption), NFA-based organic photovoltaics have demonstrated higher power conversion efficiencies (PCE) than fullerene-based analogous during the past few years^{193–195}. Compared to bilayer structure, BHJ provides an optimal domain size to enhance exciton dissociation by forming an ideal photoactive layer, a vicinal mixture of donor and acceptor¹⁹⁶.

Being rigid and symmetric, TPD can be easily modified to introduce various functional groups; subsequently, the solubility of polymers can be controlled. TPD has a strong electron-withdrawing feature attributed to the diimide nature. This results in lower band gap conjugated polymers via stabilizing the lowest unoccupied molecular orbital (LUMO). Besides, due to its quinoidal structure, TPD can stabilize excited state energy. Therefore, TPD containing conjugated polymers are supposed

to exhibit high V_{OC} values^{139,197–202}. It is well known that chalcogenophenes like selenophene, thiophene, and alkyl-substituted thiophene are introduced as p-spacer to tune frontier molecular orbital energy levels, thus band gaps^{203–209}. Conjugated polymers, including π -spacers, show red-shifted absorption²¹⁰. An effective way of enhancing PCE values of polymer-based OPVs is alkyl side-chain engineering. Such modifications improve the solubility properties of the polymers and the morphology of the donor: acceptor blend through molecular aggregation; π - π stacking, which is crucial for the device performance^{211,212}. Morphology of the active layer alters with the optimized selection of the alkyl chain. While long alkyl chains provide large domain sizes, linear and branched alkyl chains control the positions of acceptor molecules in fullerene-based BHJ blends^{213–215}. Hou's group recently reported naphtho[2,3-c]thiophene-4,9-dione-based polymers substituted with branched alkyl chains. The polymers were used as donors in non-fullerene-based BHJ OPVs. The study reveals that alkyl chains cause a conjugated core distortion, resulting in a better BHJ morphology, subsequently high PCEs²¹⁶.

Motivated by these aspects of non-fullerene acceptors and TPD moieties, our work focuses on the design and fabrication of non-fullerene BHJ OPVs and the investigation of alkyl chains' effect on the device performance. Herein, a series of new random copolymers were used as donor polymers to fabricate NFA-based organic BHJ OSCs. Random copolymers were obtained via coupling the monomers with 2,5-dibromo-3-(2-Ethylhexyl)thiophene or 2,5-Dibromothiophene, and BDT(TiC8) through Stille Polycondensation. Recently, various reports revealed TPD-based conjugated polymers for the application of non-fullerene OPVs with PCEs exceeding from 7% to 16%^{142,144,156,165,167,217–219}. Selenophene and furan were introduced as π -spacers between TPD and BDT(TiC8) to tune optoelectronic properties. Thiophene, alkyl-substituted thiophene, and BDT(TiC8) were introduced as donors into the polymer backbone to further regulate these properties. Obtained random conjugated polymers were used as donor polymers in the active layer to fabricate non-fullerene, bulk heterojunction OPVs.

2.3.2 Experimental

BDT(TiC8) was purchased from SOLARMER. Compound **1** (thiophene-3,4-dicarboxylic acid) was both synthesized and purchased from Sigma-Aldrich. All other chemicals were purchased from Sigma-Aldrich and used without any further purifications. Structural analyses of the synthesized molecules were performed via NMR (Bruker Spectrospin Avance DPX-400) and attenuated total Reflectance-Fourier-transform infrared spectroscopy (ATR-FTIR) (Thermo Scientific Nicolet™ iS10 FTIR). Weight-average and number-average molecular weights (M_w , M_n) of the polymers were determined via size exclusion chromatography (SEC) (Shimadzu LC-20AD) in chloroform at 40 °C. Electrochemical and spectroelectrochemical measurements were performed with a three-electrode system. Indium tin oxide (ITO) was utilized as the working electrode. Platinum (Pt) wire was used as the counter electrode, and silver (Ag) wire was used as the reference electrode. Cyclic voltammograms of the polymer films were obtained implementing a GAMRY Reference 600 potentiostat, while spectroelectrochemical measurements were performed with a PerkinElmer Lambda 25 UV-Vis spectrophotometer. To fabricate BHJ devices, ITO was used as the anode, PEDOT:PSS as the hole transport layer, lithium fluoride (LiF) as the cathode buffer layer, and aluminum (Al) was used as the cathode. Morphology investigations of polymer: acceptor blends were performed via Atomic Force Microscopy (AFM) (Veeco MultiMode V) and Transmission Electron Microscopy (TEM) (Tecnai G2 Spirit BioTWIN) techniques.

2.3.2.1 Synthesis of monomers and polymers

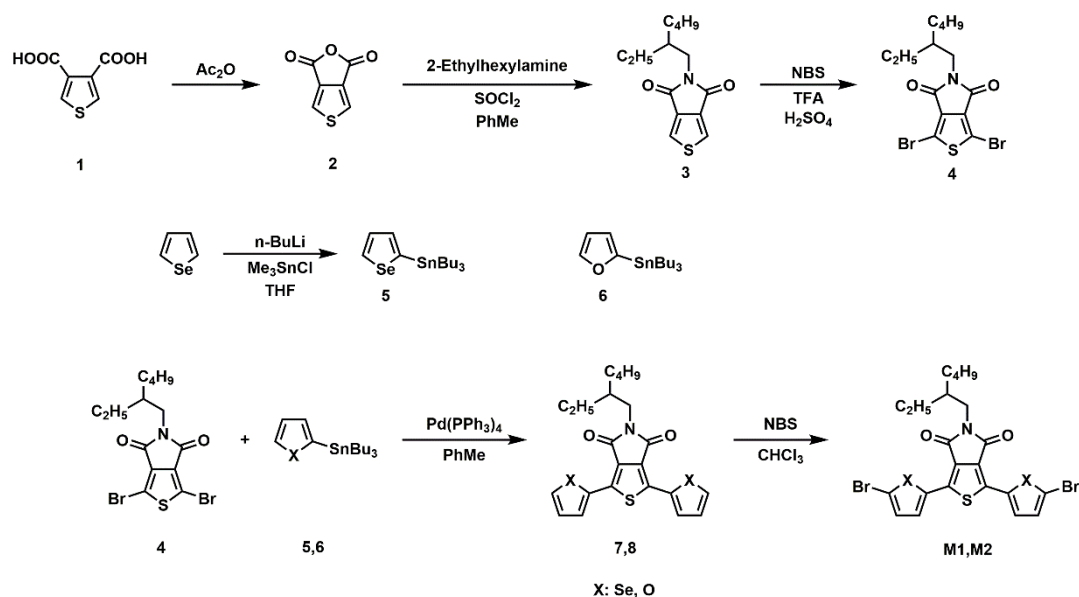


Figure 2.8. Synthetic route for M1 and M2

2.3.2.1.1 Synthesis of 1H,3H-thieno[3,4-c]furan-1,3-dione (2)

In a two-necked flask with a magnet bar under argon atmosphere, thiophene-3,4 dicarboxylic acid (1.5 g, 8.7 mmol) dissolved in acetic anhydride (45 mL) was charged. The solution was stirred at 140 °C. 24 h later, it was cooled to ambient temperature, and acetic anhydride was removed under reduced pressure. A brown solid product was obtained by crystallization from toluene. Yield: 0.71 g, 53%.

¹H NMR (400 MHz, CDCl₃, δ, ppm): 8.1 (s, 2H)

¹³C NMR (100 MHz, CDCl₃, δ, ppm): 156.3, 135.3, 129.3

2.3.2.1.2 Synthesis of 5-(2-ethylhexyl)-4H-thieno[3,4-c]pyrrole-4,6(5H)-dione (3)

In a three-necked flask under argon atmosphere, thieno[3,4-c]furan-1,3-dione (0.71 g, 4.63 mmol) was dissolved in anhydrous toluene (50 mL). 2-Ethylhexylamine (0.84

g, 6.53 mmol) was added. The mixture was stirred at 115 °C. 24 h later, the reaction mixture was cooled to ambient temperature, and the solvent was removed under reduced pressure. The solid obtained was dissolved in SOCl₂ (30 mL) and the solution was stirred at 75 °C under argon atmosphere for 3h. Subsequently, the solution was cooled to ambient temperature, and the solvent was removed under reduced pressure. The yellowish product was purified by silica column chromatography (SiO₂, Dichloromethane). Yield: 0.95 g, 77%.

¹H NMR (400 MHz, CDCl₃, δ, ppm): 7.80 (s, 2H), 3.51 (d, J = 7.28 Hz, 2H), 1.84-1.75 (m, 1H), 1.37-1.26 (m, 8H), 0.91-0.86 (m, 6H)

¹³C NMR (100 MHz, CDCl₃, δ, ppm): 163, 136.6, 125.4, 42.4, 38.2, 30.5, 28.5, 23.8, 23.0, 14.0, 10.4

2.3.2.1.3 Synthesis of 1,3-dibromo-5-(2-ethylhexyl)-4H-thieno[3,4-c]pyrrole-4,6(5H)-dione (4)

5-(2-Ethylhexyl)-4H-thieno[3,4-c]pyrrole-4,6(5H)-dione (0.95 g, 3.58 mmol) was dissolved in TFA (12 mL) and H₂SO₄ (4 mL) under argon atmosphere. N-bromosuccinimide (1.91 g, 10.74 mmol) was added portion-wise. The reaction mixture was stirred at ambient temperature. After 24 h, the mixture was quenched with water and extracted with dichloromethane. Combined organic layers were dried over Mg₂SO₄. The solvent was removed under reduced pressure, and the product was purified by silica column chromatography (SiO₂, hexane: dichloromethane, 1:2). Yield: 0.92 g, 60%.

¹H NMR (400 MHz, CDCl₃, δ, ppm): 3.49 (d, J=7.2 Hz, 2H), 1.80-1.74 (m, 1H), 1.36-1.21 (m, 8H), 0.92-0.85 (m, 6H)

¹³C NMR (100 MHz, CDCl₃, δ, ppm): 160.7, 134.7, 112.9, 42.6, 38.18, 30.5, 28.5, 23.8, 22.9, 14.0, 10.3

2.3.2.1.4 Synthesis of tributyl(selenophen-2-yl)stannane (5)

Selenophene (3 g, 35.6 mmol) was dissolved in dry THF (60 mL) under Ar atmosphere. The temperature of the solution was cooled to -78 °C in a dry ice bath. To the stirring solution, *n*-BuLi (16 mL, 2.5 M) was added dropwise in a period of 20 minutes. After stirring the reaction mixture for 45 minutes at -78 °C, SnBu₃Cl (10.7 mL, 39 mmol) was added slowly. The reaction mixture was warmed to the ambient temperature and allowed to stir overnight. THF was removed under reduced pressure. The mixture was diluted with DCM and washed with NaHCO₃, distilled water, and brine. Organic layers were dried over Mg₂SO₄, and the solvent was removed. A light yellow oil was obtained and used without any further purification.

¹H NMR (400 MHz, CDCl₃, δ, ppm): δ 8.38 (d, *J* = 3.6 Hz, 1H), 7.54 (m, 1H), 1.67-1.56 (m, 6H), 1.42-1.33 (m, 6H), 1.16-1.11 (m, 6H), 0.95-0.91 (m, 9H).

¹³C NMR (100 MHz, CDCl₃, δ, ppm): 143.6, 137.9, 135.3, 130.5, 29.0, 27.3, 13.7, 11.1.

2.3.2.1.5 5-(2-ethylhexyl)-1,3-di(selenophen-2-yl)-4H-thieno[3,4-c] pyrrole-4,6(5H)-dione (7)

Under argon, compound **4** (0.3 g, 0.7 mmol) and tetrakis(triphenylphosphine)palladium(0) (0.09 g, 0.08 mmol) were dissolved in dry toluene (25 mL). After the mixture reached 50 °C, compound **5** (0.9 g, 2.14 mmol) was added in one portion. Following 17 h stirring at 110 °C, the reaction mixture was cooled to ambient temperature, and the solvent was removed under reduced pressure. Compound **7** was obtained by purification via chromatography (SiO₂, hexane: dichloromethane, 1:1). Yield: 0.27 g, 75%.

¹H NMR (400 MHz, CDCl₃): δ: 8.21 (d, *J* = 5.6 Hz, 2H), 7.93 (d, *J* = 3.9 Hz, 2H), 7.33 (m, 2H), 3.55 (d, *J* = 7.4 Hz, 2H), 1.88-1.82 (m, 1H), 1.42-1.25 (m, 8H), 0.87-0.93 (m, 6H)

¹³C NMR (100 MHz, CDCl₃): δ: 163, 138.82, 136.39, 135.64, 131.57, 130.19, 127.53, 41.92, 38.04, 31.34, 28.39, 23.72, 22.59, 14.50, 10.35.

2.3.2.1.6 Synthesis of 5-(2-ethylhexyl)-1-(furan-2-yl)-3-(furan-3-yl)-4H-thieno[3,4-c]pyrrole-4,6(5H)-dione (8)

Compound **4** (0.4 g, 0.94 mmol) and tetrakis(triphenylphosphine)palladium(0) (0.12 g, 0.11 mmol) were dissolved in dry toluene (30 mL) under argon atmosphere. The reaction mixture was warmed up. At 50 °C, compound **6** (1.0 g, 2.84 mmol) was added dropwise, and the mixture was stirred at 115 °C for 17 h. Completion of the reaction was monitored by thin layer chromatography. The mixture was allowed to reach the ambient temperature, and the solvent was removed under rotary evaporation. The desired product was purified by chromatography (SiO₂, hexane: dichloromethane, 1:1). Yield: 0.37 g, 98.6%.

¹H NMR (400 MHz, CDCl₃, δ, ppm): 7.67 (d, J=3.4 Hz, 2H), 7.50 (d, J=1.2 Hz, 2H), 6.59 (dd, J=3.5, 1.8 Hz, 2H), 3.55 (d, J=7.3 Hz, 1H), 1.83 (dt, J=12.7, 6.6 Hz, 2H), 1.65-1.58 (m, 2H), 1.40-1.25 (m, 4H), 0.91 (m, 6H)

¹³C NMR (100 MHz, CDCl₃, δ, ppm): 162.93, 146.46, 143.78, 131.56, 127.16, 113.43, 113.06, 42.45, 38.31, 30.59, 28.60, 23.04, 14.09, 10.48

2.3.2.1.7 Synthesis of 1,3-bis(5-bromoselenophen-2-yl)-5-(2-ethylhexyl)-4H-thieno[3,4-c]pyrrole-4,6(5H)-dione (M1)

Compound **7** (0.25 g, 0.48 mmol) was dissolved in CHCl₃, (15 mL) under nitrogen. *N*-bromosuccinimide (0.22 g, 1.2 mmol) was added in one portion. The reaction mixture was stirred overnight at ambient temperature and monitored by thin-layer chromatography. After completing the reaction, the mixture was washed with water, and organic fractions were dried over Mg₂SO₄. Chloroform was removed under

reduced pressure, and the target product was isolated by column chromatography on silica gel (SiO₂, hexane: dichloromethane, 4:1). Yield: 0.25 g, 77%.

¹H NMR (400 MHz, CDCl₃): δ: 7.43 (d, *J* = 4.43 Hz, 2H), 7.21 (d, *J* = 4.43 Hz, 2H), 3.47 (d, *J* = 7.4 Hz, 2H), 1.82-1.76 (m, 1H), 1.38-1.22 (m, 8H), 0.9 (q, 6H).

¹³C NMR (100 MHz, CDCl₃): δ: 162.8, 138.0, 137.6, 133.3, 130.7, 127.8, 122.5, 42.4, 38.1, 30.4, 28.4, 23.8, 23.0, 14.0, 10.3.

2.3.2.1.8 Synthesis of 1,3-bis(5-bromofuran-2-yl)-5-(2-ethylhexyl)-4H-thieno[3,4-c]pyrrole-4,6(5H)-dione (M2)

A solution of compound **8** (0.35 g, 0.88 mmol) in chloroform (20 mL) in a two-necked flask was prepared under a nitrogen atmosphere. *N*-bromosuccinimide (0.35 g, 1.95 mmol) was added in one portion. TLC controlled reaction mixture was stirred overnight at ambient temperature. The mixture was washed with water twice, and combined organic fractions were dried over Mg₂SO₄. The solvent was removed under a rotary evaporator. The target product was obtained by column chromatography on silica gel (SiO₂, hexane: dichloromethane, 4:1). Yield: 0.36 g, 74%.

¹H NMR (400 MHz, CDCl₃, δ, ppm): 7.62 (d, *J* = 3.6 Hz, 2H), 6.50 (d, *J* = 3.6 Hz, 2H), 3.52 (d, *J* = 7.3 Hz, 2H), 1.85-1.75 (m, 1H), 1.39-1.25 (m, 8H), 0.93-0.87 (m, 6H)

¹³C NMR (100 MHz, CDCl₃, δ, ppm): 162.68, 148.19, 130.17, 127.16, 124.37, 115.76, 114.96, 42.50, 38.32, 30.57, 28.57, 23.89, 23.02, 14.07, 10.45

2.3.2.2 Polymer Syntheses

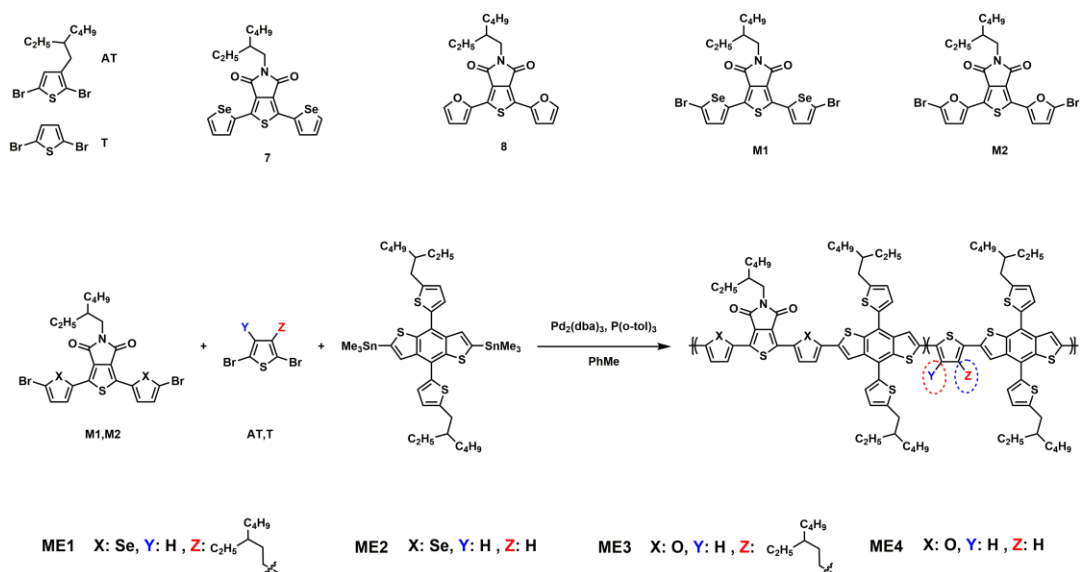


Figure 2.9. Synthetic routes for ME1-ME4

2.3.2.2.1 Syntheses of ME1 and ME2

M1 (73.4 μmol , 1 eq.), BDT(TiC8) (147 μmol , 2 eq.), $\text{P}(\text{o-tol})_3$ (50 μmol , 0.68 eq.), and $\text{Pd}_2(\text{dba})_3$ (16 μmol , 0.22 eq.) were introduced to a 25 mL Schlenk tube which was charged with a magnet bar, set up in an oil bath and connected to a vacuum-gas manifold. Following 1 h of vacuuming, Schlenk was provided with argon for the rest. Dry toluene (10 mL) was added to the mixture. The reaction mixture was heated up to 50 $^{\circ}\text{C}$ and followed by the addition of 2,5-dibromo-3-(2-ethylhexyl) thiophene or 2,5-dibromothiophene (73.4 μmol , 1 eq.). The reaction temperature was set to 100 $^{\circ}\text{C}$. The completion of the reaction was monitored by thin-layer chromatography. After stirring 24 h, the reaction mixture was allowed to cool down. The solvent was removed under reduced pressure. Cold methanol (100 mL) was added to the crude product. For the removal of catalytic residue, sodium diethyldithiocarbamate trihydrate (15 mg) was added. The mixture was stirred for 1 h, subjected to Soxhlet extractor, and washed with acetone, hexane, chloroform, and chlorobenzene. Low

molecular weight fractions were removed with acetone and hexane. Both **ME1** and **ME2** were isolated in chloroform. Solvents were removed under reduced pressure, and **ME1** (Yield: 125 mg, 91%) and **ME2** (Yield: 80 mg, 62%) were obtained as dark purple crystals following recrystallization from methanol. M_n , M_w , and PDI values for the polymers are shown in Table 2.6.

2.3.2.2.2 Syntheses of ME3 and ME4

M2 (90 μ mol, 1 eq.), BDT(TiC8) (180 μ mol, 2 eq.), P(o-tol)₃ (61 μ mol, 0.68 eq.), and Pd₂(dba)₃ (20 μ mol, 0.22 eq.) were introduced to a 25 mL Schlenk tube which was charged with a magnet bar, set up in an oil bath and connected to a vacuum-gas manifold. After keeping under vacuum for 1h, the Schlenk tube was supplied with Ar atmosphere. Dry toluene (10 mL) was added to the reaction mixture and the temperature was set to 50 °C. 2,5-dibromo-3-(2-ethylhexyl) thiophene or 2,5-dibromothiophene (90 μ mol, 1 eq.) was added. The reaction temperature was set to 100 °C. The completion of the reaction was monitored by TLC. The same steps for ME1 and ME2 were followed for purification. Yield: (ME3) 65 mg, 44%. (ME4) 80 mg, 51%. M_n , M_w , and PDI values for ME3 and ME4 are shown in Table 2.6.

Table 2.6 Molecular weights and PDI values of ME1, ME2, ME3, and ME4

Polymer	M_n (kDa)	M_w (kDa)	PDI
ME1	11	35	3.18
ME2	4.8	9.2	1.91
ME3	4.7	6.5	1.38
ME4	3.0	4.0	1.33

2.3.2.3 OSC Fabrication

For the fabrication of OPVs, a conventional BHJ device structure was built; ITO/PEDOT:PSS/Active Layer/LiF/Al. ITO-coated glass substrates were cleaned several times; ultra-sonication with toluene, detergent, water, and isopropyl alcohol (IPA), respectively. Following ultra-sonication, ITO-coated glass substrates were exposed to oxygen plasma for 5 min to remove organic contaminations and tune work function²²⁰. Polymer: acceptor blends were coated by spin coating in N₂ filled glove box. LiF (0.6 nm) and Al (100 nm) were evaporated at low pressure ($\sim 10^{-6}$ mbar) under vacuum. Current density vs. voltage measurements were performed by a Keithley 2400 digital source meter under AM 1.5 G solar radiation simulated at 100 mW.cm⁻². External quantum efficiency (EQE) measurements were carried out with monochromatic light.

2.3.3 Results

2.3.3.1 Electrochemical and spectroelectrochemical studies

HOMO and LUMO energy levels and band gap values are of great importance for conjugated polymers since they affect their applicability in different application fields like organic photovoltaics and electrochromic devices. In order to investigate the redox behaviors and HOMO/LUMO energy levels of the resulting polymers, cyclic voltammetry (CV) studies were performed, and corresponding voltammograms were depicted in Figure 2.10. Due to its certain simplicity and easy use, the CV technique was preferred for electrochemical analysis. ME1, ME2, ME3, and ME4 were dissolved in CHCl₃ (5 mg. mL⁻¹) and spray-coated on an ITO glass electrode. Single scan cyclic voltammetry of the polymer films was performed in the potential range between -2.0 V and 1.4 V for ME1 and between -1.8 V and 1.4 V for ME2 in 0.1 M tetrabutylammonium hexafluorophosphate; TBAPF₆/ACN,

electrolyte/solvent couple. For ME3 and ME4, the potential ranges were between -2.0 V and 1.5 V, 0 V and 1.5 V, respectively.

As illustrated in Figure 2.10, ME1, ME2, and ME3 exhibited ambipolar character, i.e., polymers have both p-type and n-type doping behaviors. While ME1 has reversible oxidation/reduction peaks at 1.15 V and at -1.52/-1.85 V, ME2 exhibits reversible oxidation/reduction peaks at 1.04 V and -1.31/-1.69 V in the anodic region and the cathodic region. For ME3, the corresponding values were determined as 1.43 V and -1.40/-1.82 V. For ME4, the reduction peak was determined at 1.38 V. HOMO/LUMO energy levels of ME1, ME2, and ME3 were calculated by using the oxidation and reduction onset values determined from CVs. HOMO energy level of ME4 was calculated using the oxidation onset value from the CV. However, the LUMO energy level was calculated by subtraction the optical band gap from the HOMO energy level since the polymer film did not show ambipolar characteristics.

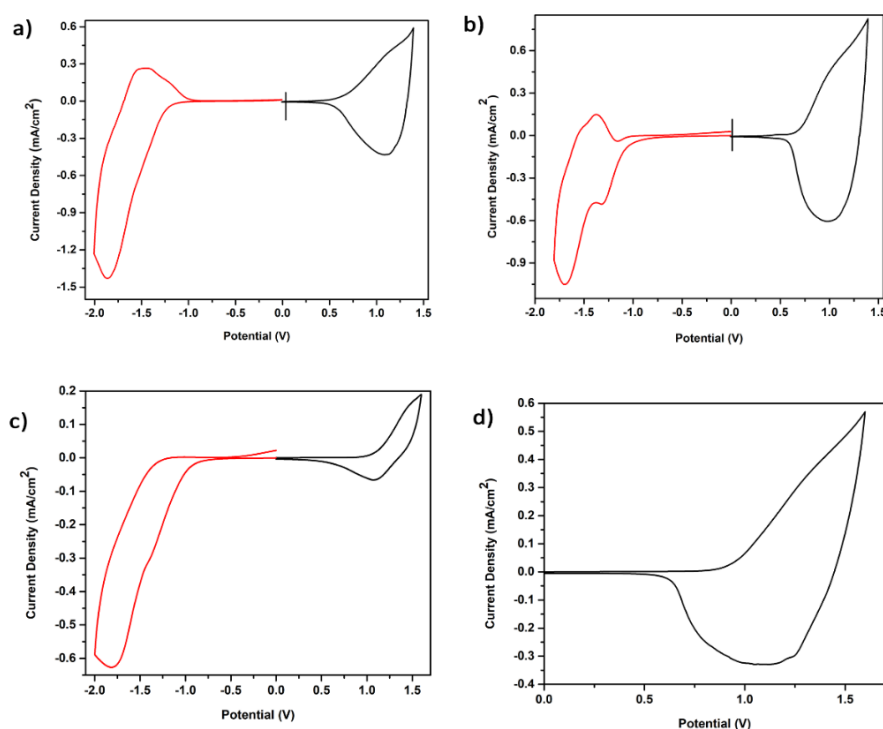


Figure 2.10. Single scan cyclic voltammograms of (a) ME1, (b) ME2, (c) ME3, and (d) ME4 on ITO electrode in 0.1 M TBAPF₆/ACN electrolyte/solvent couple at a scan rate of 100 mV/s.

Due to the ambipolar characteristics of the two polymers, HOMO/LUMO energy levels were calculated from the oxidation/reduction onset potentials as -5.38 eV/-3.52 eV for ME1 and as -5.43 eV/-3.69 eV for ME2, respectively. HOMO/LUMO energy levels of ME3 and ME4 were calculated as -5.84/-3.64 eV and -5.68/-3.84 eV, respectively. All electrochemical properties of ME1-ME4 are summarized in Table 2.7.

Table 2.7 Electrochemical properties of ME1-ME4

Polymer	$E_{p-doping}$ (V)	$E_{onset-p-doping}$ (V)	$E_{n-doping}$ (V)	$E_{onset-n-doping}$ (V)	HOMO (eV)	LUMO (eV)	E_g^{el} (eV)	E_g^{op} (eV)
ME1	1.15	0.63	-1.52/ -1.85	-1.23	-5.38	-3.52	1.86	1.78
ME2	1.04	0.68	-1.31/ -1.69	-1.06	-5.43	-3.69	1.74	1.69
ME3	1.43	1.09	-1.40/ 1.82	-1.12	-5.84	-3.63	2.21	1.60
ME4	1.38	0.93	-	-	-5.68	-3.84	-	1.84

2.3.3.2 Spectroelectrochemistry

Spectroelectrochemical analyses were carried out to examine the changes in the optical properties of ME1-ME4 via stepwise oxidation. A potentiostat integrated UV-Vis spectrophotometer was used during spectroelectrochemical studies, and progressively increasing potentials were applied while recording UV-Vis spectra. Similar to the electrochemical studies initially, polymers were dissolved in $CHCl_3$ and spray-coated on ITO-coated glass electrodes. They were dipped into 0.1 M TBAPF₆/ACN solutions to perform the spectroelectrochemical analysis. Neutral state absorptions were recorded at constant potentials (0.0 V) before the stepwise oxidation. Then electronic absorption spectra were recorded upon stepwise oxidation for ME1-ME4 (Figure 2.11). During stepwise oxidation, while the neutral state absorption bands were decreasing, new absorption bands appeared at 830 nm and 835 nm, which can be dedicated to the formation of radical cations.

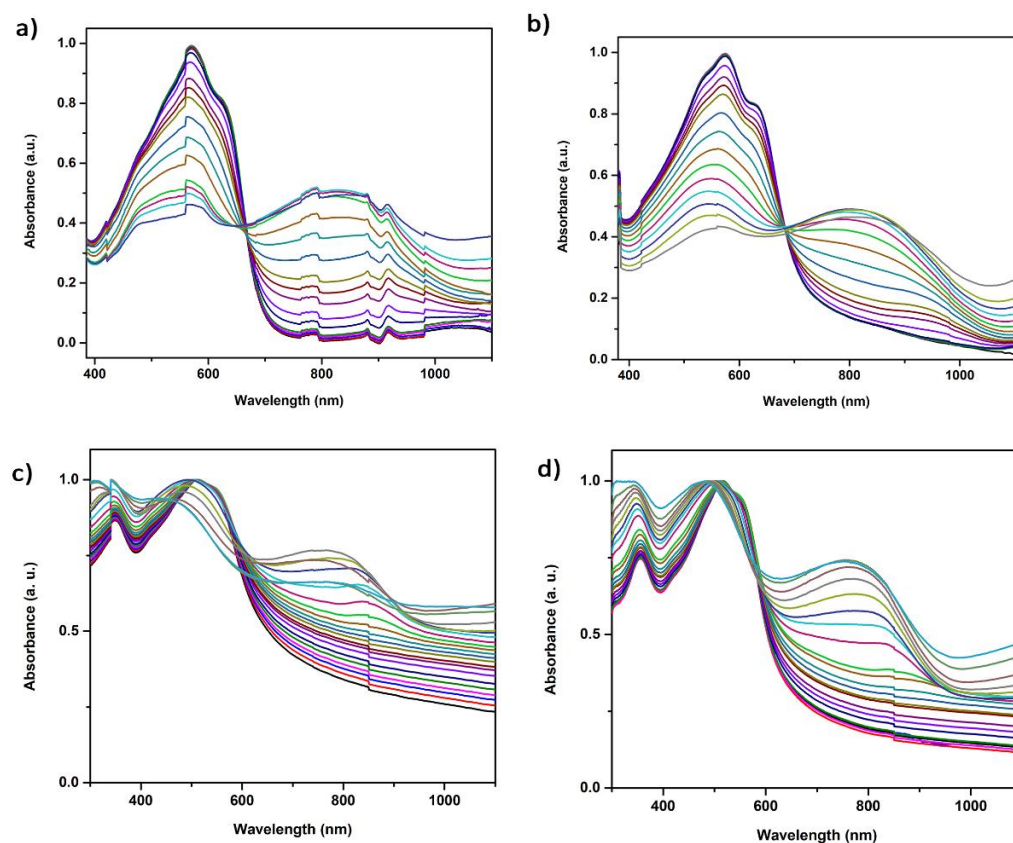


Figure 2.11. Electronic absorption spectra of ME1-ME4 in 0.1 M TBAPF₆/ACN solution between 0.0 V and 1.4 V for ME1 (a), 0.0 V and 1.4 V for ME2 (b), 0.0 V and 1.5 V for ME3 (c), and (d) 0.0 V and 1.6 V for ME4.




As illustrated in Figure 2.11, neutral state absorptions were recorded at 571 nm and 576 nm for ME1 and ME2, corresponding to the π - π^* transitions. The corresponding values for ME3 and ME4 were obtained as 515 and 520 nm. The optical band gap values ($E^{\text{opt}}_{\text{g}}$) of ME1-ME4 were calculated from the onset of the neutral state absorption according to the equation $E^{\text{opt}}_{\text{g}} = 1241/\lambda_{\text{onset}}$. As summarized in Table 2.8, $E^{\text{opt}}_{\text{g}}$ values were calculated as 1.78, 1.69, 1.60, and 1.84 eV for Me1, ME2, ME3, and ME4, respectively. All spectroelectrochemical analyses were summarized in Table 2.8.

Table 2.8 Optical properties of ME1-ME4

Polymer	λ_{\max} (nm)	$\lambda_{\text{onset}_{\max}}$ (nm)	E_g^{op} (eV)
ME1	571,630	697	1.78
ME2	576,631	734	1.69
ME3	515	775	1.60
ME4	520	674	1.84

Following electrochemical and spectroelectrochemical characterizations, the optical properties of the polymers were also investigated both in the thin film form and in CHCl_3 solution. Another important application field for conjugated polymers is electrochromic device applications. For these applications, colors and parameters like switching time and optical contrast of the resulting polymers are essential. In Table 2.9, the colors of ME1-ME4 recorded in the neutral, oxidized, and reduced states are illustrated. ME1-ME2 showed multichromic behavior and exhibited varying tones of purple with gray-colored oxidized states and grayish-blue colored reduced states. ME3 and ME4 showed grayish tones varying from orange/red color at the neutral states of the polymer films. In Table 2.9, L, a, and b values (determined by CIE (Commission Internationale de l'Eclairage)) of the polymer films were also represented.

Table 2.9 Colors of (a) ME1, (b) ME2, (c) ME3, and (d) ME4 films at neutral and oxidized/reduced states with intermediate colors

	-2.0 V	0V	1.4 V	
ME1				
L	37.21	27.81	33.73	38.04
a	-1.21	3.28	4.15	0.98
b	4.66	-1.46	2.19	-0.28


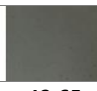
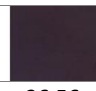


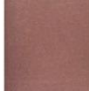

















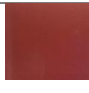




	-2.0 V	0V	1.4 V		
ME2					
L	43.95	42.65	26.56	26.56	29.70
a	-0.48	-2.83	7.40	7.40	3.86
b	3.53	3.99	-5.76	-3.93	-1.89

Table 2.9 Colors of (a) ME1, (b) ME2, (c) ME3, and (d) ME4 films at neutral and oxidized/reduced states with intermediate colors (continued)

0 V  + 1.6 V									
ME3 -OX									
L	44.65	50.24	44.47	46.72	47.11	45.45	44.90	42.68	42.23
a	20.81	19.15	14.46	9.20	5.83	4.10	3.95	2.86	2.60
b	10.64	11.49	11.98	9.04	9.50	7.05	5.77	4.78	5.93

-2.0 V  0 V								
ME3 -RED								
L	47.13	48.21	47.43	46.46	45.74	43.71	47.09	44.65
a	0.67	0.33	2.13	3.25	5.25	14.73	19.34	20.81
b	9.97	7.40	7.48	6.70	8.10	10.88	12.30	10.64

0 V  +1.5 V					
ME4-OX					
L	32.15	32.94	30.32	30.92	29.55
a	20.81	21.81	16.52	11.23	6.33
b	24.32	17.52	14.93	12.38	6.39

2.3.3.3 Kinetic studies

As mentioned before, kinetic studies were performed in order to record and analyze the optical contrast and switching time values which are crucial, especially for the electrochromic performances of resulting polymers. For that purpose, a square-wave potential method was used by applying potentials between two extreme states (oxidized/reduced states) with 5 s time intervals at λ_{max} values located at 570 nm/830

nm for ME1 and 575 nm/835 nm for ME2. The corresponding values for ME3 and ME4 are 515/775 nm and 520/780 nm, respectively.

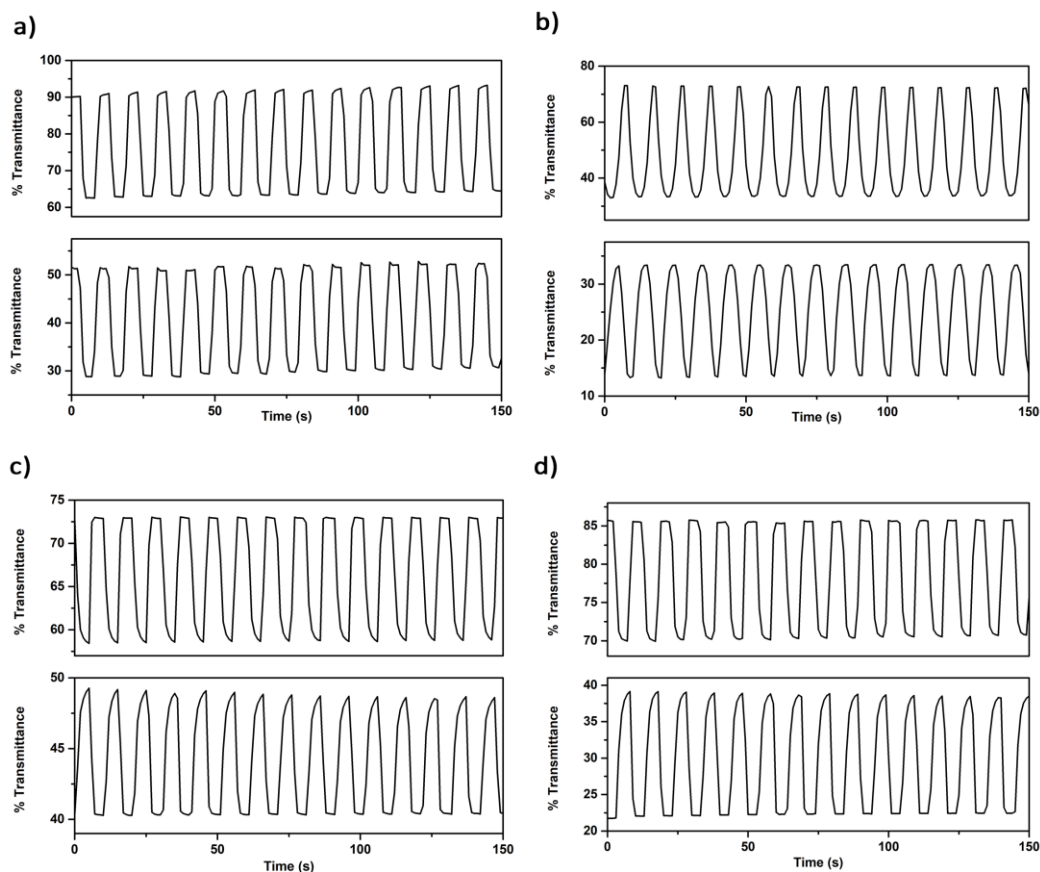


Figure 2.12. Percent transmittance changes for (a) ME1, (b) ME2, (c) ME3, and (d) ME4 in 0.1 M TBAPF₆/ACN solution.

As a result of electrochromic switching studies, percent transmittance against time graphs were recorded and illustrated in Figure 2.12 for ME1, ME2, ME3, and ME4, respectively. Percent transmittance changes were determined as 23% at 570 nm, 29% at 830 nm for ME1, and 20% at 575 nm, 40% at 835 nm for ME2. And for ME3, the percent transmittance changes were determined as 9% at 515 nm and 14% at 775 nm, whereas for ME4, the corresponding values are 17% at 520 nm and 16% at 780 nm. The time required for one complete switch between two extreme states could be defined as switching time, and for the polymers, these values were calculated and

represented in Table 2.10. Switching times for ME1 are calculated as 1.8 and 2.0 s, and for ME2, they are calculated as 2.9 and 3.7 s. For ME3 and ME4, corresponding values are calculated as 1.2 and 0.4 s, and 1.7 and 0.6 s, respectively.

Table 2.10 Kinetic properties of ME1-ME4

Polymer	λ (nm)	Optical Contrast(%)	Switching Time (s)
ME1	570	23	1.8
	830	29	2.0
ME2	575	20	2.9
	835	40	3.7
ME3	515	9	1.2
	775	14	0.4
ME4	520	17	1.7
	780	16	0.6

2.3.3.4 OPV studies

The active layer consists of the non-fullerene acceptor, ITIC, and thienopyrroledione containing donors. Various optimization studies (solvent selection, determination of donor: acceptor ratio, active layer's mass ratio optimizations, determination of the active layer's thickness, additive selection (diphenyl ether; DPE, 1-chloronaphthalene; CN and 1, 8- diiodooctane; DIO), and thermal annealing) were carried out to obtain the best performance from the devices. As a result of the optimizations, the mass ratio was determined as 30 mg. mL⁻¹. Polymers: Acceptor (ITIC) blend was dissolved in chlorobenzene (CB). Active layers were spin-coated with a rate of 2000 rpm for 30 s from ITIC: Polymer blends with and without solvent additive in N₂ filled glove box. LiF (0.6 nm) and Al (100 nm) were evaporated at low pressure (~10⁻⁶ mbar) in a vacuum environment.

J-V curves of the best devices are shown in Figure 2.13, and the photovoltaic parameters are summarized in Table 4. The best performance of the ME1: ITIC blend with the thickness of 161 nm was obtained by coating the active layer with 1: 1

Polymer: ITIC ratio and 7.94% PCE was obtained. Although additives are intended to improve film morphology, no improvement has been observed. As for ME2 based OPVs, CB was also seen as the best working solvent. The highest PCE achieved in the ME2 based OPV with a thickness of 106 nm was obtained by coating the active layer with a mass ratio of 1:1.5 at 2000 rpm, which is 1.96%. ME2 exhibited solubility problems due to a lack of alkyl chains, proving that the alkyl chain's introduction to the polymer's backbone enhances polymer solubility and electronic properties, hence photovoltaic performances²²¹. ME1 based OPVs exhibit superior performances than ME2 based ones because the M_n value of ME2 was deficient compared to ME1. As well known in the literature, the study also proves that the M_n affects the microstructure morphology and consequently PCE²²². This effect is explained in the TEM images in the active layer section. Theoretical V_{OC} of all-polymer solar cells is deduced from the difference between E_{LUMO} of the acceptor and E_{HOMO} of the donor. While the V_{OC} value of ME1 OPVs is precisely the same as expected (can be calculated from Eq. (1)), the V_{OC} value of ME2 based OPVs is lower than the theoretical value due to energetic disorder at the charge transport level²²³.

$$V_{OC} = (1/e)(|E_{Donor}^{HOMO} - E_{Acceptor}^{LUMO}|) - 0.3 \text{ V} \quad \text{Eq. 1}$$

ME1 based OSCs display better performances than ME2 based OPVs, mainly profiting the higher V_{OC} of 0.86 V and FF of 50.12%. All these findings can be supported by the fact that ME1 has higher crystallinity than ME2; The higher the crystallinity, the greater the tendency to self-aggregate, and the larger the field size in thin films with very high charge mobility²²⁴.

The devices based on ME3 and ME4 were fabricated the same way. The device based on the blend ME3: ITIC (1:1) gave an efficiency of 1.4%, with a FF of 28.55%, a V_{OC} of 0.97 V, and a J_{SC} of 5.06 mA.cm⁻². As an additive addition, the addition of DPE did not improve the device's efficiency and resulted in an efficiency of 0.78% and a dramatically decreased J_{SC} (2.71 mA.cm⁻²). The best device based on

ME4:ITIC (1:1) blend resulted in an efficiency of 1.32% with a V_{OC} of 0.96 V, a J_{SC} of 4.49 mA.cm⁻², and a FF of 30.55%. Although the polymer ME4 possessed difficulties in dissolving compared to ME3, they do not have a distinct difference between the best efficiencies.

Table 2.11 Photovoltaic parameters of ME1-ME4:ITIC devices.

Polym.	Solvent	Weight (%)	Polymer: ITIC	V_{oc} (V)	J_{sc} (mA.cm ⁻²)	PCE (%)	FF (%)	Treatment
ME1	CB	3	1:1.5	0.87	15.26	7.09	53.40	-
ME1	CB	3	1:1	0.86	18.45	7.94	50.12	-
ME1	CB	3	1:0.8	0.85	16.87	5.94	41.38	-
ME1	ODCB	3	1:1.5	0.88	8.54	4.56	60.90	-
ME1	CB	3	1:1	0.88	15.69	5.99	43.21	1% CN
ME2	CB	3	1:1.5	0.83	6.31	1.96	37.44	-
ME2	ODCB	3	1:1.5	0.74	3.75	1.26	45.41	-
ME3	CB	3	1:1	0.97	5.06	1.40	28.55	-
ME4	CB	3	1:1	0.96	4.49	1.32	30.55	-

To further compare the devices giving the best results with ITIC, PC₇₁BM was also employed as an acceptor, and the performance for each device was investigated. It turned out that ME1 and ME2 based devices did not operate better than ITIC based devices. However, the trend for ME3 and ME4 was not the same. ME3:PC₇₁BM (1:2) based device resulted in an efficiency of 2.27%, with a V_{OC} of 0.96 V, a J_{SC} of 6.61 mA.cm⁻², and a FF of 35%. The best device based on ME4:PC₇₁BM (1:2) resulted in an efficiency of 2.37%. However, when treated with DPE, the efficiency slightly increased (2.45%). Both values obtained from ME4:PC₇₁BM based devices are higher than that of ME4:ITIC.

Table 2.12 Photovoltaic parameters of ME1-ME4:PC₇₁BM devices

Polym.	Solvent	Weight (%)	Polymer: PC ₇₁ BM	V_{oc} (V)	J_{sc} (mA.cm ⁻²)	PCE (%)	FF (%)	Treatment
ME1	ODCB	3	1:2	0.83	13.96	7.62	66.0	-
ME2	ODCB	3	1:2	0.82	11.76	6.30	65.0	-
ME3	ODCB	3	1:2	0.95	5.32	1.63	32.0	-
ME3	ODCB	3	1:2	0.96	6.61	2.27	35.0	6% DPE
ME4	ODCB	3	1:2	0.93	4.70	1.46	32.1	-
ME4	ODCB	3	1:2	0.92	6.64	2.45	36.3	6% DPE

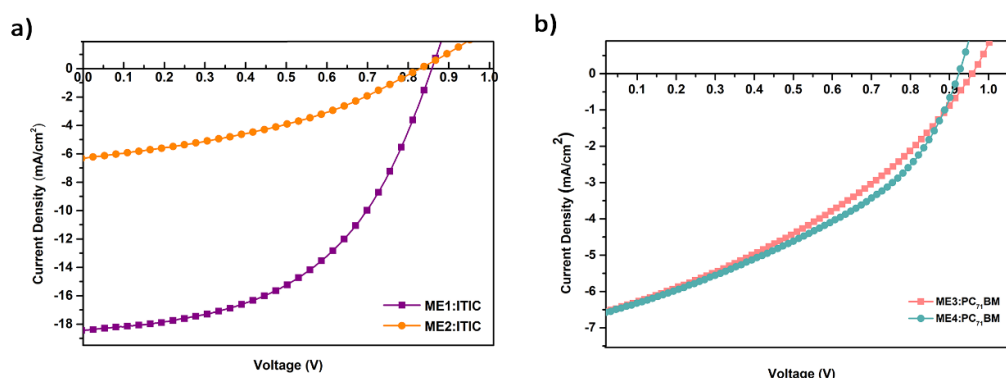


Figure 2.13. Current-voltage characteristics of (a) ME1/ME2:ITIC and (b) ME3/ME4:PC₇₁BM devices under AM 1.5 G solar simulator.

AFM images were recorded to examine the films' topographies. Figure 2.14.a, 2.14.b, and 2.14.c shows 2D AFM images of ME1 and ME2, proving how uniformly the films are coated with ITIC. ME2 based OPVs, a rough surface image, and the non-uniform coating are seen in the 3D image of ME2 based OPV (See Figure 2.15), which already has a dissolution problem. The surface roughness of the ME2:ITIC blend was the largest among others (Figure 2.14). The TEM images were examined to obtain more in-depth information about morphology (Figure 2.16). The ideal morphology formed in the active layer provides suitable interfaces for efficient charge separation and promising percolation pathways for charge carrier transport to the respective electrodes to minimize free charge recombination²²⁵. For the blend ME1:ITIC (Figure 2.16.a), ITIC is dispersed uniformly throughout the film, and percolations are thinner and precise. However, phase separation is so apparent for the ME2:ITIC blend (Figure 2.16.b) that large aggregates of ITIC (dark areas) are trapped within the polymer matrix. These aggregates are thought to interrupt charge transport, thus reducing device performance²²⁶. The FF value decreases considerably by adding 1% of CN to ME1:ITIC solution (Table 2.11). The devices made with PC₇₁BM have a morphology that allows for high yields. The films' favorable percolation pathways and small domain sizes explain the high FF and J_{SC} values, particularly in Figure 2.16.d. TEM images were used to understand the reason for this severe decrease. Comparing Figure 2.16.a and 2.16.c, the latter shows large-

scale phase separation, resulting in less charge carrier photogeneration and hindered transport, finally decreasing photovoltaic properties ²²⁷.

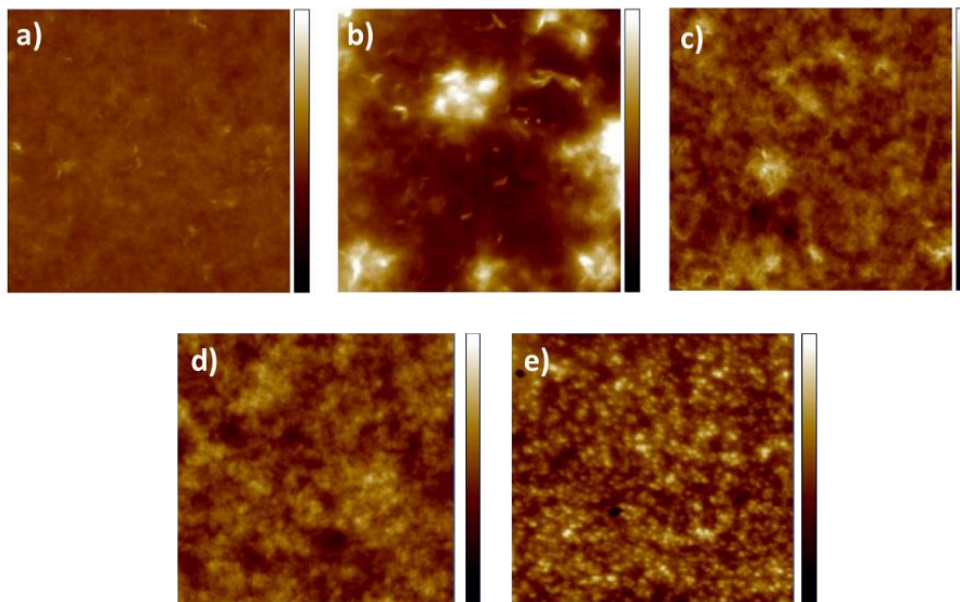


Figure 2.14. 2D AFM images of (a) ME1:ITIC, (b) ME2:ITIC, (c) ME1:ITIC w/ 1% CN, d) ME1:PC₇₁BM, e) ME2:PC₇₁BM

ME1 and ME2 based devices completed with PC₇₁BM have roughness values of 1.26 nm and 1.46 nm, respectively, and thicknesses of 149 nm and 60 nm.

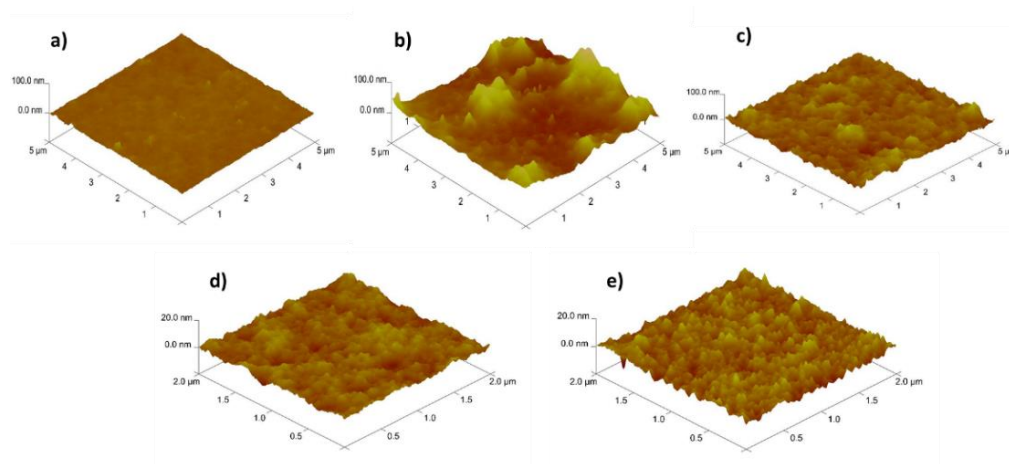


Figure 2.15. 3D AFM images of (a) ME1:ITIC, (b) ME2:ITIC, (c) ME1:ITIC w/ 1% CN, (d) ME1:PC₇₁BM, (e) ME2:PC₇₁BM

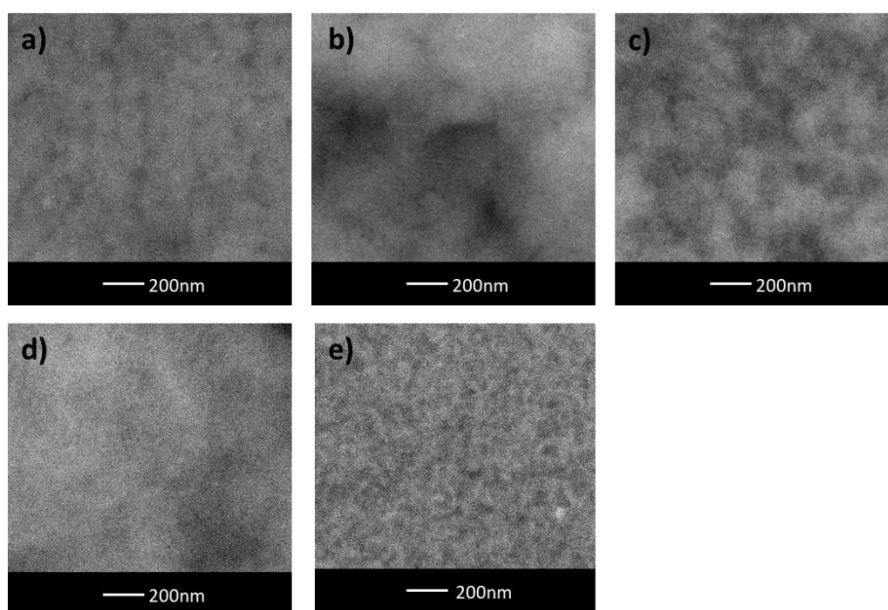


Figure 2.16. TEM images of (a) ME1:ITIC, (b) ME2:ITIC, (c) ME1:ITIC w/1% CN (d) ME1:PC₇₁BM, (e) ME2:PC₇₁BM

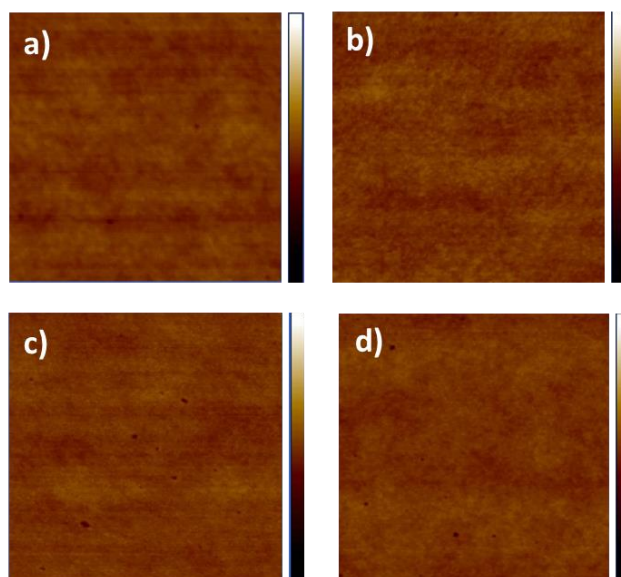


Figure 2.17. 2D AFM images of (a) ME3:PC₇₁BM, (b) ME3:PC₇₁BM w/6% DPE, (c) ME4:PC₇₁BM, (d) ME4:PC₇₁BM w/6% DPE

AFM topographical examination for ME3 and ME4 showed that the roughness values are 0.320, 0.340, 0.48, and 0.387 nm, respectively (Figures 2.18.a, 2.18.b, 2.18.c, and 2.18.d). And the film thickness values are found as 138 nm, 83nm, 111 nm, and 77 nm, respectively.

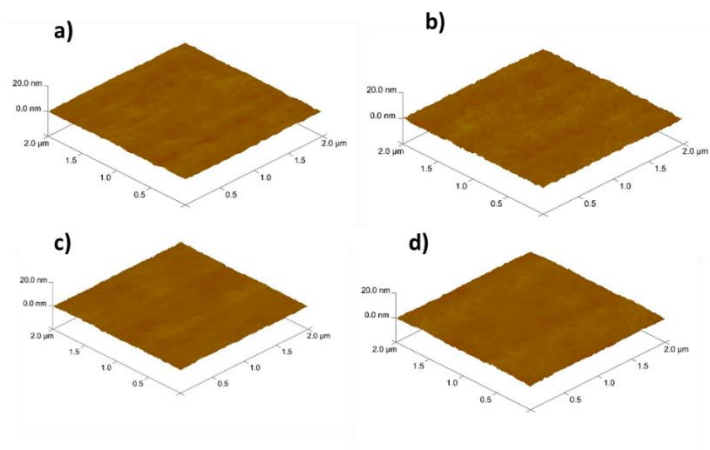


Figure 2.18. 3D AFM images of (a) ME3:PC₇₁BM, (b) ME3:PC₇₁BM w/ 6%DPE, (c) ME4:PC₇₁BM, (d) ME4:PC₇₁BM w/6%DPE

The morphology of the films obtained by using ME3 and ME4 in the active layer was examined using TEM. It was observed that PCEs increased when DPE was used as a solvent additive in ME3 and ME4 based OSCs. This is due to the use of DPE as theta solvent that optimizes the morphology. It is clearly seen that PCBM aggregations are common in the morphology obtained without using the additive in Figure 2.19.a and 2.19.c and percolation occurs even when DPE is used in Figures 2.19.b and 2.19.d.

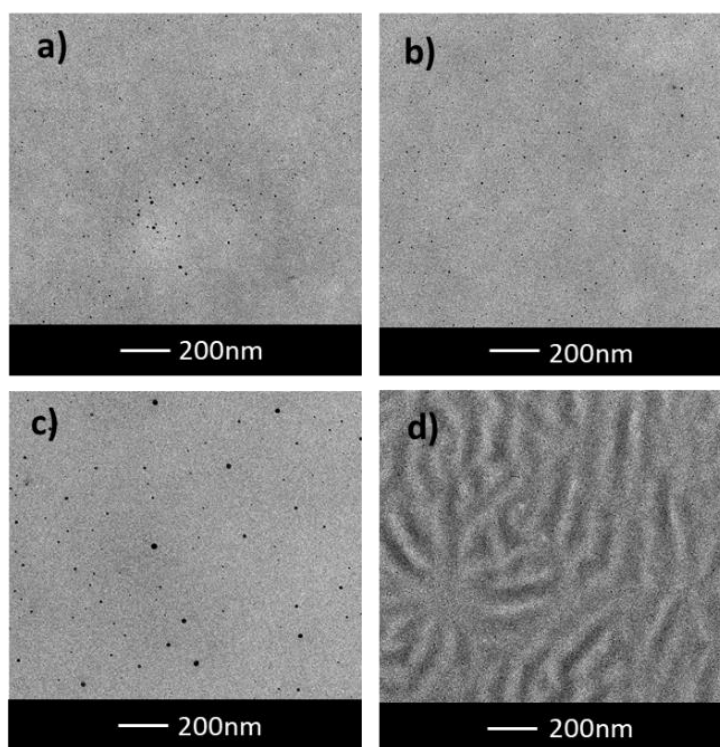


Figure 2.19. TEM images of a) ME3:PC₇₁BM, b) ME3:PC₇₁BM w/6% DPE, c) ME4:PC₇₁BM, d) ME4:PC₇₁BM w/6% DPE

The incident photon to electron conversion efficiency (IPCE) was studied to confirm the best device's photoresponse, as shown in Figure 2.20.a. The photocurrent response for both polymers was performed between 300 nm and 900 nm. The highest IPCE value for ME1 and ME2 reached 82% and 26%, respectively. The results obtained from the EQE curve are consistent with J_{SC} values in Table 2.11. For the devices based on M1-ME4:PC₇₁BM, EQE curves are illustrated in Figure 2.20.b. The IPCE values were obtained as 43%, 51 %, 45%, and 50%, respectively.

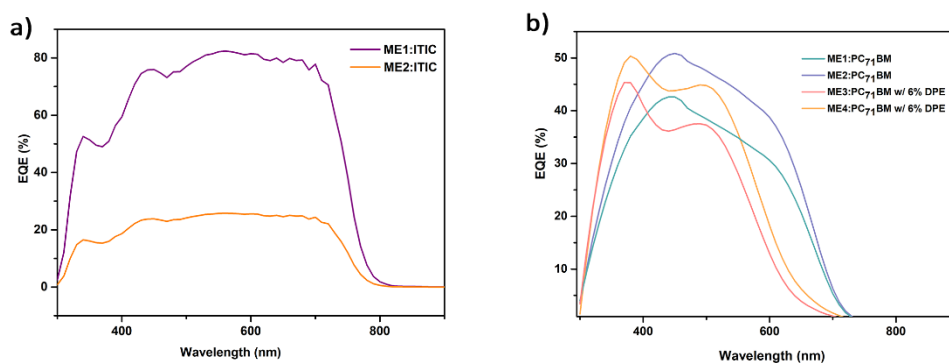


Figure 2.20. EQE curves of a) ME1: ITIC and ME2: ITIC, and b) ME1-
ME4:PC₇₁BM devices

2.3.4 Conclusions

In this study, two new random copolymers containing TPD as the core unit were synthesized. ME1 containing alkyl thiophene has a larger molecular weight than P2, which is attributed to the lack of alkyl chain, which enhances the solubility of the polymer. The electrochemical and spectroelectrochemical properties of the two polymers were investigated. TPD as an acceptor moiety enhanced V_{OC} values and provided deep HOMO levels, subsequently better OPV performances. The best result was obtained with the device based on ME1: ITIC with a PCE of 7.94%, a J_{SC} value of 18.45 mA.cm^{-2} and an FF value of 50.12%. ME2 based devices exhibited comparatively lower PCEs (1.96% max) and other OPV parameters. We believe that the lower molecular weight of ME2 disturbed film morphology of the polymer: acceptor blend, which AFM and TEM images support. Thus, ME1 exhibited relatively better OPV performances. When blended with PC₇₁BM, ME1 and ME2 did not perform better than polymer:ITIC blends. However, ME3/ME4:PC₇₁BM performed better than ME3/ME4:ITIC blends with and without solvent additive treatment. The FF values of the devices based on ME3 and ME4 increased when PC₇₁BM was employed in the fabrication. Furthermore, when 6% DPE was introduced, the PCE of ME3:PC₇₁BM based device enhanced almost 40%. The same trend was observed for ME4:PC₇₁BM based device as well. When 6% DPE was

introduced, the PCE value increased almost 68%. Previously reported studies support that new TPD-containing random copolymers and NFA-based organic photovoltaics exhibit better PCEs compared to their fullerene-based counterparts^{228–233}.

2.4 Effect of introduction of a second TPD unit with different donor moieties on photovoltaic performance

In this part, compound M1 went under random polymerization with a second TPD unit and different donor moieties, benzodithiophene and dithienopyrrole. Herein, the idea was to compare the photovoltaic performance of the polymers upon introduction of a second TPD unit since it is known that the TPD unit can both widen and lower band gaps, hence altering the optical properties and photovoltaic performance. The polymer ME5 was difficult to dissolve. Although there is a fair amount of alkyl chains on the polymer backbone, the presence of the fused structures makes it difficult to dissolve the polymer. Different halide solvents were employed to dissolve the polymer, and due to the poor solubility formation of the polymer film as a donor in the active layer of the solar cell was not uniform, and the solar device could not operate. For the same reasons, electrochemical and spectroelectrochemical investigations could not be conducted. ME6 was blended both with fullerene and ITIC. The best result was obtained from the blend ME6:PC₇₁BM with a ratio of 1:3 with a PCE of 3.94%, a V_{OC} of 0.87 V, a FF of 59, and a J_{SC} of 7.65 mA.cm⁻².

2.4.1 Syntheses of the polymers (ME5 and ME6)

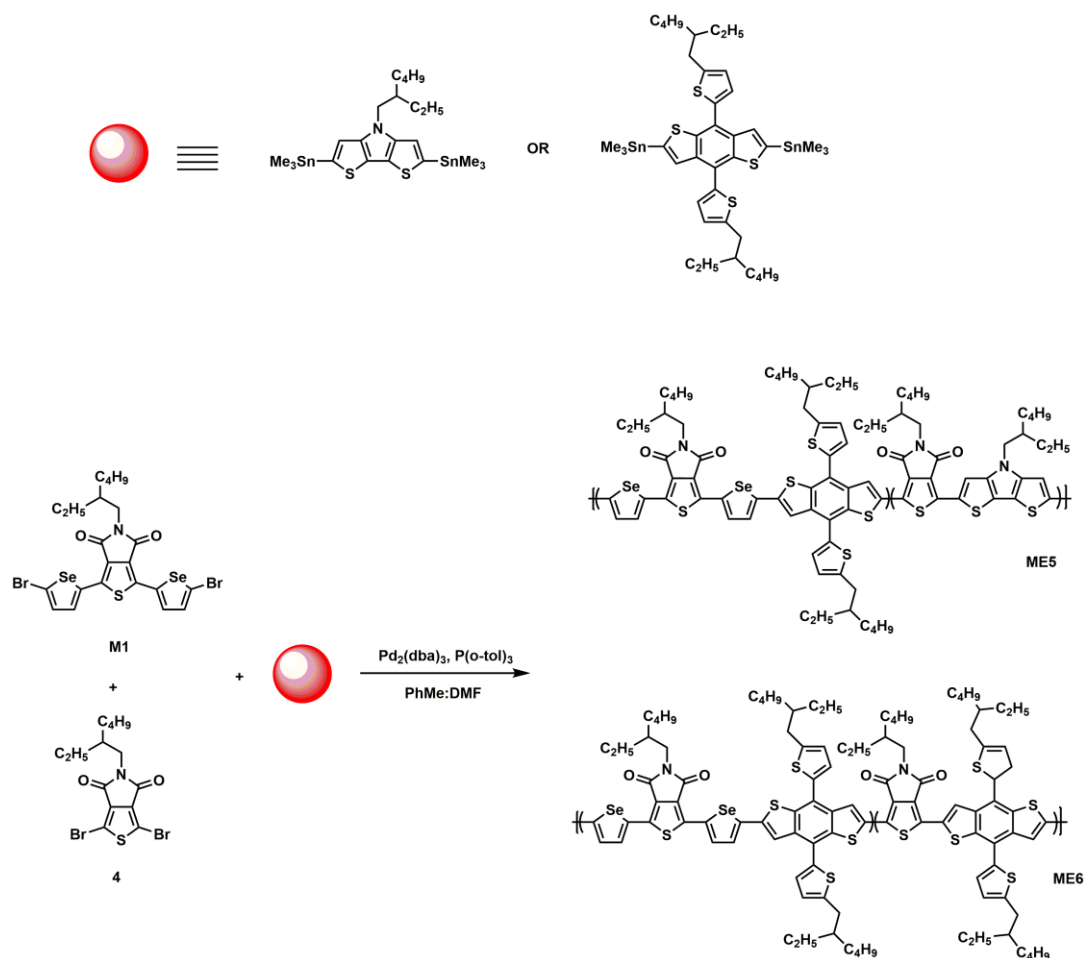


Figure 2.21. Synthetic routes for ME5 and ME6

M1 (73.4 μmol , 1 eq.), compound **4** (73.4 μmol , 1 eq.), and BDT(TiC8) or DTP (4-(2-ethylhexyl)-2,6-bis(trimethylstannyl)-4H-dithieno[3,2-b:2',3'-d]pyrrole) (73.4 μmol , 1 eq.) were dissolved in dry toluene:DMF (5 mL, 4:1 v/v) solvent system under Ar atmosphere in 25 mL Schlenk tube. $\text{Pd}_2(\text{dba})_3$ (1.0 μmol) and $\text{P}(\text{o-tolyl})_3$ (4.2 μmol) were added, and the reaction mixture was allowed to stir for 15 h at reflux. For the purification, the same procedure was followed as in the preparation of ME1-ME2. ME5 was isolated in chlorobenzene, while ME6 was isolated in both chloroform and chlorobenzene. Solvents were removed, and ME5 (Yield: 32 mg, 26%) and ME6 (Yield: 25 mg, 18% in chlorobenzene, 50 mg, 35% in chloroform)

were obtained as dark purple crystals following recrystallization from methanol. Since ME5 was obtained from chlorobenzene, it had solubility problems. That's why electrochemical and photovoltaic investigations could not be conducted. ME6 was isolated in chloroform and chlorobenzene. The portion obtained from chloroform was employed in electrochemical and photovoltaic studies. M_n and M_w for ME6 were 33.2 and 43.68 kDa (PDI=1.3), respectively.

2.4.2 Results

2.4.3 Electrochemical and spectroelectrochemical investigations

Electrochemical investigations were conducted with cyclic voltammetry. The polymer ME6 showed ambipolar characteristics (both p-dopable and n-dopable). The same procedures as for ME1-ME4 were followed for the investigations. Single scan cyclic voltammetry of ME6 films was performed in a potential range between -2.0 V and 1.4 V in 0.1 M TBAPF₆/ACN, electrolyte/solvent couple. ME6 showed reversible oxidation/reduction peaks at 1.13 V and -1.07/-1.54 V. HOMO and LUMO energy levels were calculated from oxidation/reduction values as -5.64 and -3.52 eV, respectively. The electronic band gap was determined as 2.12 eV as the difference between HOMO and LUMO levels. The electronic properties of ME6 are summarized in Table 2.13.

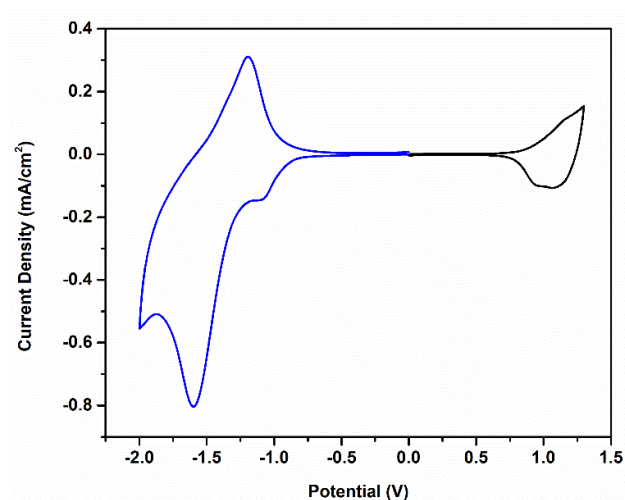


Figure 2.22. Cyclic voltammograms of ME6 on ITO electrode in 0.1 M TBAPF₆/ACN electrolyte/solvent couple at a scan rate of 100 mV/s

Table 2.13 Electrochemical properties of ME6

Polymer	E _{p-doping} (V)	E _{onset p-doping} (V)	E _{n-doping} (V)	E _{onset n-doping} (V)	HOMO (eV)	LUMO (eV)	E _{g^{el}} (eV)	E _{g^{op}} (eV)
ME6	1.13	0.89	-1.07/-1.54	-1.23	-5.64	-3.52	2.12	1.55

Electronic absorption spectra of ME6 films were recorded upon applying a stepwise potential change ranging from 0 V to 1.4 V. The continuous change in the potential decreased the neutral absorption band. A new absorption band appeared at 824 nm due to the formation of radical cations, and the maximum onset value was determined as 800 nm, from which the optical band gap was calculated. The neutral absorption state was recorded as 610 nm, corresponding to π - π^* transitions (See Figure 2.23.a).

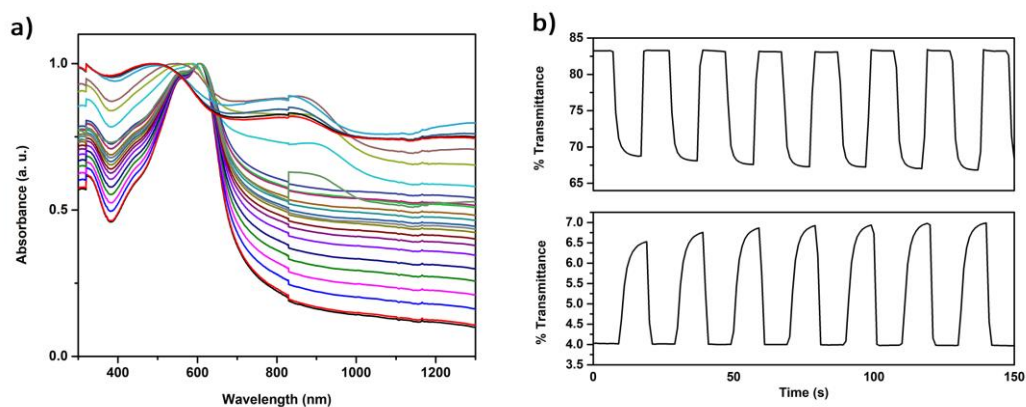


Figure 2.23. (a) Electronic absorption spectra of ME6 solution between 0.0 V and 1.4 V, (b) Percent transmittance changes for ME6 in 0.1 M TBAPF₆/ACN solution.





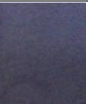
Optical properties are summarized in Table 2.14.

Table 2.14 Optical properties of ME6

Polymer	λ_{max} (nm)	$\lambda_{\text{onset max}}$ (nm)	E_g^{op} (eV)
ME6	610	800	1.55

The colors of ME6 film were recorded in neutral and reduced states. In oxidation state, the films did not show any change in color. However, when a potential between 0 and -2.0 V, the color went gray tones. L, a, and b values of the polymer film are illustrated in Table 2.15.

Table 2.15 Colors of ME6 film at neutral and reduced states

	-2.0 V				0 V
ME6-RED					
L	52.37	52.05	50.87	54.19	34.13
a	0.25	-1.47	-1.47	1.13	3.39
b	-5.31	-2.32	-2.33	-2.57	-12.41

Optical contrast and switching times were recorded via kinetic studies. A square-wave potential from 0 V to 1.4 V was used for two extreme states (oxidized/reduced states) with 5 seconds intervals at λ_{\max} located at 625 and 890 nm. Percent transmittance against time graphs are illustrated in Figure 2.23.b. Percent transmittance changes for ME6 were determined as 3% at 625 nm and 16% at 890 nm, whereas switching times were calculated as 2.9 and 0.7 s, respectively. All electrochromic switching results are summarized in Table 2.16.

Table 2.16 Kinetic properties of ME6

Polymer	λ (nm)	Optical Contrast(%)	Switching Time (s)
ME6	625	3	2.9
	890	16	0.7

2.4.4 OSC studies

For ME6 based devices, the same procedures were followed as in the fabrication of OSC devices based on ME1-ME4. Preliminary results exhibited that ME6 based devices operate better when ME6 is blended with PC₇₁BM. And the best result was 3.94% with ME6:PC₇₁BM (1:1, w/w) blend. Photovoltaic parameters for ME6 are summarized in Table 2.17, and the J-V curves are represented in Figure 2.24.

Table 2.17 Photovoltaic parameters of ME6:ITIC/PC₇₁BM devices

Polymer:Acceptor (w:w)	Solvent	Concentration (mg.mL ⁻¹)	J _{sc} (mA.cm ⁻²)	V _{oc} (V)	FF (%)	PCE (%)
ME6:ITIC (1:1)	ODCB	12	6.88	0.91	44	2.79
ME6:PC ₇₁ BM (1:2)	ODCB	20	7.25	0.86	60	3.73
ME6:PC ₇₁ BM (1:3)	ODCB	20	6.72	0.87	62	3.56
ME6:PC ₇₁ BM (1:3)	ODCB	30	7.65	0.87	59	3.94

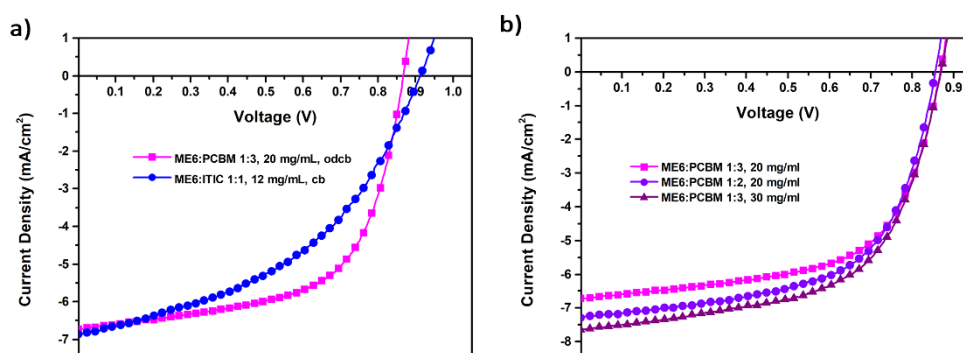


Figure 2.24. Current-voltage characteristics of (a) the best devices based on ME6:ITIC/PC₇₁BM and (b) ME6:PC₇₁BM under AM 1.5 G solar simulator.

2.5 Thienothiophene and benzochalcodiazoles containing conjugated polymers

Herein, TPD unit was introduced a fused organic spacer, thienothiophene a brief explanation of its importance was given in section 2.1.2.2. The aim was to introduce thienothiophene to the TPD unit as a spacer and then randomly polymerize this new moiety with benzochalcodiazoles acceptor and BDT donor moieties. Obtained polymers were to be used as donor materials in OSC fabrication. As preliminary results, herein, syntheses of the polymers (ME7 and ME8), electrochemical, and spectroelectrochemical results are reported.

2.5.1 Experimental

All molecules and the polymers were prepared according to the literature reports.

ME7 and ME8 were obtained via Stille Polycondensation.

2.5.2 Syntheses of the monomers and the polymers

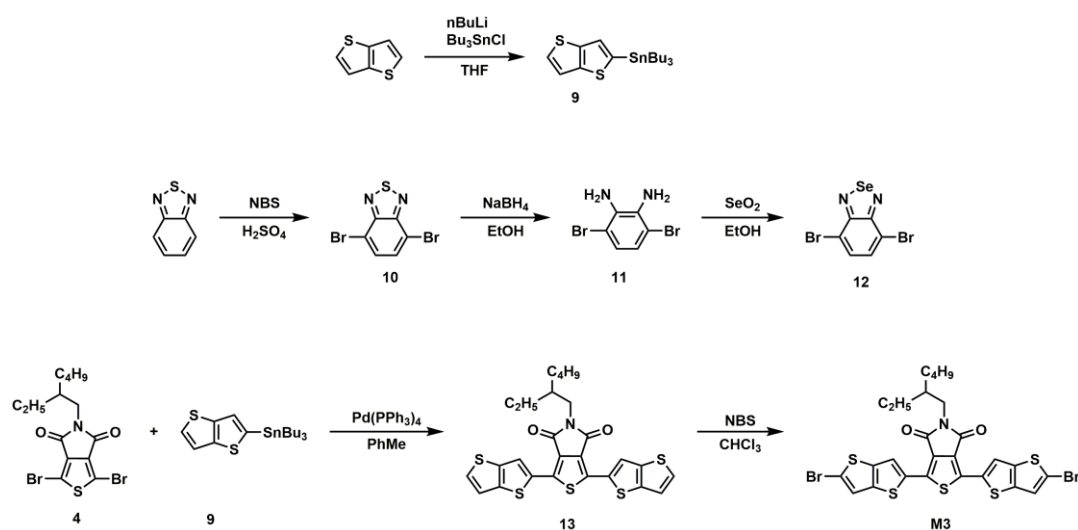


Figure 2.25. Synthetic route for the monomer M3

2.5.2.1 Synthesis of tributyl(thieno[3,2-b]thiophen-2-yl)stannane (9)

Under Ar atmosphere, thieno[3,2-b]thiophene (0.25 g, 1.8 mmol) was dissolved in dry THF. The solution was cooled to $-78\text{ }^\circ\text{C}$ in a dry ice bath. $n\text{-BuLi}$ (0.71 mL, 2.5 M) was added dropwise. The reaction mixture was allowed to stir at $-78\text{ }^\circ\text{C}$ for 1 h and followed by the addition of SnBu_3Cl (0.75 g, 2.3 mmol). The reaction mixture was warmed to ambient temperature and was allowed to stir overnight. The solvent was removed under reduced pressure, and DCM was added to the crude product. Organic layers were washed with saturated NaHCO_3 , distilled water, and brine. Washed organic layers were dried over Na_2SO_4 , and after the solvent removal, the product was used without any further purification. Yield: 0.7 g, 92%.

^1H NMR (400 MHz, CDCl_3 , δ , ppm): 7.32 (d, $J=5.1$ Hz, 1H), 7.23 (s, 1H), 7.22 (s, 1H), 1.68-1.53 (m, 6H), 1.40-1.28 (m, 6H), 1.16-1.12 (m, 6H), 0.94-0.89 (m, 9H)

^{13}C NMR (100 MHz, CDCl_3 , δ , ppm): 145.2, 141.5, 140.5, 126.8, 125.3, 118.8, 28.8, 27.1, 13.5, 11.5

2.5.2.2 Synthesis of 4,7-dibromobenzo[c][1,2,5]thiadiazole (10)

In a three-necked flask charged with a magnet bar, 2,1,3-benzothiadiazole (3 g, 22 mmol) and *N*-bromosuccinimide (8.2 g, 46 mmol) were dissolved in concentrated H_2SO_4 (30 mL). The reaction mixture was stirred for 3 h at 60 °C in an oil bath. Then the mixture was cooled to ambient temperature and transferred to an ice bath. After dropwise addition of distilled water (100 mL), the product was extracted three times with toluene. Combined organic layers were dried over anhydrous Na_2SO_4 . The solvent was removed under reduced pressure, and a white product was obtained. Yield: 3.9 g, 60%.

^1H NMR (400 MHz, CDCl_3): δ : 7.72 (s, 2H).

^{13}C NMR (100 MHz, CDCl_3): δ : 153, 132, 114.

2.5.2.3 Synthesis of 3,6-dibromobenzene-1,2-diamine (11)

In a 1 liter Erlenmeyer charged with a magnet bar, compound **10** was (1 g, 3.4 mmol) introduced. Ethanol (30 mL) was added, and the temperature of the flask cooled to 0 °C in an ice bath. NaBH_4 (5 g, 132 mmol) was added portion-wise. The reaction mixture was stirred overnight at ambient temperature. Distilled water was poured onto the mixture, and the product was extracted with Et_2O . Organic phases were washed with distilled water. The solvent was removed under reduced pressure. A beige solid was isolated. Yield: 0.72 g, 79%.

^1H NMR (400 MHz, CDCl_3): δ : 6.85 (s, 2H), 3.67 (s, 4H)

^{13}C NMR (100 MHz, CDCl_3): δ : 133.7, 123.3, 109.7.

2.5.2.4 Synthesis of 4,7-dibromobenzo[c][1,2,5]selenadiazole (12)

In EtOH (30 mL), compound **11** (1.4 g, 5.2 mmol) was dissolved. The solution was heated to reflux. A readily available solution of SeO_2 (0.6 g, 5.2 mmol) in distilled water (6 mL) was added dropwise. Following the addition of SeO_2 solution, the reaction mixture was refluxed 2 hours more. The obtained solution was poured into distilled water (100 mL) and filtered. The product was obtained through precipitation in ethyl acetate and used further without any purification. Yield: 1.4 g, 80%.

2.5.2.5 Synthesis of 5-(2-ethylhexyl)-1,3-bis(thieno[3,2-b]thiophen-2-yl)-4H-thieno[3,4-c]pyrrole-4,6(5H)-dione (13)

A 50 mL Schlenk tube was charged and connected to a Schlenk tube. Under Ar atmosphere, compound **4** (0.15 g, 0.35 mmol) and $\text{Pd}(\text{PPh}_3)_4$ (50 mg, 0.041 mmol) were dissolved in dry toluene (15 mL). The Schlenk tube was located in an oil bath, and the temperature was set as 100 °C. At 50 °C, compound **9** (0.46 g, 1.05 mmol) was added slowly. TLC controlled reaction was stirred overnight at 100 °C. Following the cooling process, the solvent was removed under reduced pressure. Purifying the crude product over column chromatography on silica gel afforded yellow crystals. Yield: 0.15 g, 80%.

^1H NMR (400 MHz, CDCl_3 , δ , ppm): 8.39 (d, $J = 3.1$ Hz, 2H), 7.49 (d, $J = 5.3$ Hz, 2H), 7.24 (d, $J = 5.3$ Hz, 2H), 3.57 (d, 2H), 1.82 (m, 1H), 1.33 (m, 8H), 0.92 (dt, $J = 13.9, 7.3$ Hz, 6H).

^{13}C NMR (100 MHz, CDCl_3 , δ , ppm): 162.8, 139.5, 136.4, 133.3, 130.0, 122.2, 119.3, 38.3, 27.7, 23.5, 22.4, 10.8.

2.5.2.6 Synthesis of 1,3-bis(5-bromothieno[3,2-b]thiophen-2-yl)-5-(2-ethylhexyl)-4H-thieno[3,4-c]pyrrole-4,6(5H)-dione (M3)

Compound **13** (0.15 g, 0.28 mmol) was dissolved in CHCl_3 (20 mL) under Ar atmosphere at the ambient temperature. *N*-bromosuccinimide (0.11 g, 0.63 mmol) was added to the stirring solution portion-wise. TLC controlled reaction mixture was stirred overnight at ambient temperature. Following the addition of distilled water, the organic layer was separated and dried over Na_2SO_4 and concentrated under reduced pressure. Precipitation in ethanol afforded orange powder. Yield: 0.165 g, 85%.

^1H NMR (400 MHz, CDCl_3) δ 8.41 (s, 2H), 8.30 (s, 2H), 3.58 (d, $J = 7.2$ Hz, 2H), 1.40-1.10 (m, 9H), 0.92 (dt, $J = 14.5, 7.3$ Hz, 3H), 0.83 (s, 3H).

2.5.2.7 Synthesis of ME7 and ME8

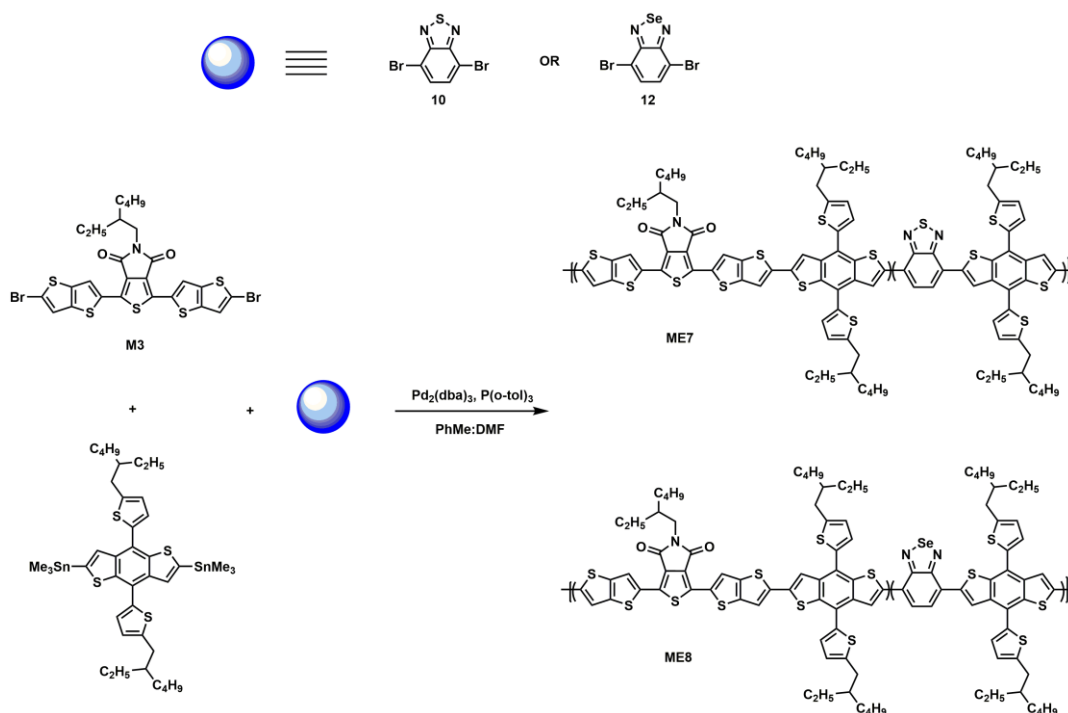


Figure 2.26. Synthetic routes for ME7 and ME8

Under Ar atmosphere **M3** (50 mg, 0.071 mmol), compound **10** (21 mg, 0.071 mmol) or compound **12** (24 mg, 0.071 mmol), BDT(TiC8) (130 mg, 0.142 mmol), Pd2(dba)3 (15 mg), and P(o-tol)3 (15 mg) were dissolved in dry toluene (10 mL). The purification was achieved following the same method as in the preparation of ME1-ME2. ME7 was isolated in both chloroform (Yield: 85 mg, 66%) and chlorobenzene (Yield: 22 mg, 17%) fractions. ME8 was also isolated in the same solvents (Yield: 32 mg, 24% in chlorobenzene, 50 mg, 38% in chloroform). M_n and M_w for ME7 and ME8 were 4 and 9 kDa (PDI=2.25) and 5.5 and 14.1 kDa (PDI=2.56), respectively.

2.5.3 Results

2.5.3.1 Electrochemical and spectroelectrochemical investigations of ME7 and ME8

The polymer ME7 showed ambipolar characteristics (both p-dopable and n-dopable), while the polymer ME8 did not get oxidized only. Single scan cyclic voltammograms of ME7 and ME8 films were conducted in a potential range between -1.8 V and 1.1 V, 0 V and 1.6 V respectively in 0.1 M TBAPF₆/ACN, electrolyte/solvent couple (See Figure 2.27). ME7 showed reversible oxidation/reduction peaks at 0.76 V and -1.6 V, whereas ME8 showed an oxidation peak at 1.1 V. HOMO and LUMO energy levels of ME7 were found as -5.39 and -5.52 eV, respectively. LUMO of ME8 was calculated using the optical band gap obtained from electronic absorption spectra. All electrochemical properties of ME7 and ME8 are summarized in Table 2.18.

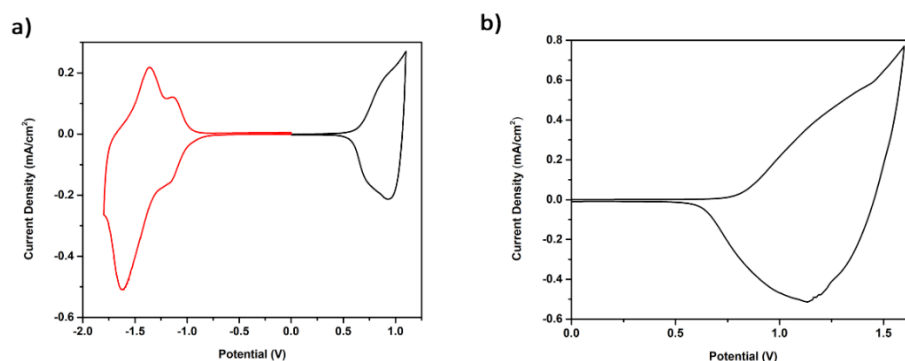


Figure 2.27. Cyclic voltammograms of ME7 and ME8 on ITO electrode in 0.1 M TBAPF₆/ACN electrolyte/solvent couple at a scan rate of 100 mV/s

Table 2.18 Electrochemical properties of ME7 and ME8

Polymer	E _{p-doping} (V)	E _{onset p-doping} (V)	E _{n-doping} (V)	E _{onset n-doping} (V)	HOMO (eV)	LUMO (eV)	E _{g^{el}} (eV)	E _{g^{op}} (eV)
ME7	0.76	0.64	-1.6	-1.16	-5.39	-3.59	1.8	1.66
ME8	1.1	0.77	-	-	-5.52	-4.02	-	1.5

Electronic absorption spectra of ME7 and ME8 films were recorded upon applying a stepwise potential change ranging from 0 V to 1.35 V and 0 V to 1.22 V, respectively (See Figure 2.28). The continuous change in the potential decreased the neutral absorption band for ME7, and a new absorption band appeared at 810 nm as a result of the formation of radical cations. The corresponding peak for ME8 was observed at 890 nm. Onset maximum values were determined as 748 nm and 828 nm, from which the optical band gaps were calculated.

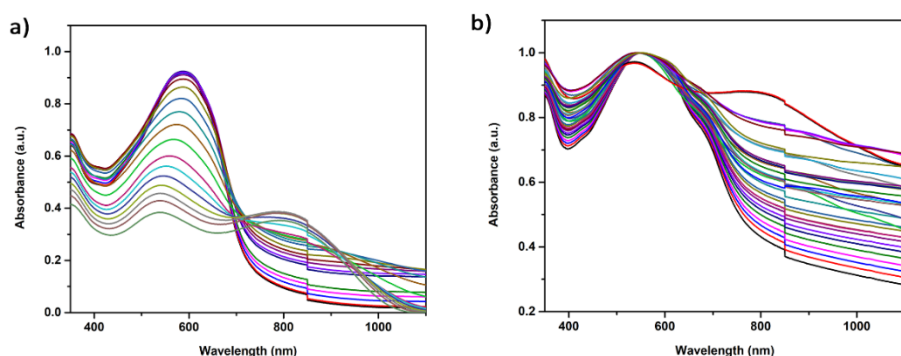














Figure 2.28. Electronic absorption spectra in 0.1 M TBAPF₆/ACN solution between (a), 0.0 V and 1.4 V for ME7 (b), 0.0 V and 1.25 V for ME8

The films of both polymers exhibited electrochromism and different colors in neutral and oxidized/reduced states upon applied potentials. In the oxidation state, the color of ME7 films went dark blue and went greyish in the reduction state. ME8 films went light pink in the oxidation state and went greyish in the reduced state. The colors and corresponding electrical potentials are illustrated in Table 2.19.

Table 2.19 Colors of ME7 and ME8 film at neutral and oxidized/reduced states

	<div style="display: flex; align-items: center; justify-content: space-around;"> -1.8 V ← 0 V → +1.3 V </div>			
ME7				
L	61.50	56.53	56.92	58.49
a	-0.39	10.66	6.59	5.06
b	-7.12	-12.08	-7.02	-7.55

	<div style="display: flex; align-items: center; justify-content: space-around;"> -2.2 V ← 0 V → +1.8 V </div>							
ME8								
L	33.74	36.82	34.07	29.77	23.98	32.58	37.14	34.55
a	0.82	1.39	0.41	-1.60	7.80	1.42	3.18	3.01
b	-2.95	-3.34	-3.09	-2.55	-3.16	-3.40	-7.81	-8.64

To investigate kinetic stability and calculate switching times with percent transmittance, kinetic studies were conducted under the same conditions followed for the previous polymers. For ME7, a square-wave potential from 0 V to 1.6 V was applied for two extreme states (oxidized/reduced states) with 5 seconds intervals at λ_{max} located at 590 and 810 nm (See Figure 2.29). The percent transmittance changes for ME7 were determined as 18% at 590 nm and 22% at 810 nm. Switching times were calculated as 2.5 and 2.3 s, respectively.

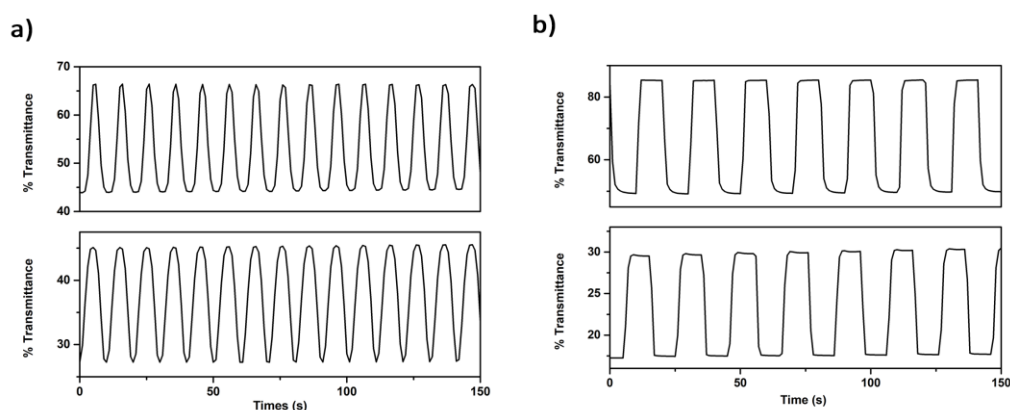


Figure 2.29. Percent transmittance changes for (a) ME7 and (b) ME8 in 0.1 M TBAPF₆/ACN solution.

For ME8, a square-wave potential from 0 V to 1.2 V was applied at λ_{max} located at 555 and 890 nm. The percent transmittance changes were found as 12% at 555 nm and 36% at 890 nm, while the switching times are calculated as 1.7 and 1.4 s, respectively. All electrochromic switching results are summarized in Table 2.20.

Table 2.20 Kinetic properties of ME7 and ME8

Polymer	λ (nm)	Optical Contrast (%)	Switching Time (s)
ME7	590	18	2.5
	810	22	2.3
ME8	555	12	1.7
	890	36	1.4

CHAPTER 3

CONSTRUCTION OF AMPEROMETRIC BIOSENSOR MODIFIED WITH CONDUCTING POLYMER/CARBON DOTS FOR THE ANALYSIS OF CATECHOL

Phenolic compounds used in food industries and pesticide industry, are environmentally toxic and pollute the rivers and ground water. For that reason, the detection of phenolic compounds such as catechol by using simple, efficient, and cost-effective devices have been becoming increasingly popular. In this study, a suitable and a novel matrix was composed using a novel conjugated polymer, namely poly[1-(5-(4,8-bis(5-(2-ethylhexyl)thiophen-2-yl)benzo[1,2-b:4,5-b'] dithiophen-2-yl)furan-2-yl)-5-(2-ethylhexyl)-3-(furan-2-yl)-4H thieno[3,4-c]pyrrole-4,6(5H)-dione] (PFTBDT) and carbon dots (CDs) to detect catechol. PFTBDT and CDs were synthesized, and the optoelectronic properties of PFTBDT were investigated via electrochemical and spectroelectrochemical studies. Laccase enzyme was immobilized onto the constructed film matrix on the graphite electrode. The proposed biosensor was found to have a low detection limit (1.23 μM) and a high sensitivity (737.44 $\mu\text{A}/\text{mM}\cdot\text{cm}^{-2}$) with a linear range of 1.25-175 μM . Finally, the applicability of the proposed enzymatic biosensor was evaluated in a tap water sample, and a satisfactory recovery (96-104%) was obtained for catechol determination.

This chapter is reproduced from J. Polym. Sci. 2020, 58, 3336–3348 with the permission of John Wiley & Sons.

3.1 Introduction

Identification and quantification of phenolic compounds have received exceptional interest from the scientific community owing to their high toxicity in nature, water resources, and human health. Between the phenolic compounds, Catechol (1, 2-hydroxybenzene or 1, 2- benzenediol), is found in many everyday products, such as cosmetics, pesticides, pharmaceuticals and food additives ²³⁴. It has been classified as a periodic toxic pollutant. The US Environmental Protection Agency (US EPA) and the European Commission (EC) have created a list and special attention has been devoted to catechol because of its low degradation rate and high toxicity ²³⁵. Different analytical methods have been utilized for the detection of catechol, such as fluorescence ²³⁶, high performance liquid chromatography ²³⁷, and chemiluminescence ²³⁸. However, most of these techniques are not considered as practical and up to expected standards mainly due to their low sensitivity, high cost, extensive time, and sample handling/ preparation requirements. Enzyme-based electrochemical biosensors that overcome the aforementioned drawbacks, can be one alternative to the current techniques. Enzyme-based electrochemical biosensors are generally robust and facile sensing systems with relatively low overall cost ²³⁹. Most importantly, enzyme-based biosensors are highly selective and sensitive due to their specific high affinity toward their substrate ²⁴⁰. Detection of catechol or other phenolic compounds can be achieved by using tyrosinase, laccase or peroxidase enzyme-based biosensors.

Laccases (benzenediol-oxygen oxidoreductase, E.C. 1.10.3.2) are copper containing enzymes found in higher plants, fungi, bacteria, and insects. They reduce oxygen to water during the oxidation of phenolic compounds in four electron transfer steps without forming hydrogen peroxide ²⁴¹. Laccases have found use in various industries, such as bioremediation, paper and pulp, pharmaceutical, textile and food industries, besides being used in biosensors ²⁴². One downside of the laccase biosensors is their stability. To provide a suitable matrix for enzyme immobilization

and enhance stability, conducting polymers (CPs) have been used in analytical systems due to their unique optoelectronic properties ^{243–245}.

The use of conducting polymer films to improve analytical performance appears to be a strong candidate for the development of biosensors. CPs permit easy localization of biomolecules on transducer surface and enhance the charge transfer between the active site of the enzyme and the electrode. Accordingly, they improve the biosensors' stability, sensitivity, and response time by providing a suitable matrix for enzyme immobilization ²⁴⁶. Thieno[3,4-c]pyrrole-4,6-dione-TPD has been used as an acceptor moiety in various conjugated polymers utilized for organic solar cells. TPD has a simple, symmetric, fused, planar, and compact structure leading to electron delocalization through the backbone of the polymer ^{247–250}. Due to geometric strain, it exhibits decreased steric repulsion between the neighboring units. Additionally, the interactions between the sulfur and oxygen atoms lead to backbone planarity. These features make TPD-based polymers have relatively lower band gaps and closer π - π interactions, facilitating improved charge transport ²⁰². Its strong electron-withdrawing effect leads to lower highest occupied molecular orbital/Lowest unoccupied molecular orbital (HOMO/LUMO) energy levels and makes TPD a good accomplice in both intermolecular and intramolecular interactions ^{199,201}. Besides, TPD is able to stabilize itself by gaining a quinoidal thiophene-maleimide structure during excitation resulting in lower band gap energy ²⁵¹. TPD moiety can also be modified easily through the donor benzodithiophene-BDT, mostly to improve polymer's solubility via the introduction of alkyl chains. Thus, due to its remarkable features, TPD moiety has been widely incorporated into conjugated polymers via Stille polycondensation reaction.

One of the most critical steps in fabricating enzyme-based biosensors is enzyme immobilization. In this step, it is important to attach the recognizing element effectively. Otherwise, the enzyme may leak from the electrode surface during analysis hence reducing the signal and sensitivity of the biosensor. Over the last 20 years, the use of nanomaterials in the construction of biosensing devices offers unique characteristics that give sensitive detection of catechol, such as carbon

nanomaterials, metal and metal alloy nanoparticles, and metal oxides. The small dimensions of nanomaterials contribute significantly in obtaining a surface that has an excellent adsorption property. Since nanomaterials have high chemical stability and high surface-to-volume ratio, they provide biocompatible matrices for biosensor applications²⁵². Carbon dots (CDs) are a relatively new class of zero-dimensional (0-D) carbon nanomaterials²⁵³. Even though CDs have become powerful tools in chemo- and bio-sensing applications, they have not been explored widely in electrochemical biosensor applications^{254–256}. Their excellent properties like low cytotoxicity, simple synthesis, remarkable conductivity, and tunable luminescence activity enable CDs to be functional nanomaterials in electrochemical biosensor applications. Besides, their large surface area, ease of modification and excellent biocompatibility allow them to increase the amperometric response significantly²⁵⁷.

Motivated by the abovementioned shortcomings of current techniques in catechol detection, we constructed a new biosensor using a thienopyrroledione based conjugated polymer (PFTBDT) and CDs on a graphite electrode. While carbon dots increase the electrochemical signal of the biosensor, the polymer enhances the stability and reduces the response time in the constructed biosensor for catechol detection. The use of an enzyme-based electrochemical biosensor is a simple, sensitive, and low-cost alternative to other analytical methods for catechol determination. The developed sensor was found to have a wider linear dynamic range (LDR), a lower limit of detection (LOD), and higher sensitivity compared to other catechol biosensors based on laccase. The results obtained here show that the biosensor is most sensitive and has potential use for catechol detection.

3.2 Experimental

Laccase (Lac, EC 1.10.3.2 from *T. versicolor*, 21.8 Unit/ mg), glucose, ethanol, glutaraldehyde (50% wt in H₂O), catechol (as a substrate), and all reagents were purchased from Sigma–Aldrich (Europe) and used without further purification. Number-average (M_n) and weight-average (M_w) molecular weights of the polymer

were obtained by size exclusion chromatography via a Shimadzu LC-20AT GPC in chloroform at 40 °C. All electrochemical measurements were performed with a three-electrode system. A platinum (Pt) wire and a silver (Ag) wire were used as the counter and the reference electrodes, respectively, while indium tin oxide (ITO) coated glass substrate was used as the working electrode. All potentials are referred to the pseudo-reference Ag electrode (+0.3 V vs. Fc/Fc⁺). Spectroelectrochemical measurements were conducted with Varian Cary 5000 UV-Vis spectrophotometer, and cyclic voltammograms of the polymer films were recorded using a GAMRY Reference 600 potentiostat. In chronoamperometric measurements, a modified graphite electrode (RW001 type, 0.07 cm²) was used as the working electrode. Amperometric studies were performed with PalmSens potentiostat. The crystallinity of carbon dots was investigated via X-ray diffraction (Rigaku Ultima-IV). Surface characterizations of the modified electrodes were performed by scanning electron microscopy (SEM) using a JEOL JSM-6400.

3.2.1 Syntheses of CDs and PFTBDT

3.2.1.1 Synthesis of Carbon Dots

CDs were synthesized according to a previously reported hydrothermal method with a minor modification ²⁵⁸. 1.0 g of citric acid and 335.0 µL ethylene diamine were first dissolved in 10 mL Millipore (Milli-Q) water and stirred using a magnetic stirrer for 30 minutes followed by 3 minutes of sonication. Then, the mixture was transferred to a Teflon-lined stainless-steel autoclave and heated at 200 °C for 6 hours. Next, the reaction mixture was allowed to cool down to room temperature and centrifuged at 7000 rpm for 45 minutes, followed by multiple steps of filtration and centrifugation (10000 rpm) to remove large precipitates. Afterward, the sample was filtered consecutively through the disposable sterile syringe filter units with 0.45 µm and 0.22 µm pore size hydrophilic PVDF membranes, respectively (Millipore, Millex-HV, Bedford, USA) in order to eliminate the large size carbon nanoparticles

and then dialyzed against pure water for 12 hours (MWCO = 1000 Da, Sigma Aldrich, St. Louis, USA) to obtain the pure S, N-CQDs. Finally, the resultant solution was lyophilized for 48 hours (at -57 °C and 0.1 mbar). The purified and lyophilized S, N-CQDs powder was further used to fabricate the modified graphite electrode after characterization.

The wide-angle X-ray diffraction (XRD) pattern of the synthesized CDs was recorded on a Rigaku Ultima IV (Rigaku, Tokyo, Japan) powder diffractometer using Cu K α radiation ($\lambda=1.541874$ Å generated at 40 kV and 30 mA) in the 2θ range of 10° - 90° , with a scan rate of $2^\circ/\text{min}$ and sampling interval of 0.02° . The XRD pattern of the CDs in Figure 1 demonstrates a broad diffraction peak centered at $\sim 20.6^\circ$ (2θ), corresponding to an interlayer spacing of ~ 4.3 Å, which is in good agreement with the previously published reports in the literature. The larger interlayer spacing is attributed to a highly disordered carbon structure with poor crystallization that is different from the bulk graphite (3.34 Å).

3.2.1.2 Synthesis PFTBDT

M2 (70 mg, 0.13 mmol), BDT(TiC8) (4,8-bis[5-(2-ethylhexyl) thiophen-2-yl]-2,6-bis(trimethylstannyl)benzo[1,2-b:4,5-b']) dithiophene (114 mg, 0.13 mmol), Pd₂(dba)₃ (6 mol%) and P(o-tol)₃ (12 mol%) were dissolved in dry toluene (15 mL) under argon atmosphere in a Schlenk tube charged with a magnet bar. The Schlenk tube was transferred to an oil bath, and the mixture was stirred for 40 h at 95 °C. The reaction mixture was allowed to reach ambient temperature, and the solvent was removed under reduced pressure. As a palladium scavenger, sodium diethyldithiocarbamate trihydrate (10 mg) was added following the addition of methanol. The mixture was filtered after 1 h stirring and washed with acetone and hexane in a Soxhlet extractor to eliminate low molecular weight fractions. The polymer was obtained in the chloroform fraction. Removal of chloroform under reduced pressure gave dark red crystals. Yield: 0.11 g, 91%.

M_n : 8.4 kDa, M_w : 22.2 kDa, PDI=2.63

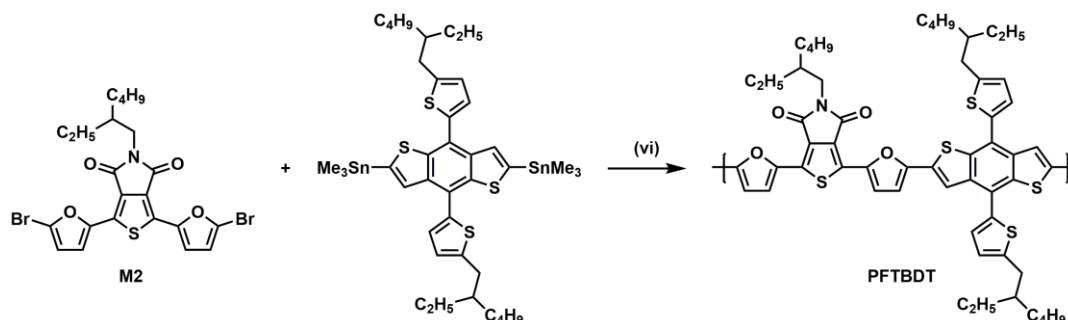


Figure 3.1. Synthetic route for PFTBDT

3.2.2 Preparation of modified electrode for biosensor application

To prepare the modified electrodes, bare graphite electrodes were first polished with emery paper and then thoroughly washed with distilled water. First, 0.5 mg mL^{-1} CDs solution was prepared and dispersed in DMF. Five microliters of the prepared solution were drop cast on the cleaned graphite electrode and allowed to air-dry for 1 h at room temperature. Afterward, $10.0 \text{ }\mu\text{L}$ of the PFTBDT solution ($1.25 \text{ mg per } 1.0 \text{ mL}$ of chloroform) was coated on CDs modified electrode. CDs/PFTBDT-modified electrodes were allowed to air-dry followed by a distilled water wash before enzyme immobilization. Ten microliters of laccase enzyme (10.9 U) in phosphate buffer solution ($\text{pH } 7.0$, 50 mM) and glutaraldehyde solution (1% in H_2O) as a cross-linking agent were added onto the modified electrodes, and CDs/PFTBDT/Lac electrodes were allowed to dry at room temperature for 2 h. Finally, the electrodes were washed with distilled water to remove any unbound enzyme molecules before used.

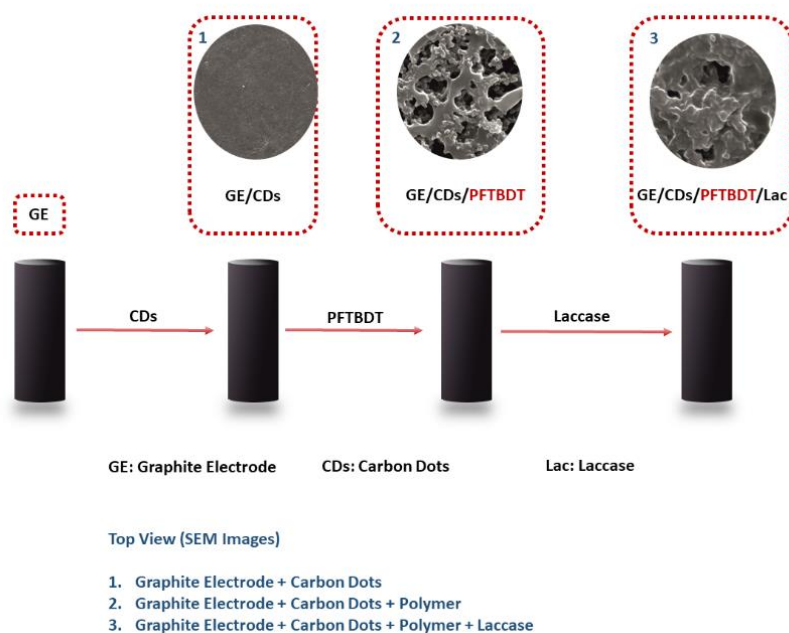


Figure 3.2. Design of the biosensor constructed for this study

3.2.3 Amperometric measurements for detection of catechol

Amperometric measurements were carried out at the ambient temperature in a sample holder that contains 10 ml sodium acetate buffer (50 mM, pH 5.5). After the working electrode reached equilibrium, catechol solution (as the substrate) was added to the buffer solution, and the current of the working electrode was monitored until a new equilibrium was established. The difference between two steady-state current values (μA) was recorded as the biosensor's response. After each measurement, the electrodes were washed with distilled water, and the reaction medium was refreshed. Amperometric measurements were performed at -0.3 V , which represents the biological activity of the enzyme.

3.2.4 Computational Studies

Density functional theory (DFT) calculations were performed by using the B3LYP/6-311G*hybrid functional ^{259–261} and basis set, using 10^{-8} RMS density matrix convergence and 10^{-6} energy change criteria in Gaussian09 (Revision A.02) ²⁶². Successful results were achieved previously at this level of calculations for donor-acceptor studies in the literature ^{263,264}. Results are validated by novel and promising TPSSh functional ²⁶⁵. HOMO, LUMO, electrostatic potential surfaces (ESP), counterpoise corrected interaction energy of PFTBDT with catechol and effect of catechol on the electronic structure such as charge transfer were calculated for the geometry optimized structures of tetramer model oligomers with methyl side chains. Vertical excitation energy of the first singlet excited state $S_0 \rightarrow S_1$ were calculated by TDDFT calculations in acetonitrile solvent effect. Vertical ionization potential and vertical electron affinity were calculated by the energy difference between the neutral tetramer and cation state of the optimized ground state geometry. Reorganization energies (λ_{reorg}) for the holes were estimated based on the formulation by Bredas et al ²⁶⁶. Periodic cells were minimized by molecular mechanics methods to understand packing structure of polymer by adopting polymer consistent force field ²⁶⁷ for 10,000 steps with 12 Å cutoff atomic distance for vdW interactions and Ewald summation for electrostatic interactions.

3.3 Results

3.3.1 Electrochemical and optical properties of the polymer

CV technique was used to investigate the electrochemical behavior of PFTBDT polymer. Using the CV technique, redox behavior and doping characteristics of the polymer were examined. Also, the HOMO energy level was calculated from cyclic voltammogram of the polymer by spray coating the polymer solution (6.0 mg of PFTBDT in 1.0 mL of chloroform) onto the glass substrate coated with ITO.

Three electrode system was used in CV experiments, constructed using a silver wire as the pseudo-reference, platinum wire as the counter, and the prepared ITO as the working electrode, respectively. The CV studies were performed at a scan rate of 100 mV/s, under a potential range between 0 and 1.7 V in 0.1 M TBAPF₆/ACN electrolytic medium. The polymer is p-dopable. It was doped at 1.47 V and de-doped at 0.98 V. The HOMO energy was determined as -5.67 eV via onset value of the corresponding oxidation potential using Equation 1 where the normal hydrogen electrode was taken as -4.75 eV against vacuum. The corresponding oxidation potential was determined from the interception of the tangent line drawn from the peak and the baseline in the related cyclic voltammograms (Figure 3.3.a).

$$\text{HOMO} = - (4.75 + E_{\text{ox, onset}}) \text{ (eV)}$$

The LUMO energy was determined from the difference between the optical band gap at the neutral state and the value of the HOMO energy level. The LUMO energy level was found as -4.15 eV. A summary of the electrochemical parameters for the polymer is shown in Figure 3.3.b.

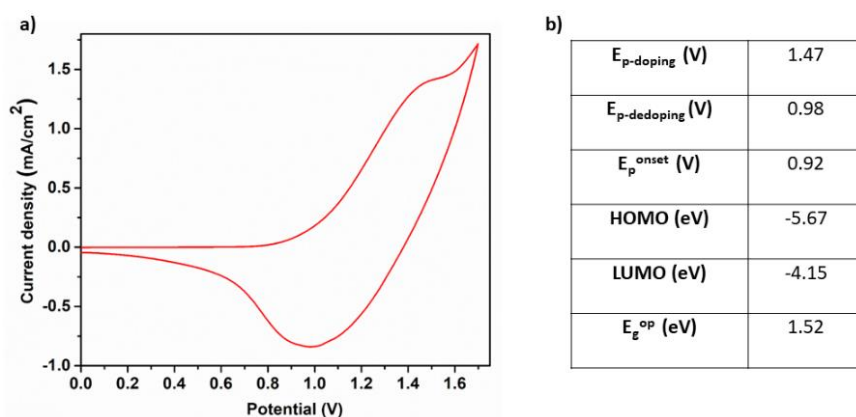


Figure 3.3. (a) Cyclic voltammogram of PFTBDT in 0.1 M TBAPF₆/ACN solution and (b) electrochemical parameters of PFTBDT.

Spectroelectrochemical studies were performed to complement the electrochemical investigation of PFTBDT thin films. The experimental procedure for the preparation of the thin film was almost the same with electrochemical studies. Here, stepwise

potential with appropriate increments was applied to the thin film. The response of the film to the applied potential was detected using UV–Vis Spectrophotometer (Figure 3.4.a). The maximum absorption peak of the polymer-coated thin film in the neutral state was observed at 515 nm. The intensity of this peak was decreased with increasing applied potential. Conversely, a polaron band arose with the increasing applied voltage. The polymer film was reddish-green at 1.7 V, while it was dark red in the neutral state. The optical band gap of the polymer was calculated as 1.52 eV using the onset value which was obtained from the intercept of the baseline and the tangent from the maximum absorption peak at the neutral state.

Colorimetric investigations of the polymer film were also performed to determine L, a, and b values defined by CIE (Commission Internationale de l'Eclairage) where L stands for luminescence, a stands for red/green, and b stands for yellow/blue coordinates, respectively. The observed color change along with the corresponding L, a, and b values are depicted in Figure 3.4.b.

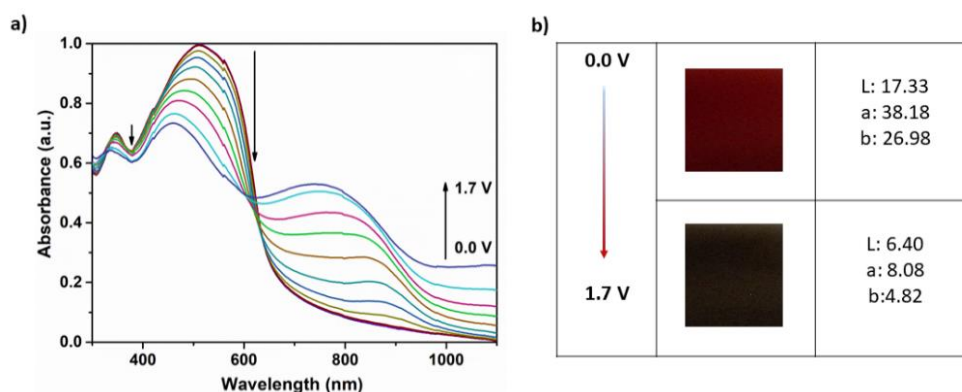


Figure 3.4. (a) Electronic absorption spectra and (b) Colorimetric measurements of PFTBDT thin film in 0.1 M TBAPF₆/ACN solution

PFTBDT polymer films are known to oscillate between their neutral and p-doped states. Hence, the kinetic studies were performed to obtain the optical contrast, the percent change in transmittance, and switching times of the polymer using a UV-Vis Spectrophotometer. Measurements were performed via the application of varying square-wave potentials between 0 and 1.7 V within 5 s periods. Percent optical

contrasts between neutral and p-doped states were measured as 9 and 30% at 515 and 755 nm, respectively. The switching times were determined as 2.5 and 0.9 s at 515 and 755 nm, respectively, from the time duration between the two applied voltages at a 95% contrast. Percent transmittance changes of the polymer film at 515 and 755 nm are depicted in Figure 3.5.a, and the obtained kinetic parameters are given in Figure 3.5.b.

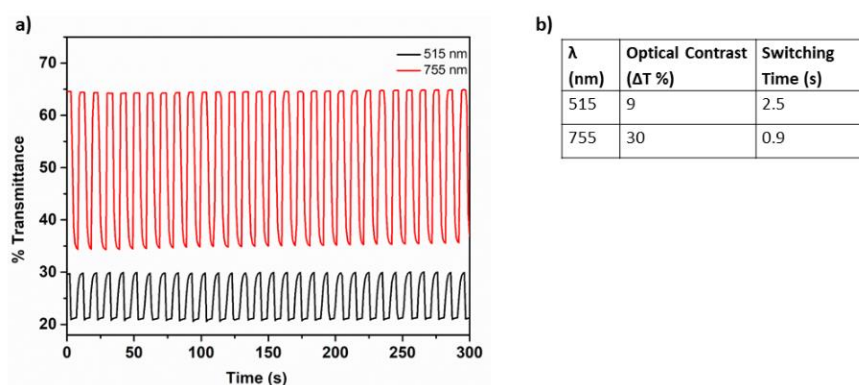
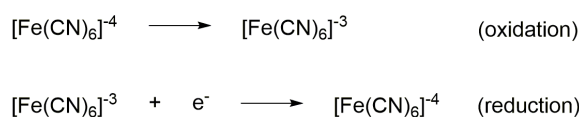


Figure 3.5. (a) Percent transmittance change at 515 and 755 nm with respect to time and (b) kinetic parameters obtained for PFTBDT thin film in 0.1 M TBAPF₆/ACN solution at 515 nm and 755 nm

3.3.2 Electrochemical and surface characterization of electrodes and carbon dot nanoparticles

Characterizations of the effective surface area of the modified electrodes were investigated via CV. Voltammograms were recorded in a solution containing 5.0 mM [Fe(CN)₆]³⁻, [Fe(CN)₆]⁴⁻, 50 mM phosphate buffer solution (pH 7.0) and 0.1 M KCl under a potential range between -0.6 and 0.8 V at 100 mV/s scan rate. Figure 3.6 displays the CVs of the bare graphite electrode (GE), modified electrode (GE/CDs/PFTBDT) and modified electrode with laccase enzyme (GE/CDs/PFTBDT/Lac) at ambient temperature. Randles-Sevcik equation affirms the direct relation between effective surface area and the peak current ²⁶⁸. The reaction taking place on the working electrode is as the following;



Here, at the bare GE electrode, the peak current was obtained as 86 μA . The peak current jumped to the value of 202 μA in the GE/CDs/PFTBDT electrode. The enhancement in the peak current proves the effect of charge transfer on the effective surface area of the modified GE/CDs/PFTBDT electrode (0.21 cm^2). When laccase enzyme was immobilized onto modified GE/CDs/ PFTBDT electrode, peak current was recorded as 150 μA . The decrease in the peak current resulting from the insulating character of the biomolecule indicates the effective immobilization of the enzyme molecule onto the modified electrode.

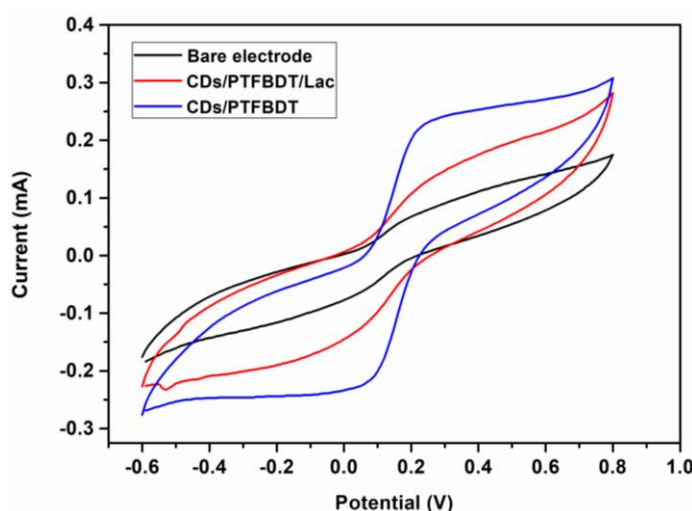


Figure 3.6. Cyclic voltammograms of GE, modified GE/CDs/PFTBDT and GE/CDs/PFTBDT/Lac electrodes

Figure 3.7 displays the surface characterizations of GE/CDs/PFTBDT and GE/CDs/PFTBDT/Lac electrodes by SEM. The surface morphology of the only carbon dot coated graphite electrode was not observable with SEM. That is attributed due to the small size of the CDs. Image of GE/CDs/PFTBDT film shows the uniform cauliflower structure (Figure 3.7.a). This uniform cauliflower structure increased the

effective surface area and provided a proper surface for enzyme immobilization. After laccase immobilization, the surface of the electrode became smoother compared to GE/CDs/PFTBDT modified electrode (Figure 3.7.b). The surface's smoothness can be considered evidence for successful enzyme immobilization.

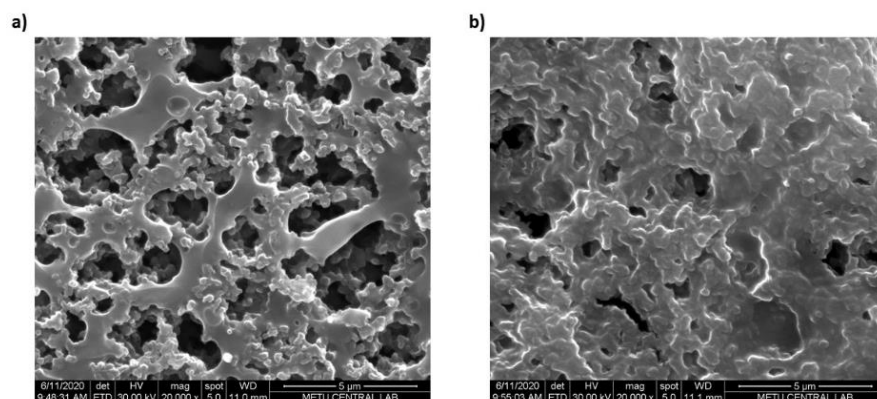


Figure 3.7. SEM images of modified surfaces (a) GE/CDs/PFTBDT (b) GE/CDs/PFTBDT/Lac

3.3.3 Optimization of the modified biosensor

First, the parameters such as the amount of carbon dots, PFTBDT, enzyme, and pH of the working medium that affect biosensor performance were optimized to enhance the response and performance of the modified biosensor. To determine the optimum amount of CDs, GE/CDs/ PFTBDT/Lac electrodes with varying CD concentrations ranging between 0.1 and 1.0 mg.mL⁻¹ were prepared and tested (Figure 3.8.a). The best response towards catechol was achieved with 0.5 mg.mL⁻¹ CD concentration as depicted in Figure 3.8.a. Therefore, in the further optimization steps, CD concentration was kept constant at 0.5 mg.mL⁻¹. The PFTBDT amount was optimized via using polymer solutions with varying PFTBDT concentrations on the CD-coated GE electrode (GE/CD). The polymer solutions with PFTBDT concentrations of 1.75, 1.50, 1.25, 1.0 and 0.75 mg.mL⁻¹ were tested to obtain the best response. The highest signal was recorded for the GE/CDs/PFTBDT/Lac

electrode with 1.25 mg.mL^{-1} PFTBDT (Figure 3.8.b). Here, the higher concentrations of PFTBDT were found to be preventing the electron transfer, while the lower concentrations of PFTBDT were found to be insufficient for effective charge transfer. The laccase amount was optimized next. To determine the optimum enzyme amount, different amounts of enzyme (4.36-17.44 U) were immobilized onto GE/CDs/PFTBDT. The highest response for catechol biosensing was obtained with 10.9 U of laccase as given in Figure 3.8.c. For enzyme activity, the pH of the working medium is also extremely important. Accordingly, to determine the best response of the laccase biosensor, the sensor was tested in different buffer solutions with varying pH values (pH 4.5-7.5). For GE/CDs/PFTBDT/Lac biosensor, the highest current was obtained in acetate buffer solution at pH 5.5 (Figure 3.8.d). In addition, the optimization experiments for constructed biosensor were performed in the presence of $125 \text{ }\mu\text{M}$ catechol at room temperature.

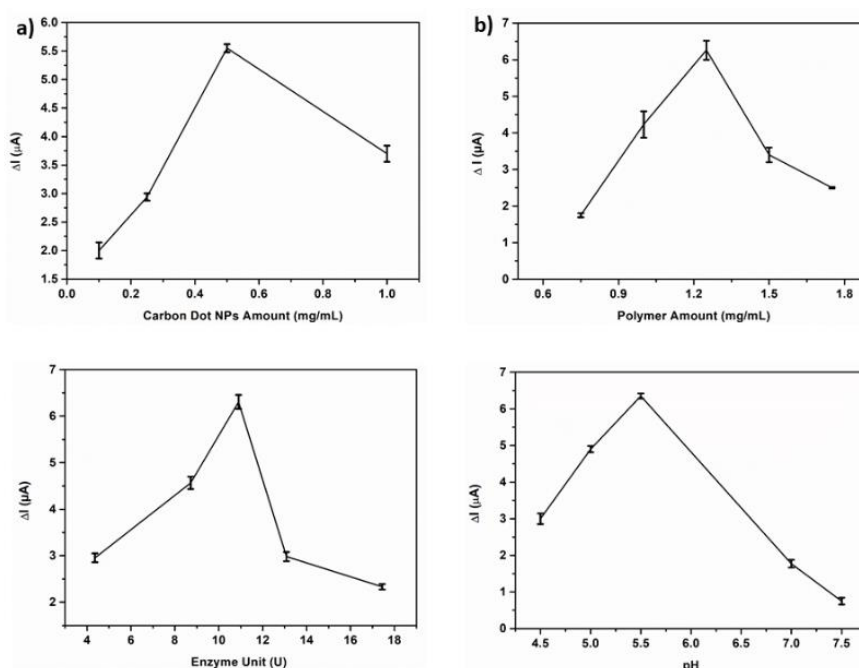


Figure 3.8. The effect of (a) CD amount, (b) polymer amount, (c) laccase amount and (d) pH on laccase biosensor response

3.3.4 Analytical merits of the catechol biosensor

Analytical characterization of the catechol biosensor was examined under the optimized conditions at -0.3 V. The amperometric response of the modified biosensor was monitored via the injection of varying catechol amounts. For GE/CDs/PFTBDT/Lac biosensor, the LDR was obtained between 1.25 and 175 μM catechol with the equation of $y = 48.31x + 0.4147$ ($R^2 = 0.9994$), while the LOD was calculated as 1.23 μM based on $S/N=3$ (Figure 3.9.a). Amperometric responses of the modified electrode in the presence of different concentrations of catechol were also represented in Figure 3.9.b. Additionally, the sensitivity of the biosensor was calculated as $737.4 \mu\text{A} \cdot \text{mM}^{-1} \cdot \text{cm}^{-2}$ and the response time of the developed biosensor was about 8 s. Stability of the catechol detection using GE/CDs/PFTBDT/Lac biosensor was also verified via the recording of amperometric response for 10 measurements under the optimized conditions in the presence of 125 μM catechol in the reaction medium. In order to test the reproducibility, three different electrodes were prepared with the same modification, and the response of these three electrodes showed a low standard deviation in the presence of 125 μM catechol. The SD of 10 measurements was found to be ± 0.072 , and the SD of measurements of three different electrodes was found to be 7.80% indicating the reproducibility, high reliability, and robustness of the developed biosensor.

Analytical performance of the developed catechol biosensor was compared to other catechol biosensors using the same laccase system in Table 3.1. The comparison reveals the wider LDR, lower LOD, and higher sensitivity of the developed biosensor in this work.

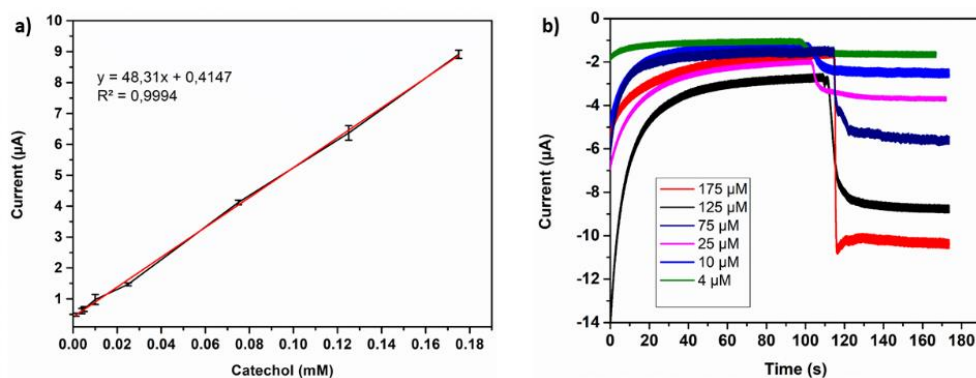


Figure 3.9. (a) Calibration curve of the modified electrode for catechol (in 50 mM acetate buffer, pH 5.5, 25 °C, -0.3 V) (b) Amperometric responses of the modified electrode in the presence of different concentrations of catechol

Table 3.1 Analytical merits comparison of the proposed biosensor and the previously reported laccase-based biosensors for electrochemical detection/sensing of catechol

Substrate(s)	Modified electrode	Detection technique	Stability (%) ^a or reproducibility ^b	Sensitivity (μA cm ⁻² mM ⁻¹)	LOD (μM; single CAT)	LDR (μM)	Sample(s) for method application	Ref.
Catechol	AgNPs-Pdop@Gr/GCE	DPV	2.0 ^b	NR	0.1	0.5–240	Pond water	269
Catechol and hydroquinone	P4VPBA/PPy/GO/GCE	CV/DPV	6.34 ^b	NR	0.96	7.0–16	Tap water	270
Catechol and hydroquinone	AuNPs/ZnO/Al ₂ O ₃ /GO, chit/GCE	CV	93.1 ^a	NR	3.10	0.5–40	Local water sample	271
Catechol	GO/PM/GCE	DPV	90.1 ^a	537.0	0.008	0.03–138	Ground and tap water	272
Catechol	Lac-F, N-CDs/GCE	CV, <i>i-t</i>	11.76 ^b	219.17	0.014	12–450	Tap and lake water	273
Catechol	Lac-a-Fe ₂ O ₃ NC-CPE	<i>i-t</i>	4.0 ^b	NR	4.28	8–800	Tap water and textile industry effluent	274
Catechol and hydroquinone	PCH/AGCE	DPV	3.03 ^b	NR	0.066	1–300	Tap and lake water	275
Catechol	MOF-ERGO-5/GCE	DPV	97.0	NR	0.1	0.1–566	Tap water	276
Catechol	CPE- B	CV	3.6 ^b	232.0	~ 1	~12.7–142.6	Green tea sample	277
Catechol	SPEs/MW CNTs/Au NWs/Tyr	<i>i-t</i>	NR	NR	0.027	0.5– 42	-	278

Table 3.1 Analytical merits comparison of the proposed biosensor and the previously reported laccase-based biosensors for electrochemical detection/sensing of catechol (continued)

Catechol and hydroquinone	rGO-Fe3O4-Au/GCE	DPV	2.3 ^b	NR	0.02	0.05–550	Artificial wastewater	²⁷⁹
Catechol, hydroquinone bisphenol A and phenol	AgNPs/MWCNT/GCE	SWV	2.6 ^b	~310	0.2	20–260	Tap water	²⁸⁰
Catechol and hydroquinone	CS/MWCNTs/PDA/AuNPs/GCE	DPV	1.38 ^b	NR	0.047	0.1–10	Tap and lake water	²⁸¹
Catechol and hydroquinone	Lac/AP-rGOs/Chit/GC	<i>i-t</i>	3.96 ^b	15.79	7.0	15–700	Tap and lake water	²⁸²
Catechol	Lac/PFTB-DT/CDs/GCE	<i>i-t</i>	1.10 ^b	737.44	1.2	1.25–175	Tap water	This work

P4VPBA: Poly (4-vinylphenylboronic acid); **CV**: Cyclic Voltammetry; **DPV**: Differential Pulse Voltammetry; **CD**: Carbon Dots; **CPE**: Carbon-Paste Electrode; **NR**: Not Reported; **GCE**: Glassy Carbon Electrode; **MOF**: Metal-Organic Framework; **CPE- B**: Carbon Paste Electrode Modified with Banana Tissue; **AuNWs**: Gold Nanowires; **MWCNTs**: Multi-Walled Carbon Nanotubes; **rGO**: Reduced Graphene Oxide; **SWV**: Square Wave Voltammetry.

Finally, the interference effects on the proposed biosensor was investigated in the presence of different substrates. Urea, ethanol, and ascorbic acid were used as the interfering agents. A volume of 0.05 mM of these agents was injected into 50 mM acetate buffer at pH 5.5. Results showed no obvious current change in the presence of interfering agents. On the other hand, the response of the modified electrode was highly stable towards catechol (Figure 3.10.a). The results obtained here clearly demonstrate the proposed biosensor's specificity and sensitivity for catechol detection. Apart from interfering substances, the response of the electrode to other phenolic compounds was investigated. A volume of 0.05 M of catechol, phenol, and hydroquinone was injected into the system, and the only non-negligible response obtained was belonging to the catechol (Figure 3.10.b). This clarifies that the proposed system was highly specific to catechol.

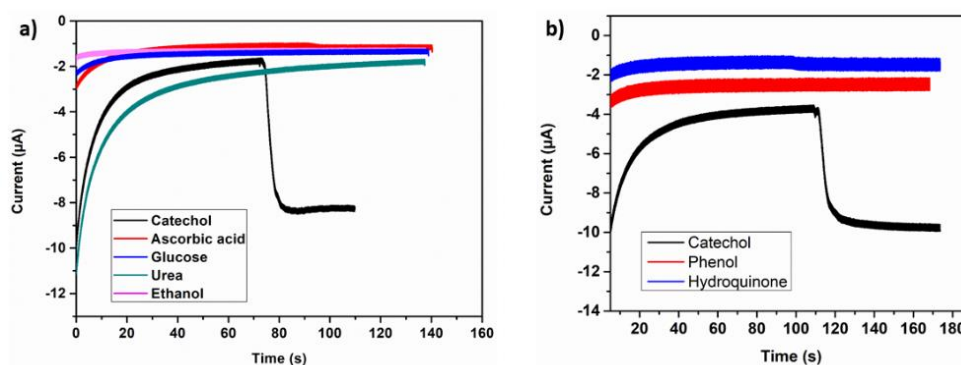


Figure 3.10. The response of the modified biosensor toward (a) different substrates including catechol (b) phenol derivatives including 125 μM catechol in 50 mM acetate buffer (pH 5.5) at - 0.3 V

3.3.5 Real sample analysis

The analytical applicability of the proposed biosensor was investigated using tap water. Results are given in Table 3.2. Recoveries were obtained by the determination of catechol concentration in the tap water sample after spiking with known concentrations of catechol. Three different concentrations (125 μM , high 25 μM , medium and 5 μM , low) of catechol were chosen for the spiking experiments. The quantitative recoveries were found to be 104, 100, and 96% for the spiked catechol concentration of 125, 25, and 5 μM , respectively. The recoveries, which are near 100% clearly indicate the method's reliability for catechol detection. The obtained data proved that the GE/CDs/PFTBDT/Lac biosensor was highly accurate and effective for detecting catechol in real samples.

Table 3.2 Determination of catechol in tap water

Sample	C _{added} (mM)	C _{found} (mM)	Recovery (%)
Tap water	0.125	0.130	104
	0.025	0.025	100
	0.005	0.0048	96

3.3.6 Computational results

Two different conformations were determined for PFTBDT tetramer. Thiophene sulfur of the TPD acceptor and furan bridge oxygen have the same direction in the first conformer (Figure 3.11.a). This conformer (conf1) has a star shape from the edge view due to the dihedral angle 6° angle between TPD and furan at both sides and 10° average angle between donor group and furan bridge. Furan oxygen atoms and pyrrole-4,6(5H)-dione oxygen atoms are on the same side in the second structure (conf2) where the dihedral angle between TPD and furan group as well as donor and furan group is less than 2° in the optimized geometry as given in Figure 3.11.b. Although conf2 has highly planar geometry, which makes it a better candidate as donor-acceptor conducting copolymer, star-shaped conf1 of PFTBDT tetramer is 0.31 eV more stable per donor:acceptor pair due to the repulsion between furan oxygen atoms and pyrrole-4,6(5H)-dione oxygen atoms in conf2. DFT calculations were performed for both conformers since molecular mechanics calculations showed that planar conf2 is more stable in multichain packing structure contrary to the single-chain energy comparison. This means that both low-density star-shaped conf1 and planar well-packed conf2 can present in the PFTBDT film. ESP mapped onto the conf1 and conf2 showed that both polymers show sequential well-differentiated donor-acceptor structures (Figure 3.11.c,d). Interestingly, the highest electron density was observed on the pyrrole-4,6 (5H)-dione oxygen atoms of TPD acceptor that overlap with the high electrostatic potential of electron donor groups. This was valid for both conformers, especially can clearly be seen in the ESP of conf2 (Figure 3.11.d). Overlap of electron density of TPD oxygen atoms with the donor is one of the important properties that provide enhanced effective coupling between the electron donor and acceptor groups and put TPD forward as an acceptor when it is used with suitable donor²⁸³.

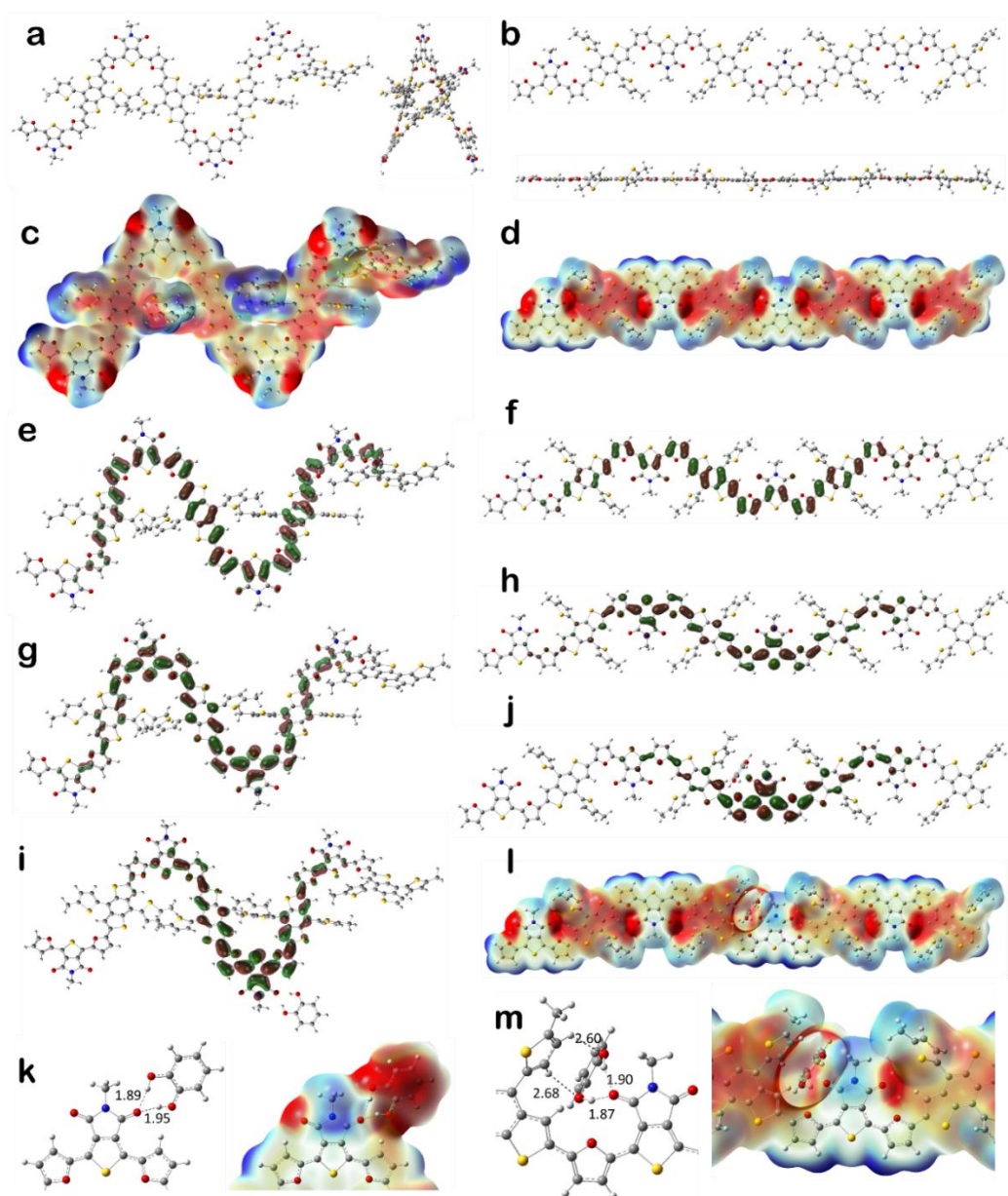


Figure 3.11. (a) Star shape conformation of PFTBDT (conf1), (b) planar conformation of PFTBDT (conf2), (c) Electrostatic potential surface (ESP) of conf1, (d) ESP of conf2, (e) Contour plots of the HOMO for conf1, (f) HOMO for conf2, (g) LUMO for conf1, (h) LUMO for conf2, (i) LUMO for conf1 and catechol complex, (j) LUMO for conf2 and catechol complex, (k) interaction and ESP of conf1 and catechol complex, (l) ESP of conf2 and catechol complex, (m) interaction and ESP of conf2 and catechol complex

Both HOMO and LUMO orbitals mapped on the PFTBDT are delocalized and distributed along the chain (Figure 3.11.e-h). The optical band gap was determined as 1.93 and 1.75 eV for conf1 by B3LYP and TPSSh functionals, respectively. There wasn't a significant difference between band gap values of conf1 and conf2. Hole reorganization energies are as low as 0.07 eV and 0.08 eV for two conformers, indicating high carrier mobilities for the pristine state.

Catechol formed two hydrogen bonding interactions with the pyrrole-4,6(5H)-dione oxygen on TPD acceptor in the lowest energy complex formed by PFTBDT and catechol. Although HOMO orbital does not show any significant difference, LUMO orbitals are more localized onto the TPD acceptor, which forms a complex with catechol (Figure 3.11.i,j). ESP maps point out a significant charge transfer from PFTBDT to catechol and disruption in the sequential (Figure 3.11.l,m). The amount of charge transfer from polymer to catechol based on the electrostatic potential fitting²⁸⁴ is determined as 0.04 e⁻/catechol for both conformers. Vertical electron affinity became more negative from -2.2 eV to -2.4 eV, and vertical ionization energy is increased from 5.6 eV to 5.7 eV for pristine and catechol interacted PFTBDT. Most importantly, basis set superposition error-corrected interaction energy between catechol and PFTBDT is calculated as -0.46 and -0.57 eV per catechol for conf1 and conf2, respectively. Higher interaction energy observed for planar conf2 is due to the additional interaction between donor side-chain hydrogens and oxygen atoms of catechol (Figure 3.11.m). Two strong hydrogen bonds between catechol and PFTBDT, charge transfer from polymer to catechol, disruption of electrostatic potential surface, localization of unoccupied orbitals on the acceptor group were determined as the main mechanisms for the observed current decrease given in Figure 3.10, leading to the successful design of catechol electrochemical biosensor with high sensitivity and selectivity by using PFTBDT.

3.4 Conclusions

In this study, the construction of a catechol electrochemical biosensor by laccase immobilization onto the modified working electrode via physical adsorption technique was reported. The modification was provided with CDs and PFTBDT coating on the graphite electrode. The proposed enzyme-based biosensor was optimized in terms of the amount of carbon dots, amount of PFTBDT, enzyme unit, and pH. The constructed biosensor exhibited linearity between 1.25 and 175 μM catechol, with a LOD of 1.23 μM and sensitivity of 737.4 $\mu\text{A}.\text{mM}^{-1}.\text{cm}^{-2}$. The probe was also highly selective toward catechol such that it did not show any response to the tested interfering agents. The applicability of the biosensor was demonstrated in tap water via the obtained high recovery rates. In conclusion, a novel, robust, and highly sensitive biosensor for catechol determination using carbon dots and PFTBDT was developed here. Compared to the previously reported studies, the developed biosensor is advantageous due to its wider LDR, lower LOD, and higher sensitivity. We believe the developed method can be a reliable alternative to the routine quantification of catechol in various matrices.

CHAPTER 4

EFFECT OF RANDOM COPOLYMERIZATION ON THE OPTICAL PROPERTIES OF SELENOPHENE AND TPD CONJUGATED POLYMERS

For the preparation of conjugated polymers having targeted band gaps, absorption, and optoelectronic properties, D-A approach has been one of the most convenient methods. Four new selenophene and thieno[3,4-c]pyrrole-4,6-dione (TPD) bearing conjugated polymers were synthesized for this study via Suzuki Stille Polycondensation. The effect of selenophene introduced as π -bridge and the introduction of a second TPD unit into the polymer backbones through random polymerization was investigated. Optoelectronic properties of the polymers were investigated via electrochemical and spectroelectrochemical studies. The study reveals the effects of TPD and selenophene moieties on absorption and band gaps of the polymer and provides a concise approach for the preparation of D-A conjugated polymers.

4.1 Introduction

The era of synthetic metals started after discovering that the conductivity of conjugated trans polyacetylene (PA) increases seven orders of magnitude upon doping with halogens ²⁸⁵. Since then, intensive research has been conducted on conjugated polymers, and tremendous progress has been made in syntheses and applications. Although highly conductive acetylene has been available, alternative conjugated polymers have been sought since the accessibility of PA was poor for applications. Academia showed great effort for new building blocks to obtain lower band gap polymers as an alternative to doped conjugated polymers ²⁸⁶. D-A approach, various electron-rich and electron-deficient groups are ordered through polymer backbones. D-A approach has led to numerous alternatives to doped

conjugated polymers, and the ease of modification and synthesis of monomers paved the way for more research and interest. D-A conjugated polymers allowed to engineer band gaps by tuning HOMO and LUMO energy levels, and their importance have proven in OSCs, OLEDs, and ECDs, etc.^{287–300}. Herein, we report four novel conjugated polymers obtained via Suzuki Polycondensation; thieno[3,4-c]pyrrole-4,6-dione (TPD) was utilized as the core unit, selenophene moieties as π -bridges, and carbazole/fluorene (Cz/FI) as donor units. TPD-based conjugated polymers provided both low and wide band gaps due to their tunable optical properties, resulting in changes in frontier energy levels^{156,199,200,301}. Quinoidal geometry, strong electron deficiency, ease of synthesis, and accessibility to the imide site for introducing pendant groups make TPD a great candidate moiety for D-A conjugated polymers. Chalcogenophenes like thiophene, selenophene, and alkyl species of these molecules, have proven efficient in tuning optical properties of conjugated polymers when introduced as π -spacers to the polymer backbone. The introduction of chalcogenophenes provides broadened absorption, tunable HOMO and LUMO energy levels. Thiophene is widely used in conjugated polymers' backbones. As an alternative to thiophene, selenophene was also utilized in D-A conjugated polymers, thanks to its similar properties with thiophene, physical and chemical. Selenophene has a lower ionization potential than thiophene; hence, introducing selenophene to polymer backbone provides reduced LUMO energy level and higher charge mobility^{203–206,210,302–304}. In the preparation of D-A conjugated polymers, carbazole (Cz) is widely used as a strong donor moiety. Full accessibility of Cz for modification provides tuning of optoelectronic properties of conjugated polymers due to connections through various open positions; 2,7-, 1,8-, and 3,6-. Cz polymers exhibited different planarity with the connection positions. Polymers obtained via connection through 2,7- and 3,6- positions provided higher planarity^{57,305,306}. Fluorene (FI) was also widely used as a donor unit in designing D-A conjugated polymers. Like Cz, FI also has various available connection positions, and the introduction of pendant groups to FI provides better solubility^{307–309}.

Hashimoto et al. reported TPD, Cz, and FI-based conjugated polymers (PC-DTTPD and PF-DTTPD) utilized to fabricate organic solar cells (OSCs) ¹⁵². The polymer backbones were introduced thiophene as the π -spacer, and optoelectronic properties were investigated for OSCs. The Cz-based polymer has an onset wavelength value of 600 nm, an optical band gap (E_g^{opt}) of 2.07 eV, and an electronic band gap (E_g^{el}) of 2.02 eV. The FI-based polymer exhibited an onset wavelength of 580 nm, an E_g^{opt} of 2.14 eV, and an E_g^{el} of 2.10 eV. PC-DTTPD and PF-DTTPD were reported by Tian et al., along with the modification of side chains, and instead of neat thiophene, alkylated thiophene was utilized as π -spacer ³¹⁰. The optical band gap of Cz-based polymer was determined as 2.28 eV, while the electronic band gap was 2.01 eV. For FI-based polymer, E_g^{opt} and E_g^{gel} were reported as 2.30 eV and 2.00 eV, respectively. Leclerc et al. reported a group of TPD and Cz comprising conjugated polymers with different alkyl side chains and optoelectronic properties were investigated ³¹¹. The optical band gaps varied between 2.05 and 2.21 eV, while the electronic band gaps changed between 1.93 and 2.02 eV. The report is a good example of the effect of alkyl side chains on optoelectronic properties. The findings of Pron et al. revealed similar values for a TPD and Cz-based conjugated polymer (E_g^{opt} =2.26 eV, E_g^{el} =2.20 eV) ³¹².

In this study, TPD, selenophene, and Cz/FI comprising conjugated polymers were synthesized via Suzuki Polycondensation. It was aimed to alter the optoelectronic properties of the polymers via the addition of a second TPD unit through random polymerization. Electrochemical and spectroelectrochemical investigations were conducted for analysis.

4.2 Methods, Instrumentation, and Experimental

Thiophene, 9,9-dioctylfluorene-2,7-diboronic acid bis(1,3-propanediol) ester, 9-(9-heptadecanyl)-9H-carbazole-2,7-diboronic acid bis(pinacol) ester, and other chemicals were purchased from Sigma Aldrich (Merck). Merck Silica Gel 60 (0.063-0.200 mm, 70-230 mesh ASTM) was used for column chromatography. Structural

characterizations were performed using a Bruker Spectrospin Avance DPX-400 Spectrometer. Number average (M_n) and weight average (M_w) molecular weights of the polymers were defined by size exclusion chromatography (SEC) on a Shimadzu LC-20AT liquid chromatograph. The optical properties of the polymers were investigated via electrochemical and spectroelectrochemical characterizations. A Gamry Reference 600 potentiostat was used to record cyclic voltammograms, and a JASCO V-770 UV-Vis-NIR Spectrophotometer was used to record spectra.

4.2.1 Synthesis of polymers

4.2.1.1 Synthesis of PS1

Under argon atmosphere **M1** (0.1 g, 0.147 mmol), 9-(heptadecan-9-yl)-2,7-bis(4,4,5,5-tetramethyl-1,3,2-dioxaborolan-2-yl)-9H-carbazole (0.96 g, 0.147 mmol), and $\text{Pd}(\text{PPh}_3)_4$ (10 mol%) were dissolved in dry toluene (15 mL) in a 25 mL Schlenk-tube charged with a magnetic stir bar. 2M K_2CO_3 (2 mL) and three drops of Aliquat 336 were added. The reaction mixture was refluxed for 16 hours, controlled by TLC. After completion of the reaction, the solvent was removed under reduced pressure, and distilled water was added. The crude product was extracted with CHCl_3 . Collected organic layers were dried over Mg_2SO_4 , and the solvent was evaporated. Following the addition of cold methanol, Sodium diethyldithiocarbamate trihydrate was added to remove any Pd residuals, and the mixture was stirred for one h. Then the crude product was filtered off and transferred to a Soxhlet thimble. The washing process was performed first with acetone and then hexane and chloroform, respectively. The polymer was recovered with the chloroform fragment. Yield: 25 mg, 19%.

^1H NMR (400 MHz, CDCl_3) δ 9.83, 8.22, 8.07, 7.92, 7.80, 7.73, 7.64, 7.51, 7.40, 4.62, 3.95, 3.90, 3.87, 3.60, 3.40, 3.12, 3.01, 2.95, 2.35, 2.03, 1.71, 1.42-1.15, 0.88-0.80.

4.2.1.2 Synthesis of PS2

The same method in the synthesis of PS1 was followed with **M1** (0.1 g, 0.147 mmol), 2,2'-(9,9-dioctyl-9H-fluorene-2,7-diyl)bis(1,3,2-dioxaborinane) (0.83 g, 0.147 mmol), and with Pd(PPh₃)₄ (10 mol%). Yield: 60 mg, 45%.

¹H NMR (400 MHz, CDCl₃) δ 7.92, 7.69, 7.56, 3.62, 3.43, 3.36, 2.05, 1.68, 1.40-1.27, 1.19, 1.10, 0.96-0.87, 0.80, 0.70.

4.2.1.3 Synthesis of RPS1

Under Ar atmosphere **M1** (50 mg, 0.07 mmol), compound **4** (32 mg, 0.07 mmol), 9-(heptadecan-9-yl)-2,7-bis(4,4,5,5-tetramethyl-1,3,2-dioxaborolan-2-yl)-9H-carbazole (0.1 g, 0.15 mmol), and Pd(PPh₃)₄ (10 mol%) were dissolved in dry toluene (10 mL). 2M K₂CO₃ (2 mL) and three drops of Aliquat 336 were added. The reaction mixture was allowed to stir for 16 h under reflux. The purification process was conducted as in the syntheses of PS1 and PS2. The polymer was isolated both in chloroform and chlorobenzene. Yield: 70 mg, 73%.

¹H NMR (400 MHz, CDCl₃): δ: 8.1, 8.0, 7.8, 7.5, 7.3, 4.6, 4.3, 3.7, 3.6, 3.5, 3.4, 2.5, 2.4, 2.0, 1.3-0.8.

4.2.1.4 Synthesis RPS2

The same method as in the syntheses of RPS1 was followed with **M1** (50 mg, 0.07 mmol), compound **4** (32 mg, 0.07 mmol), 2,2'-(9,9-dioctyl-9H-fluorene-2,7-diyl)bis(1,3,2-dioxaborinane) (0.08 g, 0.15 mmol), and Pd(PPh₃)₄ (10 mol%). Yield: 35 mg, 32%.

¹H NMR (400 MHz, CDCl₃) δ 8.23, 7.92, 7.85, 7.68, 7.57, 6.88, 3.64, 3.45, 3.37, 2.06, 1.94, 1.68, 1.35, 1.25, 1.11, 0.96, 0.92-0.69.

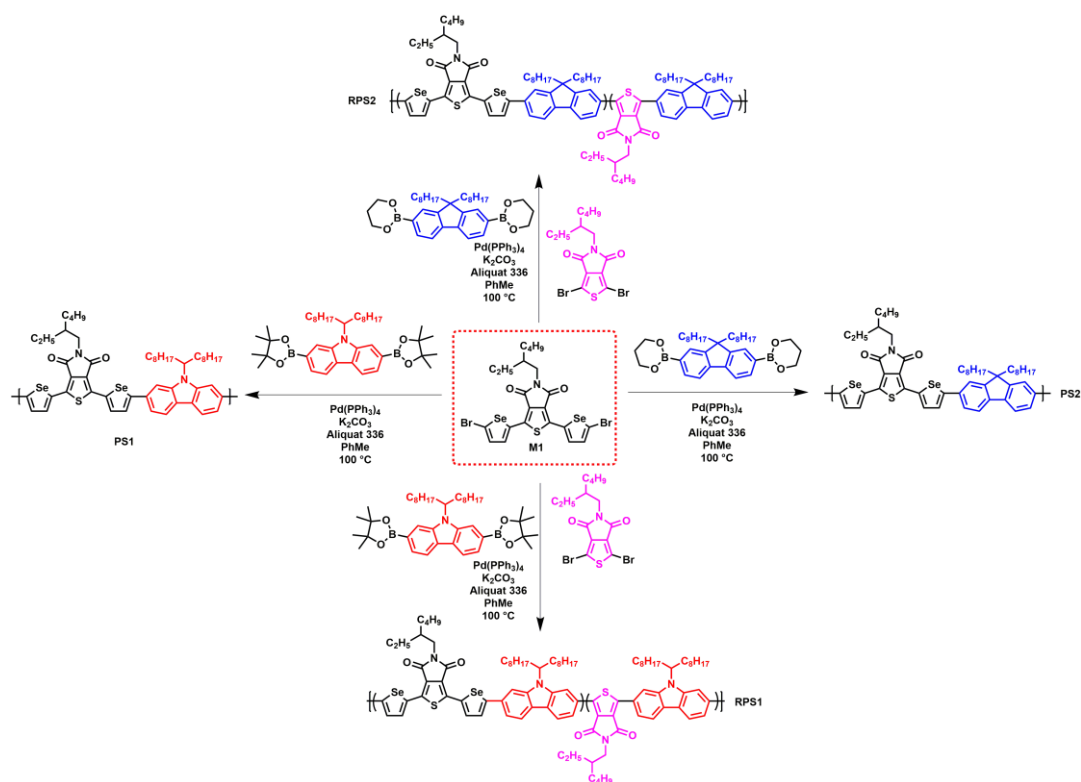


Figure 4.1. Synthetic routes for the polymers

M_n and M_w for PS1, PS2, RPS1, and RPS2 are summarized in Table 4.1.

Table 4.1 Molecular weights and PDI values of PS1, and PS2, RPS1, and RPS2

Polymer	M_n (kDa)	M_w (kDa)	PDI
PS1	1136	2633	2.31
PS2	5.3	7.3	1.37
RPS1	3.8	6.2	1.63
RPS2	3.0	5.8	1.93

4.3 Results and Discussion

Redox behavior of the polymers was investigated via cyclic voltammetry. CV is one of the methods to determine redox potentials and HOMO and LUMO energy levels. For each polymer, a 5 mg sample was dissolved in 1 mL of CHCl_3 . Polymer films were prepared upon spraying the polymer solutions on an ITO-coated glass substrate. For CV experiments, a three-electrode system was utilized in a solution of 0.1 M $\text{TBAPF}_6/\text{ACN}$. An Ag wire was used as the reference, a Pt as the counter, and the ITO itself was used as the working electrode. Single scan cyclic voltammograms were recorded via cycling at 100 mV/s at ambient temperature. As shown in Figure 4.2, PS2 exhibited an ambipolar character, both p-dopable and n-dopable. Oxidation potential was determined in the anodic region as 1.15 V for PS1, 1.34 V for PS2, 1.49 V for RPS1, and 1.46 V for RPS2, respectively. As noticed, introducing a second TPD unit to the polymer backbone increased the oxidation potentials and subsequently deepened HOMO levels. The same trend was expected for reduction potentials, but PS2 was the only exhibiting ambipolar characteristics. Hence, the LUMO energy levels for PS1, RPS1, and RPS2 were determined by the difference between HOMO levels and optical bandgaps obtained during spectroelectrochemical investigations. In the cathodic region, PS2 exhibited a reduction potential of -1.25 V. Onset potentials in anodic and cathodic areas were obtained with an intersection of the baseline and a tangent to the redox peaks. HOMO/LUMO energy levels for PS2 were calculated with respect to the normal hydrogen electrode (NHE, taken as -4.75 eV against vacuum) (Equation 1 and 2). The electronic band gap for PS2 was calculated from Equation 3. The electrochemical parameters for the polymers are summarized in Table 4.2.

$$HOMO = -(4.75 + E_{ox,onset})(\text{eV}) \quad (\text{Eq. 1})$$

$$LUMO = -(4.75 + E_{red,onset})(\text{eV}) \quad (\text{Eq. 2})$$

$$E_g^{el} = HOMO - LUMO \text{ (eV)} \quad (\text{Eq. 3})$$

Table 4.2 Electrochemical parameters for the polymers

Polymer	$E_{p\text{-doping}}$ (V)	$E_{onset\text{-}p\text{-doping}}$ (V)	$E_{n\text{-doping}}$ (V)	$E_{onset\text{-}n\text{-doping}}$ (V)	HOMO (eV)	LUMO (eV)	E_g^{el} (eV)	E_g^{op} (eV)
PS1	1.15	0.97	-	-	-5.72	-4.02	-	1.70
PS2	1.34	1.18	-1.25	-0.92	-5.93	-3.83	2.1	1.93
RPS1	1.49	1.15	-	-	-5.90	-4.12	-	1.78
RPS2	1.46	1.17	-	-	-5.92	-3.96	-	1.96

Color changes of the polymers upon the applied potentials were observed to see the applicability of the polymers for smart electrochromic devices. For electroactive conjugated polymers, electrochromism has a vital place. The polymers exhibited varying tones of their neutral state color. Except for PS2, the other three polymers showed color change at their oxidation states. Commission Internationale de l'Eclairage (ICE) defined L, a, and b values are provided in Table 4.3. L stands for the brightness of the color, a stands for red/green coordinate, and b stands for yellow/blue coordinate.

Table 4.3 Color changes and L, a, and b values of PS1, PS2, RPS1, and RPS2


























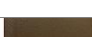








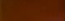



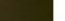
	<div> <div>0 V</div> <div>→</div> <div>+1.6 V</div> </div>			
PS1				
L	47.61	46.64	48.88	44.86
a	25.82	5.65	-0.07	0.10
b	21.62	8.23	3.60	1.27

Table 4.3 Color changes and L, a, and b values of PS1, PS2, RPS1, and RPS2 (continued)

	-1.7	0 V															+1.7 V
PS2																	
L	35.35	36.54	28.35	26.29	27.55	30.41	30.86	31.25	32.21	34.4	34.89	38.55	37.83	38.66	37.78	36.43	39.85
a	36.02	51.1	33.0	25.5	20.6	14.5	11.4	9.84	6.84	1.97	1.81	1.39	0	0	0.32	-0.4	-0.31
b	4.96	23.5	6.88	4.20	3.23	2.70	2.64	1.28	1.29	1.36	1.95	0.13	0	0	-1.15	-1.46	1.14

	0 V								+1.7 V
RPS1									
L	38.61	29.28	27.89	27.50	30.42	27.32	26.78	51.31	
a	41.16	12.84	9.50	9.77	13.75	9.05	7.20	3.25	
b	35.70	20.88	19.01	17.76	20.59	19.35	14.13	10.19	

	<div>0 V<div><div></div></div>+1.8 V</div>							
RPS								
2								
L	36.18	27.40	22.83	15.34	17.89	18.4	19.38	18.25
a	49.05	35.89	28.53	16.41	0.57	-1.04	-1.09	0.12
b	49.72	39.39	33.43	22.98	20.11	19.21	19.16	19.00

PS1 provided a color range between orange and light grayish-blue when a potential between 0 and 1.6 V was applied. PS2 was the only polymer that showed ambipolar characteristics. In the anodic region, the color of the polymer went pink under a potential of -1.7 V. In the cathodic region, the polymer passed through various colors until it went light grayish-blue under 1.7 V. Under the applied potential range (0 to 1.7 V) RPS1 and RPS2 (0 to 1.8 V) exhibited different tones of reddish and dark

green. This multichromic behavior of the polymer films paves the way for the applicability of the polymers in smart electrochromic materials.

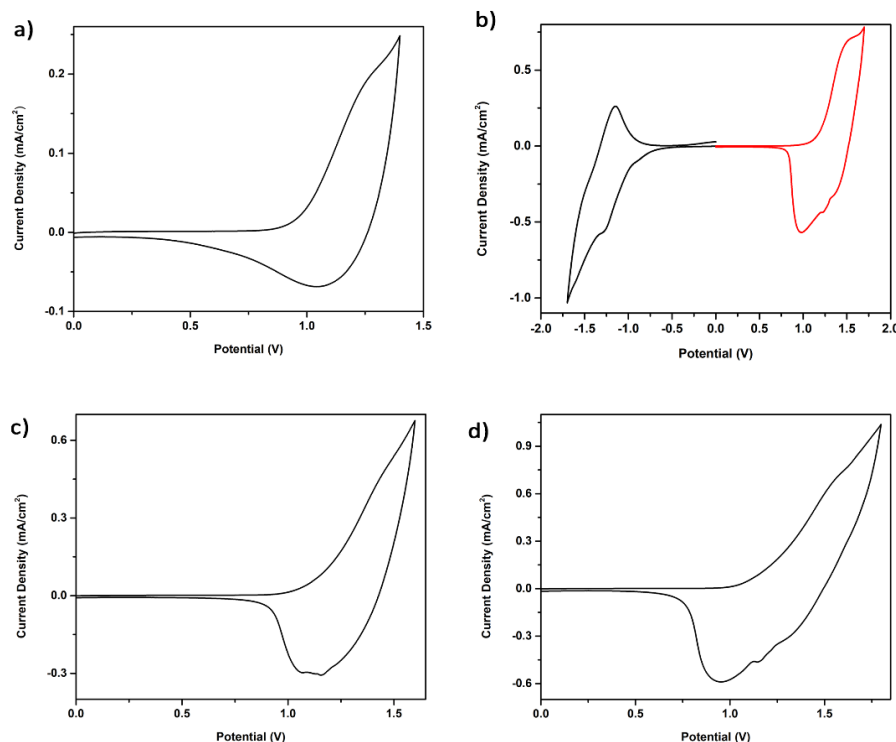


Figure 4.2. Single scan cyclic voltammograms of a) PS1, b) PS2, c) RPS1 d) RPS2 on ITO in 0.1 M TBAPF₆/ACN electrolyte/solvent couple at the scan rate of 100 mV·s⁻¹.

For spectroelectrochemical investigations, the polymer films were prepared following the same procedure for CV investigations, and the same three-electrode system was equipped. Optical changes were conducted by doping polymer films stepwise via applied potentials. First, the absorption of the neat film was recorded and followed by observation of spectral changes as the applied potential increased gradually (Figure 4.3). The potential sweep was measured differently for each polymer film, accordingly with spectral changes. For PS1, the potential sweep started from 0 to 1.45 V, for PS2 from 0 to 1.5 V, for RPS1 from 0 to 1.6 V, and for RPS2

from 0 to 1.75 V. π - π^* corresponding λ_{max} and onset absorption values for each polymer were recorded.

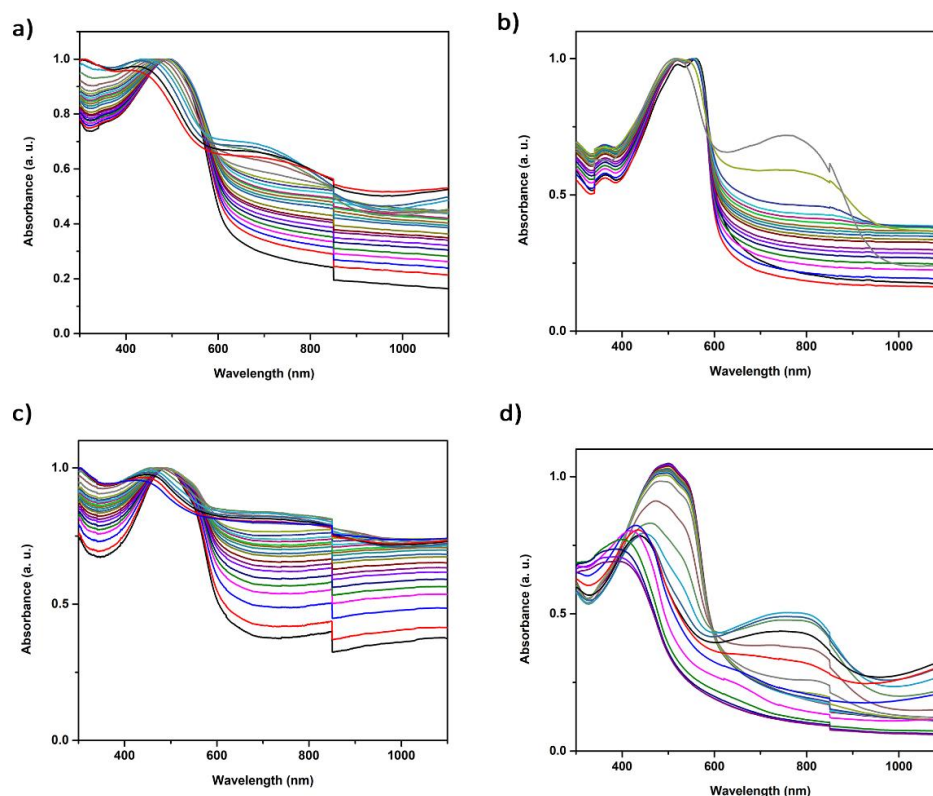


Figure 4.3. Changes in electronic absorption spectra of a) PS1, (b) PS2, c) RPS1 d) RPS2 upon stepwise oxidative doping in a 0.1 M solution of TBAPF₆/CAN

The optical properties of the polymers are summarized in Table 4.4. Herein, both the effect of introducing selenophene and a second TPD unit can be observed. It is known that with the introduction of selenophene into polymer backbone instead of thiophene as a π -spacer, the absorption behavior of the polymer alters and a red-shift in the absorption spectrum takes place ³¹³. The polymers exhibited maximum absorption values changing between 490 and 556 nm. These findings are relatively higher than those of thiophene-based polymers, previously reported [40–43]. Moreover, when alternating and random polymers are compared, λ_{max} values slightly change. While PS1 provided a λ_{max} value of 500 nm, RPS1 provided 490, while PS2 gave λ_{max} as 556 nm, RPS2 gave 500 nm. This explains that introducing a second

TPD unit to the polymer backbone causes a blue shift in the absorption range, hence providing a wider optical band gap, as summarized in Table 4.4. A change of 10 nm was observed between PS1 and RPS1, and a 44 nm shift was observed between PS2 and RPS2. The optical band gaps were determined as 1.70, 1.93, 1.78, and 1.96 eV for PS1, PS2, RPS1, and RPS2, respectively.

Table 4.4 Optical properties of PS1, PS2, RPS1, and RPS2

Polymer	λ_{max} (nm)	$\lambda_{\text{onset}_{\text{max}}}^{\text{onset}}$ (nm)	E_{g}^{op} (eV)
PS1	500	727	1.70
PS2	556	643	1.93
RPS1	490	696	1.78
RPS2	500	632	1.96

Electrochromic switching and optical contrast studies of the polymer films were performed. The polymer films were prepared with the same methodology discussed earlier. Under certain potentials and at specific wavelengths, measurements were conducted with square-wave potential by implementing a UV-Vis spectrophotometer to record percent optical contrast values. The measurements were conducted by applying 0/1.5, 1.7, 1.75, and 1.7 V, for PS1, PS2, RPS1, and RPS2, respectively, within 5 s time intervals. The percent optical contrasts were recorded with respect to the specified wavelengths; 500 and 700 for PS1, 555 and 760 nm for PS2, 750 nm for RPS1, and 505 and 740 nm for RPS2.

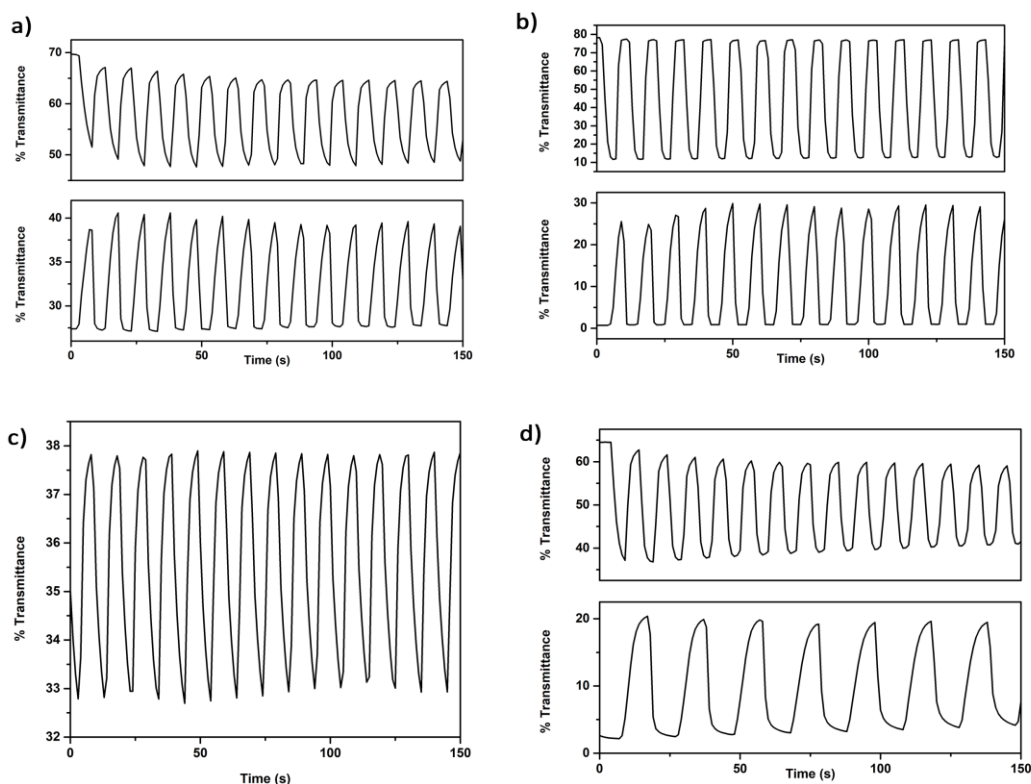


Figure 4.4. Percent transmittance and electrochromic switching changes of (a) PS1, (b) PS2, (c) RPS1, (d) RPS2

Table 4.5 Kinetic properties of PS1, PS2, RPS1, and RPS2

Polymer	λ (nm)	Optical Contrast(%)	Switching Time (s)
PS1	500,700	13,20	3.6,1.7,0.7
PS2	555,760	25,67	2.5,1.5,0.9
RPS1	500,750	15,	1.4
RPS2	505,740	21,27	3.5,2.0,1.8

4.4 Conclusions

The study exhibited that introduction of selenophene as a π -spacer leads red shift in absorbance and decreases the optical band gaps of the polymers, in accordance with the literature. Since it is known that TPD moiety can tune the optoelectronic

properties of the polymers, the introduction of a second TPD unit altered the absorption and band gaps as well. Here, the effect of the introduction of selenophene and a second TPD to the polymer backbones were investigated and explained with a synthetic approach.

CHAPTER 5

ORGANIC CATIONS FOR TREATMENT OF 3D PEROVSKITE FILMS

The growing interest in solar cells led academia to conduct intensive research on finding new materials. Low efficiencies in OSCs and expensive materials employed in the preparation process have required new approaches for harvesting the sun. Currently, the solar cell market is dominated by crystalline silicon solar cells. However, drawbacks like expensive raw materials and fabrication processes have led researchers to work on new solar cell technologies that combine both high efficiency and cost-effective materials. With perovskite materials, the concern about prices and efficiencies has been considerably reduced. Due to their outstanding performance, ease of processing, and cost-effectiveness, perovskite materials have gained great attention in academia ^{314,315}. Since Perovskite solar cells (PSCs) can easily be prepared via wet chemistry and cost-effective methodologies, they do not require expensive and complicated processes. Perovskite materials can be prepared by dip coating, spin coating, evaporation, and screen printing. Although PSCs exhibit excellent performance, poor device stability is an obstacle to the commercialization of such materials. Compared to other solar cells, efficiencies of PSCs have risen from 3% to over 20% over ten years, while others could not have this achievement over the past thirty years ^{316–318}. One of the properties that makes perovskite materials different from others is that they can be both absorber and charge transport layers. Unique properties of perovskite materials like high carrier diffusion length, high electron mobility, ambipolar charge transport, high absorption coefficient, low exciton binding energy, optimized band gap, etc., make perovskite materials significantly distinguished ^{319–322}.

5.1 Brief History

The perovskite mineral is calcium titanium oxide (CaTiO_3) found by Gustav Rose in 1939 and named after Lev Alekseevich Perovski, who conducted further research³²². Other perovskite materials are derivative of CaTiO_3 , which has a molecular structure of ABX_3 . Optoelectronic properties of organic-inorganic perovskites were investigated in the 90s³²³. The first perovskite solar cell research was reported in 2009 by Miyasaka et al.³¹⁶. The study revealed the utilization of the perovskite material as a liquid sensitizer in Dye-sensitized solar cells (DSSCs). MAPbI_3 and MAPbBr_3 were employed as liquid sensitizers. The perovskite solar cell operated with 3.8% and 3.2% efficiency. As mentioned earlier, PSCs suffer from poor stability, so this device worked only for seconds due to liquid electrolyte. In 2011, Im et al. reported utilization of quantum dots of nanomaterials and constructed DSSCs³²⁴. The obtained efficiency was 6.54%. However, due to stability problems the device operated only for 10 minutes. Since liquid electrolytes heavily cause poor stability, Kim et al. revealed an all-solid-state perovskite solar cell hoping to overcome this problem³²⁵. As hole transport layer (HTL), they employed spiro-OMeTAD. The PSC operated with an efficiency of 9.7%. The results have impacted the field not because of only the efficiency but also the stability since the device operated for around 500 hours. Following this achievement, various studies were reported revealing efficiencies from 15% to 22.1%^{326–331}. Currently, the best efficient perovskite-based solar cell exhibited 29.15% claimed by Albrecht et al.³³²

5.2 Structure of Perovskite Materials

The structure of perovskite materials is similar to CaTiO_3 with the general representation of ABX_3 . A stands for a monovalent cation, B represents lead or tin cations, and X generally stands for halides, oxygen, nitrogen, and carbon. The A group can be methylammonium (CH_3NH_3^+) or formamidinium ($\text{CH}(\text{NH}_2)_2^+$) that are located in the vertex of the face-centered cubic system. The B group can be (Pb^{2+} ,

Sn^{2+} , etc.) or halogen anions (Cl^- , Br^- , or I^-)³³³. The most famous absorbent employed in PSCs is methylammonium lead trihalide (MAPbX_3)^{334–337}.

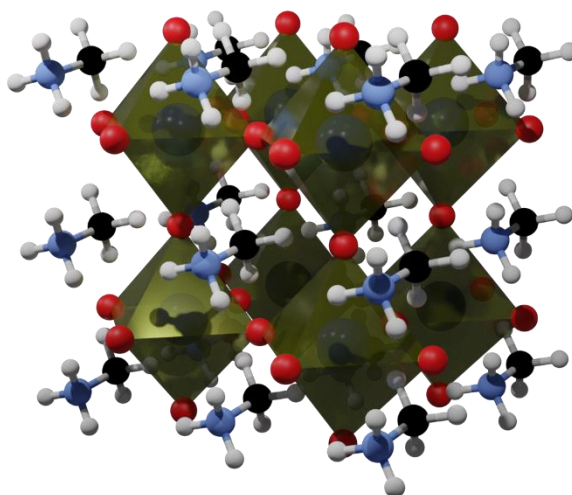


Figure 5.1. The general structure of a 3D perovskite material

5.3 Aim of the study

In this chapter, phenylmethanamine, aniline, and pyridine-based organic cations containing chalcogenophenes were synthesized for the treatment of 3D perovskite films. Organic halide cations have been known for enhancing perovskite film to stabilize the crystal structure and obtain higher PCE values. Organic halide cations are employed as salt additives containing heteroatoms. These cations form larger grains and subsequently a uniform surface. Besides, some organic halide salts are prone to react with PbI_2 and form an intermediate phase that can slowly convert to the perovskite during thermal annealing if excess MAI is present. 2D and 3D perovskite films can be enhanced when treated with organic halide salt additives with large organic moieties. They favor the formation of high-quality perovskite films with 2D perovskites on the surface of 3D perovskites, which significantly enhances the stability.

For this purpose, phenylmethanamine, aniline, and pyridine-based organic cations were designed and synthesized. This part of the thesis covers synthetic procedures of the organic cations and preliminary results of perovskite devices fabricated via the treatment of perovskite films by compound 21.

5.4 Phenylmethanamine-based organic cations

In this section, organic halide cations containing phenylmethanamine and chalcogenophene (thiophene, selenophene, and furan) were synthesized. Figure 5.2 represents the synthetic routes for each compound.

5.4.1 Syntheses of phenylmethanamine-based organic cations

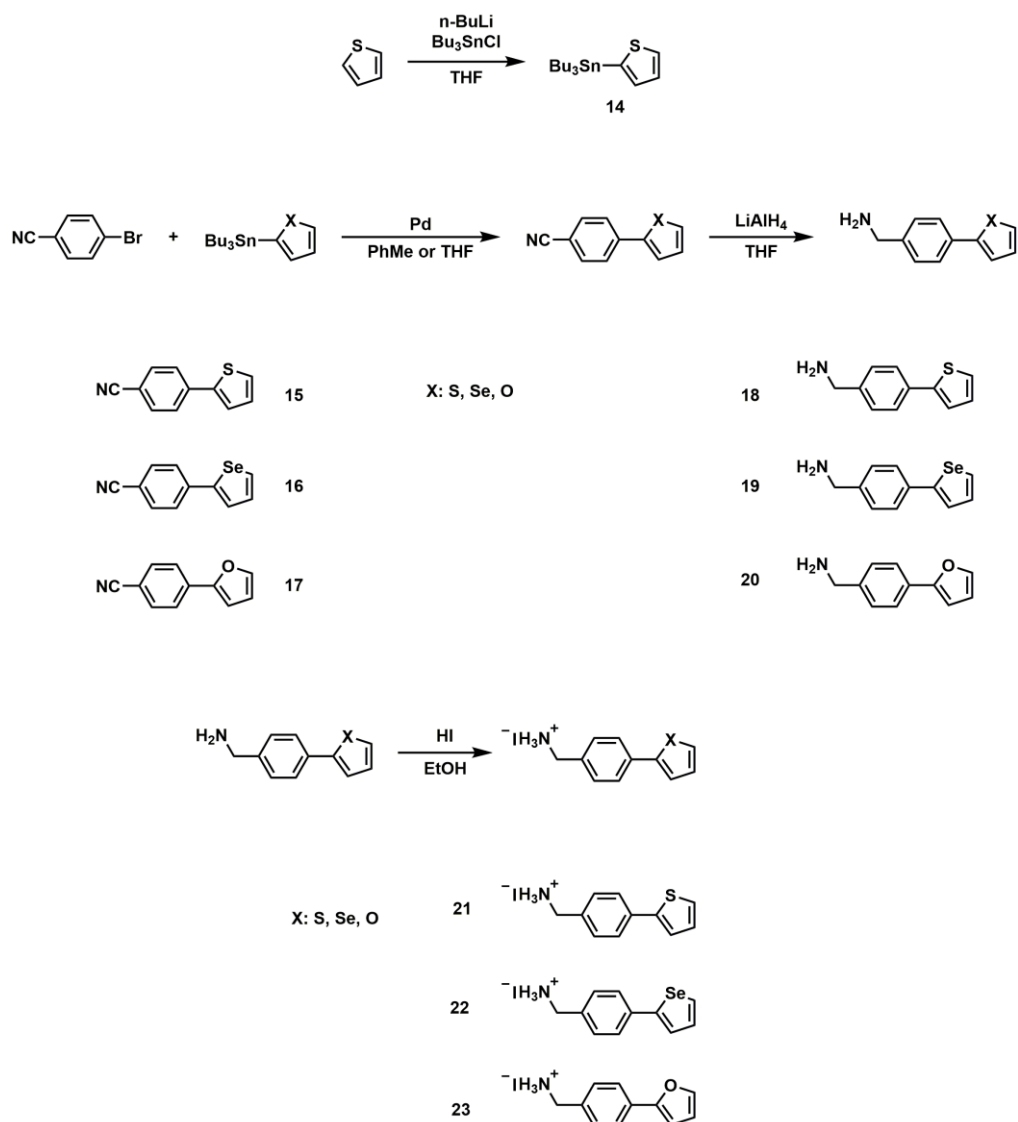


Figure 5.2. Synthetic route for the syntheses of phenylmethanamine-based organic cations

5.4.1.1 Synthesis of tributyl(thiophen-2-yl)stannane (14)

Under Ar atmosphere, to a 100 mL flask charged with a magnetic stir bar, thiophene (3 g, 35.6 mmol) was introduced. Dry THF (60 mL) was added, and the solution was stirred for 5 minutes. The temperature of the solution was set as -78 °C. *n*-BuLi (16

mL, 2.5 M) was added dropwise, and the reaction mixture was allowed to stir for 1 h at the same temperature. SnBu_3Cl (10.7 mL, 40 mmol) was added slowly, and the reaction mixture was warmed to the ambient temperature. The reaction mixture was stirred overnight, and the solvent was removed. The crude product was diluted with DCM, and organic layers were washed with NaHCO_3 , water, and brine, respectively. Combined organic layers were dried over Mg_2SO_4 , and the solvent was removed. A yellow oil was obtained and used without any further purification. Yield: 12.45 g, 93%.

^1H NMR (400 MHz, CDCl_3): δ : 7.70 (tt, $J = 5.2, 3.0$ Hz, 1H), 7.33 (dt, $J = 4.8, 2.9$ Hz, 1H), 7.29-7.23 (m, 1H), 1.76-1.48 (m, 8H), 1.48-1.30 (m, 8H), 1.29-1.06 (m, 7H), 0.96 (tt, $J = 7.2, 2.0$ Hz, 9H).

^{13}C NMR (100 MHz, CDCl_3): δ : 136.0, 135.0, 130.4, 127.7, 28.8, 27.1, 13.5, 10.7.

5.4.1.2 Synthesis of 4-(thiophen-2-yl)benzonitrile (15)

Under Ar atmosphere, 4-bromobenzonitrile (0.5 g, 2.75 mmol) and $(\text{PPh}_3)_4\text{PdCl}_2$ (40 mg) were dissolved in dry THF (10 mL). Compound **14** (1.25 g, 3.3 mmol) was added. TLC controlled reaction mixture was heated to 65 °C and allowed to stir for 16 h under reflux. Following cooling down to the ambient temperature, the mixture was extracted with DCM, and collected organic layers were washed with brine and dried over Mg_2SO_4 . The solvent was removed, and the crude product was purified on silica gel (SiO_2 , hexane: dichloromethane, 1:1). A white powder was obtained. Yield: 0.38 g, 75%.

^1H NMR (400 MHz, CDCl_3): δ : 7.79-7.58 (m, 4H), 7.50-7.40 (m, 2H), 7.40 (s, 1H), 7.12 (ddd, $J = 8.9, 5.1, 3.6$ Hz, 1H).

^{13}C NMR (100 MHz, CDCl_3): δ : 141.9, 138.5, 132.6, 128.4, 126.9, 125.9, 125.0, 118.7, 110.4.

5.4.1.3 Synthesis of 4-(selenophen-2-yl)benzonitrile (16)

4-Bromobenzonitrile (0.5 g, 2.75 mmol) and $(\text{PPh}_3)_4\text{PdCl}_2$ (40 mg) were dissolved in dry THF (10 mL) under an Ar atmosphere. Compound **5** (tributyl(selenophen-2-yl)stannane) (1.4 g, 3.3 mmol) was added slowly. The reaction mixture was heated to 65 °C and allowed to stir for 16 h under reflux. TLC controlled reaction was cooled to the ambient temperature, and the mixture was extracted with DCM. Collected organic layers were washed with brine and dried over Mg_2SO_4 . The solvent was removed under reduced pressure, and the crude product was purified on silica gel (SiO_2 , hexane: dichloromethane, 1:1). Yield: 0.6 g, 93%.

^1H NMR (400 MHz, CDCl_3): δ : 8.08 (dd, $J = 5.5, 1.1$ Hz, 2H), 7.64 (s, 3H), 7.59 (dd, $J = 3.9, 1.1$ Hz, 1H), 7.37 (dd, $J = 5.6, 3.9$ Hz, 1H).

^{13}C NMR (100 MHz, CDCl_3): δ : 148.1, 140.5, 132.6, 132.4, 130.9, 127.3, 126.4, 118.7, 110.4.

5.4.1.4 Synthesis of 4-(furan-2-yl)benzonitrile (17)

Under Ar atmosphere, in a 50 mL Schlenk tube, 4-bromobenzonitrile (0.43 g, 2.33 mmol) and $\text{Pd}(\text{PPh}_3)_4$ (0.19 mg) were dissolved in dry toluene (20 mL). At 50 °C, compound **6** (tributyl(furan-2-yl)stannane) (1.0 g, 2.8 mmol) was added slowly. The reaction mixture was heated to reflux temperature and allowed to stir overnight. Following cooling to the ambient temperature, the solvent was removed, and the crude product was eluted through silica gel (SiO_2 , hexane: DCM, 1:1). Yield: 0.37 g, 94%.

^1H NMR (400 MHz, CDCl_3): δ : 7.74 (dt, $J = 8.4, 1.9$ Hz, 2H), 7.66 (dt, $J = 8.4, 1.9$ Hz, 2H), 7.54 (q, $J = 2.1$ Hz, 1H), 6.82 (dt, $J = 3.7, 2.2$ Hz, 1H), 6.53 (dq, $J = 3.5, 2.0$ Hz, 1H).

^{13}C NMR (100 MHz, CDCl_3): δ : 150.9, 143.5, 134.5, 132.4, 123.8, 118.8, 112.1, 110.1, 108.0.

5.4.1.5 Synthesis of (4-(thiophen-2-yl)phenyl)methanamine (18)

Under Ar atmosphere, compound **15** (0.34 g, 1.48 mmol) was dissolved in dry THF (10 mL). LiAlH₄ (0.21 g, 5.5 mmol) was added slowly. The temperature of the reaction mixture was raised to 50°C, and the mixture was allowed to stir overnight. Following cooling down to the ambient temperature, saturated Na₂SO₄ was added to the mixture until no bubbles were observed. The solution was washed with Et₂O several times, and the filtrate was dried over Na₂SO₄. The solvent was removed under reduced pressure, and the product was used without any other purification.

5.4.1.6 Synthesis of (4-(selenophen-2-yl)phenyl)methanamine (19)

Under Ar atmosphere, compound **16** (0.2 g, 0.86 mmol) was dissolved in dry THF (10 mL), and to this solution was added LiAlH₄ (0.1 g, 2.6 mmol). At 50°C. The reaction mixture was allowed to stir overnight. The same procedure in the preparation of compound 21 was followed.

5.4.1.7 Synthesis of (4-(furan-2-yl)phenyl)methanamine (20)

The same procedure in the preparation of compound **18** was followed with compound **17** (0.3 g, 1.77 mmol) and LiAlH₄ (0.25 g, 6.39 mmol).

5.4.1.8 Synthesis (4-(thiophen-2-yl)phenyl)methanaminium iodide (21)

At 0 °C, compound **18** (1.5 g, 7.9 mmol) was dissolved in EtOH (50 mL). HI (57 wt% in water) (1.25 mL) was added slowly. The reaction mixture was allowed to stir for 1 h, and the solvent was removed. The precipitate was dissolved in EtOH and recrystallized by slow addition of Et₂O. Obtained crystals were filtered and washed with cold Et₂O several times, followed by drying under vacuum overnight.

Yield: 1.5 g, 60%.

¹H NMR (400 MHz, DMSO-d₆): δ: 8.13 (s, 3H), 7.73 (d, *J* = 8.2 Hz, 2H), 7.58 (t, *J* = 4.0 Hz, 2H), 7.49 (d, *J* = 8.0 Hz, 2H), 7.16 (dd, *J* = 5.0, 3.7 Hz, 1H), 4.06 (q, *J* = 5.6 Hz, 2H).

¹³C NMR (100 MHz, DMSO-d₆): δ: 142.9, 130.0, 128.9, 126.4, 125.8, 124.5, 42.2.

5.4.1.9 Synthesis of (4-(selenophen-2-yl)phenyl)methanaminium iodide (22)

Under Ar atmosphere, compound **19** (0.55 g, 2.35 mmol) was dissolved in EtOH (mL). Following the addition of HI (57 wt% in water) (0.4 mL), the reaction mixture was allowed to stir for 1 h. The same procedure in the preparation of compound **24** was followed.

Yield: 0.47 g, 62%.

¹H NMR (400 MHz, DMSO-d₆): δ: 8.17 (d, *J* = 5.6 Hz, 1H), 8.13 (s, 3H), 7.74-7.65 (m, 3H), 7.47 (d, *J* = 8.0 Hz, 2H), 7.36 (dd, *J* = 5.6, 3.8 Hz, 1H), 4.06 (t, *J* = 5.4 Hz, 2H).

¹³C NMR (100 MHz, DMSO-d₆): δ: 131.8, 131.2, 130.0, 126.5, 126.3, 124.9, 42.2.

5.4.1.10 Synthesis of (4-(furan-2-yl)phenyl)methanaminium iodide (23)

The same procedure in the preparation of compound **22** was followed with compound **20** (0.24 g, 1.4 mmol) and HI (57 wt% in water) (0.25 mL).

Yield: 0.25 g, 59%.

¹H NMR (400 MHz, DMSO-d₆): δ: 8.13 (s, 3H), 7.76 (d, *J* = 7.7 Hz, 2H), 7.51 (d, *J* = 8.0 Hz, 2H), 7.01 (d, *J* = 3.4 Hz, 1H), 6.62 (p, *J* = 2.7 Hz, 2H), 4.06 (d, *J* = 5.5 Hz, 2H).

¹³C NMR (100 MHz, DMSO-d₆): δ: 152.8, 143.5, 133.2, 130.7, 129.8, 123.8, 112.5, 106.8, 42.3.

5.4.2 Experimental and results

In order to fabricate perovskite solar cells, a glass substrate coated ITO was employed. Onto ITO layer SnO_2 was coated, and the perovskite layer was prepared onto this layer. The organic cations are coated between the perovskite layer and a spiro compound (Spiro OMeTAD) employed as electron transport layer (ETL). Finally, Ag was evaporated as the cathode. The architecture of the devices is illustrated in Figure 5.3.

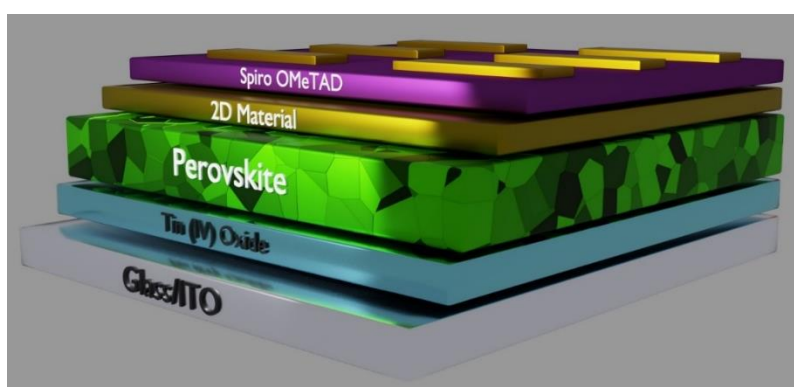


Figure 5.3. Structure of the devices fabricated in this study

A detailed methodology for the preparation of the perovskite layer and the fabrication of devices are illustrated in Figure 5.4.

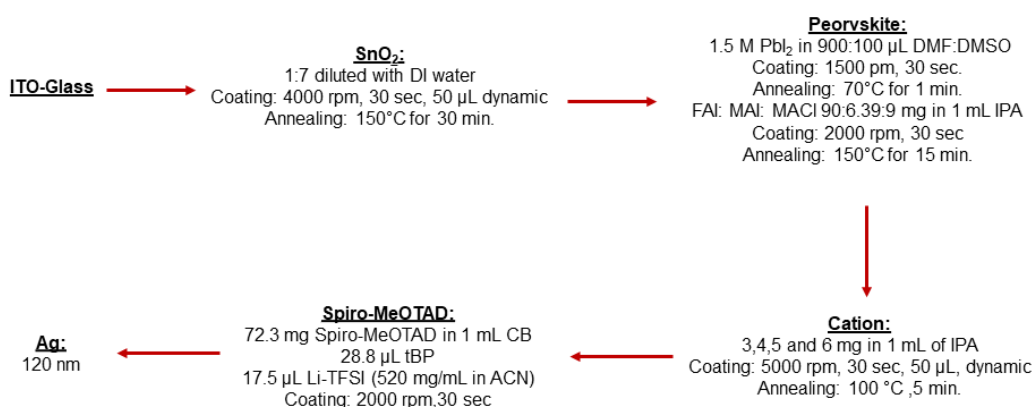


Figure 5.4. Methodology of device fabrication

Solutions of compound **21** were prepared in various concentrations (3 mg.mL⁻¹, 4 mg.mL⁻¹, 5 mg.mL⁻¹, and 6 mg.mL⁻¹). The average device parameters are shown in Table 5.1. Preliminary results showed that the best PCE (22.43%) was obtained from compound **21**, 5 mg.mL⁻¹. As the concentration increased, PCE decreased due to low FF.

Table 5.1 Photovoltaic parameters of compound **21** containing devices with different concentrations

Device parameters	V _{oc} (V)	J _{sc} (mA.cm ⁻²)	FF (%)	PCE (%)
Reference	1.09	22.67	82.78	20.46
Comp. 21 , 3 mg.mL ⁻¹	1.14	22.48	81.76	21.33
Comp. 21 , 4 mg.mL ⁻¹	1.15	22.75	80.98	21.19
Comp. 21 , 5 mg.mL ⁻¹	1.16	24.15	80.06	22.43
Comp. 21 , 6 mg.mL ⁻¹	1.16	22.45	77.13	20.09

The highest PCE was achieved by compound **21**, 5 mg.mL⁻¹ (22.43%). J_{SC} was obtained as 24.15 mA.cm⁻² from J-V measurement, and its integrated J_{SC} (by EQE) was measured 22.78 mA.cm⁻². For the reference device, the highest PCE was 20.46% with a J_{SC} of 22.67 mA.cm⁻², and its integrated J_{SC} was calculated as 21.65 mA.cm⁻² from the EQE measurements.

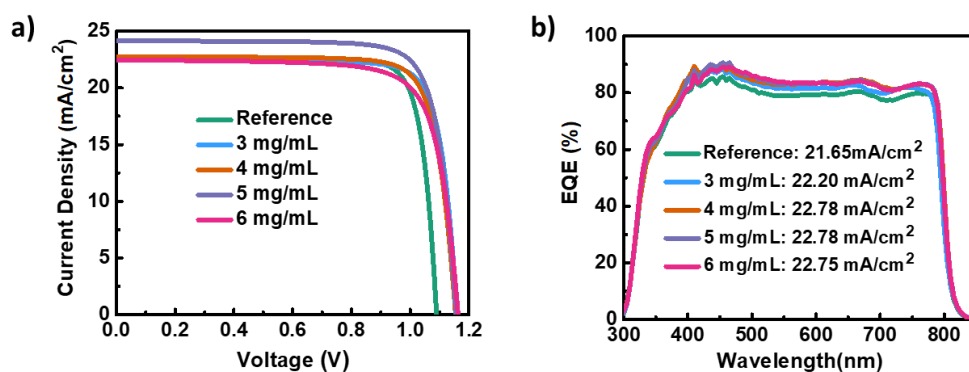


Figure 5.5. Photovoltaic parameters of compound **21** containing devices with different concentrations (a) J-V, (b) EQE

5.5 Syntheses of aniline-based organic halide cations

In this section, organic halide cations containing aniline and chalcogenophene (thiophene, selenophene) were synthesized. Figure 5.6 represents the synthetic routes for each compound. Compounds **28** and **29** will be employed for the treatment of 3D perovskite films.

5.5.1 Synthesis

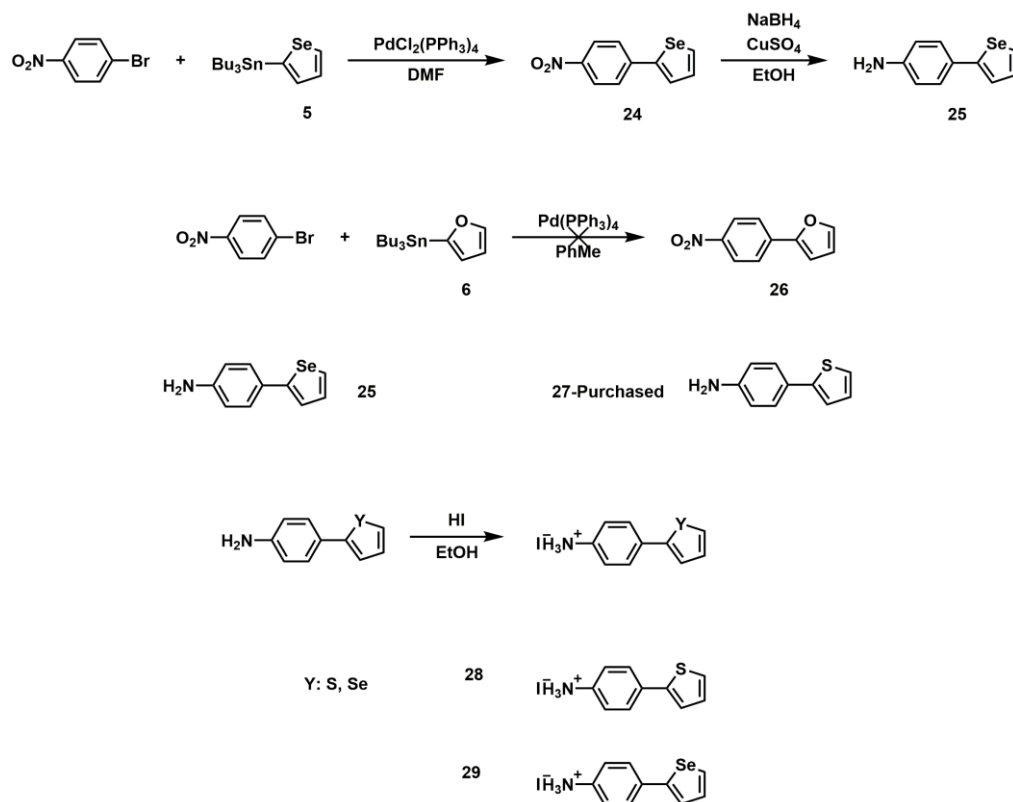


Figure 5.6. Synthetic routes for the compounds **28** and **29**

5.5.1.1 Synthesis of 2-(4-nitrophenyl)selenophene (**24**)

Under Ar atmosphere, 1-bromo-4-nitrobenzene (1 g, 5.8 mmol), compound **5** (2.1 g, 5.0 mmol), and $\text{PdCl}_2(\text{PPh}_3)_2$ (0.12 g, 0.16 mmol) were dissolved in dry DMF (10 mL). the reaction mixture was allowed to stir for 24 h at 90 °C. The reaction was quenched with MeOH and saturated KF solution, followed by cooling down the reaction mixture to the ambient temperature. Organic layers were extracted with DCM and dried over Mg_2SO_4 . The solvent was removed under reduced pressure. The desired product was obtained via purification with column chromatography (SiO_2 , DCM: hexane, 1:3). Yield: 0.9 g, 61%.

^1H NMR (400 MHz, CHCl_3): δ : 8.22 (d, J = 8.9 Hz, 2H), 8.12 (d, J = 5.5 Hz, 1H), 7.71 – 7.62 (m, 3H), 7.39 (t, J = 4.7 Hz, 1H).

^{13}C NMR (100 MHz, CHCl_3): δ : 147.62, 146.52, 142.44, 133.17, 131.06, 127.95, 126.43, 124.32.

5.5.1.2 Synthesis of 4-(selenophen-2-yl)aniline (25)

Compound **24** (0.5, 1.98 mmol) was dissolved in ethanol, and CuSO_4 (20 mg, 2 M in water) was added. The temperature of the reaction mixture was decreased to 0 °C, and NaBH_4 (30 mg, 0.08 mmol) was added portion-wise. The TLC-controlled reaction was allowed to stir under ambient conditions. The mixture was diluted with ethyl acetate, washed with distilled water, and dried over Mg_2SO_4 . The solvent was removed under reduced pressure, and the obtained product was used without further purification. Yield: 0.43 g, 97%.

5.5.1.3 Synthesis of 4-(thiophen-2-yl)benzenaminium iodide (28)

HI (57 wt% in water) (1.72 mmol) was added to the solution of 4-(thiophen-2-yl)aniline (0.25 g, 1.43 mmol) in ethanol (10 mL) at 0 °C. The reaction mixture was stirred for 4 h at 0 °C. The solvent was removed under reduced pressure, and the crude product was recrystallized in diethyl ether. The product was further washed with cold diethyl ether two times. The final product was dried under reduced pressure and obtained as a yellowish powder. Yield: 0.35 g, 81%.

^1H NMR (400 MHz, DMSO-d_6): δ : 7.74 (d, J = 8.55, 2H), 7.58 (d, J = 5.07 Hz, 1H), 7.53 (d, J = 3.61 Hz, 1H), 7.30 (d, J = 8.54 Hz, 2H), 7.15 (dd, J = 8.55 Hz, 1H).

^{13}C NMR (100 MHz, DMSO-d_6): δ : 128.60, 127.75, 126.57, 126.07, 124.93, 124.11-124.05, 122.85-122.77, 118.14.

5.5.1.4 Synthesis of 4-(selenophen-2-yl)benzenaminium iodide (29)

To a solution of compound **25** (0.4 g, 1.8 mmol) in EtOH (10 mL), HI (57% in water) (2.17 mmol) was added at 0 °C. The reaction mixture was allowed to stir for 3 hours at the same temperature. The solvent was removed, and the crude product was precipitated in cold Et₂O. The final product was further washed with cold Et₂O several times and dried under vacuum. A yellow powder was obtained. Yield: 0.28 g, 45%.

¹H NMR (400 MHz, CDCl₃) δ: 8.28 – 8.19 (m, 2H), 8.12 (dd, *J* = 5.6, 1.1 Hz, 1H), 7.70 (d, *J* = 2.0 Hz, 2H), 7.68 (d, *J* = 2.1 Hz, 1H), 7.39 (dd, *J* = 5.6, 3.9 Hz, 1H), 3.29 (s, 3H).

¹³C NMR (100 MHz, CDCl₃): δ: 147.60, 142.45, 133.10, 131.0, 127.90, 126.40, 124.30.

5.6 Synthesis of pyridine-based organic halide cation

In this section, an organic halide cation containing pyridine and thiophene was synthesized. Figure 5.7 represents the synthetic routes for each compound. These molecules will be employed for the treatment of 3D perovskite films.

5.6.1 Synthesis

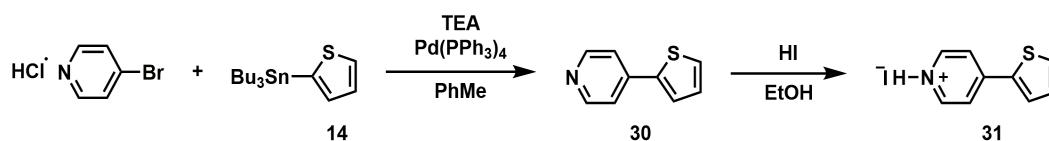


Figure 5.7. Synthetic route for the compound 31

5.6.1.1 Synthesis of 4-(thiophen-2-yl)pyridine (30)

Under Ar atmosphere, 4-bromopyridine hydrochloride (0.5 g, 2.57 mmol) and trimethylamine (0.4 mL) were introduced to a 50 mL Schlenk tube charged with a magnetic stir bar. Dry toluene (15 mL) was added. To this mixture, Pd(PPh₃)₄ (0.3 g, 10% mol) was added. The reaction mixture was allowed to stir for 30 minutes at the ambient temperature, and compound **14** (1.0 g, 2.83 mmol) was added. The reaction mixture was stirred for an additional 30 minutes at the ambient temperature, and the temperature was set to 110 °C. After 30 h, the reaction mixture was cooled down to the ambient temperature and filtered through celite pad. The desired product was obtained from column chromatography (SiO₂, 3% triethyl amine in hexane: ethyl acetate, 1:1). Yield: 0.375 g, 82%.

¹H NMR (400 MHz, CDCl₃): δ: 8.58 (d, *J* = 6.1 Hz, 2H), 7.67 (m, 2H), 7.53 (m, 1H), 7.30 (m, 1H), 7.14 (m, 1H).

¹³C NMR (100 MHz, CDCl₃): δ: 149, 132, 128.4, 127.13, 125.26, 119.59.

5.6.1.2 Synthesis of 4-(thiophen-2-yl)pyridin-1-ium iodide (31)

Compound **30** (0.375 g, 2.3 mmol) was dissolved in EtOH (10 mL) at 0 °C. To this solution, HI (57% in water) (2.8 mmol) was added. The reaction mixture was allowed to stir for 4 hours at the same temperature. The solvent was removed under reduced pressure, and the crude product was precipitated in cold Et₂O. The product was filtered and further washed with Et₂O several times. The product was dried under a vacuum. Yield: 0.18 g, 67%.

¹H NMR (400 MHz, DMSO-d₆): δ: 8.84 (m, 2H), 8.26 (m, 3H), 8.1 (m, 1H), 7.38 (m, 1H).

¹³C NMR (100 MHz, DMSO-d₆): δ: 143, 137.9, 134.1, 131.9, 130.3, 121.8.

CHAPTER 6

OUTLOOK

This thesis reports the design, synthesis, characterization, and optoelectronic applications of thienopyrroledione (TPD)-based conjugated polymers and organic cations. The first chapter provides a brief introduction for CPs, including preparation of CPs and application areas. Although several preparation methods for CPs, Stille Polycondensation, Suzuki Polycondensation, and Direct Heteroarylation Polymerization techniques, are shortly reviewed in the first chapter. In addition, application areas of CPs like OSCs, biosensors, and electrochromism are briefly reviewed in the first chapter.

The second chapter of the thesis focuses on the design, synthesis, characterization, and NFA OSCs applications of TPD-based random conjugated polymers. For this study, eight new random conjugated polymers (ME1-ME8) were designed and synthesized to be employed as donor materials. In the first part of the chapter, investigations of the effect of alkyl chains on the performance of NFA OSCs were reported along with the effect of different chalcogenophenes, and this part of the chapter was partially published in *Renewable Energy*. Although the main aim was to fabricate NFA OSCs, for comparison, the polymers were blended with PC₇₁BM as well. In the second part of the chapter, two different random polymers (ME5 and ME6) were to be employed as donor materials in the fabrication of OSCs. However, we were able to process only ME6 due to the solubility problems of ME5. ME6 was blended with both PC₇₁BM and ITIC to fabricate OSCs, and preliminary results are included. For the last part of the chapter, two random conjugated polymers (ME7 and ME8) were studied. The chapter consists of only synthesis, electrochemical, and spectroelectrochemical investigations for these polymers. As a post-study, OSC fabrications will be performed.

The third chapter of the thesis reveals our findings on the fabrication of an amperometric biosensor modified with CDs and a TPD-based conjugated polymer. The construction of the biosensor by laccase immobilization onto the modified electrode via physical adsorption technique was reported. The enzyme-based biosensor was optimized in terms of the amount of CDs, amount of the employed conjugated polymer, the enzyme unit, and pH. The biosensor exhibited linearity between 1.25 and 1.75 μM catechol, with a limit of detection (LOD) of 1.23 μM and sensitivity of 737.4 $\mu\text{A} \cdot \text{mM}^{-1} \cdot \text{cm}^{-2}$. This study was published in Journal of Polymer Science.

In the fourth chapter of the thesis, the effect of random polymerization on the optoelectronic properties of a series of conjugated polymers obtained via Suzuki Polycondensation is investigated. The study revealed that the introduction of selenophene as a π -spacer leads to redshift in absorbance, decreasing the polymers' optical band gaps. The effect of the introduction of a second TPD to the polymer backbones was also investigated and explained with a synthetic approach.

The final and last chapter of the thesis focuses on the syntheses and utilization of phenylmethanamine, aniline, and pyridine-containing organic cations to treat 3D perovskite layers. One of the phenylmethanamine-based organic cations (Compound **21**) was employed to treat 3D perovskite layers. The maximum PCE value obtained from the perovskite solar cells was found as 22.43%. Other organic cations will be utilized for the same purpose as a post-study.

REFERENCES

1. Li, Z., Chueh, C. C. & Jen, A. K. Y. Recent advances in molecular design of functional conjugated polymers for high-performance polymer solar cells. *Prog. Polym. Sci.* **99**, (2019).
2. Chiang, C. K. *et al.* Electrical conductivity in doped polyacetylene. *Phys. Rev. Lett.* **39**, 1098–1101 (1977).
3. Burroughes, J.H., Bradley, D.D.C., Brown, A.R., Marks, R.N., Mackay, K., Friend, R.H., Burn, P.L., Holmes, A. B. *et al.* Light-emitting diodes based on conjugated polymers. *Nature* **347**, 539–541 (1990).
4. Zhang, Z. *et al.* Conjugated Polymers for Flexible Energy Harvesting and Storage. *Adv. Mater.* **30**, 1–19 (2018).
5. Dai, C. & Liu, B. Conjugated polymers for visible-light-driven photocatalysis. *Energy Environ. Sci.* **13**, 24–52 (2020).
6. Bredas, J. L. & Street, G. B. Polarons, Bipolarons, and Solitons in Conducting Polymers. *Acc. Chem. Res.* **18**, 309–315 (1985).
7. An, Y. *et al.* Effects of incorporating different chalcogenophene comonomers into random acceptor terpolymers on the morphology and performance of all-polymer solar cells. *Polym. Chem.* **9**, 593–602 (2018).
8. Han, Y. *et al.* Tuning Nonlinear Optical Behavior by Incorporation of the Chalcogenophene into Twistacenes. *J. Phys. Chem. B* **124**, 10766–10775 (2020).
9. Liu, Y., Zhan, X. & Leu, Y. High-mobility conjugated polymers based on fused-thiophene building blocks. *Macromol. Chem. Phys.* **212**, 428–443 (2011).
10. Adachi, Y., Arai, F., Sakabe, M. & Ohshita, J. Effect of the conjugation

pathway on the electronic structures of p- π^* conjugated polymers with fused borepin units. *Polym. Chem.* **12**, 3471–3477 (2021).

11. Cevher, S. C. *et al.* Fused structures in the polymer backbone to investigate the photovoltaic and electrochromic properties of donor-acceptor-type conjugated polymers. *J. Polym. Sci. Part A Polym. Chem.* **51**, 1933–1941 (2013).
12. Huang, H. *et al.* Unprecedented side reactions in Stille coupling: Desired ones for Stille polycondensation. *Chem. Commun.* **51**, 15846–15849 (2015).
13. Shin, W., Ko, W., Jin, S., Earmme, T. & Hwang, Y. Reproducible and rapid synthesis of a conjugated polymer by Stille polycondensation in flow : Effects of reaction parameters on molecular weight. *Chem. Eng. J.* **412**, 128572 (2021).
14. Lee, S. M., Park, K. H., Jung, S., Park, H. & Yang, C. Stepwise heating in Stille polycondensation toward no batch-to-batch variations in polymer solar cell performance. *Nat. Commun.* **9**, (2018).
15. Milstein, D. & Stille, J. K. A General, Selective, and Facile Method for Ketone Synthesis from Acid Chlorides and Organotin Compounds Catalyzed by Palladium. *Journal of the American Chemical Society* vol. 100 3636–3638 (1978).
16. Stille, J. K. The Palladium- Catalyzed Cross- Coupling Reactions of Organotin Reagents with Organic Electrophiles. *Angewandte Chemie International Edition in English* vol. 25 508–524 (1986).
17. Carsten, B., He, F., Son, H. J., Xu, T. & Yu, L. Stille polycondensation for synthesis of functional materials. *Chem. Rev.* **111**, 1493–1528 (2011).
18. Miyaura, N. & Suzuki, A. Palladium-Catalyzed Cross-Coupling Reactions of Organoboron Compounds. *Chem. Rev.* **95**, 2457–2483 (1995).
19. Hardeman, T., Van Den Eede, M. P., Verheyen, L. & Koeckelberghs, G.

Synthetic Methods for Conjugated Polymers and Carbon Materials. (Wiley-WCH, 2017).

20. Mercier, L. G. & Leclerc, M. Direct (hetero)arylation: A new tool for polymer chemists. *Acc. Chem. Res.* **46**, 1597–1605 (2013).
21. Pouliot, J. R., Grenier, F., Blaskovits, J. T., Beaupré, S. & Leclerc, M. Direct (Hetero)arylation Polymerization: Simplicity for Conjugated Polymer Synthesis. *Chem. Rev.* **116**, 14225–14274 (2016).
22. Bura, T., Blaskovits, J. T. & Leclerc, M. Direct (Hetero)arylation Polymerization: Trends and Perspectives. *J. Am. Chem. Soc.* **138**, 10056–10071 (2016).
23. Yu, S. *et al.* Eco-friendly direct (hetero)-arylation polymerization: scope and limitation. *J. Mater. Chem. C* **5**, 29–40 (2017).
24. Blaskovits, J. T., Johnson, P. A. & Leclerc, M. Mechanistic Origin of β -Defect Formation in Thiophene-Based Polymers Prepared by Direct (Hetero)arylation. *Macromolecules* **51**, 8100–8113 (2018).
25. Tang, C. W. Two-layer organic photovoltaic cell. *Appl. Phys. Lett.* **48**, 183–185 (1986).
26. Jin, K., Xiao, Z. & Ding, L. 18.69% PCE from organic solar cells. *J. Semicond.* **42**, (2021).
27. Yu, G., Gao, J., Hummelen, J. C., Wudl, F. & Heeger, A. J. Polymer photovoltaic cells: Enhanced efficiencies via a network of internal donor-acceptor heterojunctions. *Science (80-.)*. **270**, 1789 (1995).
28. Piralaee, M. & Asgari, A. Bimetallic core-shell nanoparticles to improve the absorption of P3HT: PCBM organic solar cell. *Appl. Opt.* **60**, 9087 (2021).
29. Ghazy, O., Freisinger, B., Lieberwith, I. & Landfester, K. Tuning the size and morphology of P3HT/PCBM composite nanoparticles: Towards optimized

- water-processable organic solar cells. *Nanoscale* **12**, 22798–22807 (2020).
30. Koul, S. & Hakim, N. ud din. Investigation of Non-ideality Factors for a P3HT: PCBM Based Bulk Heterojunction Organic Solar Cell in Presence of Silver Nanoparticles. *Trans. Electr. Electron. Mater.* **21**, 293–304 (2020).
 31. Zidan, M. N., Ismail, T. & Fahim, I. S. Effect of thickness and temperature on flexible organic P3HT:PCBM solar cell performance. *Mater. Res. Express* **8**, (2021).
 32. Abdallaoui, M., Sengouga, N., Chala, A., Meftah, A. F. & Meftah, A. M. Comparative study of conventional and inverted P3HT: PCBM organic solar cell. *Opt. Mater. (Amst)*. **105**, 109916 (2020).
 33. Chen, F. C., Ko, C. J., Wu, J. L. & Chen, W. C. Morphological study of P3HT:PCBM blend films prepared through solvent annealing for solar cell applications. *Sol. Energy Mater. Sol. Cells* **94**, 2426–2430 (2010).
 34. Schafferhans, J., Baumann, A., Wagenpfahl, A., Deibel, C. & Dyakonov, V. Oxygen doping of P3HT:PCBM blends: Influence on trap states, charge carrier mobility and solar cell performance. *Org. Electron.* **11**, 1693–1700 (2010).
 35. Ismail, Y. A. M., Soga, T. & Jimbo, T. Improvement in light harvesting and performance of P3HT:PCBM solar cell by using 9,10-diphenylanthracene. *Sol. Energy Mater. Sol. Cells* **93**, 1582–1586 (2009).
 36. Halls, J. J. M., Pichler, K., Friend, R. H., Moratti, S. C. & Holmes, A. B. Exciton diffusion and dissociation in a poly(p-phenylenevinylene)/C60 heterojunction photovoltaic cell. *Appl. Phys. Lett.* **68**, 3120–3122 (1996).
 37. Nunzi, J. M. Organic photovoltaic materials and devices. *Comptes Rendus Phys.* **3**, 523–542 (2002).
 38. Gu, S., Neugebauer, H. & Sariciftci, N. S. Conjugated Polymer-Based Organic Solar Cells. *Chem. Rev.* 1324–1338 (2007) doi:10.1021/cr050149z.

39. Lin, Y. *et al.* Self-assembled monolayer enables hole transport layer-free organic solar cells with 18% efficiency and improved operational stability. *ACS Energy Lett.* **5**, 2935–2944 (2020).
40. Lu, W. *et al.* Hole transport layer free bulk heterojunction organic solar cells with high work function ITO anodes. *AIP Adv.* **8**, (2018).
41. Wang, D. H., Kyaw, A. K. K., Gupta, V., Bazan, G. C. & Heeger, A. J. Enhanced efficiency parameters of solution-processable small-molecule solar cells depending on ito sheet resistance. *Adv. Energy Mater.* **3**, 1161–1165 (2013).
42. Kanwat, A., Milne, W. & Jang, J. Solar Energy Materials & Solar Cells Vertical phase separation of PSS in organic photovoltaics with a nickel oxide doped PEDOT : PSS interlayer. *Sol. Energy Mater. Sol. Cells* **132**, 623–631 (2015).
43. Kim, J. K. *et al.* Enhanced performance and stability of polymer BHJ photovoltaic devices from dry transfer of PEDOT:PSS. *ChemSusChem* **7**, 1957–1963 (2014).
44. Lin, Y. *et al.* 17% Efficient Organic Solar Cells Based on Liquid Exfoliated WS₂ as a Replacement for PEDOT:PSS. *Adv. Mater.* **31**, (2019).
45. Zhang, W. *et al.* Isopropanol-treated PEDOT : PSS as electron transport layer in polymer solar cells. *Org. Electron.* **15**, 3445–3451 (2014).
46. Cheng, J. *et al.* Intensification of Vertical Phase Separation for Efficient Polymer Solar Cell via Piecewise Spray Assisted by a Solvent Driving Force. *Sol. RRL* **4**, 1–11 (2020).
47. Zhao, H. *et al.* Solvent-Vapor-Annealing-Induced Interfacial Self-Assembly for Simplified One-Step Spraying Organic Solar Cells. *ACS Appl. Energy Mater.* **4**, 7316–7326 (2021).
48. Xiao, Y. *et al.* Large-Area Blade-Coated Solar Cells: Advances and

Perspectives. *Advanced Energy Materials* vol. 11 1–20 (2021).

49. Reshma, L., Ramaraj, B., Shin, P. K. & Santhakumar, K. Spray-coated high-efficiency small molecule solar cell based on DTS[PTTH2]2: PC71BM configurations through integrated molecular and solvent engineering. *J. Mater. Sci. Mater. Electron.* **32**, 5965–5977 (2021).
50. Yuan, J. *et al.* Patterned Blade Coating Strategy Enables the Enhanced Device Reproducibility and Optimized Morphology of Organic Solar Cells. *Adv. Energy Mater.* **11**, 1–10 (2021).
51. Page, Z. A., Liu, Y., Duzhko, V. V, Russell, T. P. & Emrick, T. Fulleropyrrolidine interlayers: Tailoring electrodes to raise organic solar cell efficiency. *Science* (80-.). **346**, 441–444 (2014).
52. Vivo, P., Jukola, J., Ojala, M., Chukharev, V. & Lemmetyinen, H. Influence of Alq3/Au cathode on stability and efficiency of a layered organic solar cell in air. *Sol. Energy Mater. Sol. Cells* **92**, 1416–1420 (2008).
53. Pandey, A. K., Shaw, P. E., Samuel, I. D. W. & Nunzi, J. M. Effect of metal cathode reflectance on the exciton-dissociation efficiency in heterojunction organic solar cells. *Appl. Phys. Lett.* **94**, 1–4 (2009).
54. Yang, L., Zhou, H. & You, W. Quantitatively analyzing the influence of side chains on photovoltaic properties of polymer-fullerene solar cells. *J. Phys. Chem. C* **114**, 16793–16800 (2010).
55. Scharber, M. C. *et al.* Design rules for donors in bulk-heterojunction solar cells - Towards 10 % energy-conversion efficiency. *Adv. Mater.* **18**, 789–794 (2006).
56. Zhou, H., Yang, L. & You, W. Rational design of high performance conjugated polymers for organic solar cells. *Macromolecules* vol. 45 607–632 (2012).
57. Sathiyar, G., Sivakumar, E. K. T., Ganesamoorthy, R., Thangamuthu, R. &

- Sakthivel, P. Review of carbazole based conjugated molecules for highly efficient organic solar cell application. *Tetrahedron Lett.* **57**, 243–252 (2016).
58. Qi, B. & Wang, J. Fill factor in organic solar cells. *Phys. Chem. Chem. Phys.* **15**, 8972–8982 (2013).
 59. Karim, F. & Fakhruddin, A. N. M. Recent advances in the development of biosensor for phenol: A review. *Rev. Environ. Sci. Biotechnol.* **11**, 261–274 (2012).
 60. Goode, J. A., Rushworth, J. V. H. & Millner, P. A. Biosensor Regeneration: A Review of Common Techniques and Outcomes. *Langmuir* **31**, 6267–6276 (2015).
 61. Wang, J. Electrochemical biosensors: Towards point-of-care cancer diagnostics. *Biosens. Bioelectron.* **21**, 1887–1892 (2006).
 62. Lei, Y., Chen, W. & Mulchandani, A. Microbial biosensors. *Anal. Chim. Acta* **568**, 200–210 (2006).
 63. Kapan, B., Kurbanoglu, S., Esenturk, E. N., Soylemez, S. & Toppare, L. Electrochemical catechol biosensor based on β -cyclodextrin capped gold nanoparticles and inhibition effect of ibuprofen. *Process Biochem.* **108**, 80–89 (2021).
 64. Wang, C. *et al.* A Dual Antibody-modified Nanochannel Biosensor for Capture and Identification of Exosomes. *Sensors Actuators, B Chem.* **314**, (2020).
 65. Clark, L. C., Kaplan, S., Matthews, E. C., Edwards, F. K. & Helmsworth, J. A. Monitor and control of blood oxygen tension and pH during total body perfusion. *J. Thorac. Surg.* **36**, 488–496 (1958).
 66. Sharma, S. K., Sehgal, N. & Kumar, A. Biomolecules for development of biosensors and their applications. *Curr. Appl. Phys.* **3**, 307–316 (2003).

67. Daniel, R. T., Toth K., Durst, R. A., Wilson, G. S. Electrochemical Biosensors: Recommended Definitions and Classification. *Pure Appl. Chem.* **41**, 655–657 (1987).
68. Inshyna, N. M., Chorna, I. V., Primova, L. O., Hrebenyk, L. I. & Khyzhnia, Y. V. Biosensors: Design, classification and application. *J. Nano- Electron. Phys.* **12**, 1–9 (2020).
69. Davis, G. Electrochemical techniques for the development of amperometric biosensors. *Biosensors* **1**, 161–178 (1985).
70. Sadeghi, S. J. *Encyclopedia of Biophysics. Encyclopedia of Biophysics* (Springer, Berlin, Heidelberg, 2013). doi:10.1007/978-3-642-16712-6.
71. Evans, R. J. *Encyclopedia of Biophysics. Encyclopedia of Biophysics* (New York, NY: Springer, 2013). doi:10.1007/978-3-642-16712-6.
72. Thévenot, D. R., Toth, K., Durst, R. A. & Wilson, G. S. Electrochemical biosensors: Recommended definitions and classification. *Biosens. Bioelectron.* **16**, 121–131 (2001).
73. D’Orazio, P. Biosensors in clinical chemistry. *Clin. Chim. Acta* **334**, 41–69 (2003).
74. Grieshaber, D., MacKenzie, R., Vörös, J. & Reimhult, E. Electrochemical biosensors - Sensor principles and architectures. *Sensors* **8**, 1400–1458 (2008).
75. Newman, J. D. & Setford, S. J. Enzymatic biosensors. *Molecular Biotechnology* vol. 32 249–268 (2006).
76. Zhao, W., Xu, J. & Chen, H. Biosensors and Bioelectronics Photoelectrochemical enzymatic biosensors. *Biosens. Bioelectron.* **92**, 294–304 (2017).
77. Sassolas, A., Blum, L. J. & Leca-bouvier, B. D. Immobilization strategies to

- develop enzymatic biosensors. *Biotechnol. Adv.* **30**, 489–511 (2012).
78. Albareda-Sirvent, M., Merkoçi, A. & Alegret, S. Configurations used in the design of screen-printed enzymatic biosensors. A review. *Sensors Actuators, B Chem.* **69**, 153–163 (2000).
 79. Jesionowski, T., Zdarta, J. & Krajewska, B. Enzyme immobilization by adsorption: A review. *Adsorption* vol. 20 801–821 (2014).
 80. Choi, M. M. F. Progress in enzyme-based biosensors using optical transducers. *Microchimica Acta* vol. 148 107–132 (2004).
 81. Barbosa, O. *et al.* Glutaraldehyde in bio-catalysts design: A useful crosslinker and a versatile tool in enzyme immobilization. *RSC Adv.* **4**, 1583–1600 (2014).
 82. Dos Santos, J. C. S. *et al.* Characterization of supports activated with divinyl sulfone as a tool to immobilize and stabilize enzymes via multipoint covalent attachment. Application to chymotrypsin. *RSC Adv.* **5**, 20639–20649 (2015).
 83. Sheldon, R. A., Schoevaart, R. & Van Langen, L. M. Cross-linked enzyme aggregates (CLEAs): A novel and versatile method for enzyme immobilization (a review). *Biocatal. Biotransformation* **23**, 141–147 (2005).
 84. Platt, J. R. Electrochromism, a possible change of color producible in dyes by an electric field. *J. Chem. Phys.* **34**, 862–863 (1961).
 85. Deb, S. K. A Novel Electrophotographic System. *Appl. Opt.* **8**, 192 (1969).
 86. Liang, L. *et al.* High-performance flexible electrochromic device based on facile semiconductor-To-metal transition realized by WO₃·2H₂O ultrathin nanosheets. *Sci. Rep.* **3**, 1–8 (2013).
 87. Besnardiere, J. *et al.* Structure and electrochromism of two-dimensional octahedral molecular sieve h⁺-WO₃. *Nat. Commun.* **10**, 1–9 (2019).
 88. Niklasson, G. A. & Granqvist, C. G. Electrochromics for smart windows: Thin

films of tungsten oxide and nickel oxide, and devices based on these. *J. Mater. Chem.* **17**, 127–156 (2007).

89. Zhang, J., Wang, X. L., Xia, X. H., Gu, C. D. & Tu, J. P. Electrochromic behavior of WO₃ nanotree films prepared by hydrothermal oxidation. *Sol. Energy Mater. Sol. Cells* **95**, 2107–2112 (2011).
90. Deb, S. K. Opportunities and challenges in science and technology of WO₃ for electrochromic and related applications. *Sol. Energy Mater. Sol. Cells* **92**, 245–258 (2008).
91. Kline, W. M., Lorenzini, R. G. & Sotzing, G. A. A review of organic electrochromic fabric devices. *Color. Technol.* **130**, 73–80 (2014).
92. Argun, A. A. *et al.* Multicolored electrochromism in polymers: Structures and devices. *Chem. Mater.* **16**, 4401–4412 (2004).
93. Monk, P. M. S., Rosseinsky, D. R. & Mortimer, R. J. Electrochromic Materials and Devices Based on Viologens. *Electrochromic Mater. Devices* **77**, 57–90 (2015).
94. Zhao, S., Huang, W., Guan, Z., Jin, B. & Xiao, D. A novel bis(dihydroxypropyl) viologen-based all-in-one electrochromic device with high cycling stability and coloration efficiency. *Electrochim. Acta* **298**, 533–540 (2019).
95. Dt, C. The effect of ferrocyanide on the performance of heptyl viologen-based electrochromic display devices. *J. Electroanal. Chem.* **8**, 175–179 (1997).
96. Cinnsealach, R., Boschloo, G., Rao, S. N. & Fitzmaurice, D. Electrochromic windows based on viologen-modified nanostructured TiO₂ films. *Sol. Energy Mater. Sol. Cells* **55**, 215–223 (1998).
97. Madasamy, K., Velayutham, D., Suryanarayanan, V., Kathiresan, M. & Ho, K. C. Viologen-based electrochromic materials and devices. *J. Mater. Chem. C* **7**, 4622–4637 (2019).

98. Granqvist, C. G. Electrochromism and smart window design. *Solid State Ionics* **53–56**, 479–489 (1992).
99. Yang, P. *et al.* Large-Scale fabrication of pseudocapacitive glass windows that combine electrochromism and Energy Storage. *Angew. Chemie* **126**, 12129–12133 (2014).
100. Yu, X. *et al.* Colorless-to-Black Electrochromism from Binary Electrochromes toward Multifunctional Displays. *ACS Appl. Mater. Interfaces* **12**, 39505–39514 (2020).
101. Beaujuge, P. M. & Reynolds, J. R. Color control in π -conjugated organic polymers for use in electrochromic devices. *Chem. Rev.* **110**, 268–320 (2010).
102. Mortimer, R. J., Dyer, A. L. & Reynolds, J. R. Electrochromic organic and polymeric materials for display applications. *Displays* vol. 27 2–18 (2006).
103. Mortimer, R. J. Organic electrochromic materials. *Electrochim. Acta* **44**, 2971–2981 (1999).
104. Mortimer, R. J. Electrochromic materials. *Chem. Soc. Rev.* **26**, 147–156 (1997).
105. Anthony, J. E., Facchetti, A., Heeney, M., Marder, S. R. & Zhan, X. N-Type organic semiconductors in organic electronics. *Adv. Mater.* **22**, 3876–3892 (2010).
106. Xiong, J. *et al.* Fused-ring bislactone building blocks for polymer donors. *Sci. Bull.* **65**, 1792–1795 (2020).
107. Fan, B. *et al.* Tailoring Regioisomeric Structures of π -Conjugated Polymers Containing Monofluorinated π -Bridges for Highly Efficient Polymer Solar Cells. *ACS Energy Lett.* **5**, 2087–2094 (2020).
108. Kimpel, J. & Michinobu, T. Conjugated polymers for functional applications: lifetime and performance of polymeric organic semiconductors in organic

field-effect transistors. *Polym. Int.* **70**, 367–373 (2021).

109. Li, X. *et al.* Donor-Acceptor Conjugated Polymers with Efficient Thermally Activated Delayed Fluorescence: Random versus Alternative Polymerization. *Macromolecules* **54**, 5260–5266 (2021).
110. Yasa, M. *et al.* Construction of amperometric biosensor modified with conducting polymer/carbon dots for the analysis of catechol. *J. Polym. Sci.* **58**, 3336–3348 (2020).
111. Yasa, M., Surmeli, S., Depci, T., Toppare, L. & Hacıoglu, S. O. S. O. Synthesis of a Multifunctional Quinoxaline and Benzodithiophene Bearing Polymer and Its Electrochromic Device Applications. *Macromol. Chem. Phys.* **221**, 1–10 (2020).
112. Yuksel, R. *et al.* Silver Nanowire/Conducting Polymer Nanocomposite Electrochromic Supercapacitor Electrodes. *J. Electrochem. Soc.* **164**, A721–A727 (2017).
113. Rodriguez, D. *et al.* Mechanical Properties of Solution-Processed Small-Molecule Semiconductor Films. *ACS Appl. Mater. Interfaces* **8**, 11649–11657 (2016).
114. He, Y., Chen, H. Y., Hou, J. & Li, Y. Indene - C60 bisadduct: A new acceptor for high-performance polymer solar cells. *J. Am. Chem. Soc.* **132**, 1377–1382 (2010).
115. Celik Bedeloglu, A., Demir, A., Bozkurt, Y. & Sariciftci, N. S. Photovoltaic properties of polymer based organic solar cells adapted for non-transparent substrates. *Renew. Energy* **35**, 2301–2306 (2010).
116. Seyler, H., Wong, W. W. H., Jones, D. J. & Holmes, A. B. Continuous flow synthesis of fullerene derivatives. *J. Org. Chem.* **76**, 3551–3556 (2011).
117. Nielsen, C. B., Holliday, S., Chen, H. Y., Cryer, S. J. & McCulloch, I. Non-Fullerene Electron Acceptors for Use in Organic Solar Cells. *Acc. Chem. Res.*

- 48, 2803–2812 (2015).
118. Hu, Z. *et al.* Natural drying effect on active layer for achieving high performance in polymer solar cells. *Renew. Energy* **74**, 11–17 (2015).
 119. Ye, L. *et al.* Unraveling the influence of non-fullerene acceptor molecular packing on photovoltaic performance of organic solar cells. *Nat. Commun.* **11**, 1–9 (2020).
 120. Lin, F., Jiang, K., Kaminsky, W., Zhu, Z. & Jen, A. K. Y. A Non-fullerene Acceptor with Enhanced Intermolecular π -Core Interaction for High-Performance Organic Solar Cells. *J. Am. Chem. Soc.* **142**, 15246–15251 (2020).
 121. Ouyang, G., Wu, H., Qiao, X., Zhang, J. & Li, H. Modulating Surface Morphology and Thin-Film Transistor Performance of Bi-thieno[3,4-c]pyrrole-4,6-dione-Based Polymer Semiconductor by Altering Preaggregation in Solution. *ACS Omega* **3**, 9290–9295 (2018).
 122. Chen, C. A., Yang, P. C., Wang, S. C., Tung, S. H. & Su, W. F. Side Chain Effects on the Optoelectronic Properties and Self-Assembly Behaviors of Terthiophene-Thieno[3,4-c]pyrrole-4,6-dione Based Conjugated Polymers. *Macromolecules* **51**, 7828–7835 (2018).
 123. Robitaille, A., Perea, A., Bélanger, D. & Leclerc, M. Poly(5-alkyl-thieno[3,4-c]pyrrole-4,6-dione): A study of π -conjugated redox polymers as anode materials in lithium-ion batteries. *J. Mater. Chem. A* **5**, 18088–18094 (2017).
 124. Çakal, D., Cihaner, A. & Önal, A. M. Synthesis and electropolymerization of thieno[3,4-c]pyrrole-4,6-dione based donor-acceptor-donor type monomers. *J. Electroanal. Chem.* **862**, (2020).
 125. Zhang, S. *et al.* Bi-thieno[3,4]pyrrole-4,6-dione based copolymers: 1,2-Bis(2-thienyl)ethene unit vs 1,2-diphenylethene unit. *Org. Electron.* **56**, 146–151 (2018).

126. Bathula, C. *et al.* Selenophene based benzodithiophene polymers as potential candidates for optoelectronic applications. *Dye. Pigment.* **149**, 639–643 (2018).
127. Kim, J., Lee, W. H., Park, J. B., Hwang, D. H. & Kang, I. N. Synthesis and characterization of the fluorinated thieno[3,4-c]pyrrole-4,6-dione-based donor-acceptor polymers for organic solar cells. *Dye. Pigment.* **160**, 403–409 (2019).
128. Çakal, D., Cihaner, A. & Önal, A. M. Polyhedral oligomeric silsesquioxanes appended conjugated soluble polymers based on thieno[3,4-c]pyrrole-4,6- dione acceptor unit. *Electrochim. Acta* **377**, (2021).
129. Gao, Y., Yang, Y. & Zhang, Y. Synthesis and Photovoltaic Properties of a Copolymer based on thieno [2, 3-f] benzofuran and thienopyrroledione. *IOP Conf. Ser. Mater. Sci. Eng.* **274**, (2017).
130. Zhao, Y. *et al.* Thieno[3,2-b]thiophene-Bridged Conjugated Polymers Based on Dithieno[3,2-b:2',3'-d]silole and Thieno[3,4-c]pyrrole-4,6-dione for Polymer Solar Cells: Influence of Side Chains on Optoelectronic Properties. *Macromol. Chem. Phys.* **219**, 2–7 (2018).
131. Weller, T. *et al.* Fluorination in thieno[3,4-c] pyrrole-4,6-dione copolymers leading to electron transport, high crystallinity and end-on alignment. *J. Mater. Chem. C* **5**, 7527–7534 (2017).
132. Tang, A. *et al.* The Introduction of Fluorine and Sulfur Atoms into Benzotriazole-Based p-Type Polymers to Match with a Benzotriazole-Containing n-Type Small Molecule: “The Same-Acceptor-Strategy” to Realize High Open-Circuit Voltage. *Adv. Energy Mater.* **8**, 1–9 (2018).
133. Xiao, B. *et al.* Quinoxaline-Containing Nonfullerene Small-Molecule Acceptors with a Linear A2-A1-D-A1-A2 Skeleton for Poly(3-hexylthiophene)-Based Organic Solar Cells. *ACS Appl. Mater. Interfaces* **10**, 10254–10261 (2018).

134. Geng, S. Z. *et al.* Non-fullerene Acceptors with a Thieno[3,4-c]pyrrole-4,6-dione (TPD) Core for Efficient Organic Solar Cells. *Chinese J. Polym. Sci. (English Ed.)* **37**, 1005–1014 (2019).
135. Wu, W. *et al.* Wide Bandgap Molecular Acceptors with a Truxene Core for Efficient Nonfullerene Polymer Solar Cells: Linkage Position on Molecular Configuration and Photovoltaic Properties. *Adv. Funct. Mater.* **28**, 1–12 (2018).
136. Holliday, S. *et al.* A rhodanine flanked nonfullerene acceptor for solution-processed organic photovoltaics. *J. Am. Chem. Soc.* **137**, 898–904 (2015).
137. Li, J. *et al.* A thieno[3,4-b] pyrazine-based A2-A1-D-A1-A2 type low bandgap non-fullerene acceptor with 1,1-dicyanomethylene-3-indanone (IC) as the terminal group. *J. Mater. Chem. C* **7**, 8820–8824 (2019).
138. Guo, X. *et al.* Bithiopheneimide-dithienosilole/dithienogermole copolymers for efficient solar cells: Information from structure-property-device performance correlations and comparison to thieno[3,4- c]pyrrole-4,6-Dione analogues. *J. Am. Chem. Soc.* **134**, 18427–18439 (2012).
139. Bang, S. M. *et al.* Thienopyrroledione and benzodithiophene/thiophene-based random terpolymer for polymer solar cells with improved fill factor. *Dye. Pigment.* **140**, 229–235 (2017).
140. Blouin, N. *et al.* Toward a Rational Design of Poly (2 , 7-Carbazole) Derivatives for Solar Cells. *J. Am. Chem. Soc.* **130**, 732–742 (2008).
141. Zou, Y. Y. *et al.* Recent advances in the development of biosensor for phenol: A review. *Org. Electron.* **3**, 1–7 (2020).
142. Hwang, H., Park, C., Sin, D. H., Song, E. & Cho, K. High absorption coefficient π -conjugation-extended donor-acceptor copolymers for ternary-blend solar cells. *Org. Electron.* **83**, 105738 (2020).
143. Zhao, B. *et al.* Efficient non-fullerene polymer solar cells enabled by side-

- chain conjugated. *React. Funct. Polym.* **145**, 104378 (2019).
144. Park, J. S. *et al.* Importance of Optimal Crystallinity and Hole Mobility of BDT-Based Polymer Donor for Simultaneous Enhancements of Voc, Jsc, and FF in Efficient Nonfullerene Organic Solar Cells. *Adv. Funct. Mater.* **2005787**, 1–9 (2020).
 145. Kim, J. *et al.* Environmental Science dione based conjugated polymers for high. *Energy Environ. Sci.* **8**, 2352–2356 (2015).
 146. Zhang, Q. T., Tour, J. M. & Carolina, S. Low Optical Bandgap Polythiophenes by an Alternating Donor/Acceptor Repeat Unit Strategy. *J. Am. Chem. Soc.* **119**, 5065–5066 (1997).
 147. Berrouard, P., Grenier, F., Pouliot, J-R., Gagnon, E., Tessier, C., Leclerc, M. Synthesis and Characterization of Derivatives As New Monomers for Conjugated Copolymers. *Org. Lett.* **13**, 38–41 (2011).
 148. Warnan, J. *et al.* Ordering effects in benzo[1,2-b:4,5-b']difuran-thieno[3,4-c]pyrrole-4,6- dione polymers with >7% solar cell efficiency. *Adv. Mater.* **26**, 4357–4362 (2014).
 149. Qiao, X. *et al.* Bithienopyrroledione vs. thienopyrroledione based copolymers: dramatic increase of power conversion efficiency in bulk heterojunction solar cells. *Chem. Commun.* **53**, 3543–3546 (2017).
 150. Cabanetos, C. *et al.* Linear side chains in benzo[1,2-b:4,5-b']dithiophene-thieno[3,4-c] pyrrole-4,6-dione polymers direct self-assembly and solar cell performance. *J. Am. Chem. Soc.* **135**, 4656–4659 (2013).
 151. Huang, J. *et al.* π -Conjugation Effects of Oligo(thienylenevinylene) Side Chains in Semiconducting Polymers on Photovoltaic Performance. *Macromolecules* **50**, 3557–3564 (2017).
 152. Zhou, E., Cong, J., Tajima, K., Yang, C. & Hashimoto, K. Conjugated polymers based on 1,3-dithien-2-yl-thieno[3,4- c]pyrrole-4,6-dione:

- Synthesis, characterization, and solvent effects on photovoltaic performance. *J. Phys. Chem. C* **116**, 2608–2614 (2012).
153. Phan, S. & Luscombe, C. K. Recent Advances in the Green, Sustainable Synthesis of Semiconducting Polymers. *Trends Chem.* **1**, 670–681 (2019).
 154. Berrouard, P. *et al.* Synthesis of 5-alkyl[3,4-c]thienopyrrole-4,6-dione-based polymers by direct heteroarylation. *Angew. Chemie - Int. Ed.* **51**, 2068–2071 (2012).
 155. Li, Y. *et al.* Quinoxaline-thiophene based thick photovoltaic devices with an efficiency of ~8%. *J. Mater. Chem. A* **4**, 9967–9976 (2016).
 156. Hadmojo, W. T., Wibowo, F. T. A., Ryu, D. Y., Jung, I. H. & Jang, S. Y. Fullerene-Free Organic Solar Cells with an Efficiency of 10.2% and an Energy Loss of 0.59 eV Based on a Thieno[3,4-c]Pyrrole-4,6-dione-Containing Wide Band Gap Polymer Donor. *ACS Appl. Mater. Interfaces* **9**, 32939–32945 (2017).
 157. Yang, F. *et al.* Performance limitations in thieno[3,4-c]pyrrole-4,6-dione-based polymer:ITIC solar cells. *Phys. Chem. Chem. Phys.* **19**, 23990–23998 (2017).
 158. Chen, S. *et al.* Ultrafast Channel II process induced by a 3-D texture with enhanced acceptor order ranges for high-performance non-fullerene polymer solar cells. *Energy Environ. Sci.* **11**, 2569–2580 (2018).
 159. Aryal, U. K. *et al.* The effect of irregularity from asymmetric random π -conjugated polymers on the photovoltaic performance of fullerene-free organic solar cells. *Polym. Chem.* **10**, 4407–4412 (2019).
 160. Liao, C. *et al.* Processing Strategies for an Organic Photovoltaic Module with over 10 % Efficiency Processing Strategies for an Organic Photovoltaic Module with over 10 % Efficiency. *Joule* **4**, 189–206 (2019).
 161. R. Chagas, G., Darmanin, T. & Guittard, F. One-Step and Templateless

- Electropolymerization Process Using Thienothiophene Derivatives to Develop Arrays of Nanotubes and Tree-like Structures with High Water Adhesion. *ACS Appl. Mater. Interfaces* **8**, 22732–22743 (2016).
162. Thiam, E. H. Y. *et al.* Designing Nanoporous Membranes through Templateless Electropolymerization of Thieno[3,4- b]thiophene Derivatives with High Water Content. *ACS Omega* **4**, 13080–13085 (2019).
 163. Ramos Chagas, G., Darmanin, T., Godeau, G. & Guittard, F. Nanocups and hollow microspheres formed by a one-step and templateless electropolymerization of thieno[3,4-b]thiophene derivatives as a function of the substituent. *Electrochim. Acta* **269**, 462–478 (2018).
 164. Ramos Chagas, G. *et al.* Electrodeposited Poly(thieno[3,2-b]thiophene) Films for the Templateless Formation of Porous Structures by Galvanostatic and Pulse Deposition. *Chempluschem* **82**, 1351–1358 (2017).
 165. Lin, F. *et al.* Thieno[3,4-c]pyrrole-4,6(5H)-dione Polymers with Optimized Energy Level Alignments for Fused-Ring Electron Acceptor Based Polymer Solar Cells. *Chem. Mater.* **29**, 5636–5645 (2017).
 166. Xie, Y. *et al.* High-Performance Fullerene-Free Polymer Solar Cells Featuring Efficient Photocurrent Generation from Dual Pathways and Low Nonradiative Recombination Loss. *ACS Energy Lett.* **4**, 8–16 (2019).
 167. Zhang, C. H. *et al.* Methyl Thioether Functionalization of a Polymeric Donor for Efficient Solar Cells Processed from Non-Halogenated Solvents. *Chem. Mater.* **31**, 3025–3033 (2019).
 168. Park, J. B., Ha, J. W., Jung, I. H. & Hwang, D. H. High-Performance Nonfullerene Organic Photovoltaic Cells Using a TPD-Based Wide Bandgap Donor Polymer. *ACS Appl. Energy Mater.* **2**, 5692–5697 (2019).
 169. Park, J. S. *et al.* Elucidating Roles of Polymer Donor Aggregation in All-Polymer and Non-Fullerene Small-Molecule-Polymer Solar Cells. *Chem.*

Mater. **32**, 3585–3596 (2020).

170. Donaghey, J. E. *et al.* Pyrroloindacenodithiophene containing polymers for organic field effect transistors and organic photovoltaics. *J. Mater. Chem.* **21**, 18744–18752 (2011).
171. Li, Q. *et al.* The alkyl chain positioning of thieno[3,4-c]pyrrole-4,6-dione (TPD)-Based polymer donors mediates the energy loss, charge transport and recombination in polymer solar cells. *J. Power Sources* **480**, 229098 (2020).
172. Zhao, J. *et al.* Shorter alkyl chain in thieno[3,4-c]pyrrole-4,6-dione (TPD)-based large bandgap polymer donors – Yield efficient non-fullerene polymer solar cells. *J. Energy Chem.* **53**, 69–76 (2020).
173. Howard, J. B. & Thompson, B. C. Design of Random and Semi-Random Conjugated Polymers for Organic Solar Cells. *Macromol. Chem. Phys.* **218**, 1–15 (2017).
174. Wang, J., Kong, L. & Liang, Z. Fine Control of Side Chains in Random π -Conjugated Terpolymers for Organic Photovoltaics. *Macromol. Chem. Phys.* **217**, 1513–1520 (2016).
175. Wang, Z. *et al.* A Conjugated Random Copolymer of Benzodithiophene-Difluorobenzene-Diketopyrrolopyrrole with Full Visible-Light Absorption for Bulk-Heterojunction Solar Cells. *Macromol. Chem. Phys.* **215**, 2119–2124 (2014).
176. Burkhart, B., Khlyabich, P. P. & Thompson, B. C. Semi-random two-acceptor polymers: Elucidating electronic trends through multiple acceptor combinations. *Macromol. Chem. Phys.* **214**, 681–690 (2013).
177. Lee, C. *et al.* Importance of 2D Conjugated Side Chains of Benzodithiophene-Based Polymers in Controlling Polymer Packing, Interfacial Ordering, and Composition Variations of All-Polymer Solar Cells. *Chem. Mater.* **29**, 9407–9415 (2017).

178. Kim, A. *et al.* Highly efficient and highly stable terpolymer-based all-polymer solar cells with broad complementary absorption and robust morphology. *J. Mater. Chem. A* **6**, 10095–10103 (2018).
179. Feng, W., Lin, Z., Lin, C., Wang, W. & Ling, Q. Bicomponent Random Approach for the Synthesis of Donor Polymers for Efficient All-Polymer Solar Cells Processed from A Green Solvent. *ACS Appl. Mater. Interfaces* **11**, 43441–43451 (2019).
180. Duan, C. *et al.* Improving Performance of All-Polymer Solar Cells Through Backbone Engineering of Both Donors and Acceptors. *Sol. RRL* **2**, 1–10 (2018).
181. Yasa, M. *et al.* Non-fullerene organic photovoltaics based on thienopyrroledione comprising random copolymers; effect of alkyl chains. *Renew. Energy* **178**, 202–211 (2021).
182. Liu, S. *et al.* Thieno[3,4-c]pyrrole-4,6-dione-3,4-difluorothiophene Polymer Acceptors for Efficient All-Polymer Bulk Heterojunction Solar Cells. *Angew. Chemie - Int. Ed.* **55**, 12996–13000 (2016).
183. Liu, S. *et al.* Thieno[3,4-c]Pyrrole-4,6-Dione-Based Polymer Acceptors for High Open-Circuit Voltage All-Polymer Solar Cells. *Adv. Energy Mater.* **7**, (2017).
184. Wang, Y. *et al.* Dual Imide-Functionalized Unit-Based Regioregular D-A1-D-A2 Polymers for Efficient Unipolar n-Channel Organic Transistors and All-Polymer Solar Cells. *ACS Appl. Mater. Interfaces* (2019) doi:10.1021/acsami.9b05537.
185. Shaheen, S. E. *et al.* 2.5% Efficient Organic Plastic Solar Cells. *Appl. Phys. Lett.* **78**, 841–843 (2001).
186. Ramki, K., Venkatesh, N., Sathiyam, G., Thangamuthu, R. & Sakthivel, P. A comprehensive review on the reasons behind low power conversion efficiency

- of dibenzo derivatives based donors in bulk heterojunction organic solar cells. *Org. Electron.* **73**, 182–204 (2019).
187. Armin, A. *et al.* A History and Perspective of Non-Fullerene Electron Acceptors for Organic Solar Cells. *Adv. Energy Mater.* **11**, 1–42 (2021).
 188. Roy, D., Shastri, B., Imamuddin, M., Mukhopadhyay, K. & Rao, K. U. B. Nanostructured carbon and polymer materials - Synthesis and their application in energy conversion devices. *Renew. Energy* **36**, 1014–1018 (2011).
 189. Riedel, I. *et al.* Polymer solar cells with novel fullerene-based acceptor. *Thin Solid Films* **451–452**, 43–47 (2004).
 190. Solá, M., Mestres, J., Martí, J. & Duran, M. An AM1 study of the reactivity of buckminsterfullerene (C60) in a Diels-Alder model reaction. *Chem. Phys. Lett.* **231**, 325–330 (1994).
 191. Duan, L., Elumalai, N. K., Zhang, Y. & Uddin, A. Progress in non-fullerene acceptor based organic solar cells. *Sol. Energy Mater. Sol. Cells* **193**, 22–65 (2019).
 192. Zang, Y. *et al.* Integrated molecular, interfacial, and device engineering towards high-performance non-fullerene based organic solar cells. *Adv. Mater.* **26**, 5708–5714 (2014).
 193. Zhang, H. *et al.* Over 14% Efficiency in Organic Solar Cells Enabled by Chlorinated Nonfullerene Small-Molecule Acceptors. *Adv. Mater.* **30**, 1–7 (2018).
 194. Meng, L. *et al.* Organic and solution-processed tandem solar cells with 17.3% efficiency. *Science (80-.)*. **361**, 1094–1098 (2018).
 195. Sun, J. *et al.* Dithieno[3,2-b:2',3'-d]pyrrol Fused Nonfullerene Acceptors Enabling Over 13% Efficiency for Organic Solar Cells. *Adv. Mater.* **30**, 1–8 (2018).

196. Chen, J. *et al.* Hole (donor) and electron (acceptor) transporting organic semiconductors for bulk-heterojunction solar cells. *EnergyChem* **2**, 100042 (2020).
197. Song, K. W., Choi, M. hee, Han, M. hee & Moon, D. K. Open circuit voltage increase by substituted spacer and thieno[3,4-c]pyrrole-4,6-dione for polymer solar cells. *J. Ind. Eng. Chem.* **20**, 426–434 (2014).
198. Piliego, C. *et al.* Synthetic control of structural order in N-alkylthieno[3,4- c]pyrrole-4,6-dione-based polymers for efficient solar cells. *J. Am. Chem. Soc.* **132**, 7595–7597 (2010).
199. Yuan, M. C., Chiu, M. Y., Liu, S. P., Chen, C.-M. M. & Wei, K.-H. H. A thieno[3,4-c]pyrrole-4,6-dione-based donor-acceptor polymer exhibiting high crystallinity for photovoltaic applications. *Macromolecules* **43**, 6936–6938 (2010).
200. Zheng, Q., Jung, B. J., Sun, J. & Katz, H. E. Ladder-type oligo- p -phenylene-containing copolymers with high open-circuit voltages and ambient photovoltaic activity. *J. Am. Chem. Soc.* **132**, 5394–5404 (2010).
201. Zhang, Y. *et al.* Efficient polymer solar cells based on the copolymers of benzodithiophene and thienopyrroledione. *Chem. Mater.* **22**, 2696–2698 (2010).
202. Zou, Y., Najari, A., Berrouard, P. & Beaupre, S. A Thieno[3,4-c]pyrrole-4,6-dione-Based Copolymer for Efficient Solar Cells. *J. Am. Chem. Soc.* **132**, 5330–5331 (2010).
203. Keles, D. *et al.* Conjugated polymers with benzothiadiazole and benzotriazole moieties for polymer solar cells. *Renew. Energy* **139**, 1184–1193 (2019).
204. Liang, Z. *et al.* Near-infrared absorbing non-fullerene acceptors with selenophene as π bridges for efficient organic solar cells. *J. Mater. Chem. A* **6**, 8059–8067 (2018).

205. Guo, P. *et al.* Effect of alkylthiophene spacers and fluorine on the optoelectronic properties of 5,10-bis(dialkylthien-2-yl)dithieno[2,3-d:2',3'-d']benzo[1,2-b:4,5-b']dithiophene-*alt*-benzothiadiazole derivative copolymers. *RSC Adv.* **7**, 22845–22854 (2017).
206. Gunasekaran, R. K. *et al.* Open atmospheric processed perovskite solar cells using dopant-free, highly hydrophobic hole-transporting materials: Influence of thiophene and selenophene π -spacers on charge transport and recombination properties. *Sol. Energy Mater. Sol. Cells* **199**, 66–74 (2019).
207. Agbolaghi, S. Well-functioned photovoltaics based on nanofibers composed of PBDT-TIPS-DTNT-DT and graphenic precursors thermally modified by polythiophene, polyaniline and polypyrrole. *Polym. Int.* **68**, 1516–1523 (2019).
208. Liu, D. *et al.* Extended Conjugation Length of Nonfullerene Acceptors with Improved Planarity via Noncovalent Interactions for High-Performance Organic Solar Cells. *Adv. Energy Mater.* **8**, 1–8 (2018).
209. Wu, W. *et al.* Photovoltaic performance and long-term stability of quasi-solid-state fluoranthene dyes-sensitized solar cells. *Renew. Energy* **35**, 1724–1728 (2010).
210. Zhang, X., Wang, Q., Liang, Z., Li, M. & Geng, Y. Low-bandgap non-fullerene acceptors based on selenophene π spacer and alkylated indaceno[1,2-b:5,6-b']dithiophene for organic solar cells. *Org. Electron.* **69**, 200–207 (2019).
211. Pang, S. *et al.* Alkyl Chain Length Effects of Polymer Donors on the Morphology and Device Performance of Polymer Solar Cells with Different Acceptors. *Adv. Energy Mater.* **9**, 1–12 (2019).
212. Yu, Y., Wang, N., Meng, B., Liu, J. & Wang, L. Effect of Alkyl Side Chains of Polymer Donors on Photovoltaic Performance of All-Polymer Solar Cells. *ACS Appl. Polym. Mater.* **3**, 42–48 (2021).

213. Wang, C. *et al.* Intermolecular Arrangement of Fullerene Acceptors Proximal to Semiconducting Polymers in Mixed Bulk Heterojunctions. *Angew. Chemie - Int. Ed.* **57**, 7034–7039 (2018).
214. Kouijzer, S. *et al.* Predicting morphologies of solution processed polymer:Fullerene blends. *J. Am. Chem. Soc.* **135**, 12057–12067 (2013).
215. Van Franeker, J. J., Turbiez, M., Li, W., Wienk, M. M. & Janssen, R. A. J. A real-time study of the benefits of co-solvents in polymer solar cell processing. *Nat. Commun.* **6**, 1–8 (2015).
216. Bi, X. *et al.* Enhanced photovoltaic effect from naphtho[2,3-*c*] thiophene-4,9-dione-based polymers through alkyl side chain induced backbone distortion. *J. Mater. Chem. A* **8**, 14706–14712 (2020).
217. Zhao, J. *et al.* Bithieno[3,4-*c*]pyrrole-4,6-dione-Mediated Crystallinity in Large-Bandgap Polymer Donors Directs Charge Transportation and Recombination in Efficient Nonfullerene Polymer Solar Cells. *ACS Energy Lett.* 367–375 (2020) doi:10.1021/acsenergylett.9b02842.
218. Ha, J. W. *et al.* Highly Efficient and Photostable Ternary Organic Solar Cells Enabled by the Combination of Non-Fullerene and Fullerene Acceptors with Thienopyrrolo-dione-based Polymer Donors. *ACS Appl. Mater. Interfaces* **12**, 51699–51708 (2020).
219. Yang, F. *et al.* Boosting the Performance of Non-Fullerene Organic Solar Cells via Cross-Linked Donor Polymers Design. *Macromolecules* **52**, 2214–2221 (2019).
220. Park, Y. S., Kim, E., Hong, B. & Lee, J. Characteristics of ITO films with oxygen plasma treatment for thin film solar cell applications. *Mater. Res. Bull.* **48**, 5115–5120 (2013).
221. Zhang, Z. *et al.* Small Molecular Donor/Polymer Acceptor Type Organic Solar Cells: Effect of Molecular Weight on Active Layer Morphology.

Macromolecules **52**, 8682–8689 (2019).

- 222. Li, Z. *et al.* Morphology optimization via molecular weight tuning of donor polymer enables all-polymer solar cells with simultaneously improved performance and stability. *Nano Energy* **64**, 103931 (2019).
- 223. Mihailetschi, V. D., Blom, P. W. M., Hummelen, J. C. & Rispen, M. T. Cathode dependence of the open-circuit voltage of polymer:fullerene bulk heterojunction solar cells. *J. Appl. Phys.* **94**, 6849–6854 (2003).
- 224. Guo, X. *et al.* Design, synthesis and photovoltaic properties of a new D- π -A polymer with extended π -bridge units. *J. Mater. Chem.* **22**, 21024–21031 (2012).
- 225. Bernardo, G. & G., D. Recent Progress in the Understanding and Manipulation of Morphology in Polymer: Fullerene Photovoltaic Cells. *Optoelectron. - Adv. Mater. Devices* (2013) doi:10.5772/51115.
- 226. Lu, Y. *et al.* Temperature-dependent morphology evolution of P3HT:PCBM blend solar cells during annealing processes. *Synth. Met.* **162**, 2039–2046 (2012).
- 227. Song, X., Gasparini, N. & Baran, D. The Influence of Solvent Additive on Polymer Solar Cells Employing Fullerene and Non-Fullerene Acceptors. *Adv. Electron. Mater.* **4**, 1–7 (2018).
- 228. Beaupré, S., Shaker-Sepasgozar, S., Najari, A. & Leclerc, M. Random D-A1-D-A2 terpolymers based on benzodithiophene, thiadiazole[3,4-e]isoindole-5,7-dione and thieno[3,4-c]pyrrole-4,6-dione for efficient polymer solar cells. *J. Mater. Chem. A* **5**, 6638–6647 (2017).
- 229. Tamilavan, V. *et al.* Highly efficient imide functionalized pyrrolo[3,4-c]-pyrrole-1,3-dione-based random copolymer containing thieno[3,4-c]pyrrole-4,6-dione and benzodithiophene for simple structured polymer solar cells. *J. Mater. Chem. A* **2**, 20126–20132 (2014).

230. Zhou, E., Cong, J., Hashimoto, K. & Tajima, K. Introduction of a conjugated side chain as an effective approach to improving donor-acceptor photovoltaic polymers. *Energy Environ. Sci.* **5**, 9756–9759 (2012).
231. Azeri, Ö. *et al.* Efficient benzodithiophene and thienopyrroledione containing random polymers as components for organic solar cells. *Polymer (Guildf)*. **133**, 60–67 (2017).
232. Zhang, G., Fu, Y., Qiu, L. & Xie, Z. Synthesis and characterization of thieno[3,4-c]pyrrole-4,6-dione and pyrrolo[3,4-c]pyrrole-1,4-dione-based random polymers for photovoltaic applications. *Polymer (Guildf)*. **53**, 4407–4412 (2012).
233. Advincula, A. A., Pelse, I. & Reynolds, J. R. Side chain independent photovoltaic performance of thienopyrroledione conjugated donor-acceptor polymers. *J. Mater. Chem. C* **8**, 16452–16462 (2020).
234. Liu, W., Wu, L., Zhang, X. & Chen, J. Highly-selective electrochemical determination of catechol based on 3-aminophenylboronic acid-3,4,9,10-perylene tetracarboxylic acid functionalized carbon nanotubes modified electrode. *Anal. Methods* **6**, 718–724 (2014).
235. De Luis, A. M., Lombraña, J. I., Menéndez, A. & Sanz, J. Analysis of the toxicity of phenol solutions treated with H₂O₂/UV and H₂O₂/Fe oxidative systems. *Ind. Eng. Chem. Res.* **50**, 1928–1937 (2011).
236. Ye, Q. *et al.* Sensors and Actuators B: Chemical Constructing a fluorescent probe for specific detection of catechol based on 4-carboxyphenylboronic acid-functionalized carbon dots. *Sensors Actuators B. Chem.* **250**, 712–720 (2017).
237. Kanamori, T., Isokawa, M., Funatsu, T. & Tsunoda, M. Development of analytical method for catechol compounds in mouse urine using hydrophilic interaction liquid chromatography with fluorescence detection. *J. Chromatogr. B* **985**, 142–148 (2015).

238. Nagaraja, P., Vasantha, R. A. & Sunitha, K. R. A sensitive and selective spectrophotometric estimation of catechol derivatives in pharmaceutical preparations. *Talanta* **55**, 1039–1046 (2001).
239. Zhao, W. W., Xu, J. J. & Chen, H. Y. Photoelectrochemical DNA biosensors. *Chemical Reviews* vol. 114 7421–7441 (2014).
240. Sarma, A. K., Vatsyayan, P., Goswami, P. & Minter, S. D. Recent advances in material science for developing enzyme electrodes. *Biosensors and Bioelectronics* vol. 24 2313–2322 (2009).
241. Haghighi, B., Gorton, L., Ruzgas, T. & Jönsson, L. J. Characterization of graphite electrodes modified with laccase from *Trametes versicolor* and their use for bioelectrochemical monitoring of phenolic compounds in flow injection analysis. in *Analytica Chimica Acta* vol. 487 3–14 (2003).
242. Yang, J. *et al.* Laccases: Production, expression regulation, and applications in pharmaceutical biodegradation. *Front. Microbiol.* **8**, (2017).
243. Ramanavicius, A. *et al.* Conducting and Electrochemically Generated Polymers in Sensor Design (Mini Review). *Procedia Eng.* **47**, 825–828 (2012).
244. Soylemez, S., Bekmezci, S. A., Goker, S. & Toppare, L. Fabrication of a Novel Polymeric Scaffold for Amperometric Laccase Biosensor. *J. Polym. Sci.* **57**, 2333–2339 (2019).
245. Bulut, U. *et al.* A biosensor platform based on amine functionalized conjugated benzenediamine-benzodithiophene polymer for testosterone analysis. *J. Appl. Polym. Sci.* **137**, (2020).
246. Geraedr, M., Choubey, A. & Malhotra, B. . Review: Application of Conducting Polymer to Biosensors. *Biosens. Bioelectron.* **17**, 345–359 (2001).
247. Zhang, Y. *et al.* Conjugated polymers based on C, Si and N-bridged

- dithiophene and thienopyrroledione units: Synthesis, field-effect transistors and bulk heterojunction polymer solar cells. *J. Mater. Chem.* **21**, 3895–3902 (2011).
248. Ham, H., Kim, H. su, Hwang, D. H. & Kang, I. N. Synthesis and characterization of a wide-bandgap polymer based on perfluorinated and alkylthiolated benzodithiophene with a deep highest occupied molecular orbital level for organic photovoltaics. *J. Polym. Sci.* **58**, 2755–2763 (2020).
 249. Muller, E. W. *et al.* Synthesis of 1,6-didecyl naphtho[1,2-b:5,6-b']difuran-based copolymers by direct heteroarylation polymerization. *J. Polym. Sci.* **58**, 1299–1310 (2020).
 250. Guo, X. *et al.* Thieno[3,4- c]pyrrole-4,6-dione-based donor - Acceptor conjugated polymers for solar cells. *Macromolecules* **44**, 269–277 (2011).
 251. Hong, Y. R., Wong, H. K., Moh, L. C. H., Tan, H. S. & Chen, Z. K. Polymer solar cells based on copolymers of dithieno[3,2-b:2',3'-d]silole and thienopyrroledione. *Chem. Commun.* **47**, 4920–4922 (2011).
 252. Kurbanoglu, S. & Toppare, L. Ethanol biosensor based on immobilization of alcohol Oxidase in a conducting polymer matrix via Crosslinking with Glutaraldehyde. *Rev. Roum. Chim.* **60**, 453–460 (2015).
 253. Huang, Q. *et al.* Carbon dots and chitosan composite film based biosensor for the sensitive and selective determination of dopamine. *Analyst* **138**, 5417–5423 (2013).
 254. Bhattacharya, S., Sarkar, R., Chakraborty, B., Porgador, A. & Jelinek, R. Nitric Oxide Sensing through Azo-Dye Formation on Carbon Dots. *ACS Sensors* **2**, 1215–1224 (2017).
 255. Li, M., Chen, T., Gooding, J. J. & Liu, J. Review of carbon and graphene quantum dots for sensing. *ACS Sensors* **4**, 1732–1748 (2019).
 256. Pandit, S., Banerjee, T., Srivastava, I., Nie, S. & Pan, D. Machine Learning-

- Assisted Array-Based Biomolecular Sensing Using Surface-Functionalized Carbon Dots. *ACS Sensors* **4**, 2730–2737 (2019).
257. Campuzano, S., Yáñez-Sedeño, P. & Pingarrón, J. M. Carbon dots and graphene quantum dots in electrochemical biosensing. *Nanomaterials* **9**, 1–18 (2019).
 258. Zhu, S. *et al.* Highly Photoluminescent Carbon Dots for Multicolor Patterning, Sensors, and Bioimaging. *Angew. Chemie* **125**, 4045–4049 (2013).
 259. Stephen, P. J., Devlin, F. J., Chabalowski, C. F. & Frisch, M. J. Ab Initio Calculation of Vibrational Absorption. *J. Phys. Chem.* **98**, 11623–11627 (1994).
 260. A. D. Becke. Density-functional exchange-energy approximation with correct asymptotic behavior. *Phys. Rev. A* **38**, 3098 (1998).
 261. Lee, C., Yang, W., Parr, R. G. Development of the Colle-Salvetti correlation-energy formula into a functional of the electron density. *Phys. Rev. B* **37**, (1987).
 262. Van Der Spoel, D. *et al.* GROMACS: Fast, flexible, and free. *J. Comput. Chem.* **26**, 1701–1718 (2005).
 263. Turan, H. T., Kucur, O., Kahraman, B., Salman, S. & Aviyente, V. Design of donor-acceptor copolymers for organic photovoltaic materials: A computational study. *Phys. Chem. Chem. Phys.* **20**, 3581–3591 (2018).
 264. Alkan, E. A. *et al.* The impact of [1,2,5]chalcogenazolo[3,4-f]-benzo[1,2,3]triazole structure on the optoelectronic properties of conjugated polymers. *J. Polym. Sci.* **58**, 956–968 (2020).
 265. Perdew, J. P., Tao, J., Staroverov, V. N. & Scuseria, G. E. Meta-generalized gradient approximation: Explanation of a realistic nonempirical density functional. *J. Chem. Phys.* **120**, 6898–6911 (2004).

266. Brédas, J. L., Beljonne, D., Coropceanu, V. & Cornil, J. Charge-transfer and energy-transfer processes in π -conjugated oligomers and polymers: A molecular picture. *Chem. Rev.* **104**, 4971–5003 (2004).
267. Sun, H., Mumby, S. J., Maple, J. R. & Hagler, A. T. An ab Initio CFF93 All-Atom Force Field for Polycarbonates. *J. Am. Chem. Soc.* 2978–2987 (1994).
268. Zhu, P. & Zhao, Y. Cyclic voltammetry measurements of electroactive surface area of porous nickel: Peak current and peak charge methods and diffusion layer effect. *Mater. Chem. Phys.* **233**, 60–67 (2019).
269. Huang, K. J., Wang, L., Li, J., Yu, M. & Liu, Y. M. Electrochemical sensing of catechol using a glassy carbon electrode modified with a composite made from silver nanoparticles, polydopamine, and graphene. *Microchim. Acta* **180**, 751–757 (2013).
270. Mao, H. *et al.* Applied Surface Science Poly (4-vinylphenylboronic acid) functionalized polypyrrole / graphene oxide nanosheets for simultaneous electrochemical determination of catechol and hydroquinone. *Appl. Surf. Sci.* **420**, 594–605 (2017).
271. Nazari, M., Kashanian, S., Moradipour, P. & Maleki, N. A novel fabrication of sensor using ZnO-Al₂O₃ ceramic nano fi bers to simultaneously detect catechol and hydroquinone. *J. Electroanal. Chem.* **812**, 122–131 (2018).
272. Palanisamy, S. *et al.* Voltammetric determination of catechol based on a glassy carbon electrode modified with a composite consisting of graphene oxide and polymelamine. *Microchim. Acta* **184**, 1051–1057 (2017).
273. Liu, L. *et al.* Electrochemical sensor based on F , N-doped carbon dots decorated laccase for detection of catechol. *J. Electroanal. Chem.* **840**, 84–92 (2019).
274. Sarika, C. *et al.* A novel amperometric catechol biosensor based on α -Fe₂O₃ nanocrystals-modified carbon paste electrode. *Artif. Cells, Nanomedicine*

Biotechnol. **45**, 625–634 (2017).

275. Benabda, O., M'Hir, S., Kasmi, M., Mnif, W. & Hamdi, M. Optimization of Protease and Amylase Production by *Rhizopus oryzae* Cultivated on Bread Waste Using Solid-State Fermentation. *J. Chem.* **2019**, (2019).
276. Chen, Q. *et al.* Determination of catechol and hydroquinone with high sensitivity using MOF-graphene composites modified electrode. *J. Electroanal. Chem.* **789**, 114–122 (2017).
277. Broli, N., Vallja, L., Shehu, A. & Vasjari, M. Determination of catechol in extract of tea using carbon paste electrode modified with banana tissue. *J. Food Process. Preserv.* **43**, 1–6 (2019).
278. Kurbanoglu, S. & Ozkan, S. A. A Novel Enzymatic Biosensor for the Detection of Catechol Using Multi-walled Carbon Nanotubes and Gold Nanowires. *Electrocatalysis* **9**, 252–257 (2018).
279. Shimomura, T., Itoh, T., Sumiya, T. & Hanaoka, T. Sensors and Actuators B : Chemical Amperometric detection of phenolic compounds with enzyme immobilized in mesoporous silica prepared by electrophoretic deposition. *Sensors Actuators B. Chem.* **153**, 361–368 (2011).
280. Goulart, L. A., Gonçalves, R., Correa, A. A., Pereira, E. C. & Mascaro, L. H. Synergic effect of silver nanoparticles and carbon nanotubes on the simultaneous voltammetric determination of hydroquinone, catechol, bisphenol A and phenol. *Microchim. Acta* **185**, (2018).
281. Lekshmi, I. C. *et al.* Enhanced catechol biosensing on metal oxide nanocrystal sensitized graphite nanoelectrodes through preferential molecular adsorption. *J. Electroanal. Chem.* **867**, 114190 (2020).
282. Zhou, X., Liu, L., Bai, X. & Shi, H. Sensors and Actuators B : Chemical A reduced graphene oxide based biosensor for high-sensitive detection of phenols in water samples. *Sensors Actuators B. Chem.* **181**, 661–667 (2013).

283. Kim, T. *et al.* Flexible , highly efficient all-polymer solar cells. *Nat. Commun.* 1–7 (2015) doi:10.1038/ncomms9547.
284. Breneman, C. M. & Wiberg, K. B. Determining atom- centered monopoles from molecular electrostatic potentials. The need for high sampling density in formamide conformational analysis. *J. Comput. Chem.* **11**, 361–373 (1990).
285. Shirakawa, H., Louis, E. J., MacDiarmid, A. G., Chiang, C. K. & Heeger, A. J. Synthesis of electrically conducting organic polymers: Halogen derivatives of polyacetylene, (CH)_x. *J. Chem. Soc. Chem. Commun.* 578–580 (1977) doi:10.1039/C39770000578.
286. Scharber, M. C. & Sariciftci, N. S. Low Band Gap Conjugated Semiconducting Polymers. *Adv. Mater. Technol.* **6**, (2021).
287. Wu, J. S., Cheng, S. W., Cheng, Y. J. & Hsu, C. S. Donor-acceptor conjugated polymers based on multifused ladder-type arenes for organic solar cells. *Chem. Soc. Rev.* **44**, 1113–1154 (2015).
288. Stalder, R., Mei, J. & Reynolds, J. R. Isoindigo-based donor-acceptor conjugated polymers. *Macromolecules* **43**, 8348–8352 (2010).
289. Zhang, B. & Cheng, Y. Recent Advances in Conjugated TADF Polymer Featuring in Backbone-Donor/Pendant-Acceptor Structure: Material and Device Perspectives. *Chem. Rec.* **19**, 1624–1643 (2019).
290. Cevher, S. C. *et al.* A comprehensive study: Theoretical and experimental investigation of heteroatom and substituent effects on frontier orbitals and polymer solar cell performances. *J. Polym. Sci.* **58**, 2792–2806 (2020).
291. Aslan, S. T. *et al.* Synthesis of selenophene substituted benzodithiophene and fluorinated benzothiadiazole based conjugated polymers for organic solar cell applications. *Electrochim. Acta* **398**, 139298 (2021).
292. Kuwabara, J. & Kanbara, T. Step-Economical Synthesis of Conjugated Polymer Materials Composed of Three Components: Donor, Acceptor, and π

Units. *Macromol. Rapid Commun.* **42**, 1–8 (2021).

293. Khammultri, P. *et al.* Red to orange thermally activated delayed fluorescence polymers based on 2-(4-(diphenylamino)-phenyl)-9H-thioxanthen-9-one-10,10-dioxide for efficient solution-processed OLEDs. *RSC Adv.* **11**, 24794–24806 (2021).
294. Yaylali, F. V. *et al.* ProTOT: Synthesis of the missing member of the 3,4-chalcogen substituted bridged thiophenes and its utilization in donor-acceptor polymers. *Polymer (Guildf)*. **212**, 123076 (2021).
295. Li, M. *et al.* Colorless to black electrochromic devices using subtractive color mixing of two electrochromes: A conjugated polymer with a small organic molecule. *Org. Electron.* **84**, 105748 (2020).
296. Beaujuge, P. M., Amb, C. M. & Reynolds, J. R. Spectral engineering in π -conjugated polymers with intramolecular donor-acceptor interactions. *Acc. Chem. Res.* **43**, 1396–1407 (2010).
297. Deng, Y. *et al.* Donor-acceptor conjugated polymers with dithienocarbazoles as donor units: Effect of structure on semiconducting properties. *Macromolecules* **45**, 8621–8627 (2012).
298. Colladet, K. *et al.* Low band gap donor-acceptor conjugated polymers toward organic solar cells applications. *Macromolecules* **40**, 65–72 (2007).
299. He, M. *et al.* Wide bandgap donor-acceptor conjugated polymers with alkylthiophene as side chains for high-performance non-fullerene polymer solar cells. *Org. Electron.* **65**, 31–38 (2019).
300. Rao, J. *et al.* Meta Junction Promoting Efficient Thermally Activated Delayed Fluorescence in Donor-Acceptor Conjugated Polymers. *Angew. Chemie - Int. Ed.* **59**, 17903–17909 (2020).
301. Shi, S. *et al.* Efficient polymer solar cells based on a broad bandgap D-A copolymer of ‘zigzag’ naphthodithiophene and thieno[3,4-c]pyrrole-4,6-

- dione. *J. Mater. Chem. A* **1**, 1540–1543 (2013).
302. Yu, H. *et al.* Effect of alkyl chain spacer on charge transport in n-type dominant polymer semiconductors with a diketopyrrolopyrrole-thiophene-bithiazole acceptor-donor-acceptor unit. *J. Mater. Chem. C* **5**, 3616–3622 (2017).
 303. Chen, H. Y., Yeh, S. C., Chen, C. T. & Chen, C. T. Comparison of thiophene- and selenophene-bridged donor-acceptor low band-gap copolymers used in bulk-heterojunction organic photovoltaics. *J. Mater. Chem.* **22**, 21549–21559 (2012).
 304. Negash, A. *et al.* Ladder-type high gap conjugated polymers based on indacenodithieno[3,2-b]thiophene and bithiazole for organic photovoltaics. *Org. Electron.* **74**, 211–217 (2019).
 305. Chen, C. H. *et al.* Donor-Acceptor Effect of Carbazole-Based Conjugated Polymer Electrets on Photoresponsive Flash Organic Field-Effect Transistor Memories. *ACS Appl. Mater. Interfaces* **12**, 6144–6150 (2020).
 306. Zhu, L. *et al.* High-Efficiency Perovskite Solar Cells Based on New TPE Compounds as Hole Transport Materials: The Role of 2,7- and 3,6-Substituted Carbazole Derivatives. *Chem. - A Eur. J.* **23**, 4373–4379 (2017).
 307. Sun, M. *et al.* Fluorene-based single-chain copolymers for color-stable white light-emitting diodes. *Macromol. Chem. Phys.* **208**, 988–993 (2007).
 308. Zhou, L. *et al.* Synthesis and solar cells applications of EO-PF-DTBT polymer. *J. Appl. Polym. Sci.* **131**, 1–7 (2014).
 309. Song, X. *et al.* Fluorene Side-Chained Benzodithiophene Polymers for Low Energy Loss Solar Cells. *Macromolecules* **50**, 6880–6887 (2017).
 310. Wen, S. *et al.* Synthesis and photovoltaic properties of thieno[3,4-c]pyrrole-4,6-dione- based donor-acceptor Copolymers. *J. Polym. Sci. Part A Polym. Chem.* **50**, 3758–3766 (2012).

311. Najari, A. *et al.* High Open-Circuit Voltage Solar Cells Based on New Thieno[3,4-c]pyrrole-4,6-dione and 2,7-Carbazole Copolymers. *Macromolecules* **45**, 1833 (2012).
312. Ottone, C. *et al.* Donor-acceptor alternating copolymers containing thienopyrroledione electron accepting units: Preparation, redox behaviour, and application to photovoltaic cells. *Polym. Chem.* **3**, 2355–2365 (2012).
313. Shahid, M. *et al.* Low band gap selenophene-diketopyrrolopyrrole polymers exhibiting high and balanced ambipolar performance in bottom-gate transistors. *Chem. Sci.* **3**, 181–185 (2012).
314. Roy, P., Kumar Sinha, N., Tiwari, S. & Khare, A. A review on perovskite solar cells: Evolution of architecture, fabrication techniques, commercialization issues and status. *Sol. Energy* **198**, 665–688 (2020).
315. Zhou, D., Zhou, T., Tian, Y., Zhu, X. & Tu, Y. Perovskite-Based Solar Cells: Materials, Methods, and Future Perspectives. *J. Nanomater.* **2018**, (2018).
316. Kojima, A., Teshima, K., Shirai, Y. & Miyasaka, T. Organometal halide perovskites as visible-light sensitizers for photovoltaic cells. *J. Am. Chem. Soc.* **131**, 6050–6051 (2009).
317. Sahli, F. *et al.* Fully textured monolithic perovskite/silicon tandem solar cells with 25.2% power conversion efficiency. *Nat. Mater.* **17**, 820–826 (2018).
318. Zheng, L. *et al.* A perovskite/silicon hybrid system with a solar-to-electric power conversion efficiency of 25.5%. *J. Mater. Chem. A* **7**, 26479–26489 (2019).
319. Mei, A. *et al.* A hole-conductor-free, fully printable mesoscopic perovskite solar cell with high stability. *Science (80-.).* **345**, 295–298 (2014).
320. Valverde-Chávez, D. A. *et al.* Intrinsic femtosecond charge generation dynamics in single crystal CH₃NH₃PbI₃. *Energy Environ. Sci.* **8**, 3700–3707 (2015).

321. Xing, G. *et al.* Long-range balanced electron-and hole-transport lengths in organic-inorganic CH₃NH₃PbI₃. *Science* (80-.). **342**, 344–347 (2013).
322. Miyata, A. *et al.* Direct measurement of the exciton binding energy and effective masses for charge carriers in organic-inorganic tri-halide perovskites. *Nat. Phys.* **11**, 582–587 (2015).
323. Mitzi, D. B., Chondroudis, K. & Kagan, C. R. Design, structure, and optical properties of organic-inorganic perovskites containing an oligothiophene chromophore. *Inorg. Chem.* **38**, 6246–6256 (1999).
324. Im, J. H., Lee, C. R., Lee, J. W., Park, S. W. & Park, N. G. 6.5% Efficient Perovskite Quantum-Dot-Sensitized Solar Cell. *Nanoscale* **3**, 4088–4093 (2011).
325. Kim, H. S. *et al.* Lead iodide perovskite sensitized all-solid-state submicron thin film mesoscopic solar cell with efficiency exceeding 9%. *Sci. Rep.* **2**, 1–7 (2012).
326. Burschka, J. *et al.* Sequential deposition as a route to high-performance perovskite-sensitized solar cells. *Nature* **499**, 316–319 (2013).
327. Wang, F., Yu, H., Xu, H. & Zhao, N. HPbI₃: A new precursor compound for highly efficient solution-processed perovskite solar cells. *Adv. Funct. Mater.* **25**, 1120–1126 (2015).
328. Giordano, F. *et al.* Enhanced electronic properties in mesoporous TiO₂ via lithium doping for high-efficiency perovskite solar cells. *Nat. Commun.* **7**, 1–6 (2016).
329. Yang, W. S. *et al.* High-performance photovoltaic perovskite layers fabricated through intramolecular exchange. *Science* (80-.). **348**, 1234–1237 (2015).
330. Li, X. *et al.* A vacuum flash-assisted solution process for high-efficiency large-area perovskite solar cells. *Science* (80-.). **353**, 58–62 (2016).

331. Yang, Z., Zhang, S., Li, L. & Chen, W. Research progress on large-area perovskite thin films and solar modules. *J. Mater.* **3**, 231–244 (2017).
332. Caprioglio, P. *et al.* Monolithic perovskite/silicon tandem solar cell with >29% efficiency by enhanced hole extraction. *Science* (80-.). **370**, 1300–1309 (2020).
333. Kim, H. S., Im, S. H. & Park, N. G. Organolead halide perovskite: New horizons in solar cell research. *J. Phys. Chem. C* **118**, 5615–5625 (2014).
334. Saleh, G. *et al.* Methylammonium Governs Structural and Optical Properties of Hybrid Lead Halide Perovskites through Dynamic Hydrogen Bonding. *Chem. Mater.* **33**, 8524–8533 (2021).
335. Zhou, S. Rapid separation and purification of lead halide perovskite quantum dots through differential centrifugation in nonpolar solvent. *RSC Adv.* **11**, 28410–28419 (2021).
336. Dintakurti, S. S. H. *et al.* Composition-tuned MAPbBr₃nanoparticles with addition of Cs⁺cations for improved photoluminescence. *RSC Adv.* **11**, 24137–24143 (2021).
337. Xie, L. *et al.* Broadband Detection of X-ray, Ultraviolet, and Near-Infrared Photons using Solution-Processed Perovskite–Lanthanide Nanotransducers. *Adv. Mater.* **33**, 1–7 (2021).

APPENDICES

A. NMR Spectra

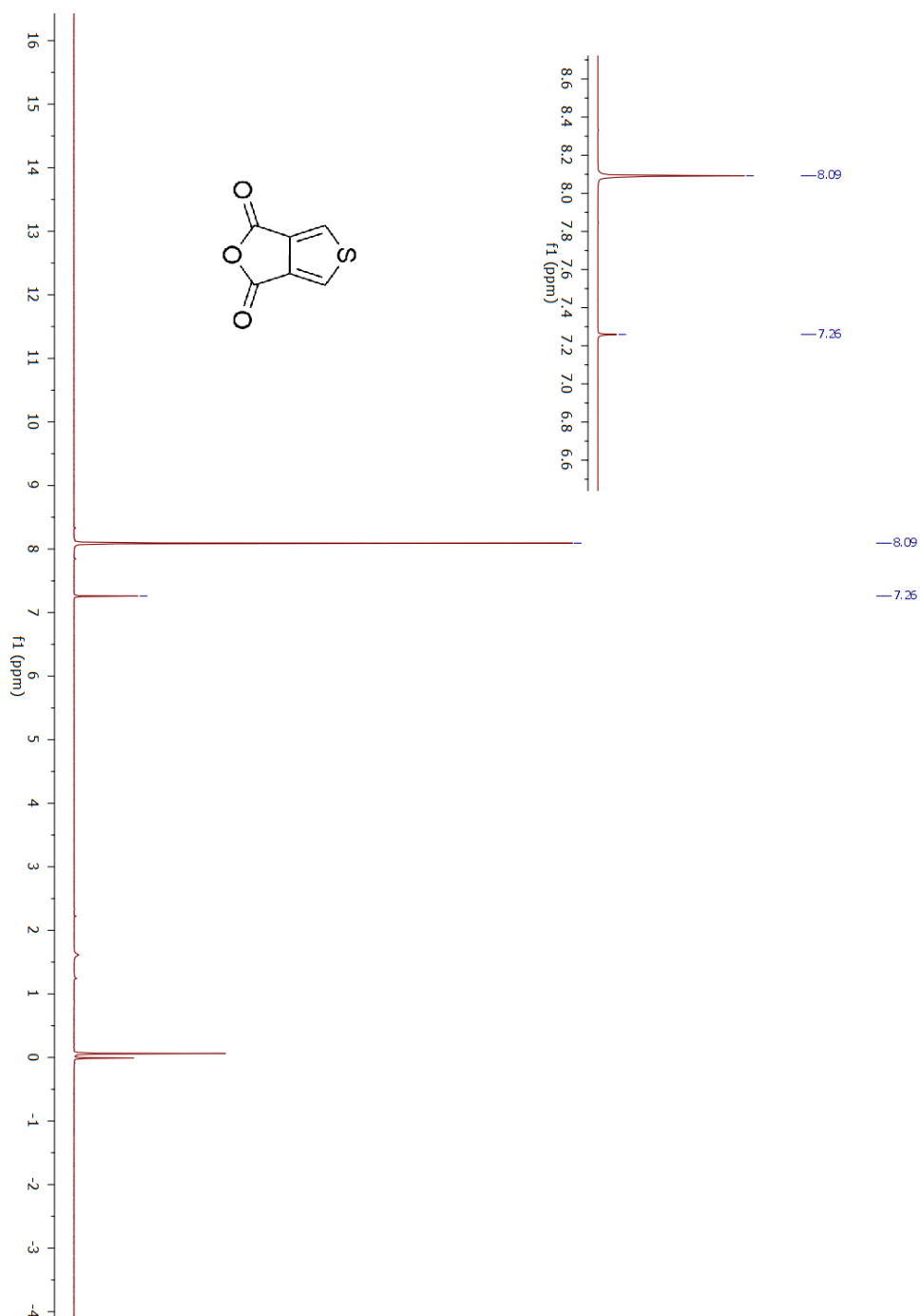


Figure A1. ^1H NMR spectrum of compound 2 in CDCl_3

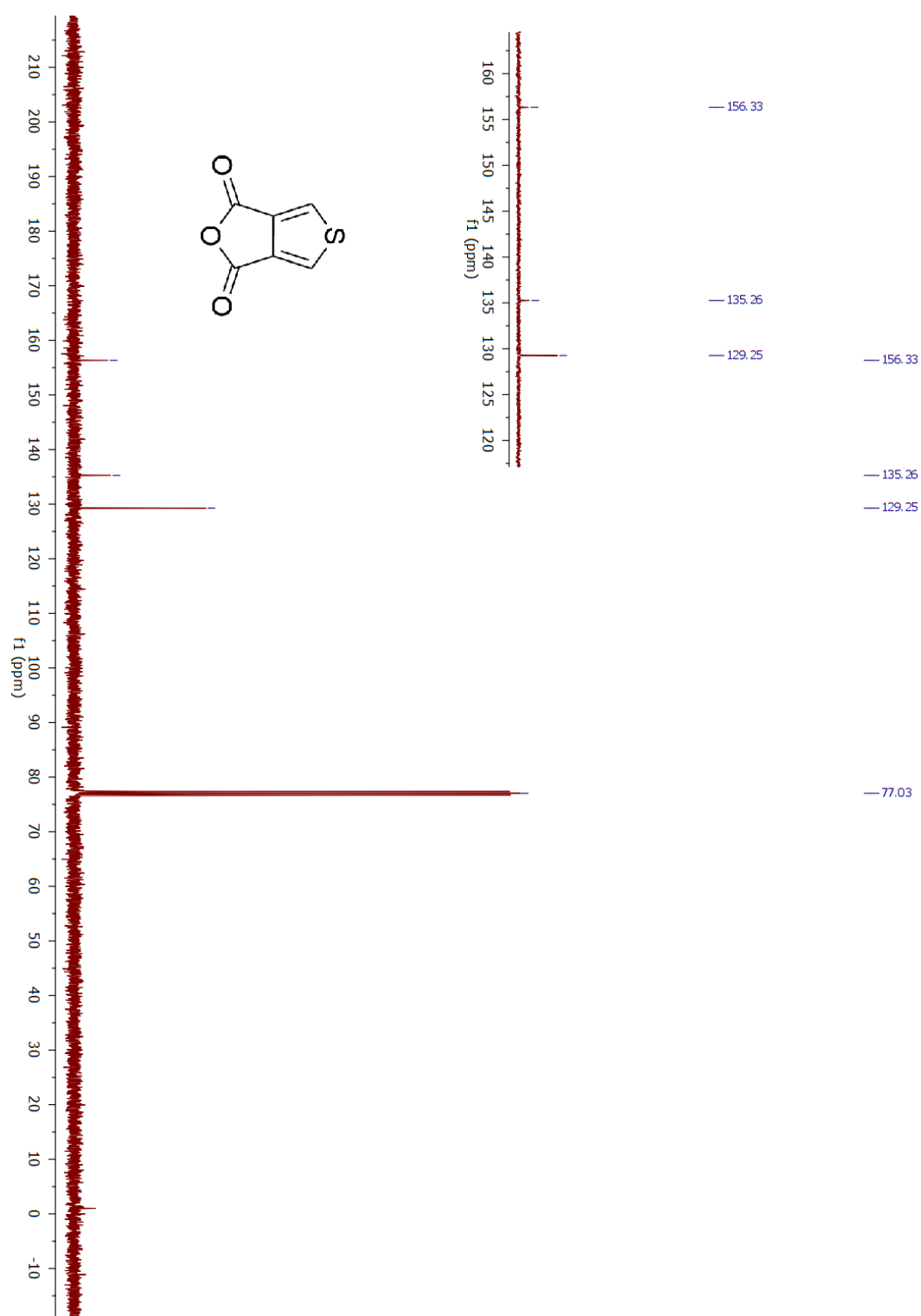
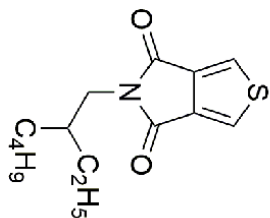


Figure A2. ^{13}C NMR spectrum of compound 2 in CDCl_3



183

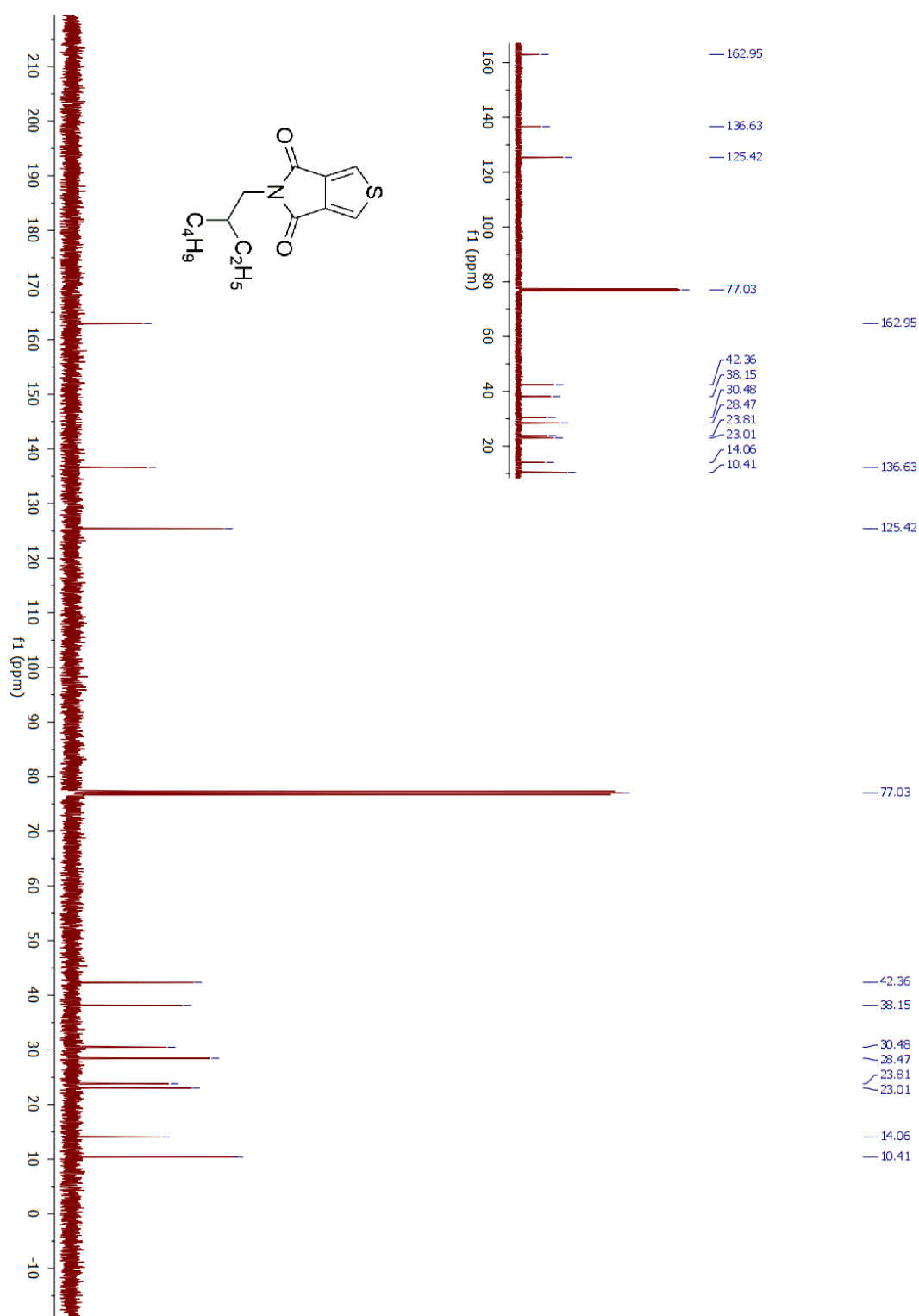


Figure A4. ^{13}C NMR spectrum of compound 3 in CDCl_3

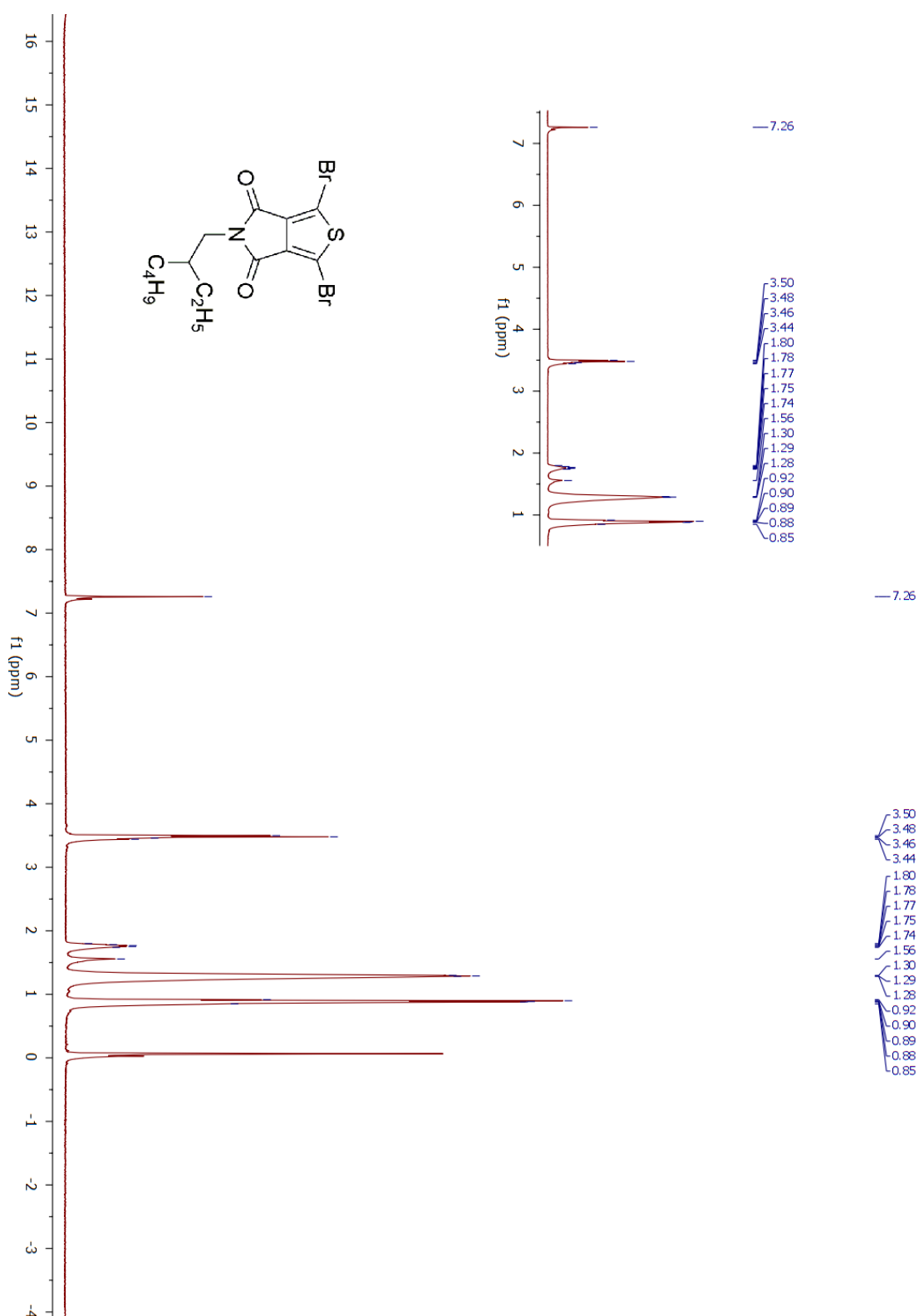


Figure A5. ¹H NMR spectrum of compound 4 in CDCl₃

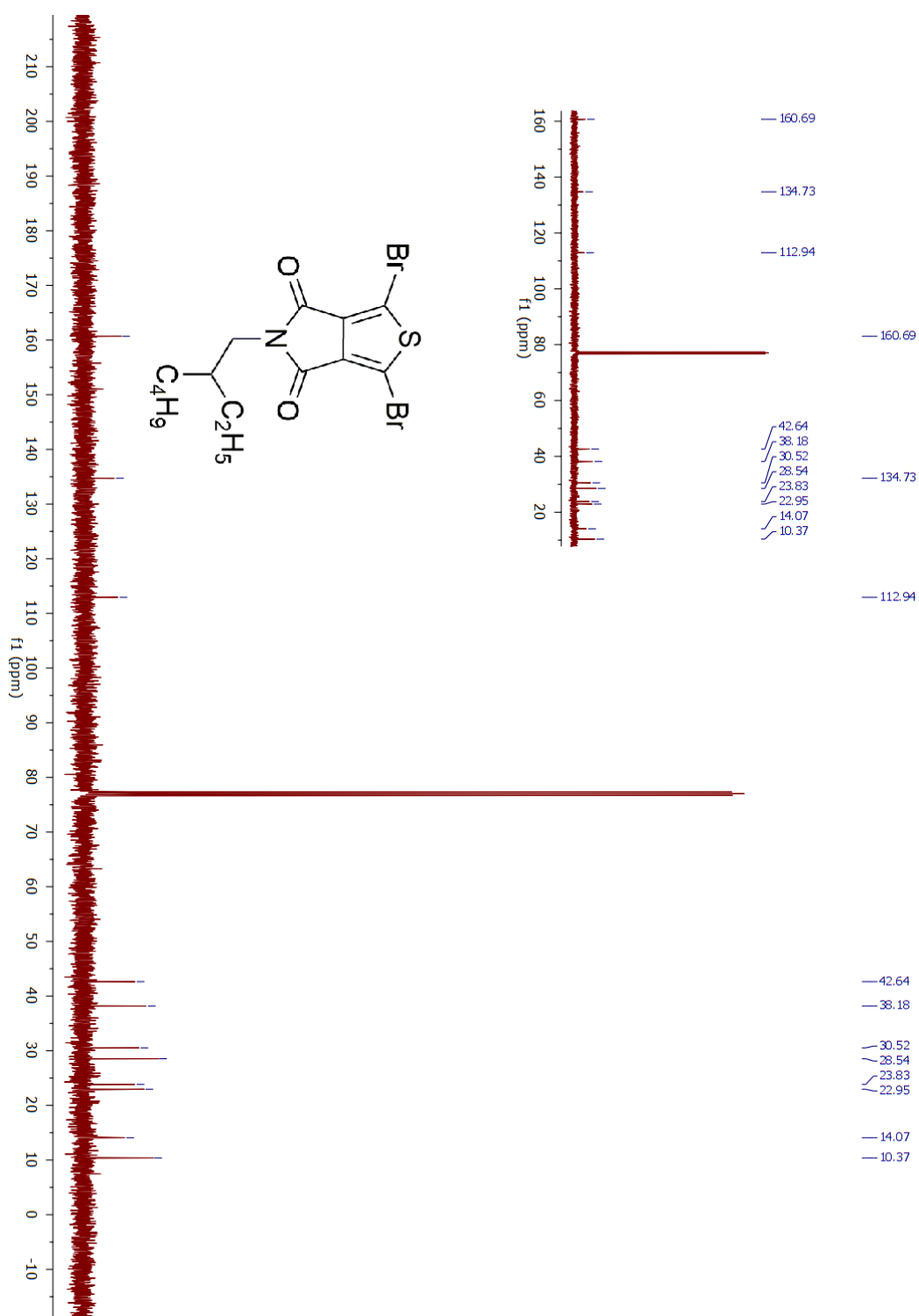


Figure A6. ^{13}C NMR spectrum of compound 4 in CDCl_3

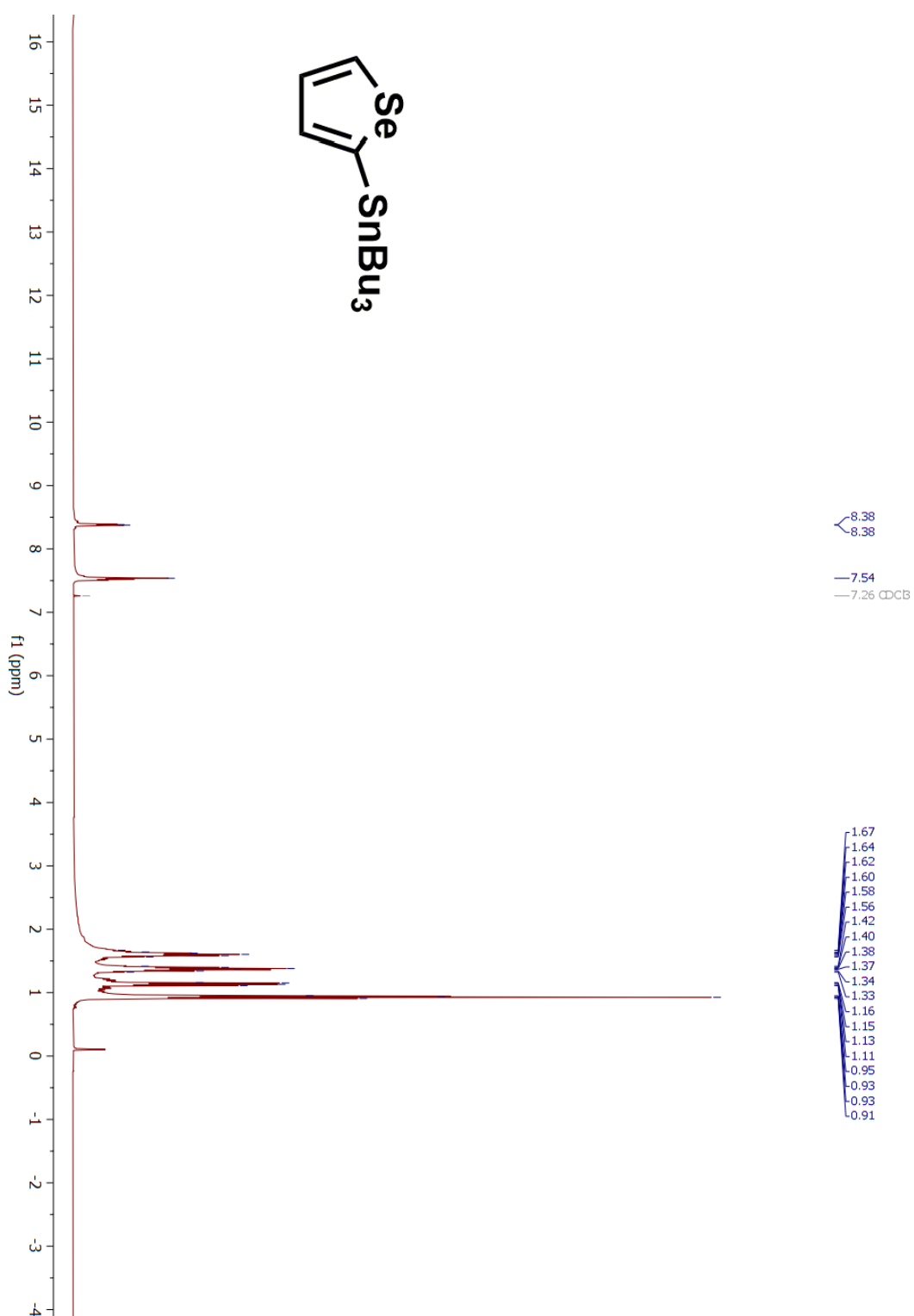


Figure A7. ¹H NMR spectrum of compound 5 in CDCl₃

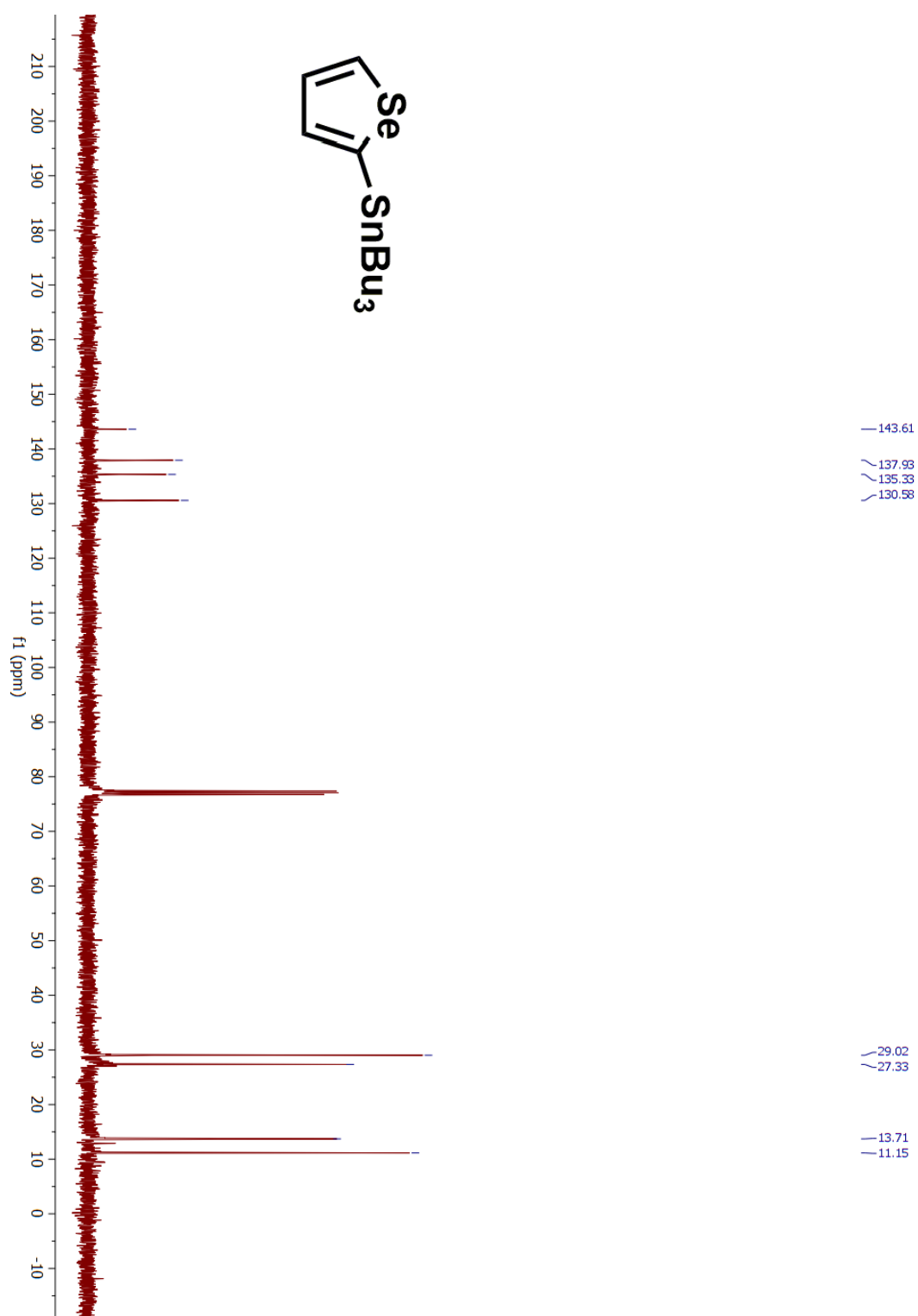


Figure A8. ^{13}C NMR spectrum of compound 5 in CDCl_3

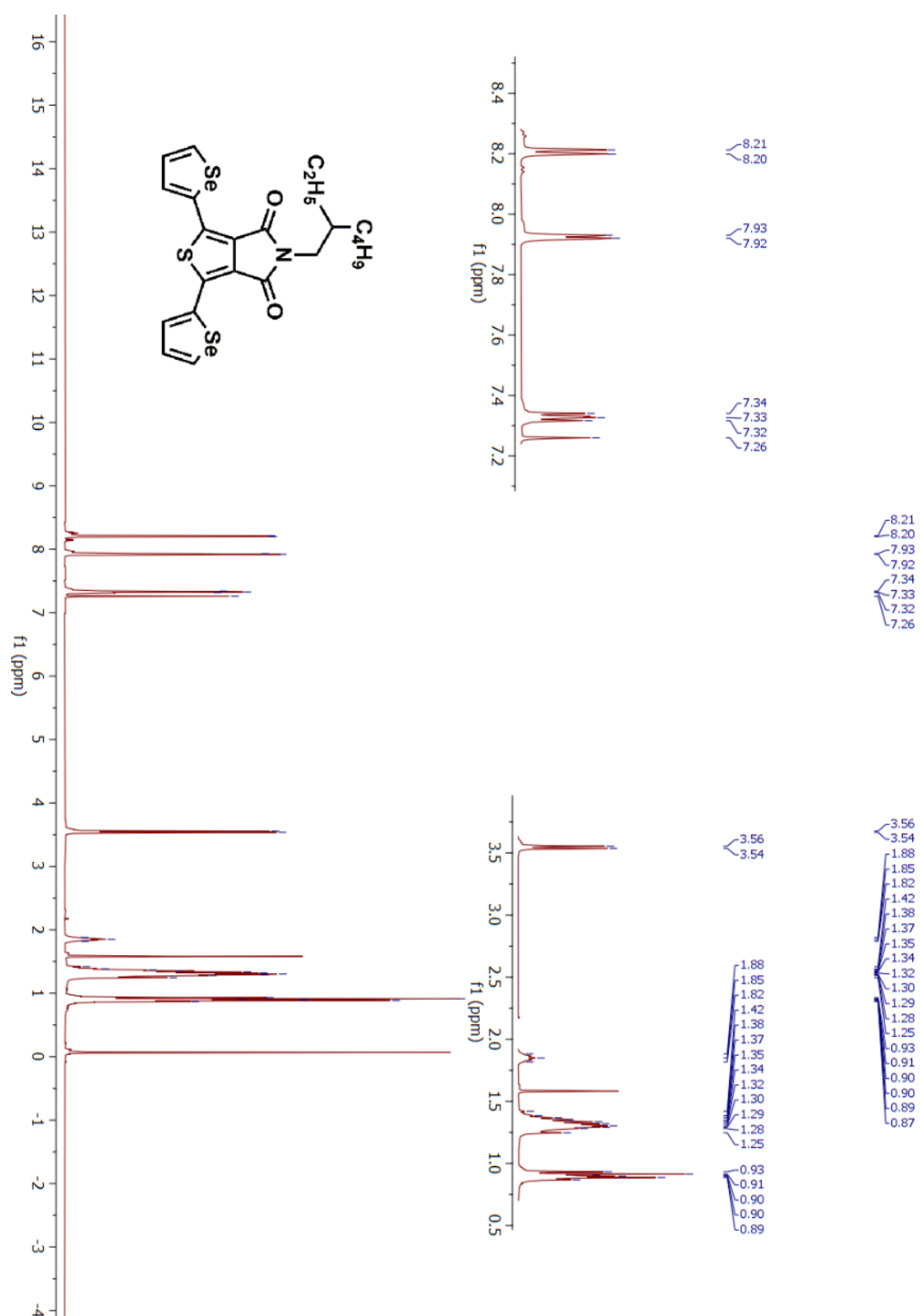


Figure A9. ¹H NMR spectrum of compound 7 in CDCl₃

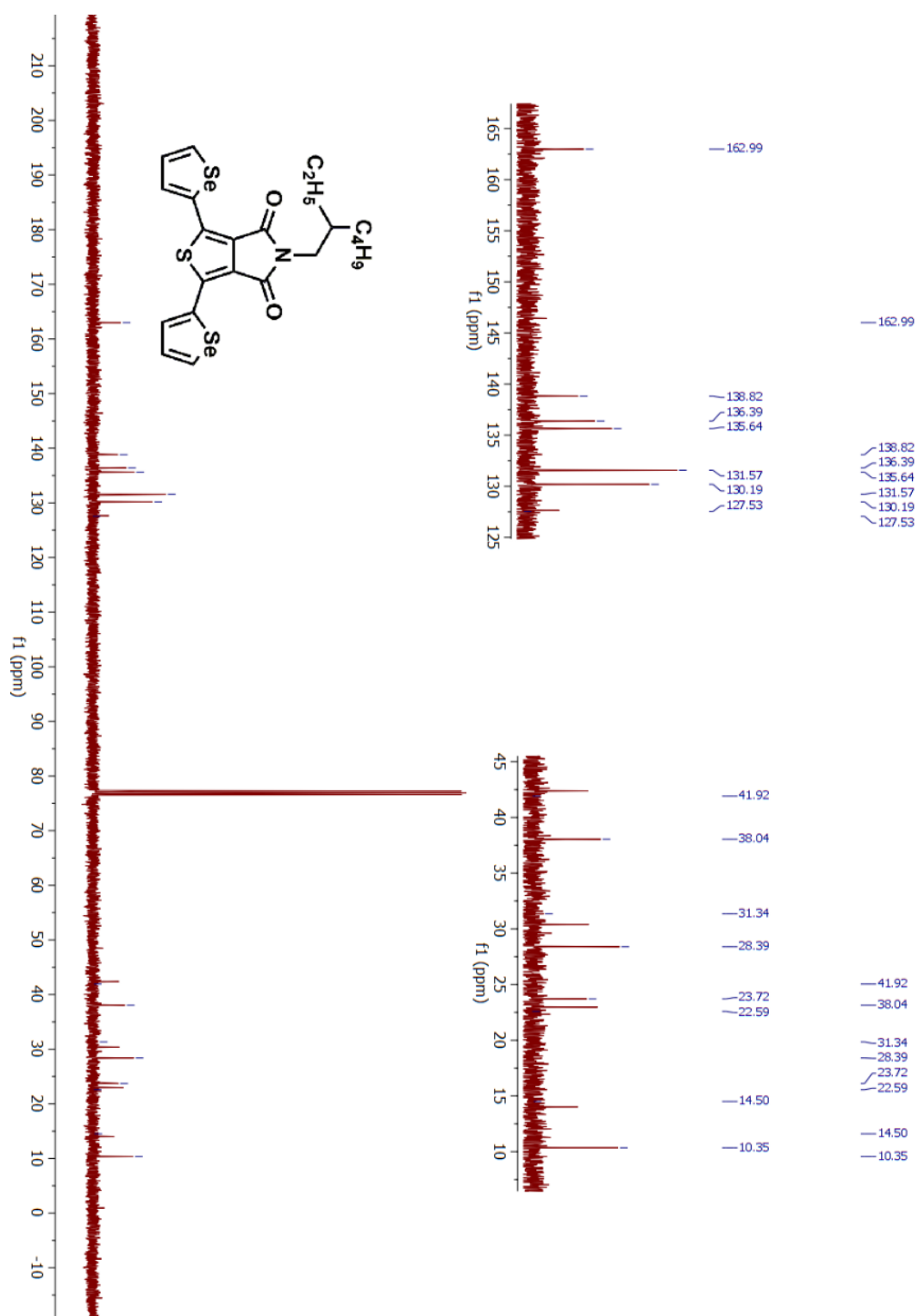


Figure A10. ^{13}C NMR spectrum of compound 7 in CDCl_3

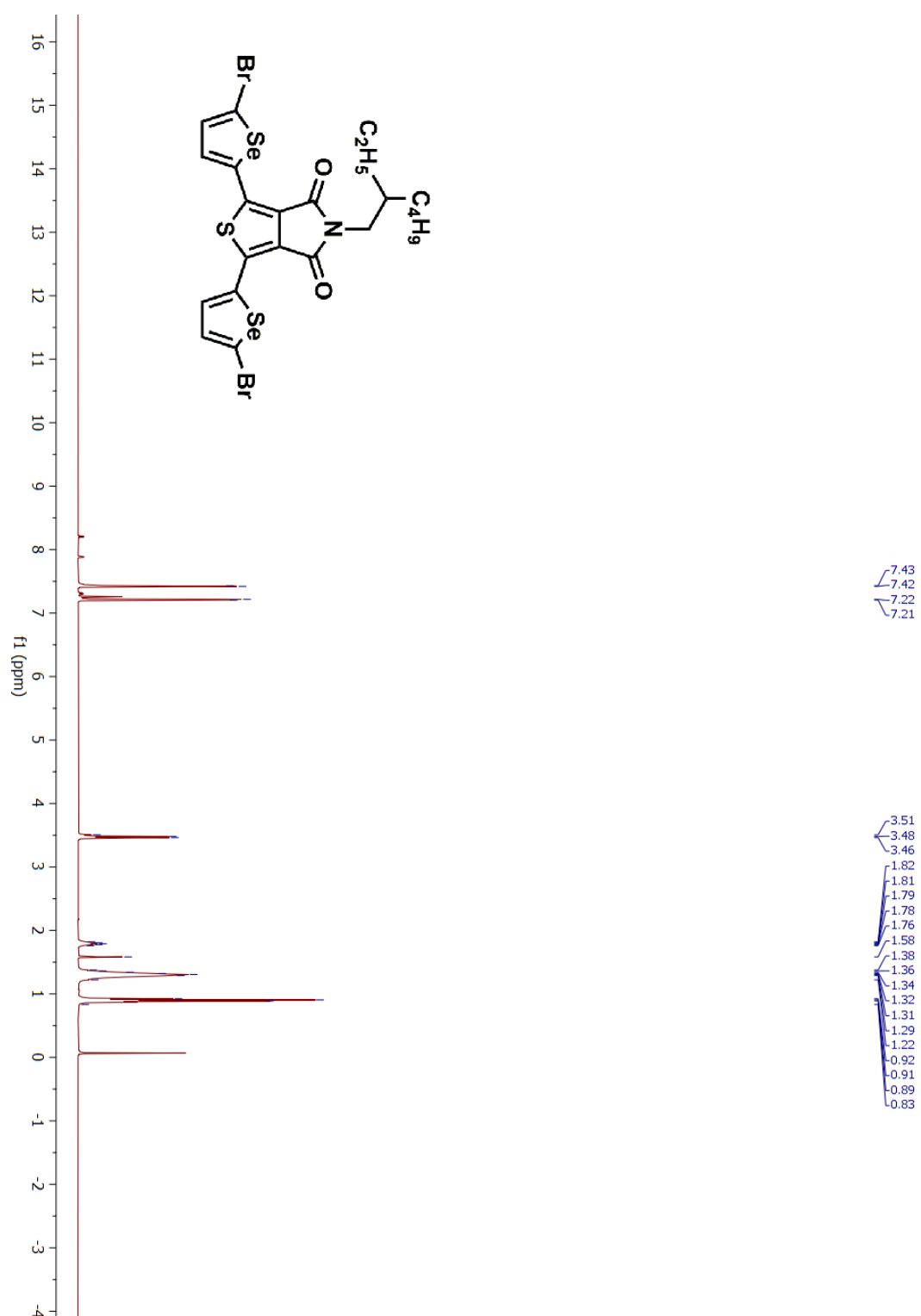


Figure A11. ¹H NMR spectrum of compound M1 in CDCl₃

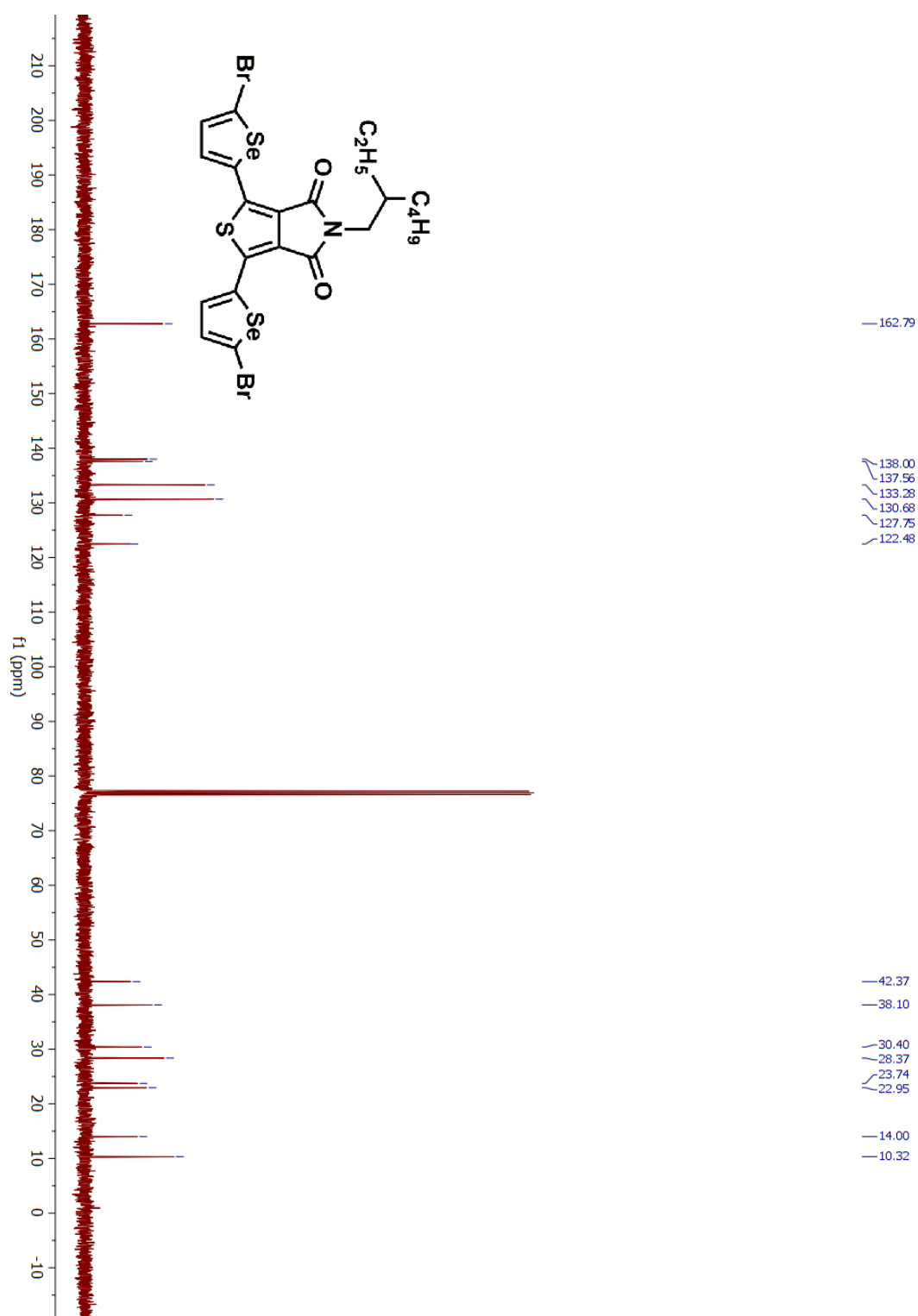


Figure A12. ^{13}C NMR spectrum of compound M1 in CDCl_3

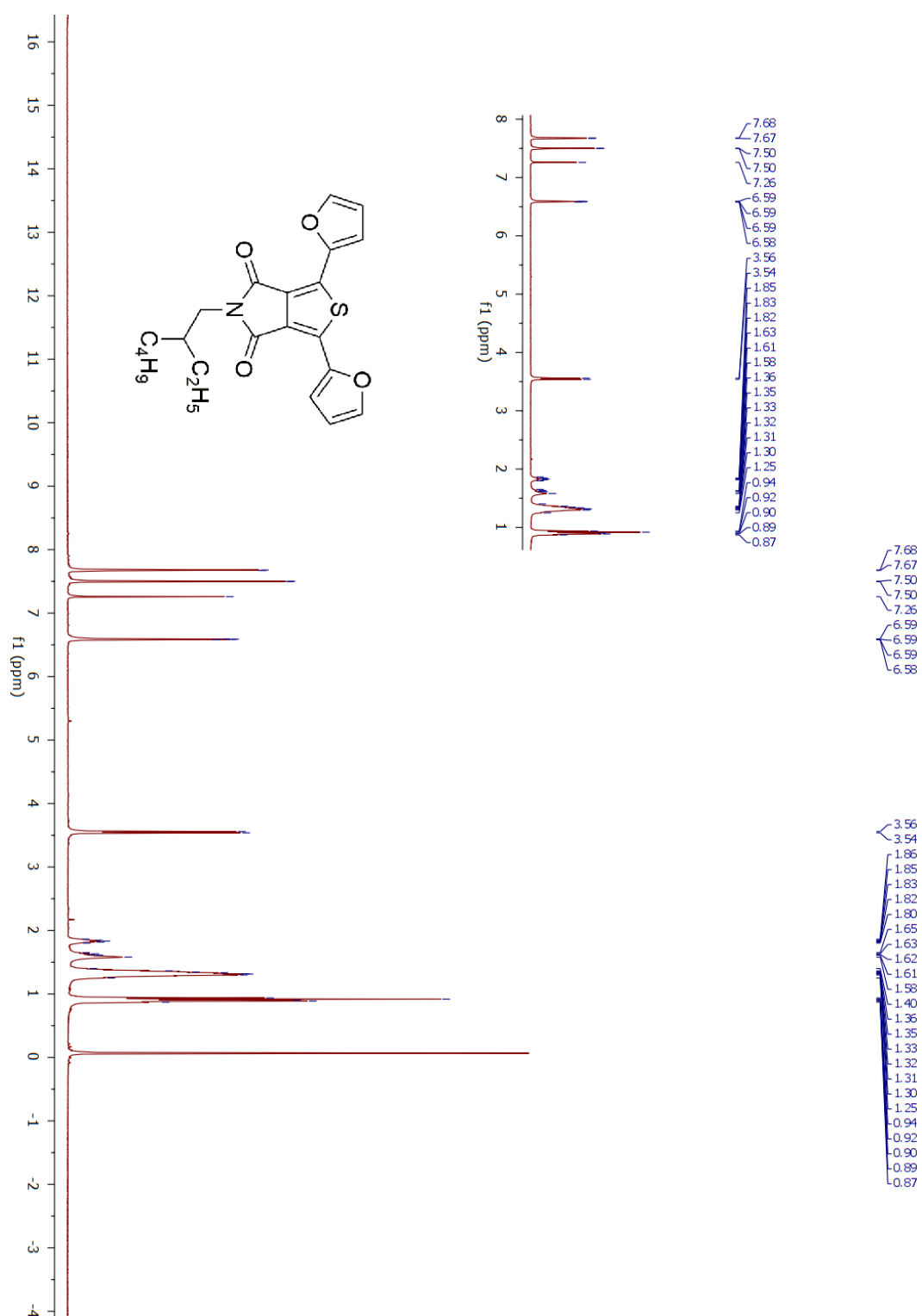


Figure A13. ^1H NMR spectrum of compound 8 in CDCl₃

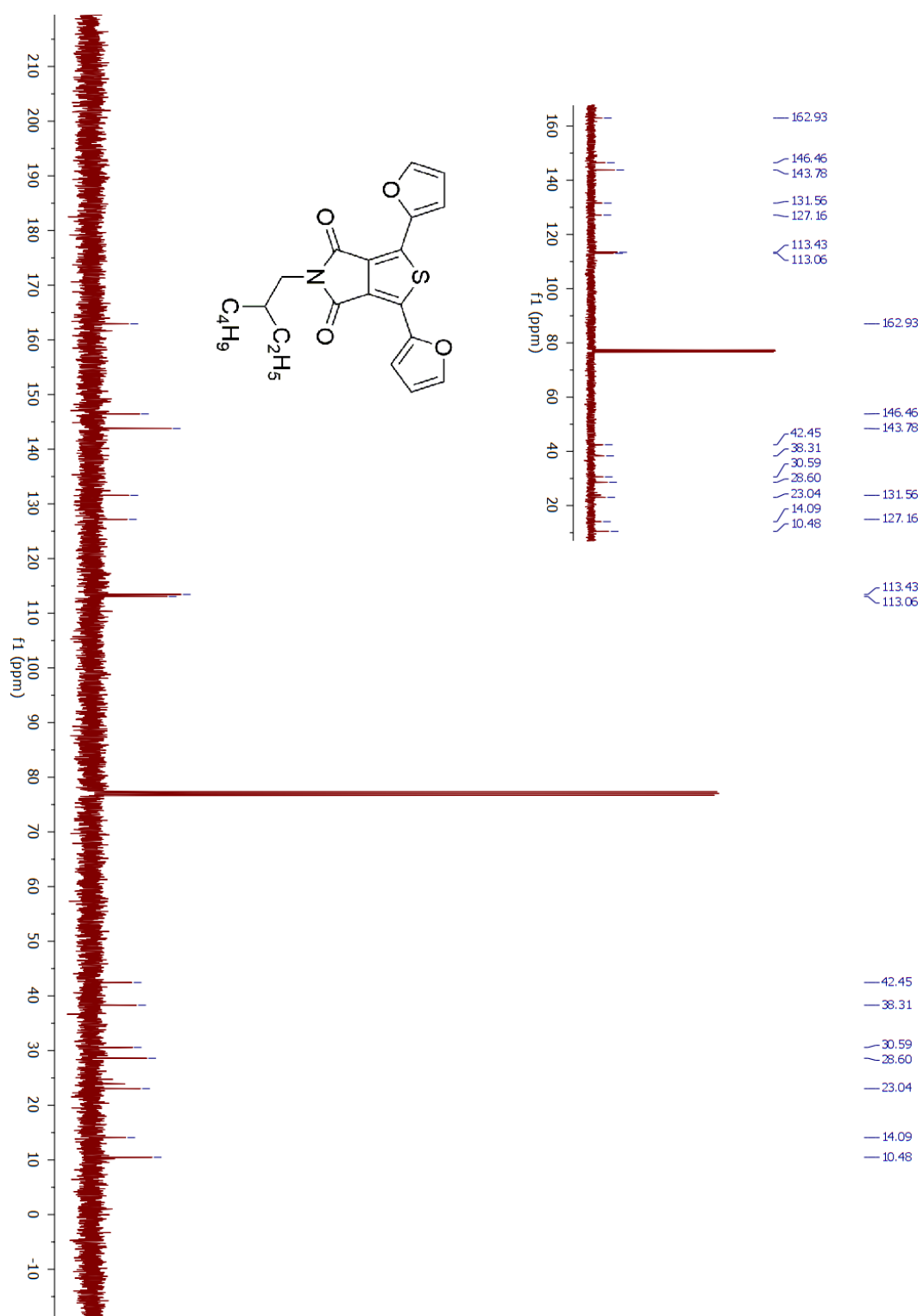


Figure A14. ^{13}C NMR spectrum of compound 8 in CDCl_3

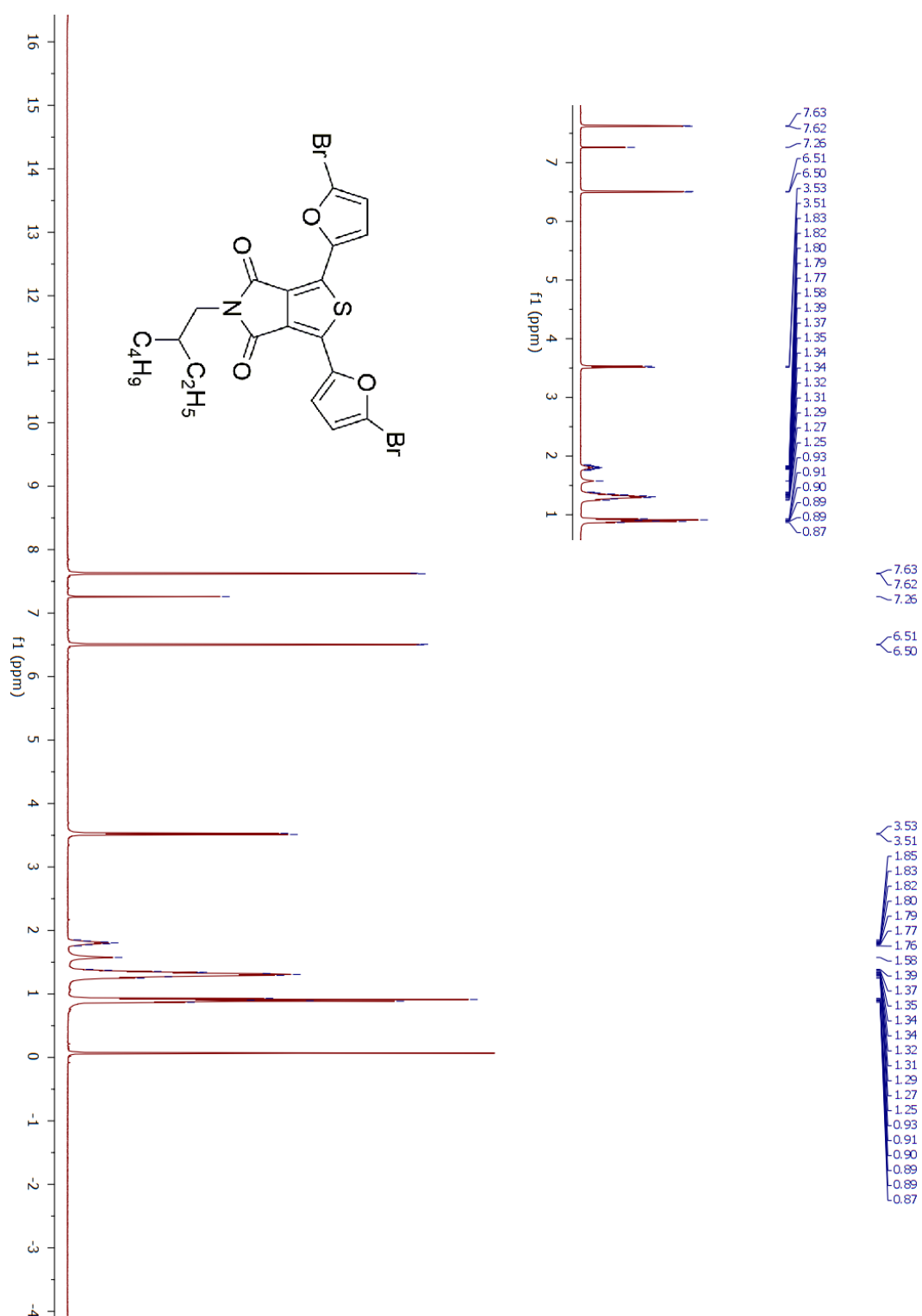


Figure A15. ^1H NMR spectrum of M2 in CDCl_3

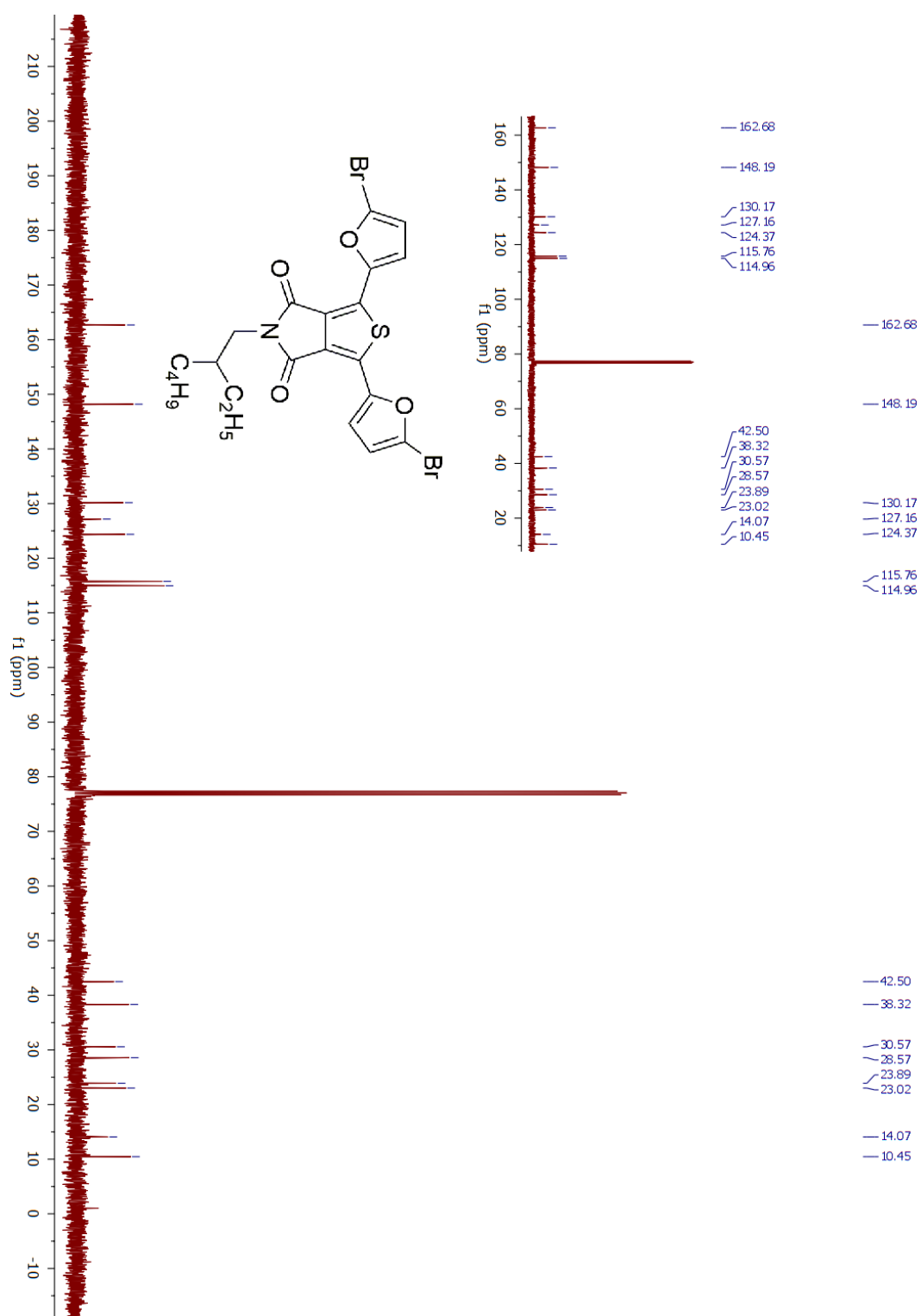


Figure A16. ¹³C NMR spectrum of M2 in CDCl₃

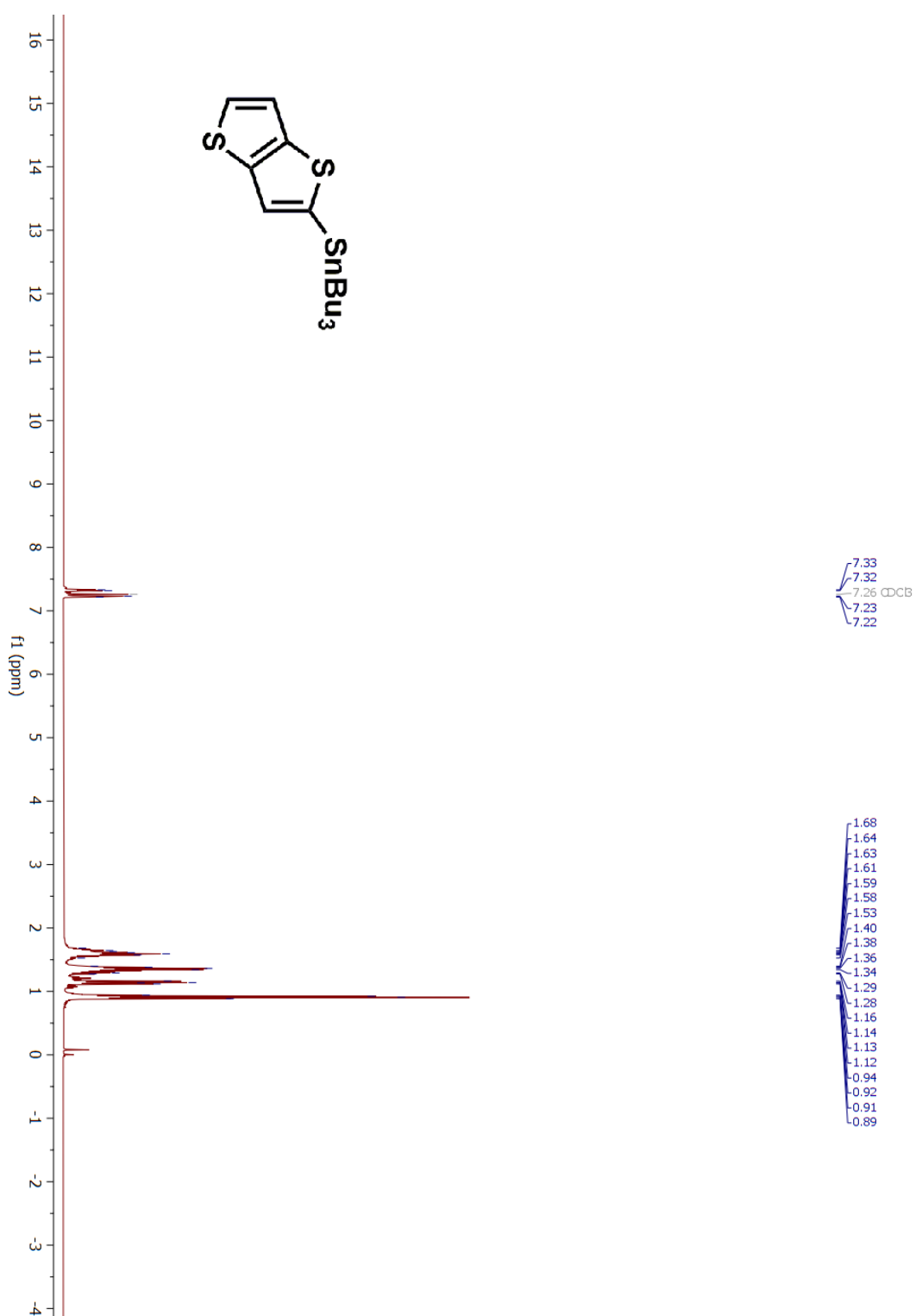


Figure A17. ¹H NMR spectrum of compound 9 in CDCl₃

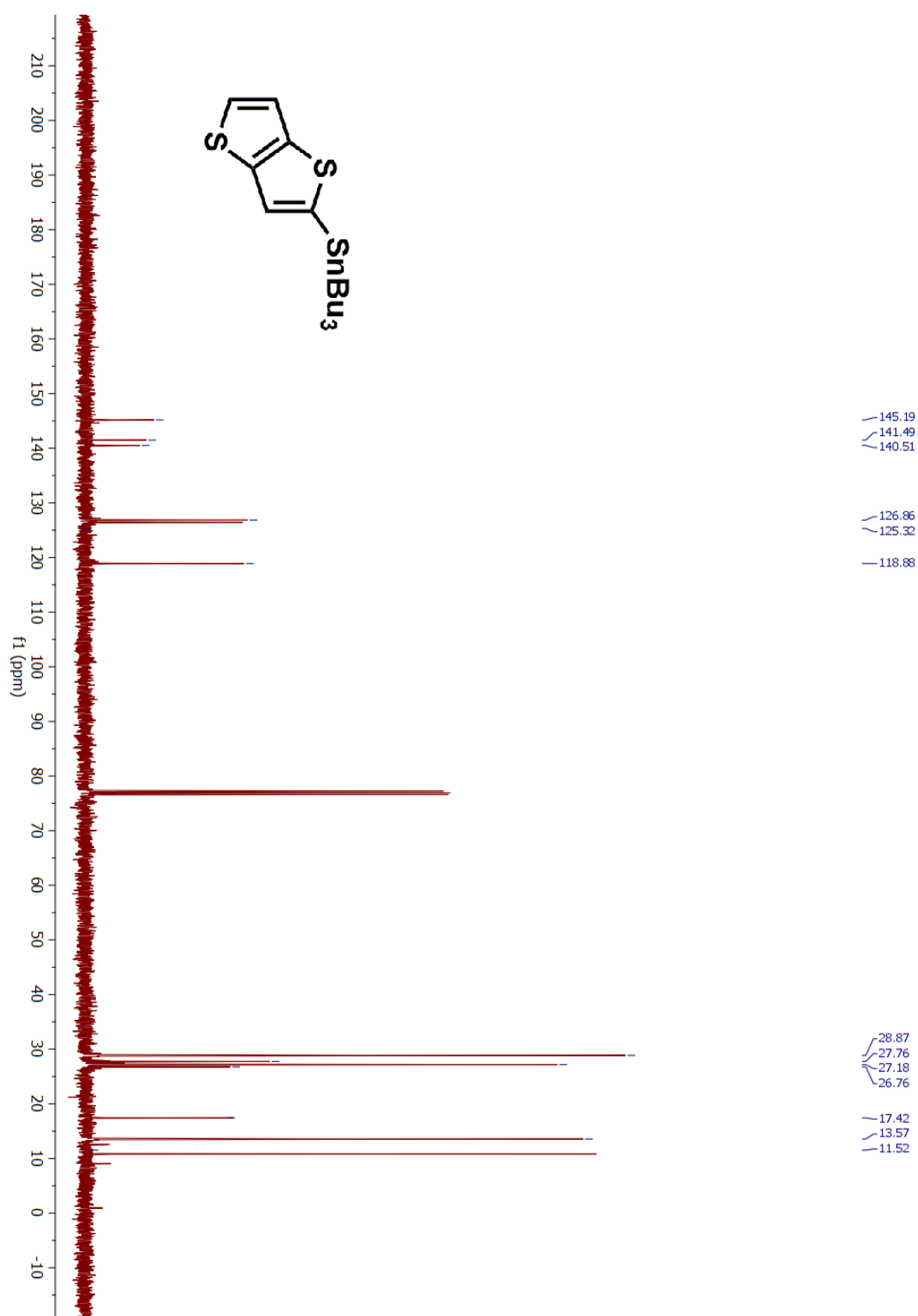


Figure A18. ^{13}C NMR spectrum of compound 9 in CDCl₃

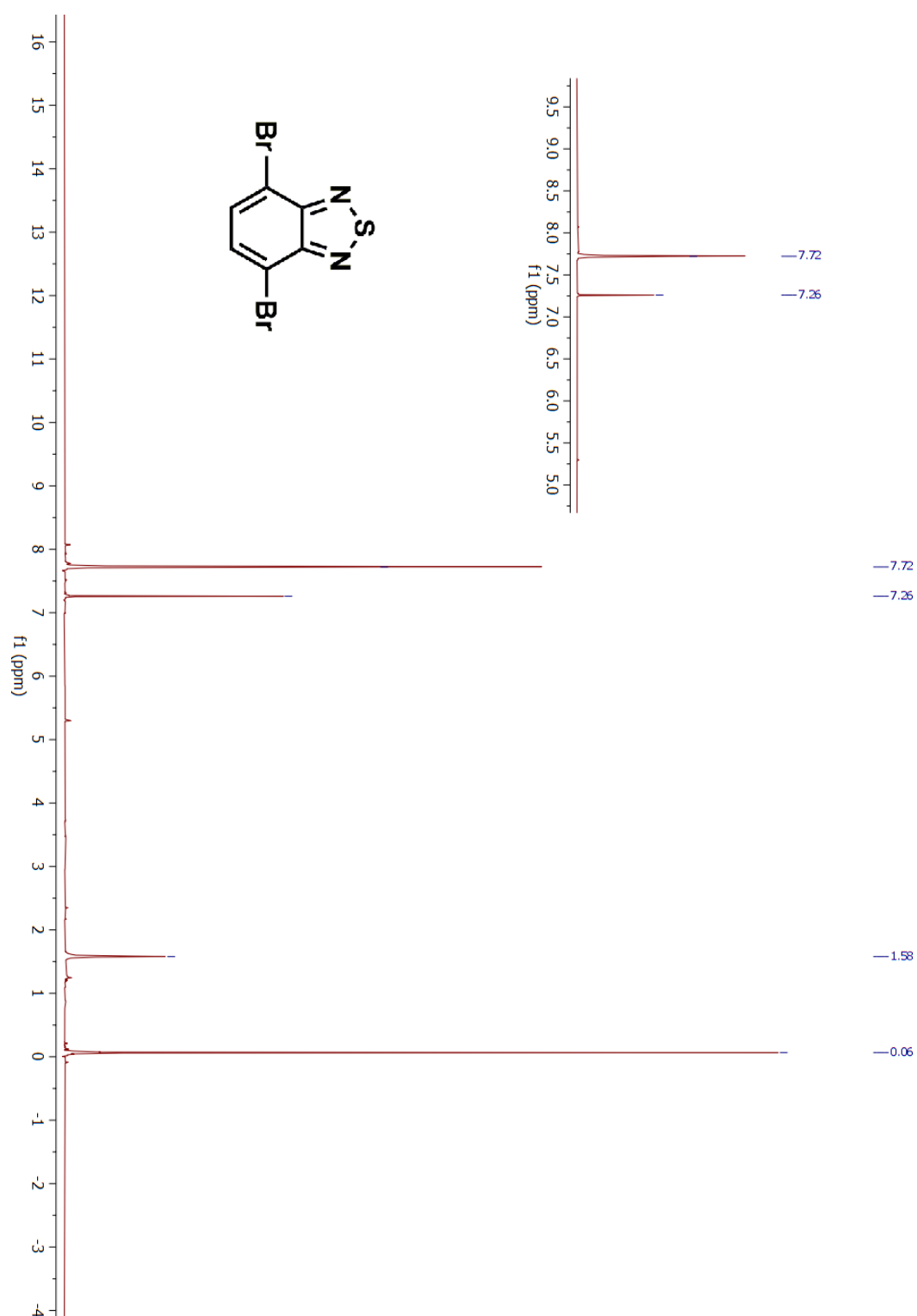


Figure A19. ^1H NMR spectrum of compound 10 in CDCl_3

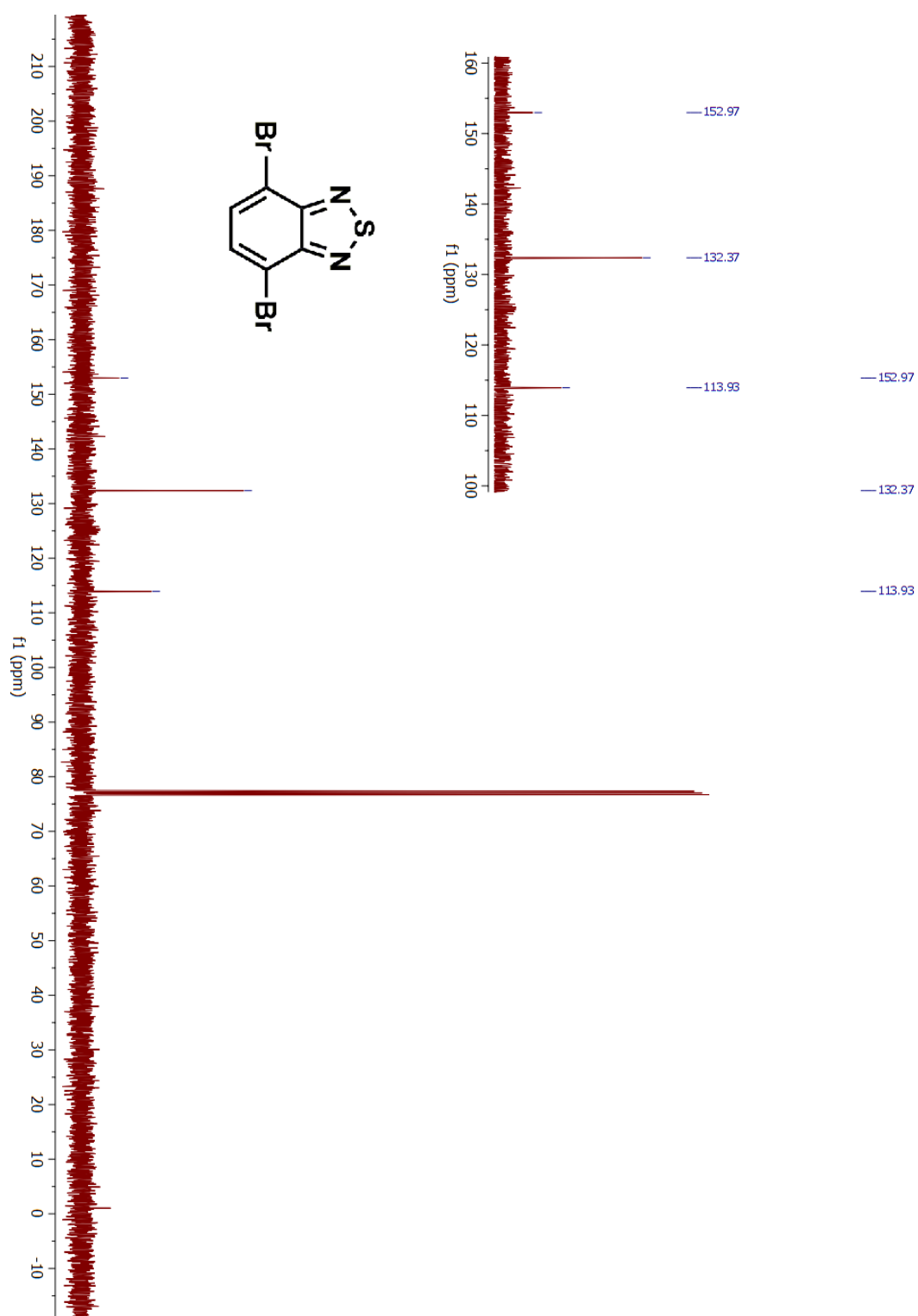


Figure A20. ^{13}C NMR spectrum of compound 10 in CDCl_3

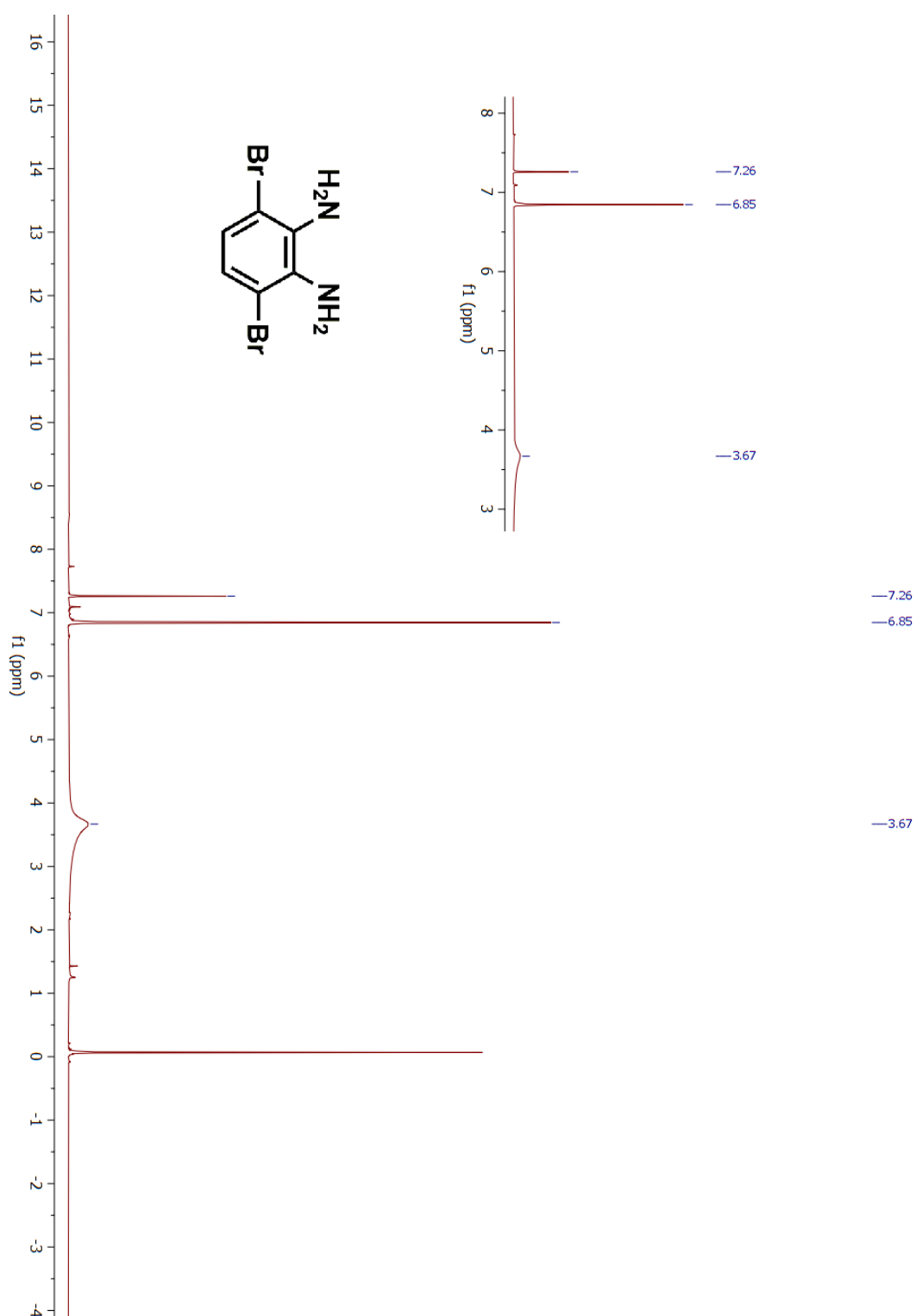


Figure A21. ¹H NMR spectrum of compound 11 in CDCl₃

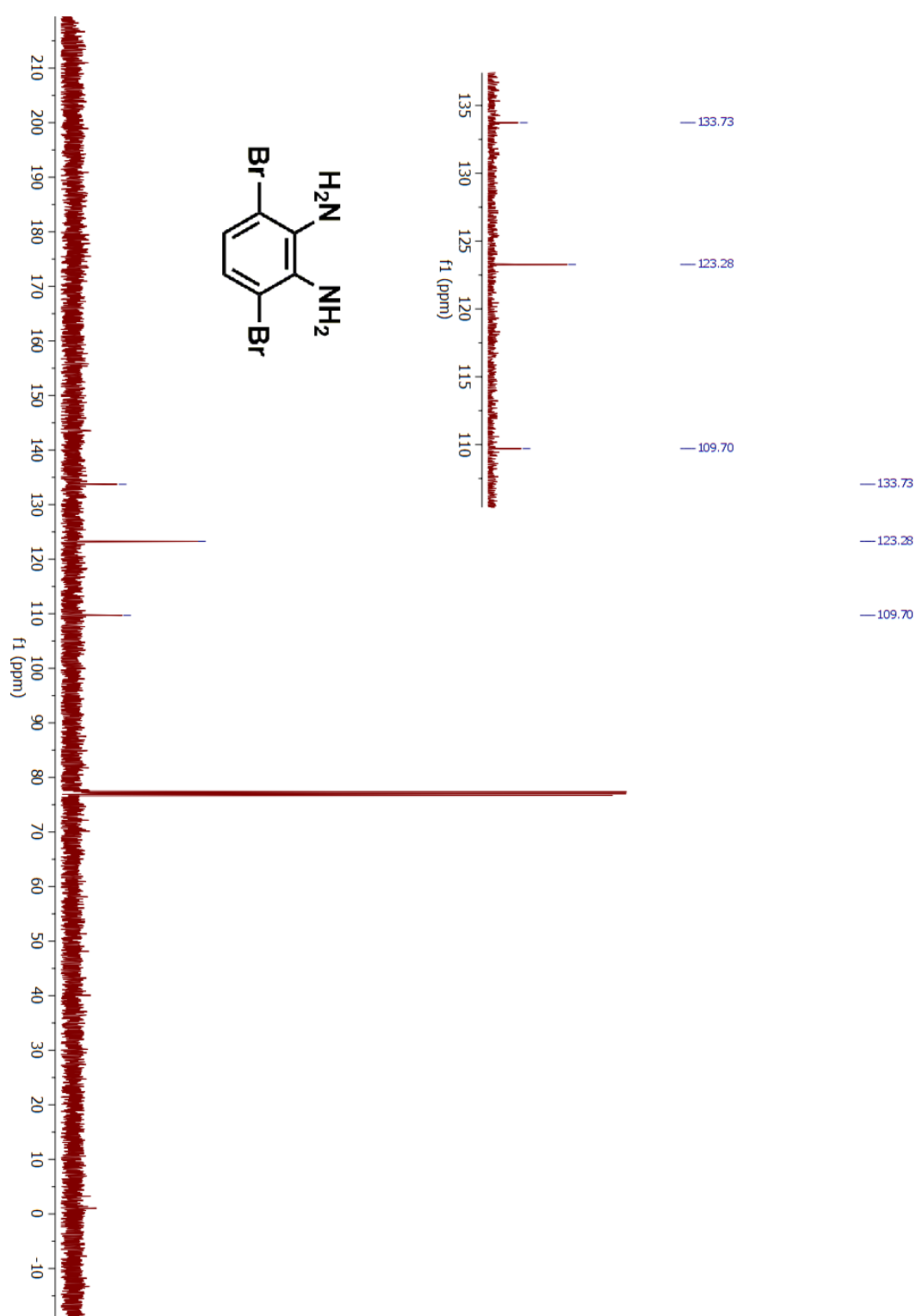


Figure A22. ^{13}C NMR spectrum of compound 11 in CDCl_3

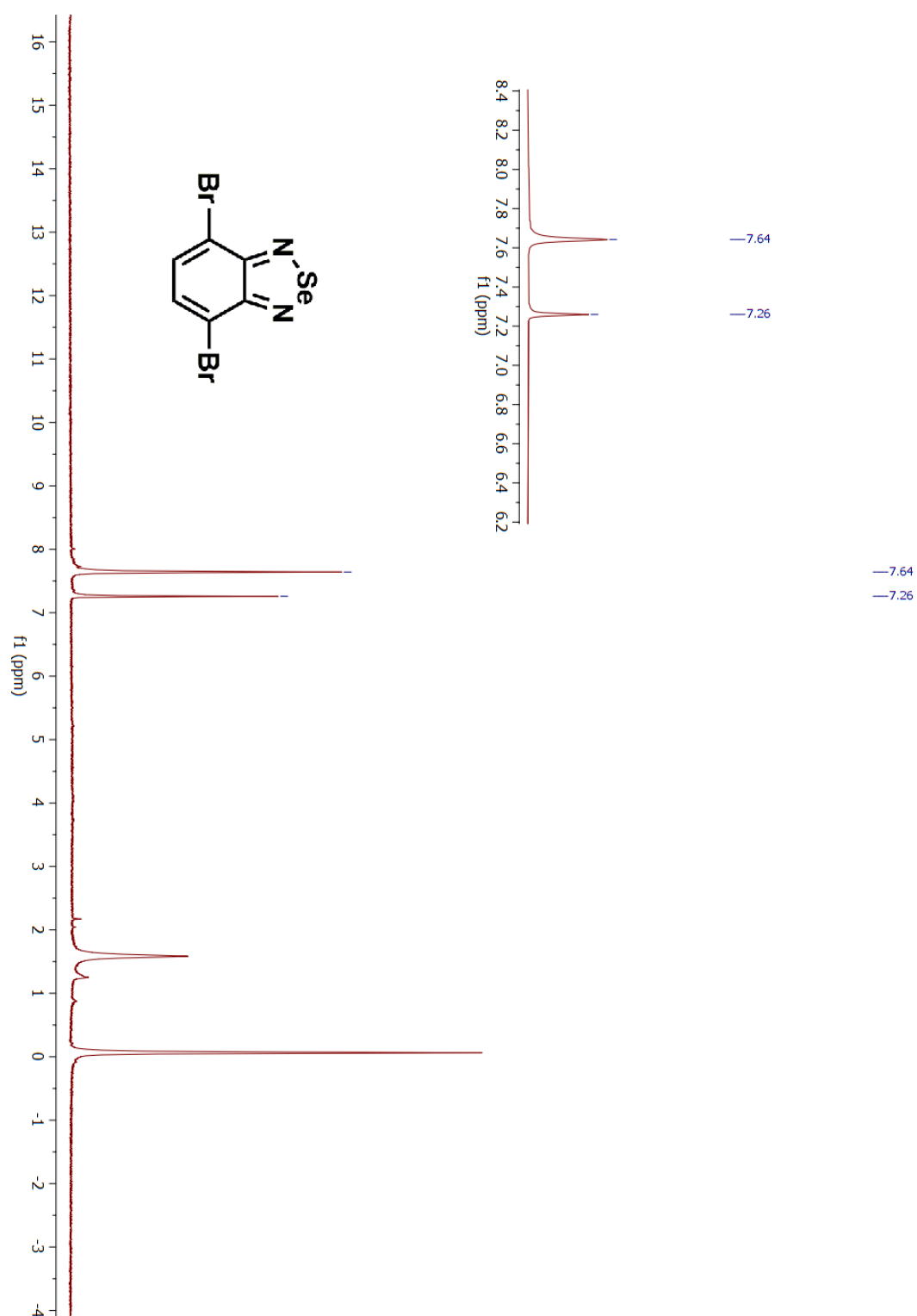


Figure A23. ^1H NMR spectrum of compound 12 in CDCl_3

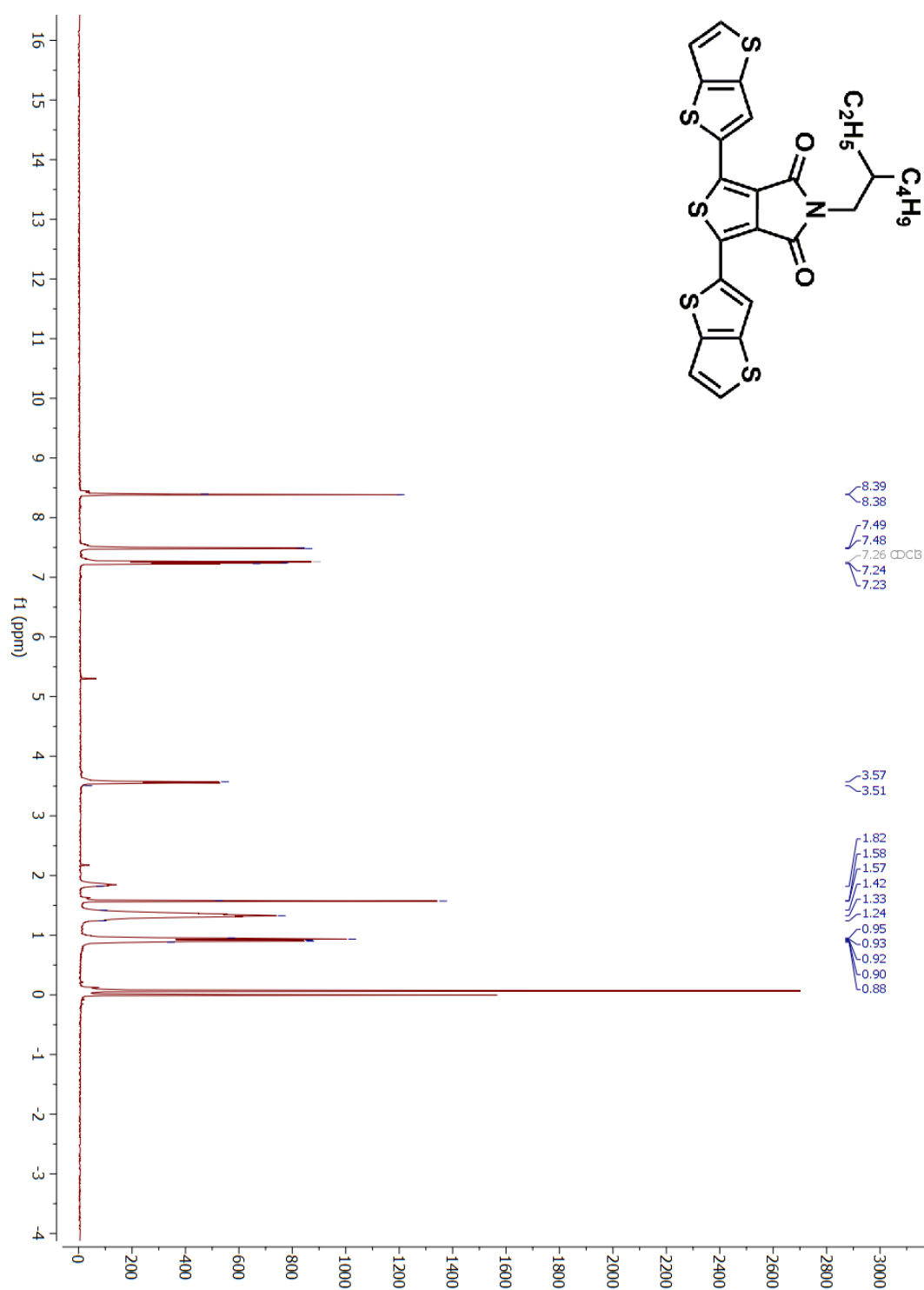


Figure A24. ¹H NMR spectrum of compound 13 in CDCl₃

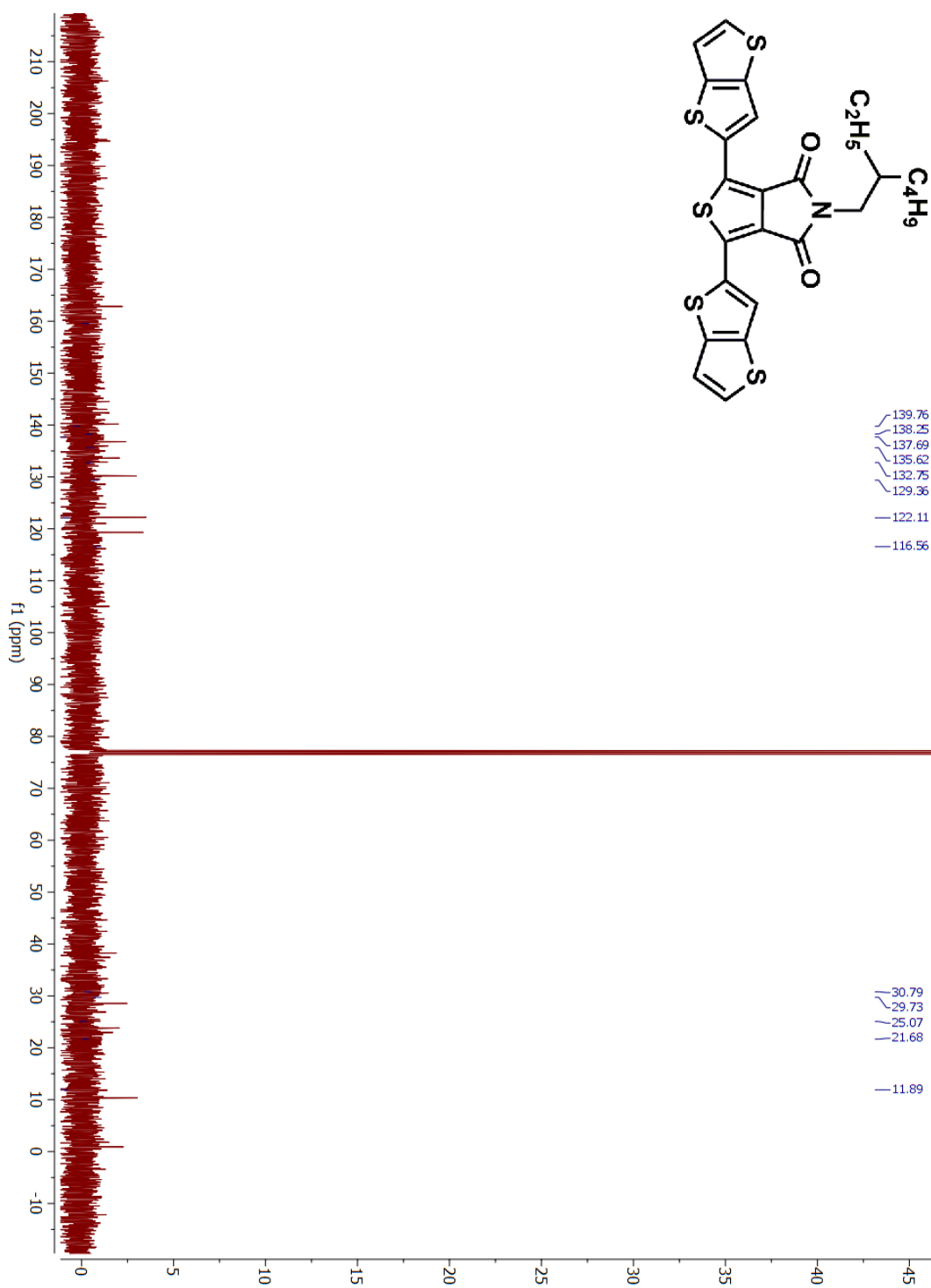


Figure A25. ^{13}C NMR spectrum of compound 13 in CDCl_3

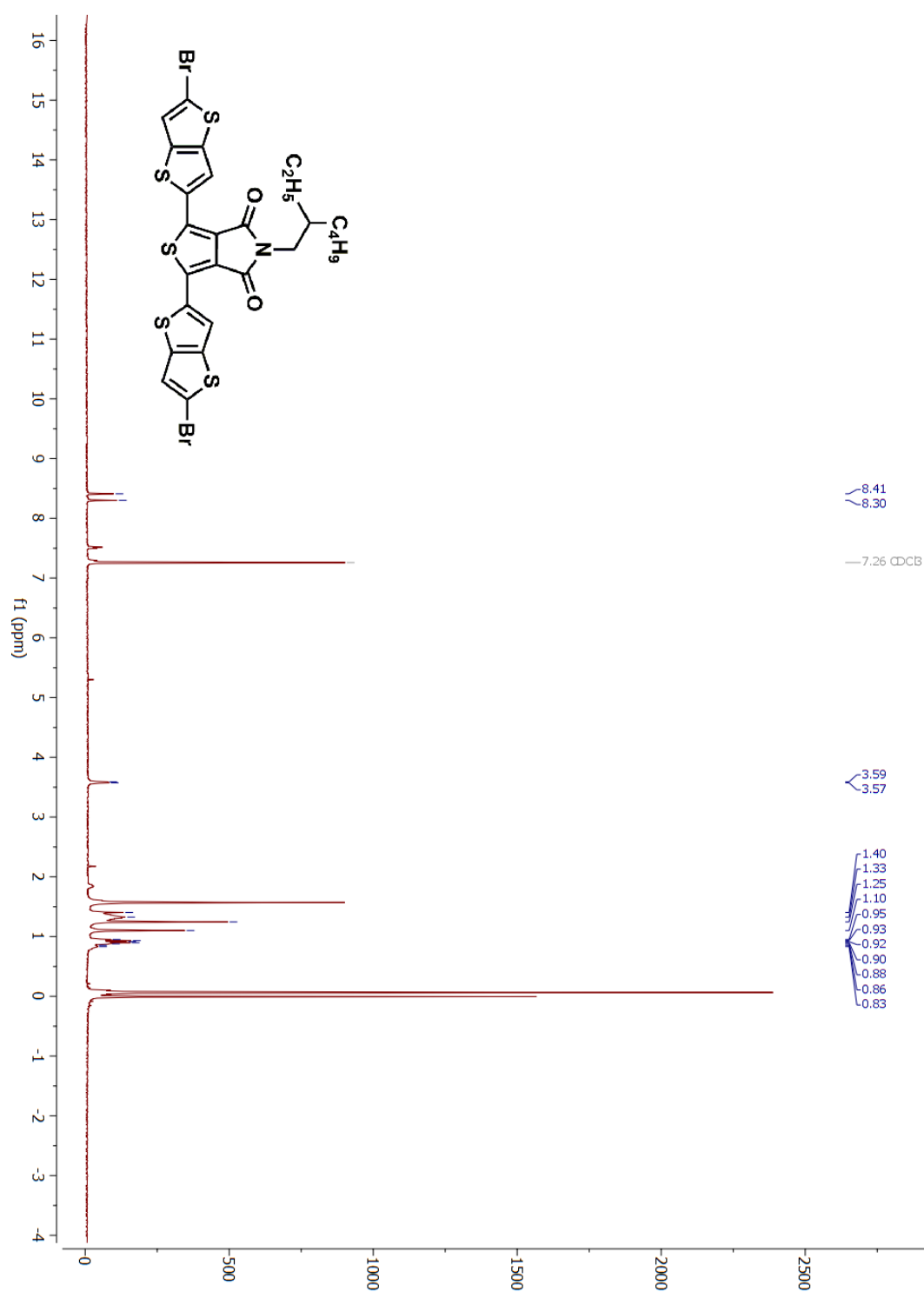
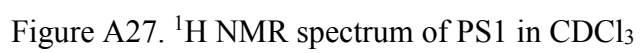
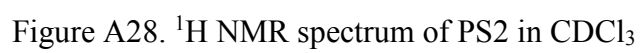


Figure A26. ^1H NMR spectrum of compound M3 in CDCl₃





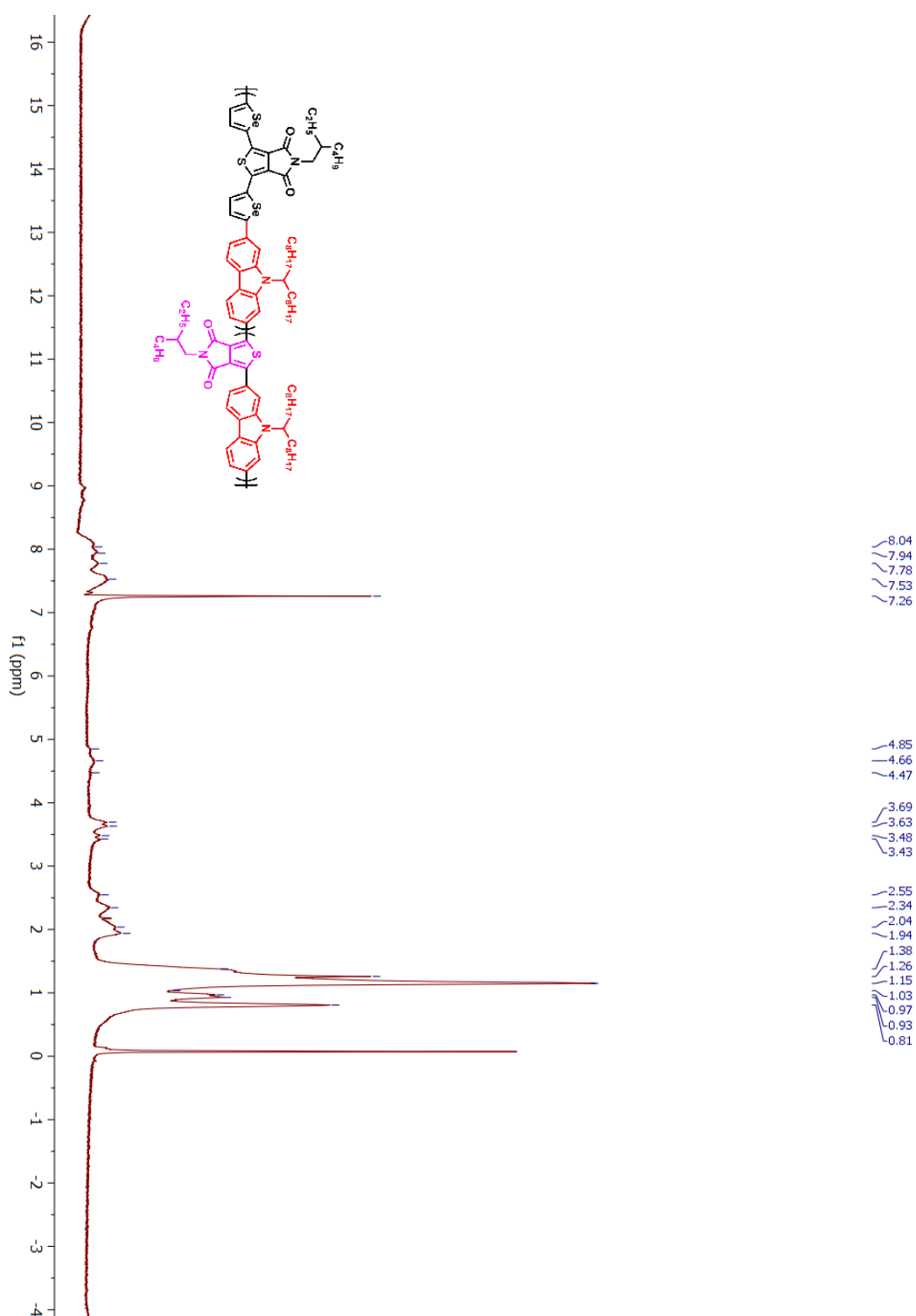


Figure A29. ¹H NMR spectrum of RPS1 in CDCl₃

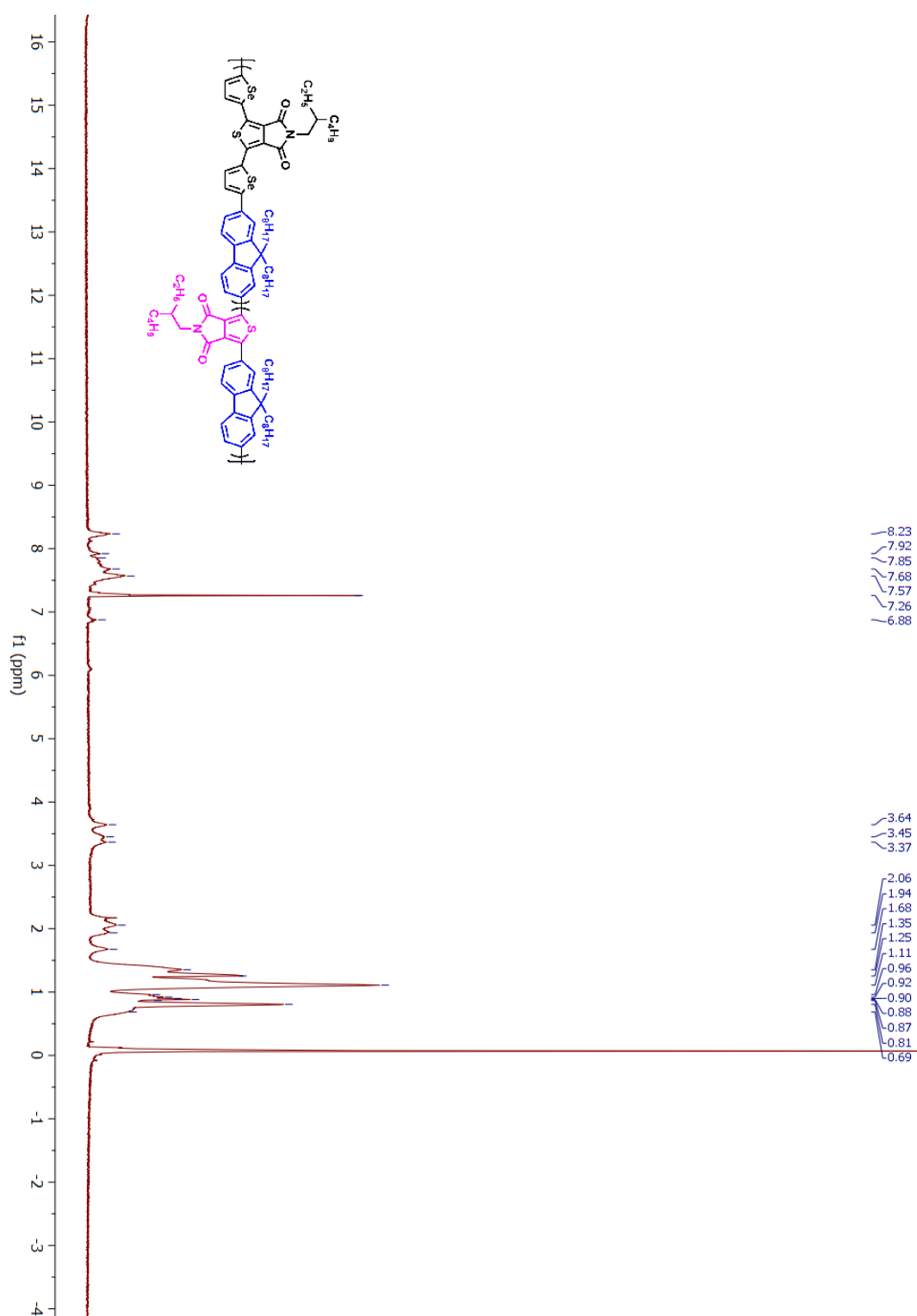


Figure A30. ^1H NMR spectrum of RPS2 in CDCl_3

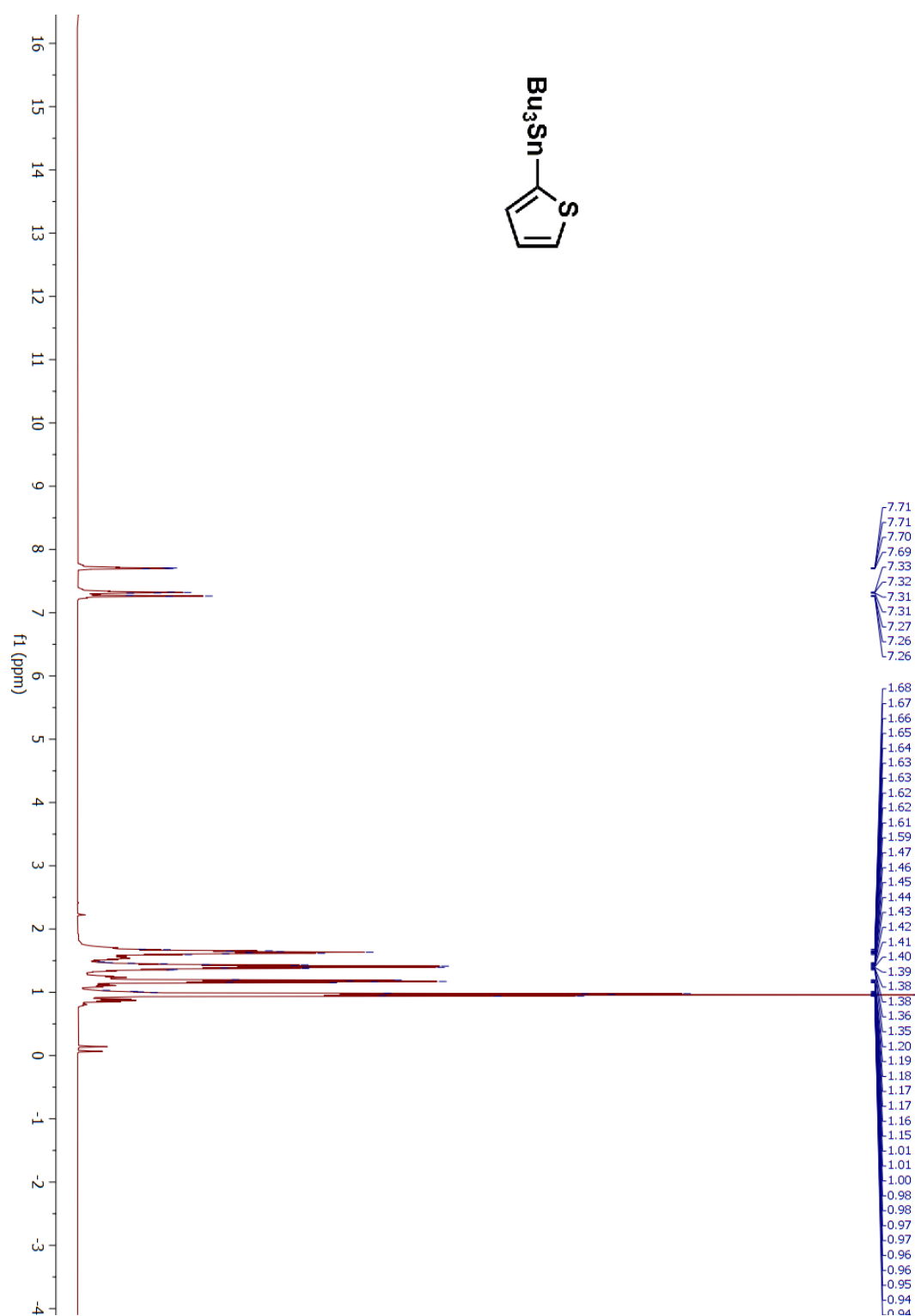


Figure A31. ^1H NMR spectrum of compound 14 in CDCl_3

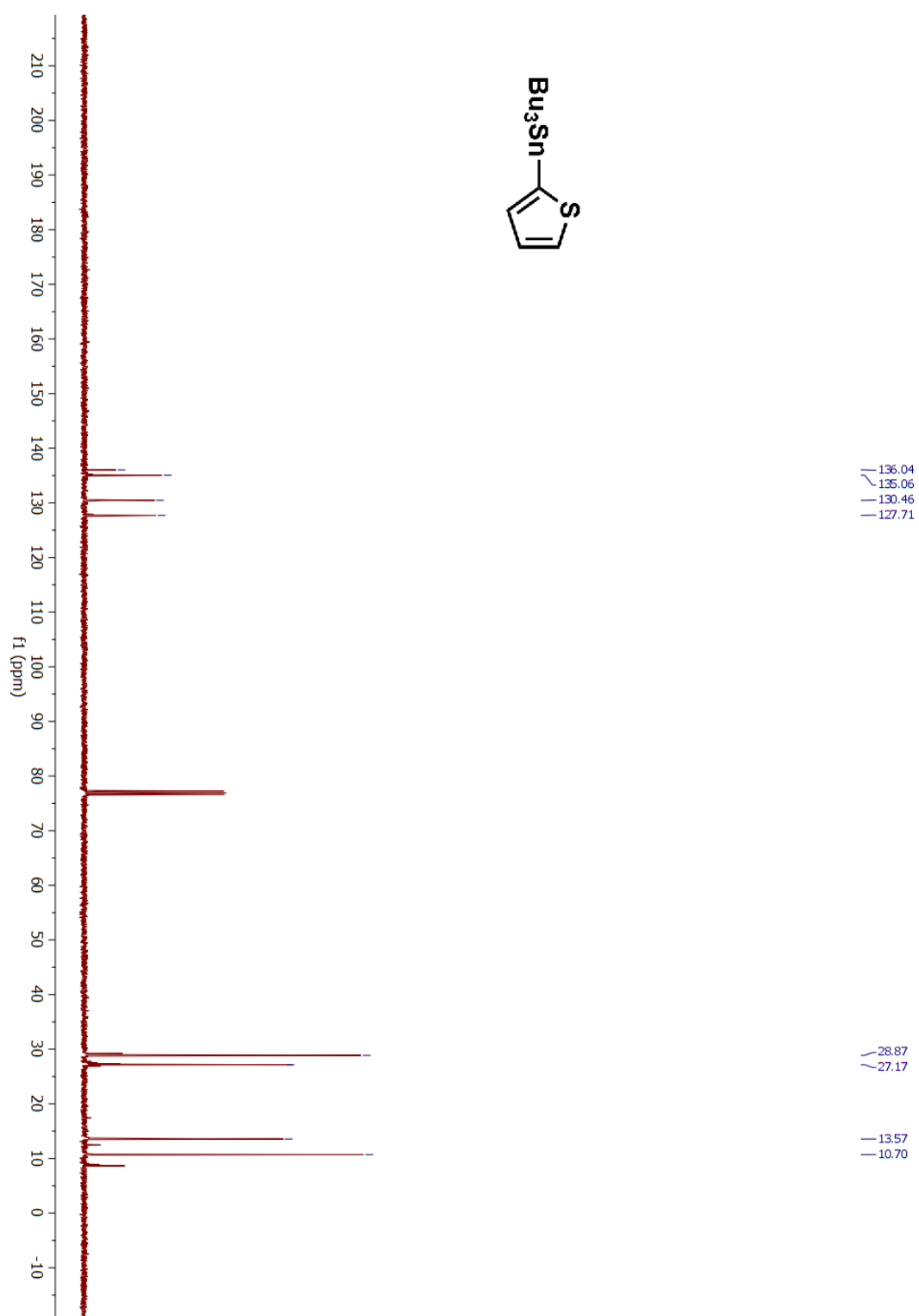


Figure A32. ^{13}C NMR spectrum of compound 14 in CDCl_3

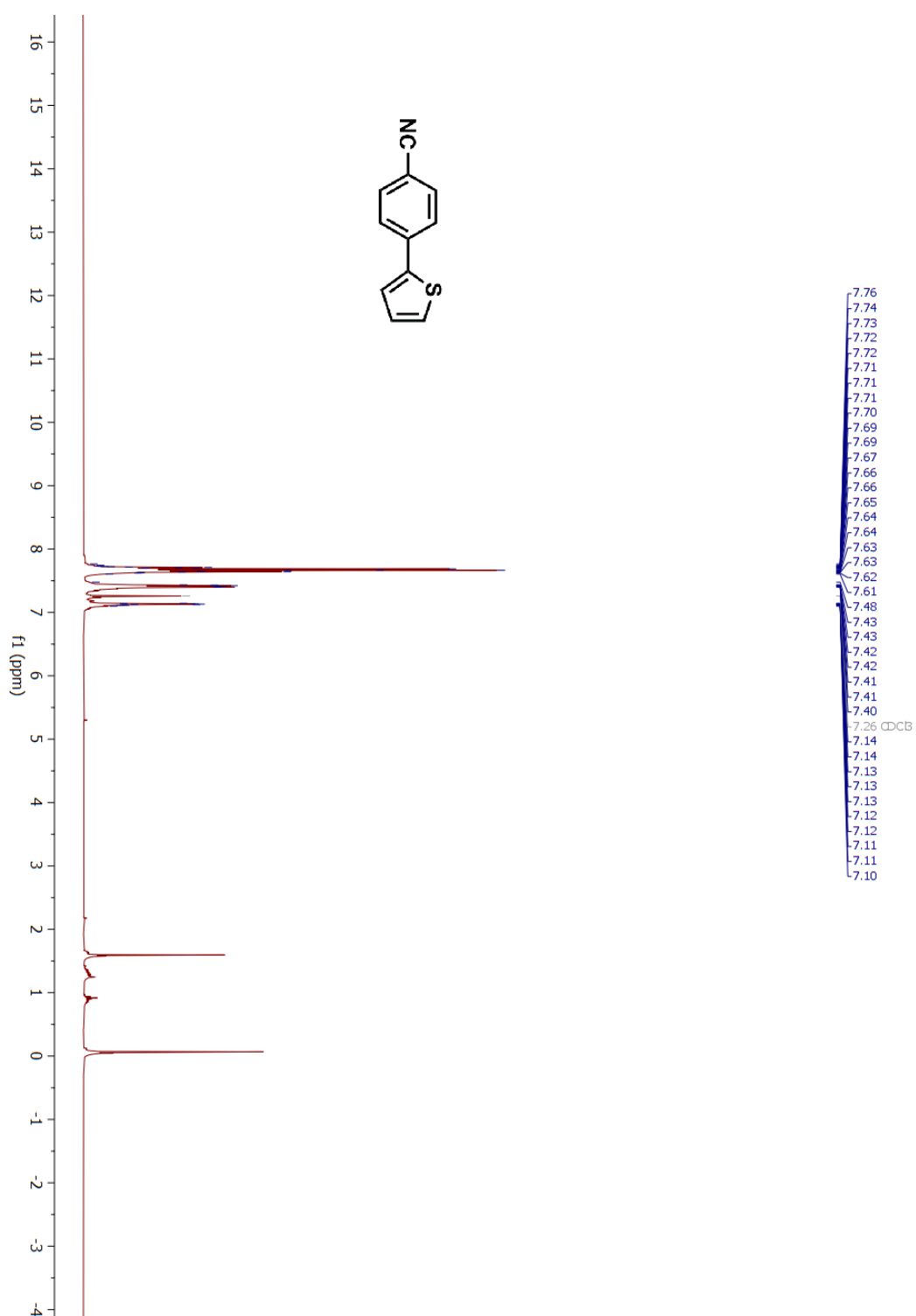


Figure A33. ¹H NMR spectrum of compound 15 in CDCl₃

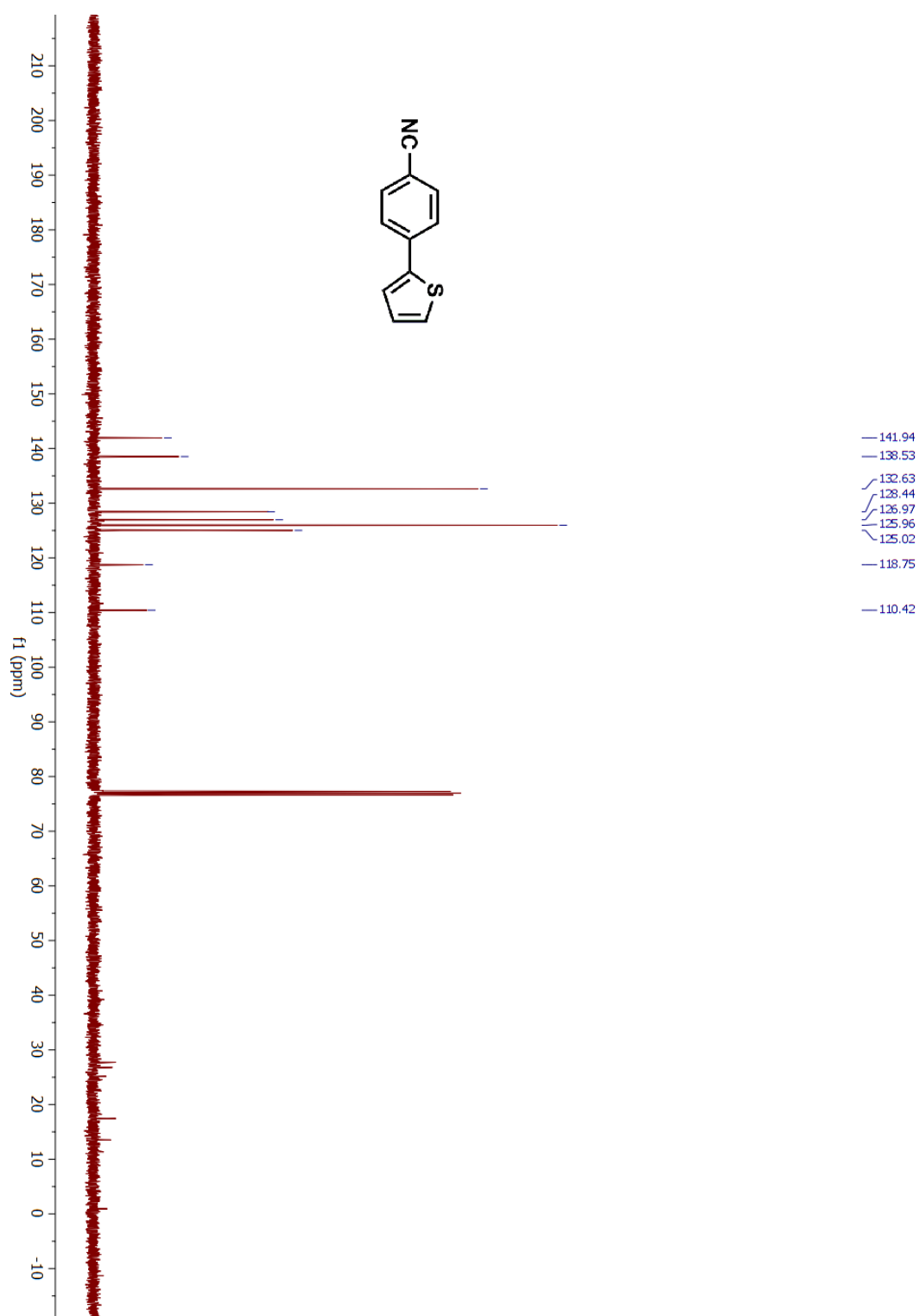


Figure A34. ^{13}C NMR spectrum of compound 15 in CDCl₃

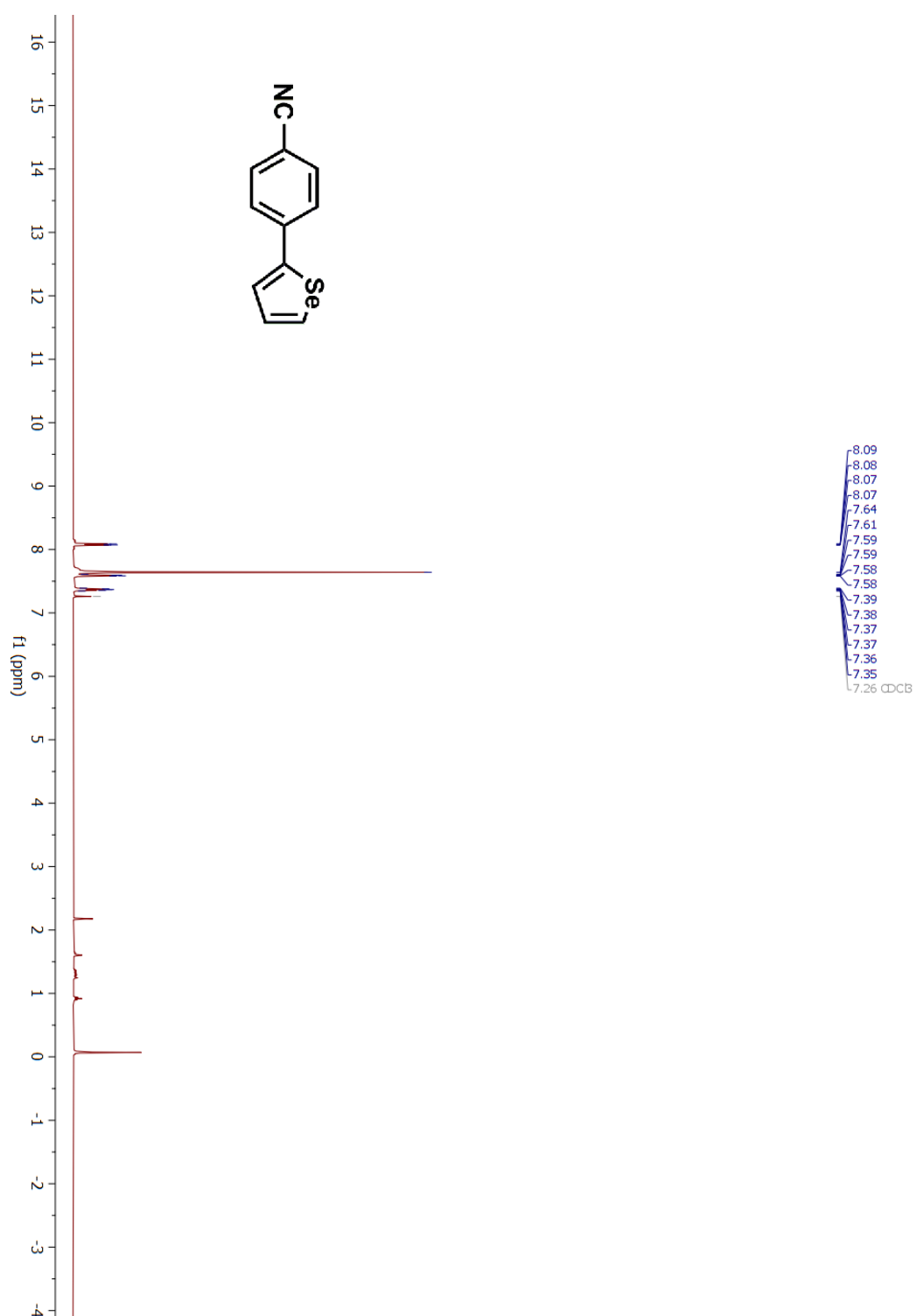


Figure A35. ^1H NMR spectrum of compound 16 in CDCl₃

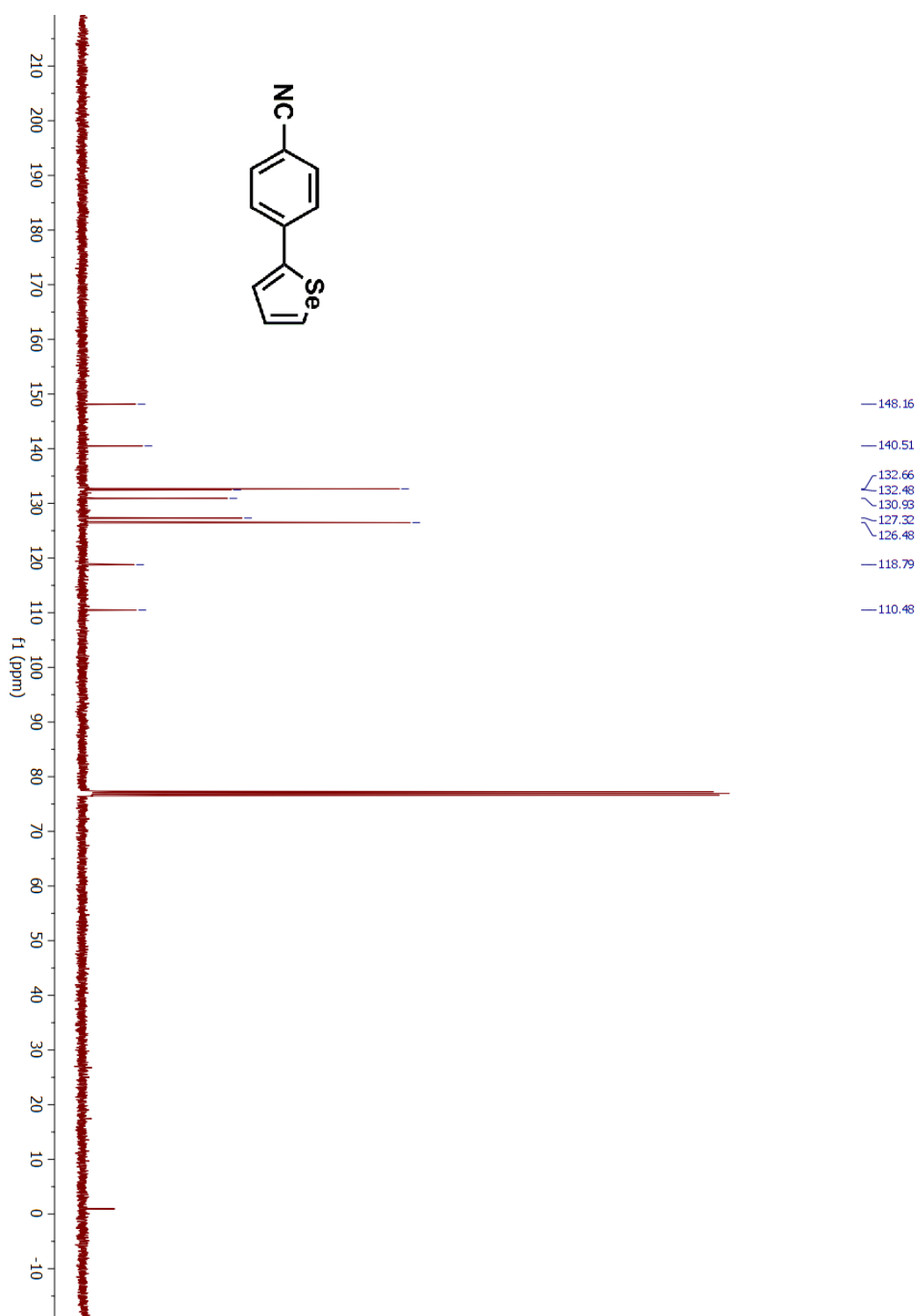


Figure A36. ^{13}C NMR spectrum of compound 16 in CDCl_3

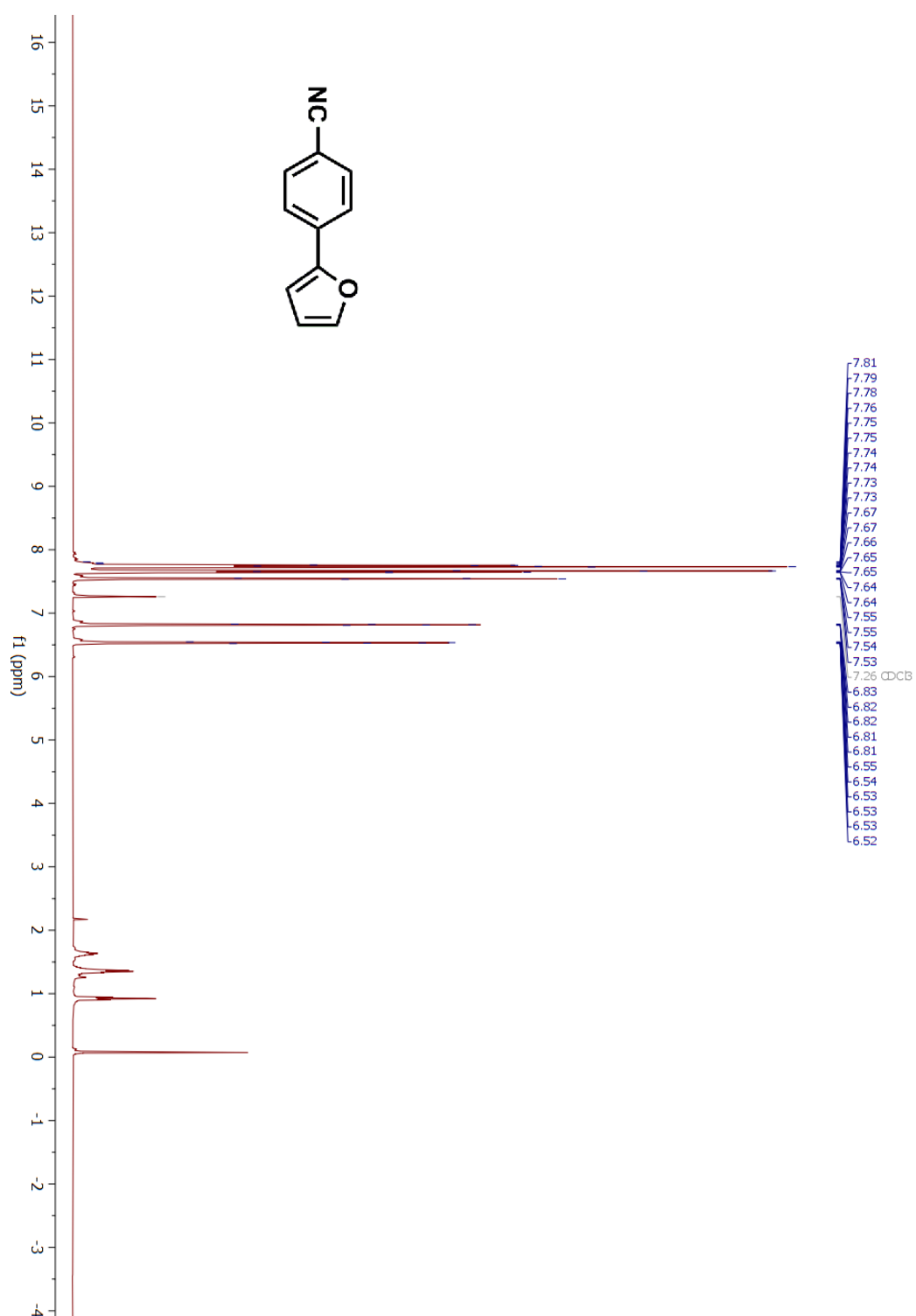


Figure A37. ^1H NMR spectrum of compound 17 in CDCl₃

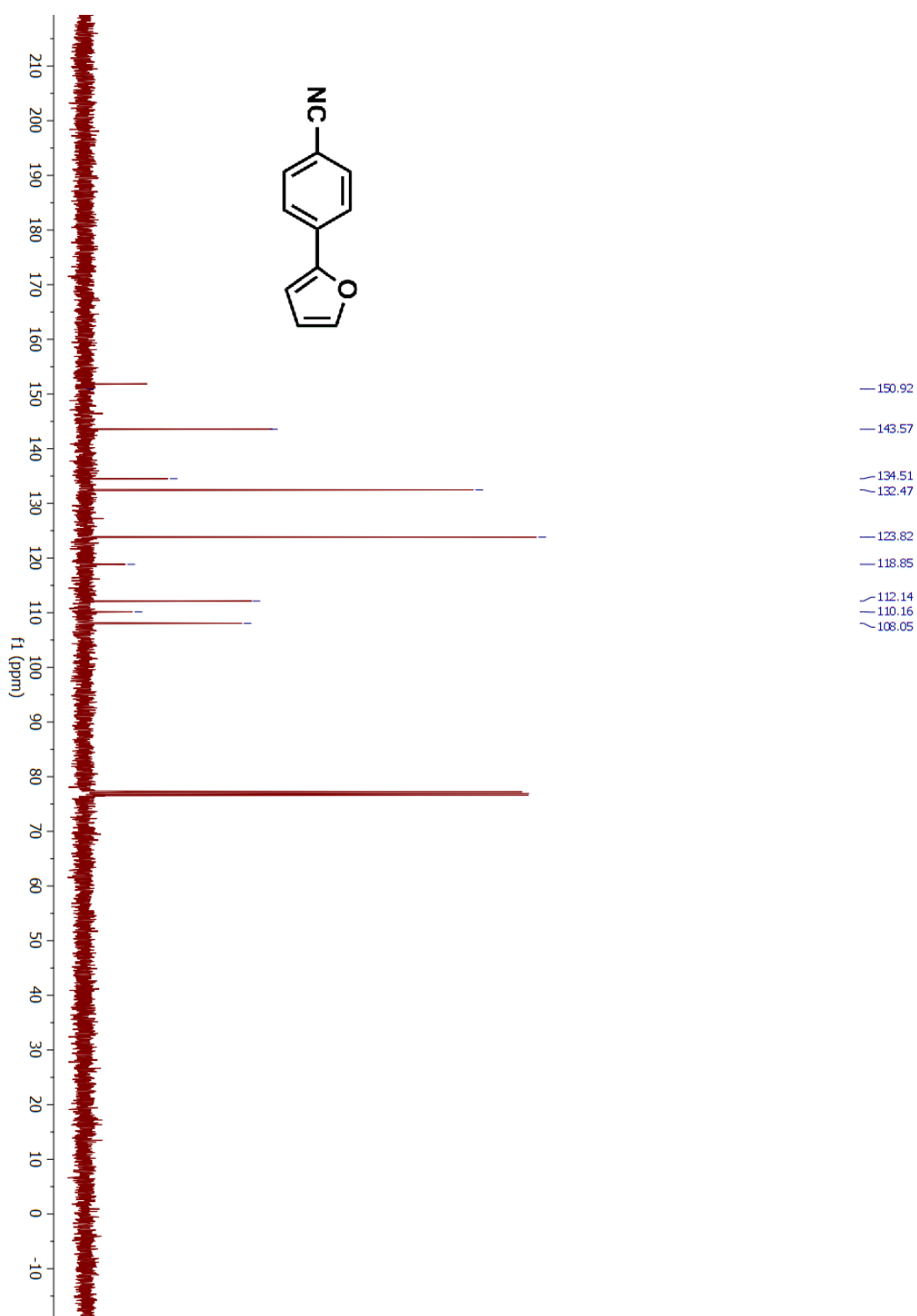


Figure A38. ^{13}C NMR spectrum of compound 17 in CDCl₃

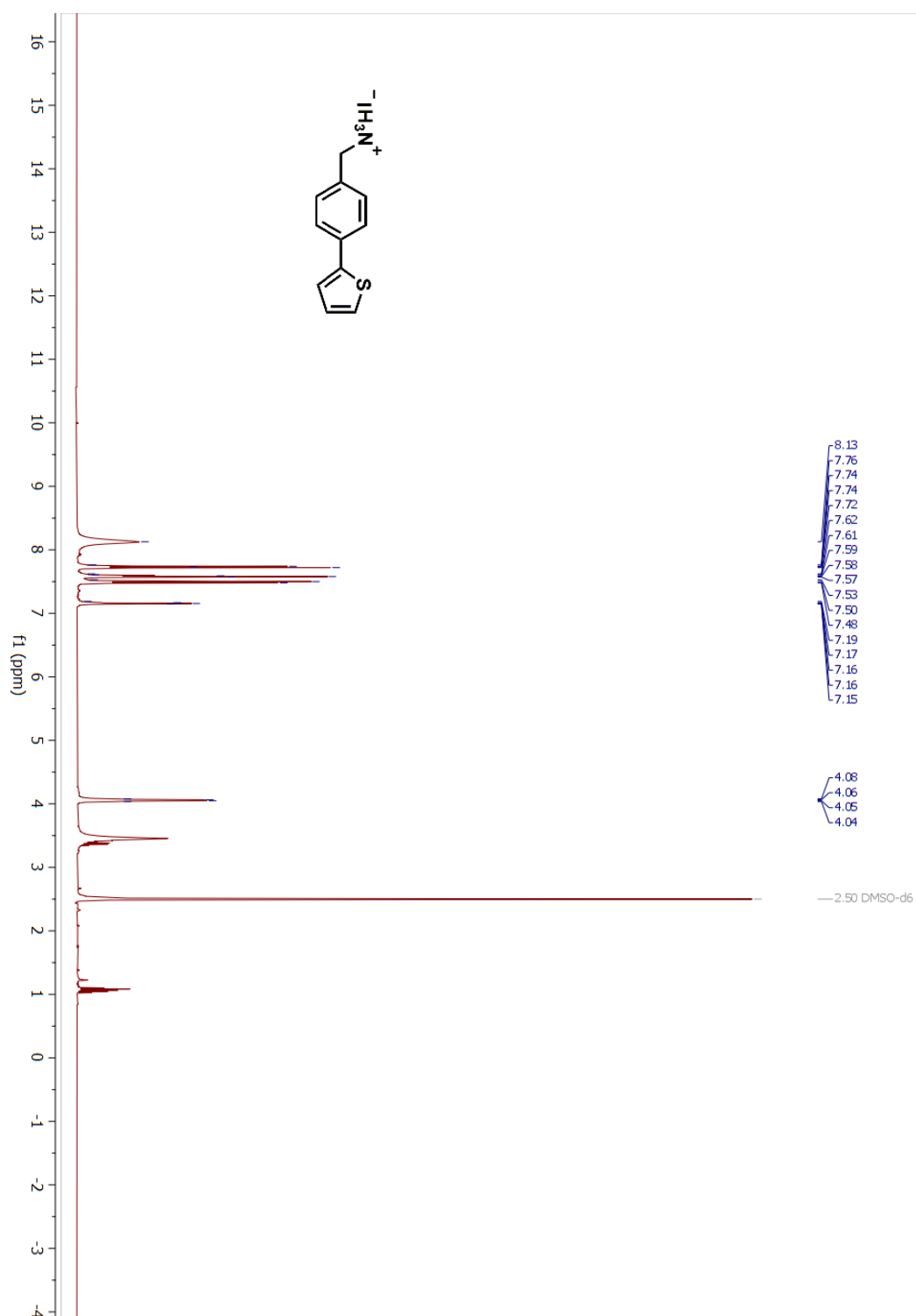


Figure A39. ¹H NMR spectrum of compound 21 in DMSO-d₆

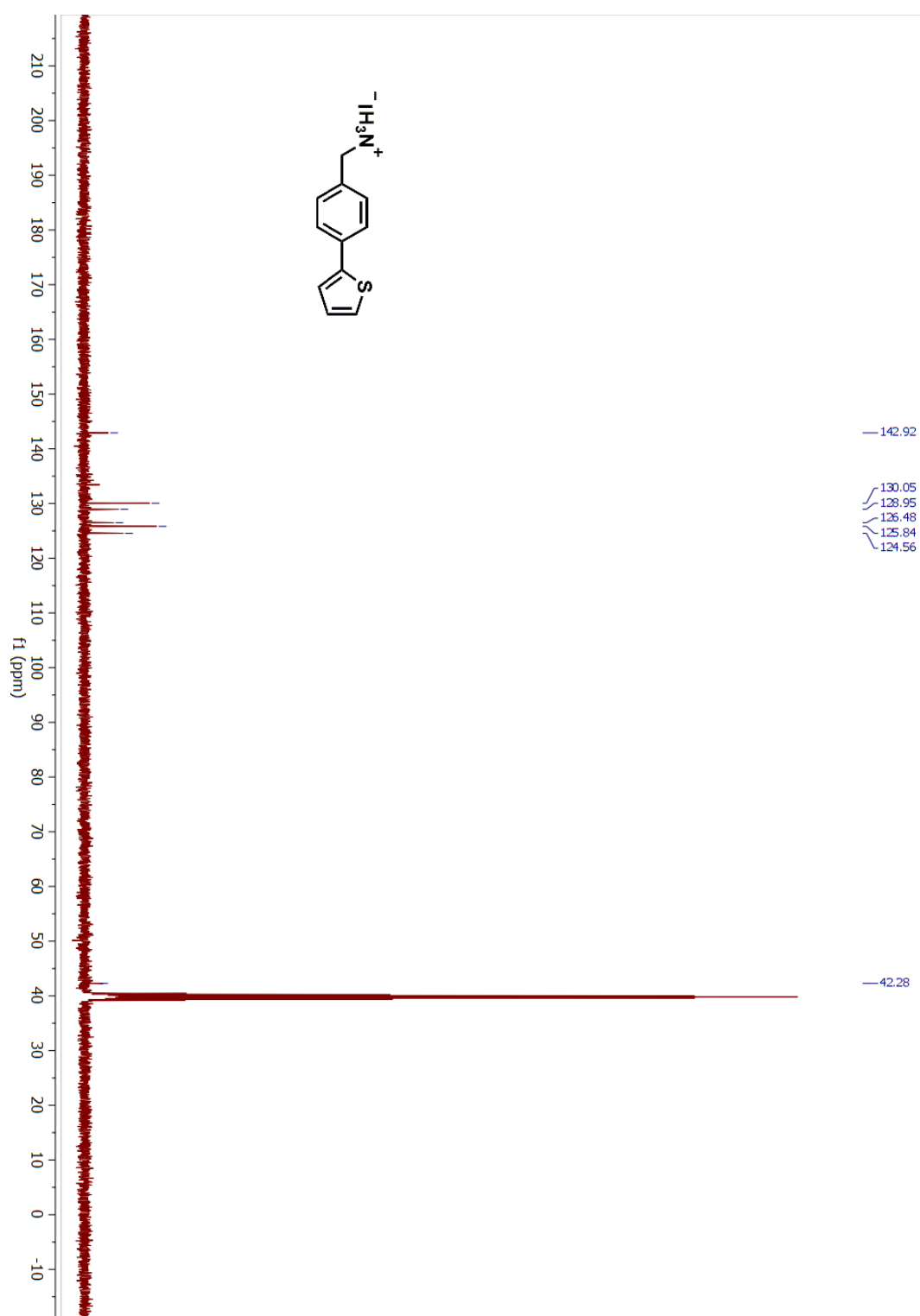


Figure A40. ^{13}C NMR spectrum of compound 21 in DMSO-d_6

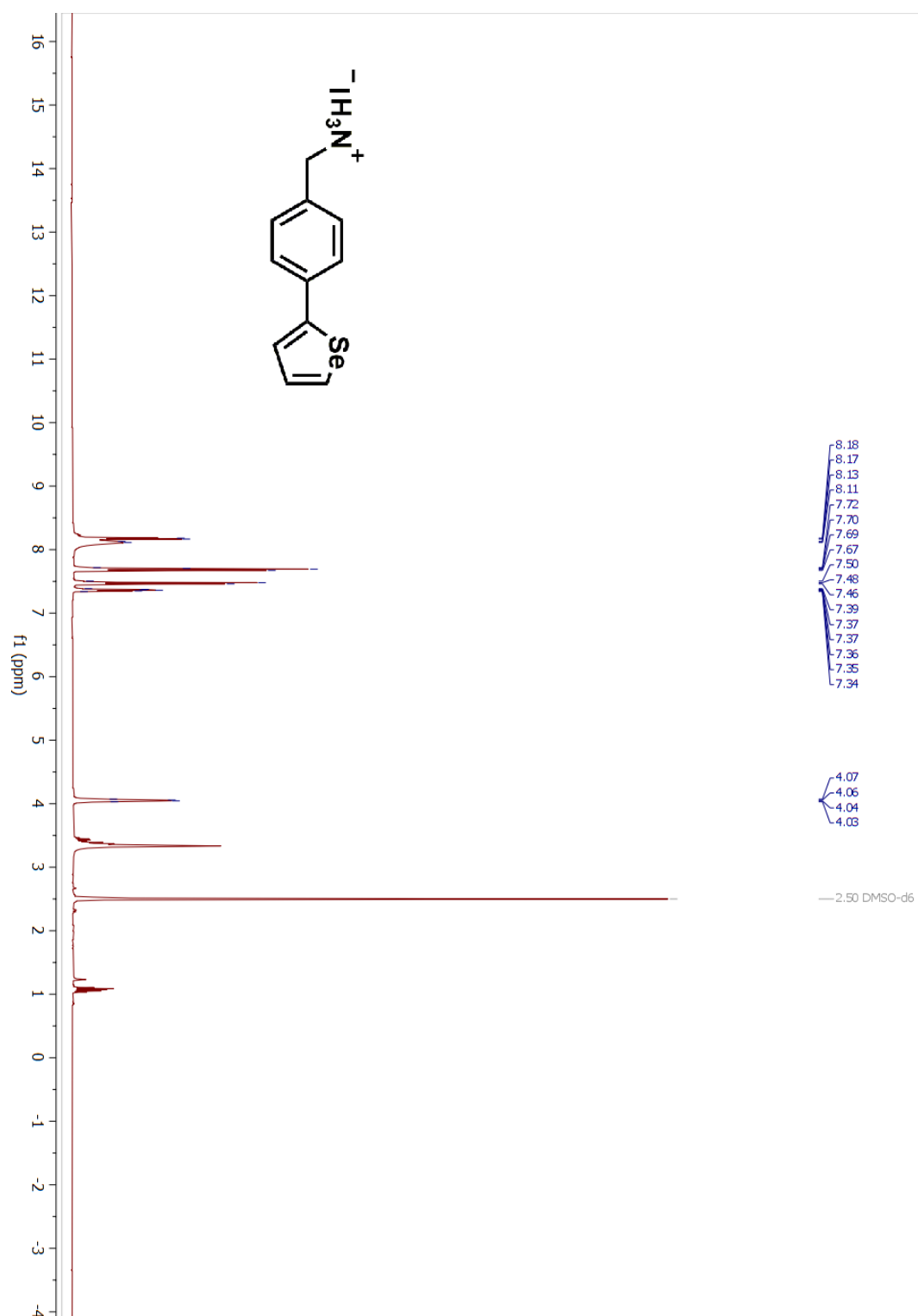


Figure A41. ¹H NMR spectrum of compound 22 in DMSO-d₆

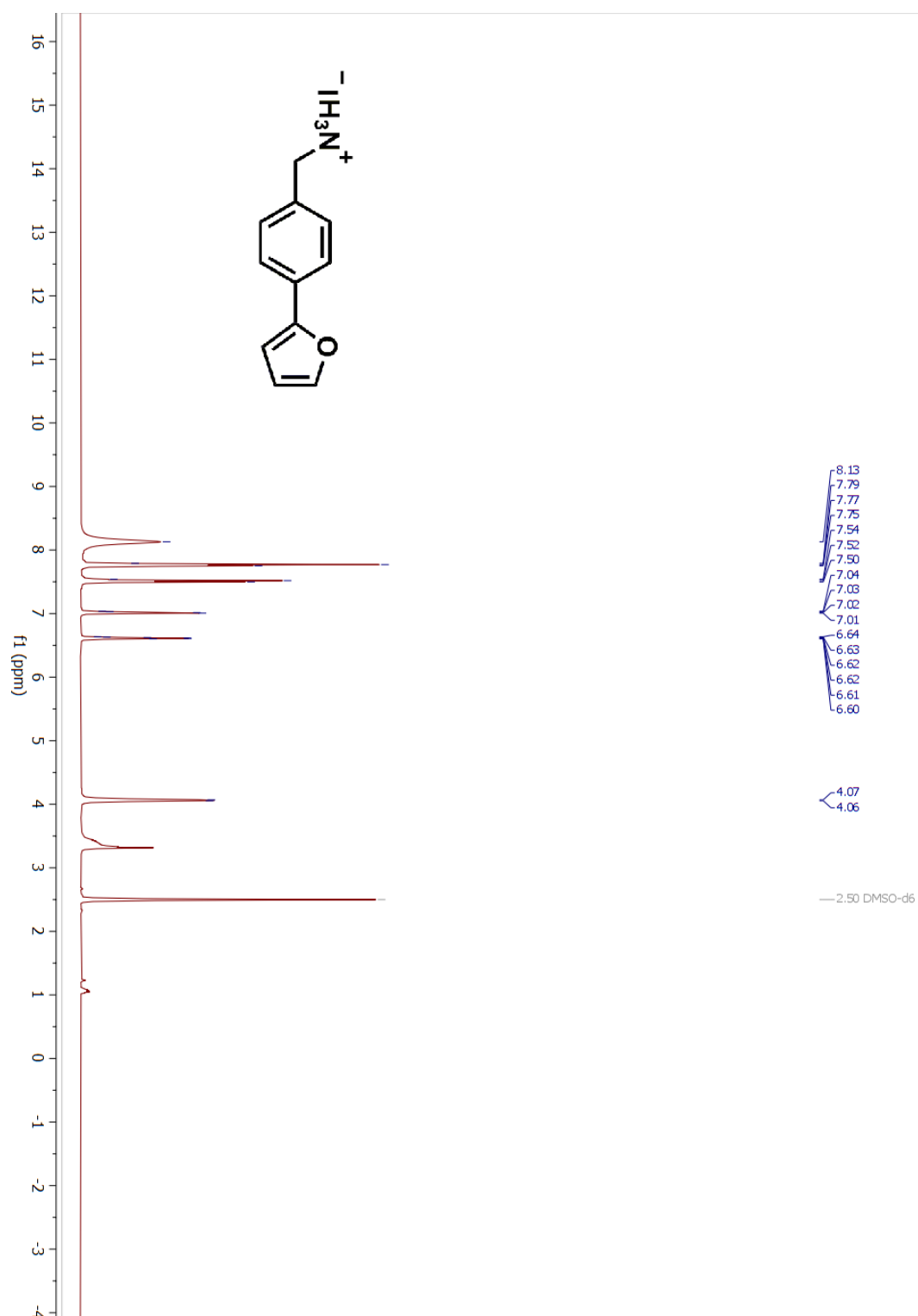


Figure A43. ¹H NMR spectrum of compound 23 in DMSO-d₆

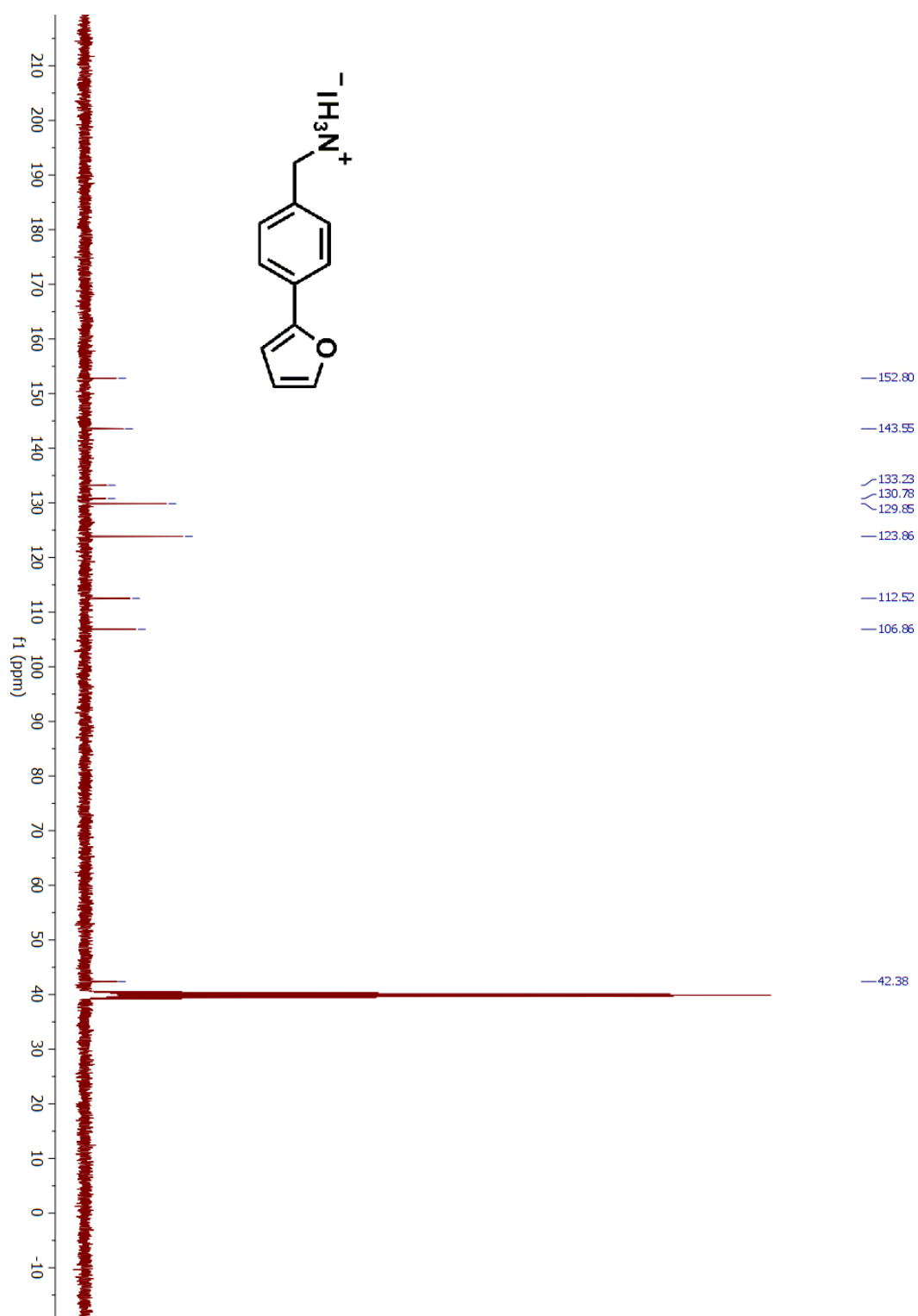


Figure A44. ^{13}C NMR spectrum of compound 23 in DMSO- d_6

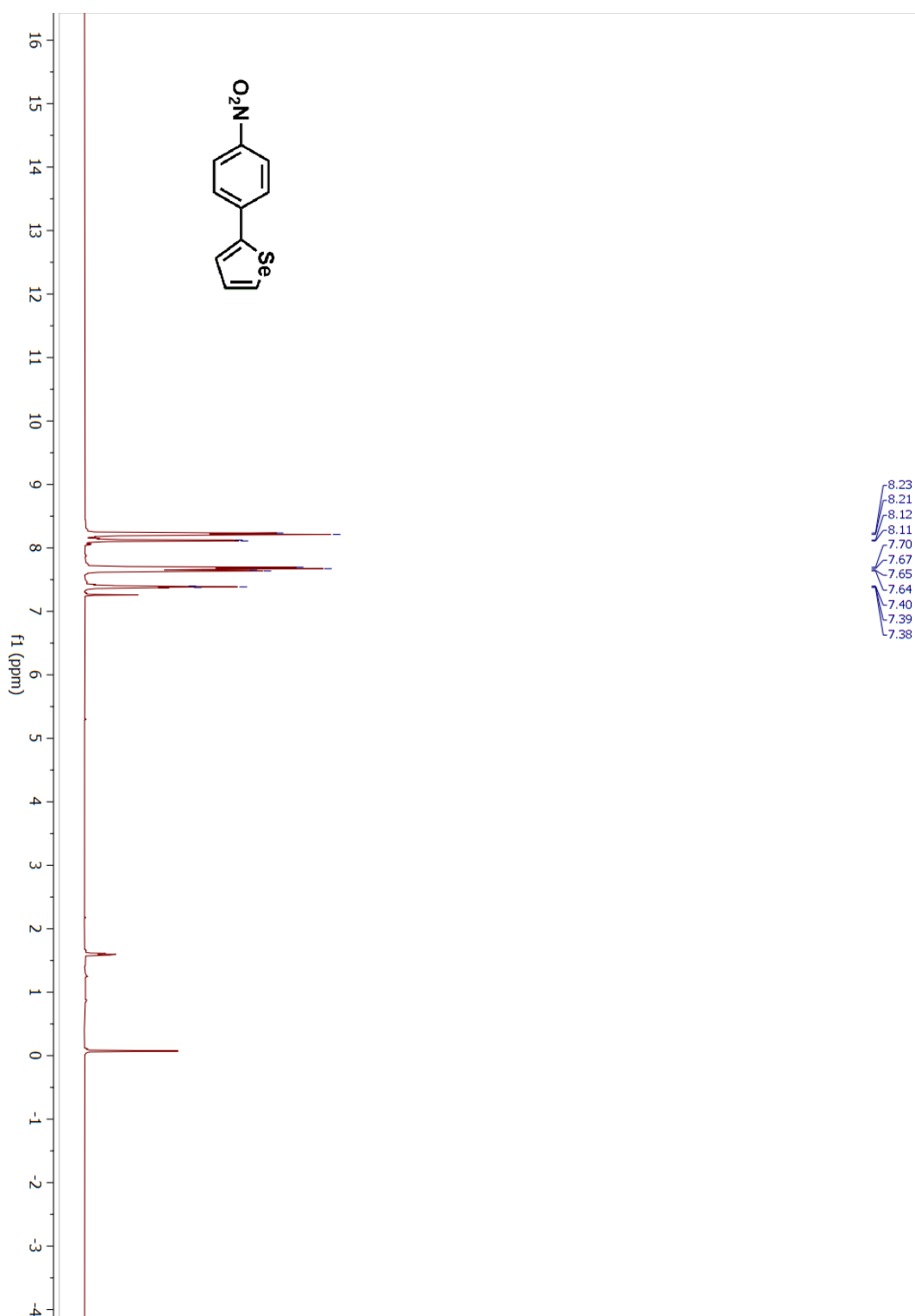


Figure A45. ^1H NMR spectrum of compound 24 in CDCl_3

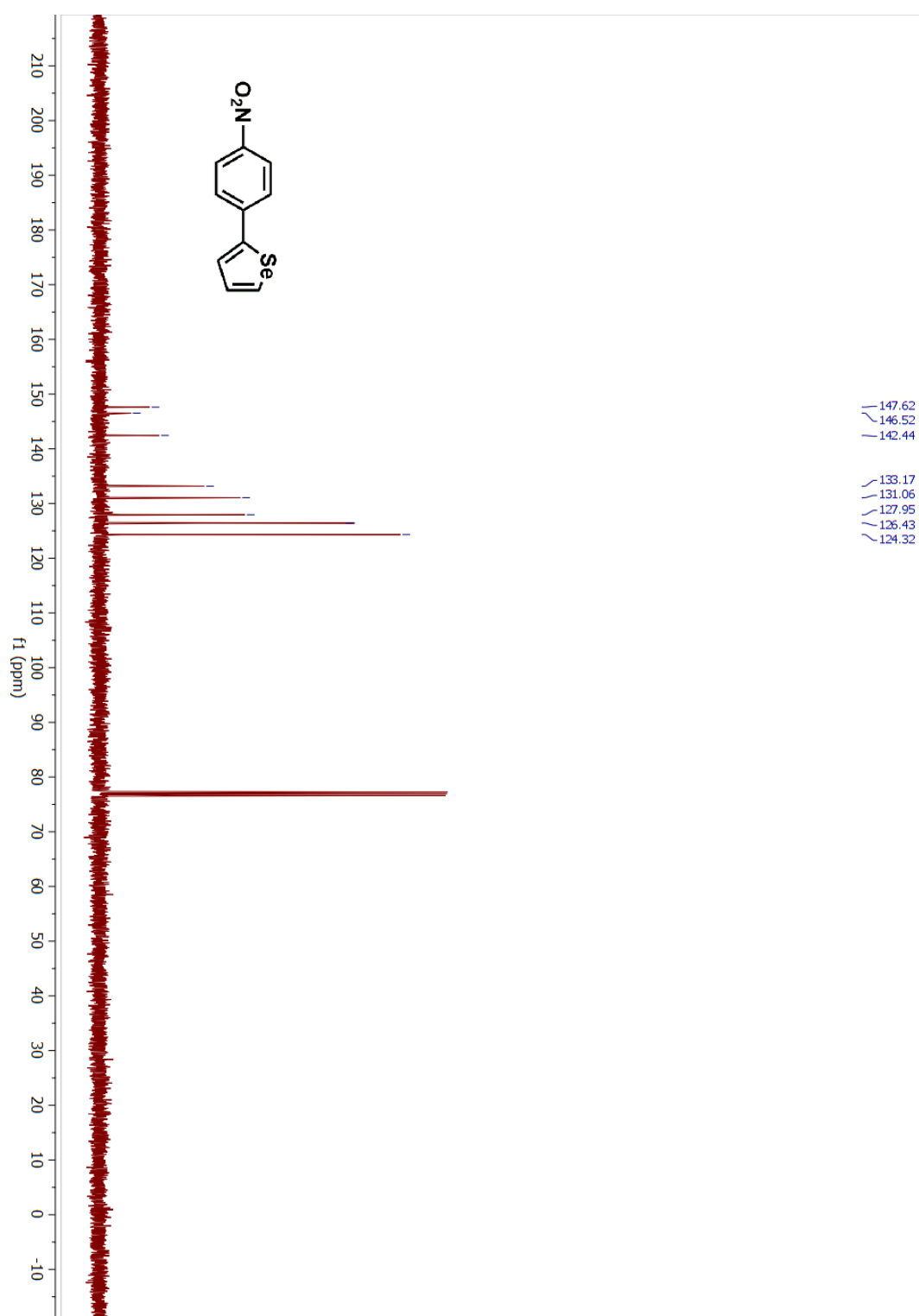


Figure A46. ¹H NMR spectrum of compound 24 in CDCl₃

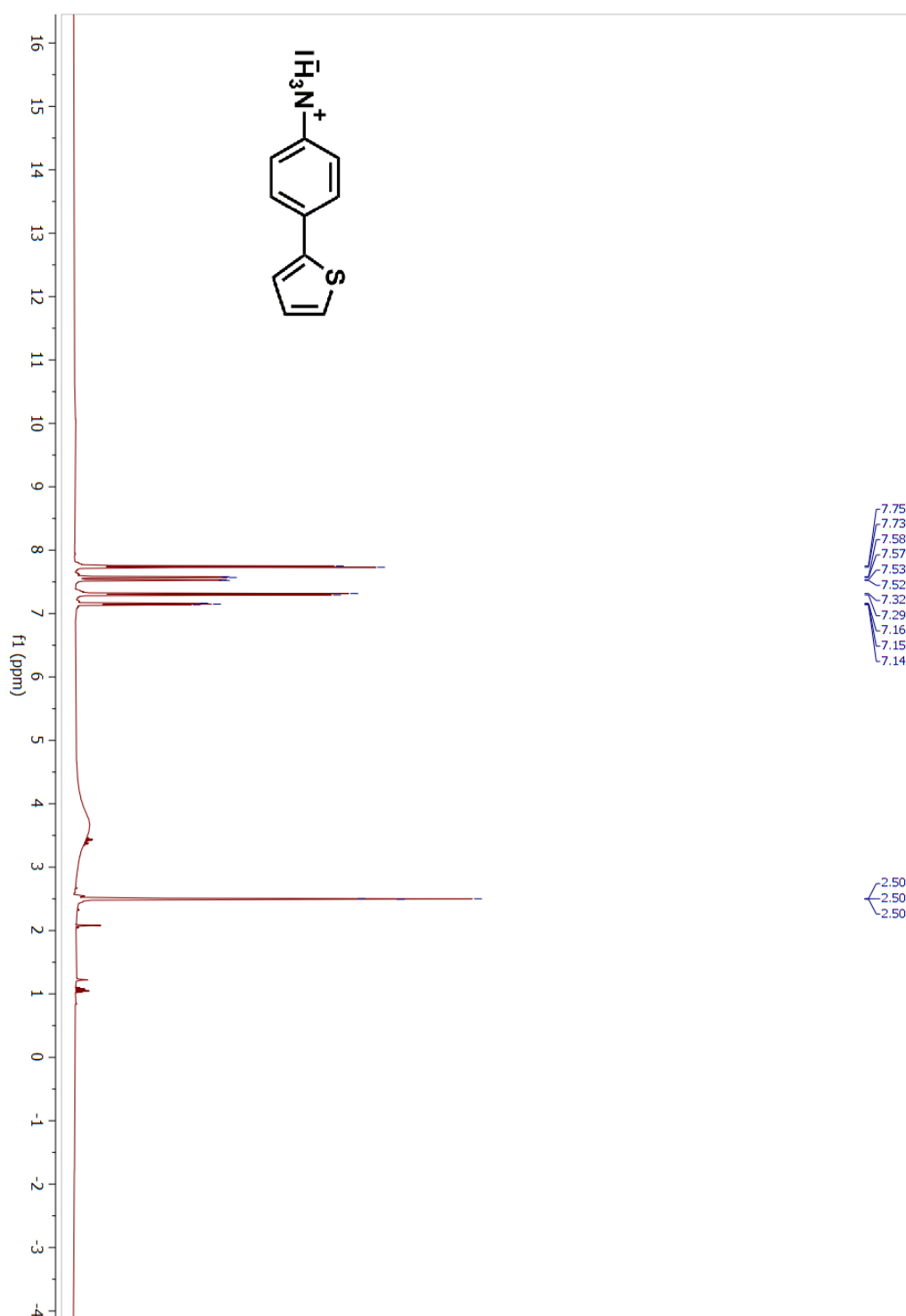


Figure A47. ^1H NMR spectrum of compound 28 in DMSO-d_6

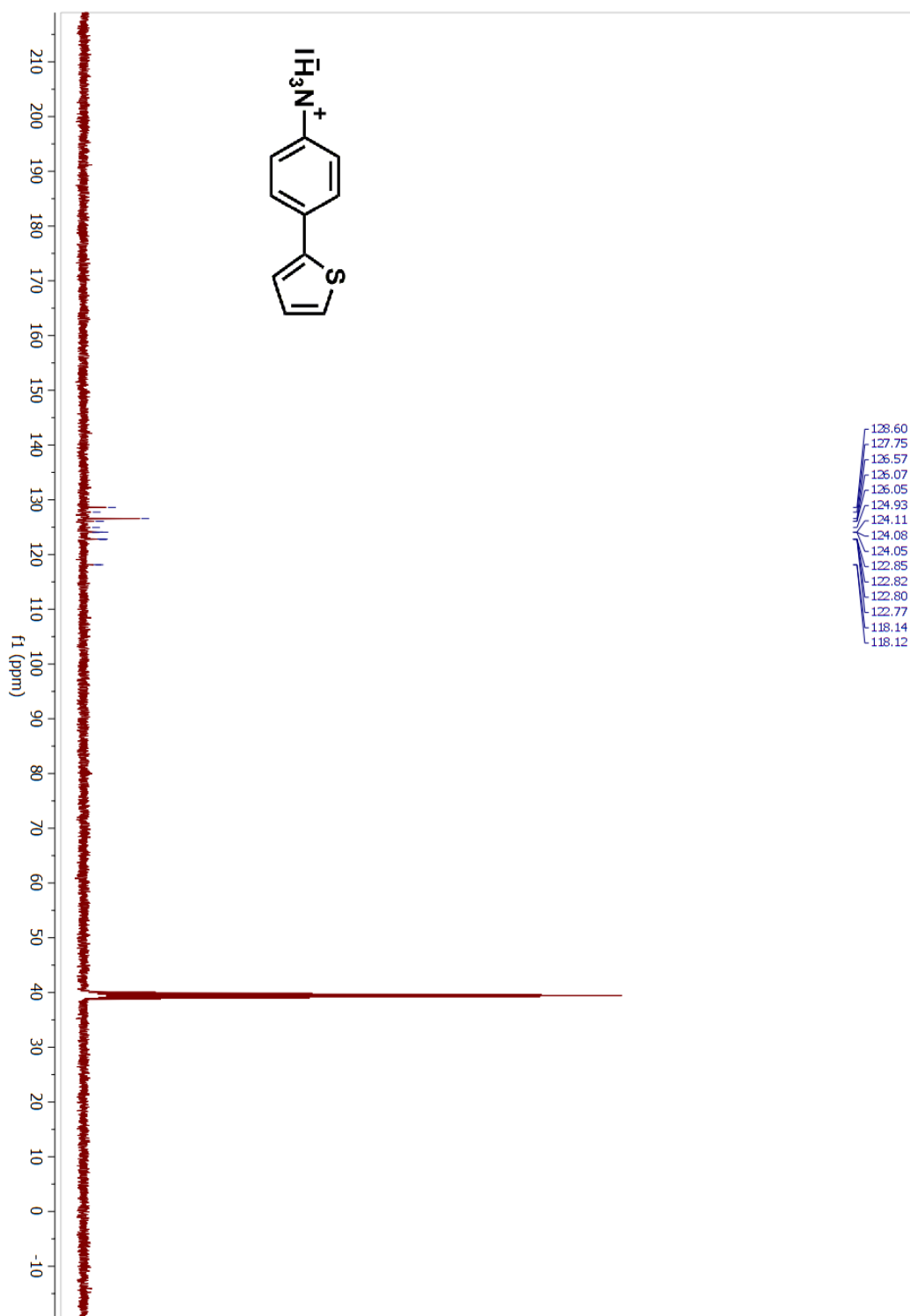


Figure A48. ^{13}C NMR spectrum of compound 28 in DMSO-d_6

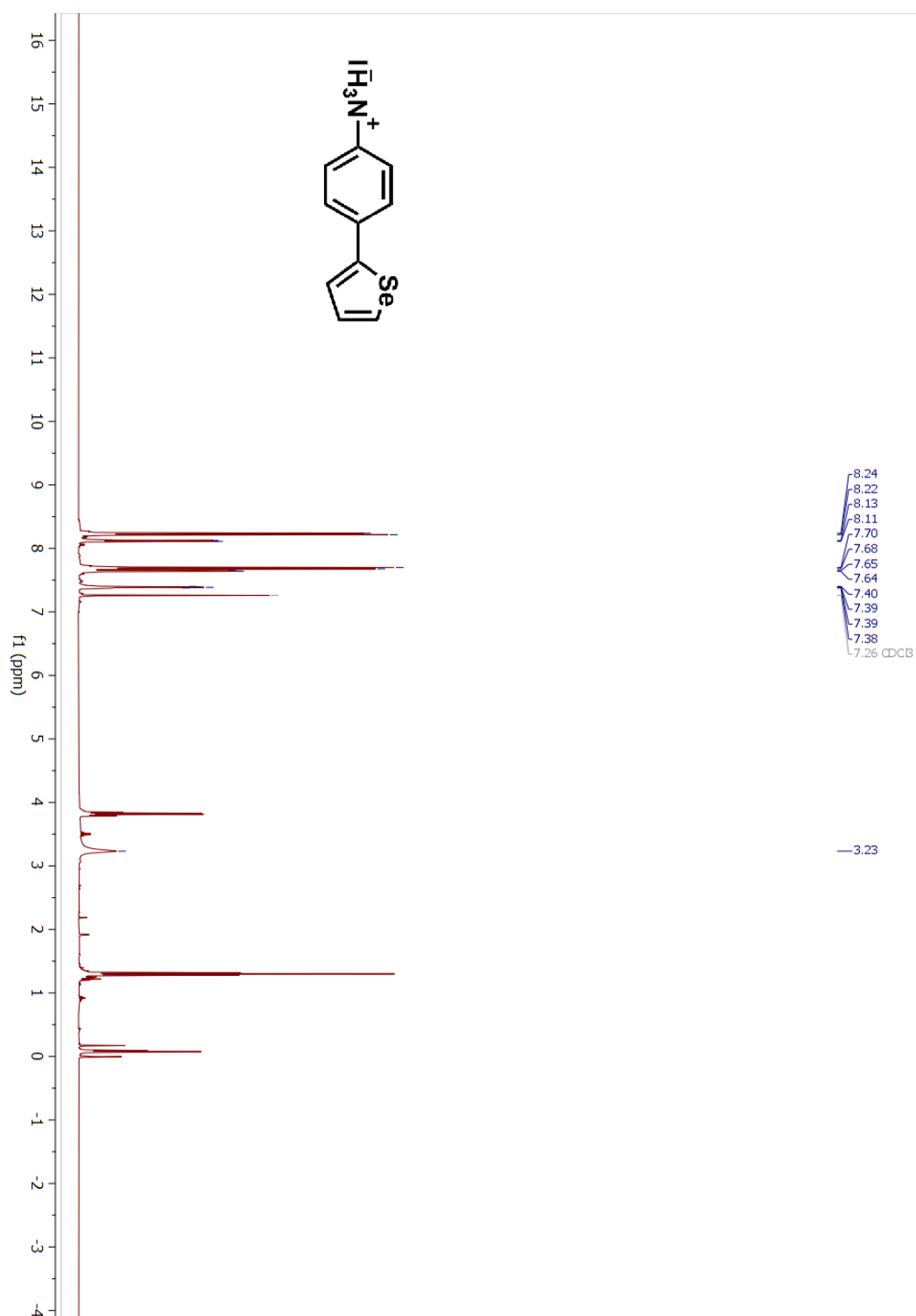


Figure A49. ¹H NMR spectrum of compound 29 in DMSO-d₆

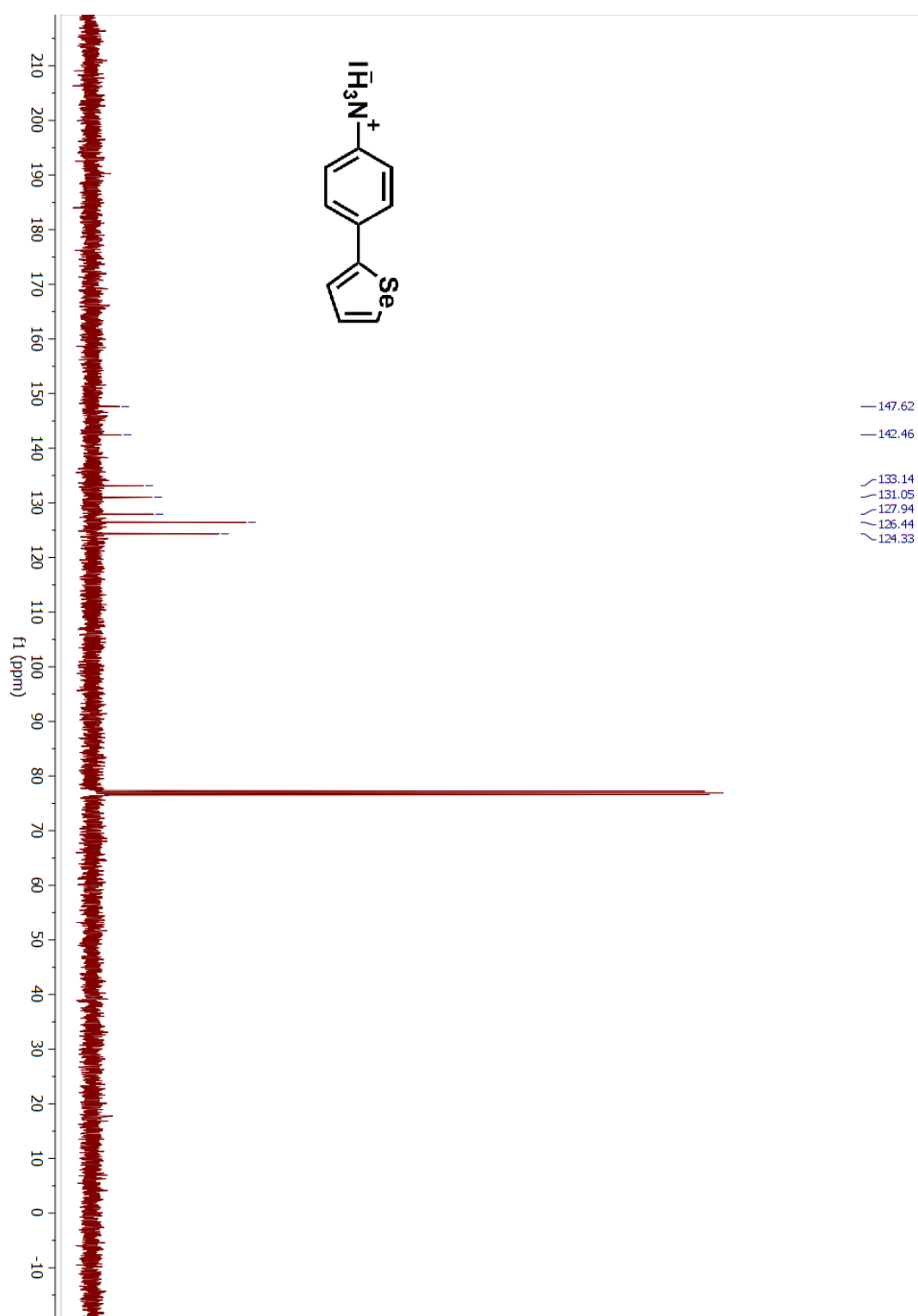


Figure A50. ¹³C NMR spectrum of compound 29 in DMSO-d₆

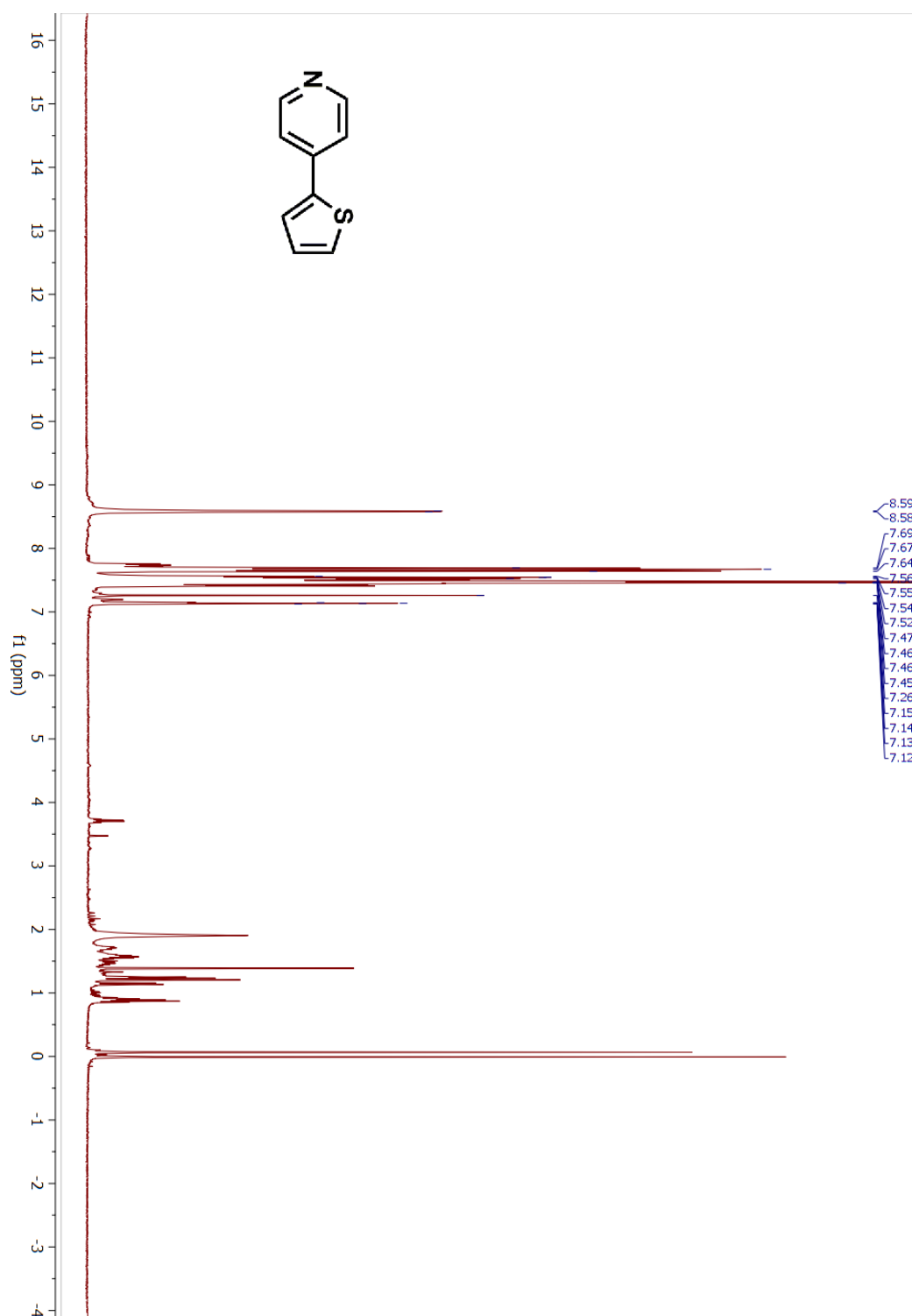


Figure A51. ^1H NMR spectrum of compound 30 in CDCl₃

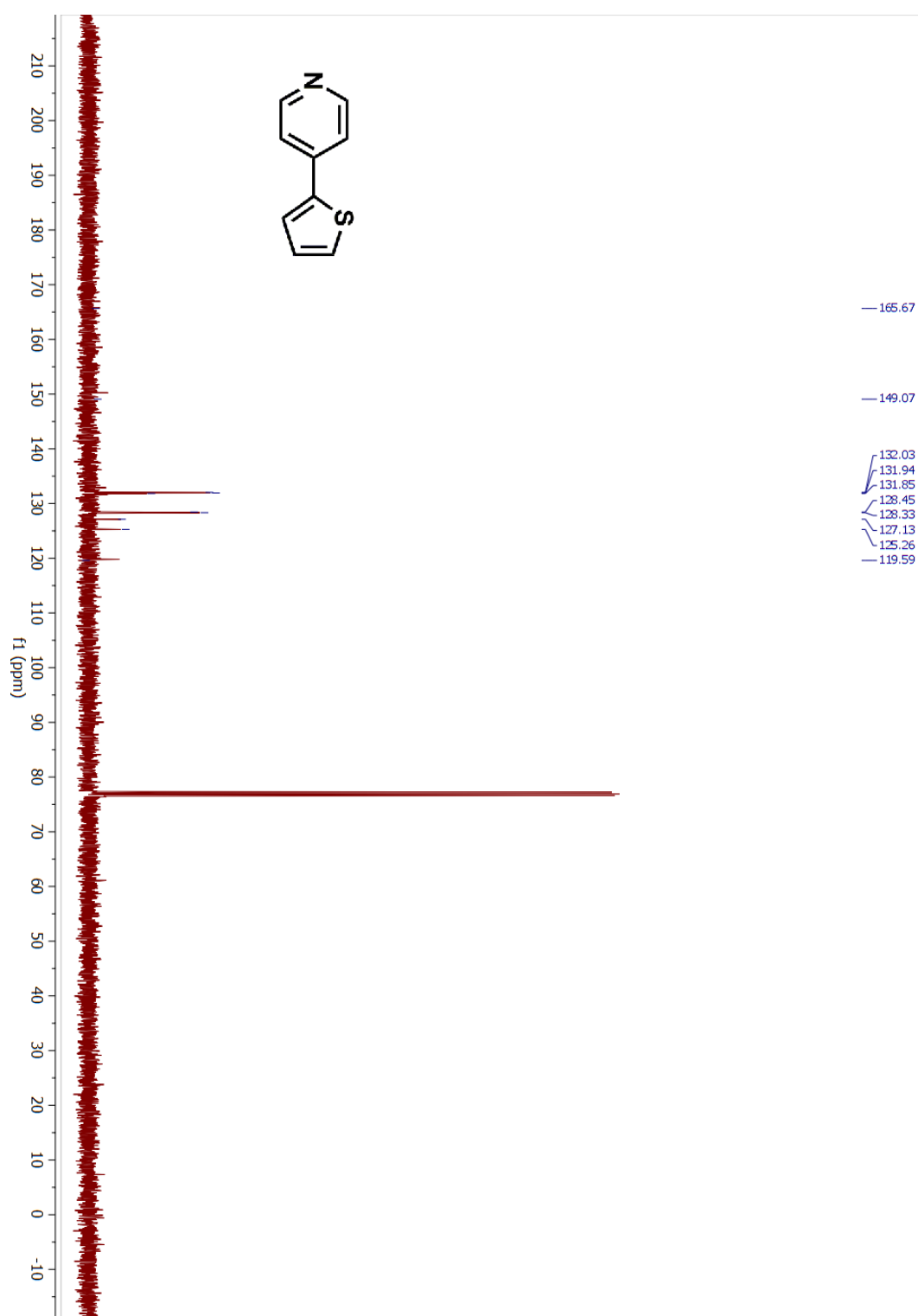


Figure A52. ^{13}C NMR spectrum of compound 30 in CDCl₃

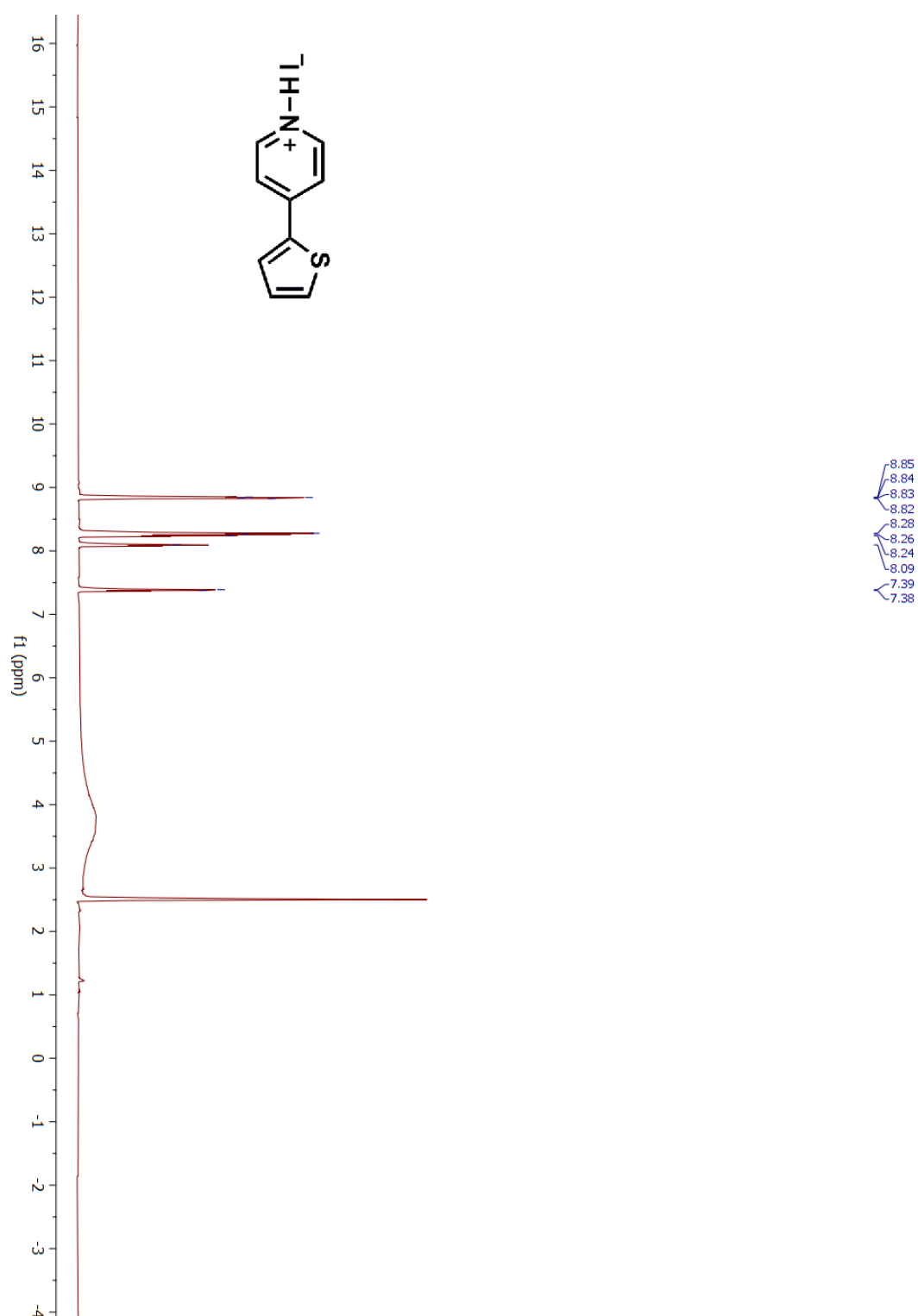


Figure A53. ¹H NMR spectrum of compound 31 in DMSO-d₆

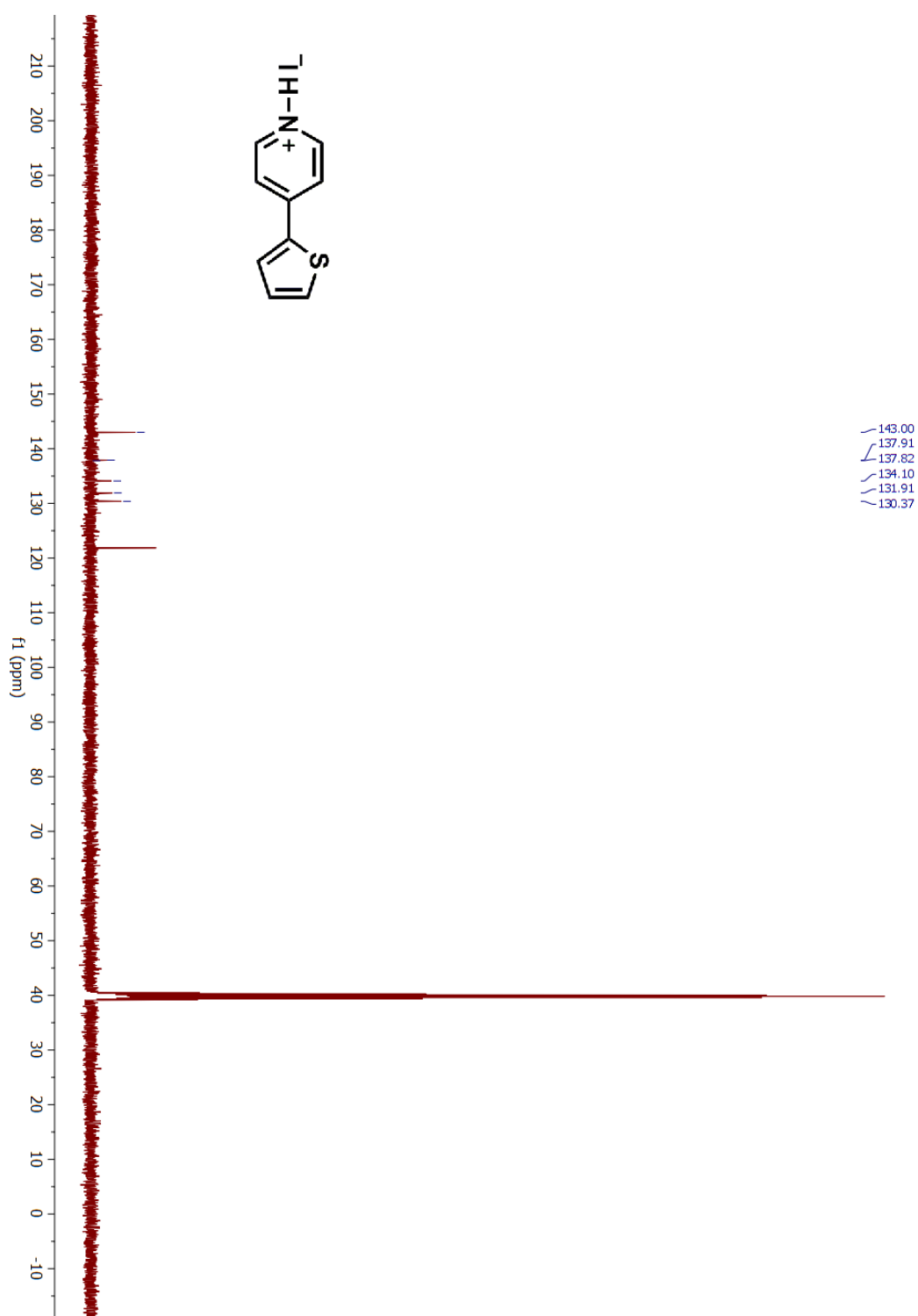


Figure A54. ¹³C NMR spectrum of compound 31 in DMSO-d₆

CURRICULUM VITAE

